STRESS INTENSITY FACTOR SOLUTIONS FOR LASER WELDS IN LAP-SHEAR SPECIMENS AND SPOT WELDS IN THE SQUARE OVERLAP PARTS OF CROSS-TENSION SPECIMENS

by

Kulthida Sripichai

A dissertation submitted in partial fulfillment
of the requirements for the degree of Doctor
of Philosophy
(Mechanical Engineering)
in The University of Michigan
2012

Doctoral Committee:

Professor Jwo Pan, Chair
Professor Will Hansen
Professor Elijah Kannatey-Asibu
Associate Professor Wei Lu

Dedicated to my father, mother and family
for their continuous support, understanding and love.

ACKNOWLEDGMENTS

I would like to express my sincere gratitude and thanks to my advisor, Professor Jwo Pan, for his continuous guidance, support and unlimited patience throughout my study. His guidance was essential to the completion of this dissertation. I also wish to extend my gratitude to my doctoral committee, Professor Elijah Kannatey-Asibu, Professor Wei Lu, Professor Will Hansen and Professor Jason P. McCormick for their guidance and valuable suggestions.

I am also thankful Dr. Jaewon Lee and Dr. Pai-Chen Lin. Their suggestions with the computational part of my thesis are very valuable. I also acknowledge the advice and support that I received from Dr. Van-Xuan Tran, on both the academic and personal levels. I am also grateful to Dr. Kamran Asim for his support on the laser welded lap-shear experiment. The stress-life fatigue test data for SAE 950X was provided by Dr. Peter Friedman, for which I am very grateful to him. I also appreciate the support from Professor Jwo Pan's research group, Teresa Jean Franklin, Katherine Avery and Hong, Seung Hoon for their help throughout my study.

TABLE OF CONTENTS

LIST OF FIGURES

LIST OF TABLES

CHAPTER I

INTRODUCTION

This thesis is written in two parts. The first part is related to the study of the analytical stress intensity factor solutions of laser welds in lap-shear specimens under cyclic loading conditions. The estimations of fatigue life based on the analytical stress intensity factor solutions are also investigated. Chapter II details the first part of the thesis. The second part of this thesis is related to the study of the stress intensity factor solutions for spot welds in the square overlap parts of cross-tension specimens. Chapters III, IV and V detail the second part of the thesis. Note that all these chapters were prepared as independent papers. Therefore, some parts of the thesis may be found repeated in these chapters.

1.1. Part I: Stress intensity factor solutions of laser welds in lap-shear specimens

Laser welding has been used more widely in the industry because of its advantages such as narrow heat affected zone, small distortion, and relatively high welding speed. A lap joint is one of common weld joints in laser welding due to its relative less restricted tolerance requirement. Due to the geometry of a lap joint, natural crack tips or notch tips are presented at the edges of the weld bead. Fatigue cracks usually are initiated from the natural crack or notch tips of lap joints. Laser welded components with lap joints are often subjected to cyclic loading conditions. In order to analyze the experimental results

for laser welded lap joints under cyclic loading condition based on a fracture mechanics approach, the stress intensity factor solutions of laser welded lap joints are required. However, there are no stress intensity factor solutions clearly given as functions of the geometric parameters for laser welded lap joints in the literature. Therefore, stress intensity factor solutions for laser welded lap joints are developed in this investigation for engineering applications. In Chapter II, fatigue experiments of laser welded lap-shear specimens of Asim et al. [1] are first reviewed. The analytical global stress intensity factor solutions for the main or natural cracks are then derived based on the beam bending theory. Finite element analyses of laser welded lap-shear specimens with different weld widths were carried out to obtain the stress intensity factor solutions of the main cracks for comparison with the analytical solutions. Based on the analytical stress intensity factor solutions obtained from the beam bending theory and the elasticity theory for two solids with connection, the transition weld width is determined and compared with the computational solutions. Approximate closed-form stress intensity factor solutions based on the results of the finite element analyses in combination with the analytical solutions for a full range of the normalized weld widths are developed for future engineering applications. Next, finite element analyses of laser welded lap-shear specimens with two weld widths were conducted to obtain the local stress intensity factor solutions for kinked cracks as functions of the kink length. The global stress intensity factor solutions and local stress intensity factor solutions for vanishing and finite kinked cracks are then adopted in a fatigue crack growth model to estimate the fatigue lives of the laser welds. Also, a structural stress model based on the beam bending theory is adopted to estimate the fatigue lives of the welds. The fatigue life estimations based on

the fatigue crack growth model and the structural stress model are then compared with the experimental results. Finally, conclusions are made.

1.2. Part II: Stress intensity factor solutions for spot welds in the square overlap parts of cross-tension specimens

Resistance spot welding is widely used to join sheet metals in the automotive industry. The fatigue lives of spot welds have been investigated by many researchers. Due to the geometry of spot welds, natural crack tips or notch tips are presented along the nugget circumference. Fatigue cracks usually are initiated from the natural crack or notch tips of lap joints. Stress intensity factor solutions for spot welds at the critical locations in various types of specimens have been developed to investigate the fatigue lives of spot welds. Lin and Pan [2, 3] proposed the closed-form structural stress and stress intensity factor solutions for spot welds in various types of specimens. In order to examine the accuracy of the analytical structural stress and stress intensity factor solutions for spot welds in lap-shear, square-cup, U-shape, cross-tension and coach-peel specimens presented in Lin and Pan [2, 3], it is necessary to first examine the analytical solutions for the square overlap parts of these specimens. Due to the structural stress solutions of Lin and Pan [13, 14] are based on the superposition of the solutions for a rigid inclusion in a square plate under opening loading and counter-bending loading conditions, in this part of the thesis, the investigation of the stress intensity factor solutions for spot welds in the square overlap parts of cross-tension specimens are written in three chapters.

In Chapter III, the structural stress solutions for a rigid inclusion in a square plate under opening loading conditions are first investigated. When the plate with the ratio of the plate width to the rigid inclusion becomes large, the structural stress solutions along the rigid inclusion circumference become uniform. Based on this assumption, the square plate then can be idealized to be a circular plate with an equivalent radius and the analytical structural stress solutions for a rigid inclusion in a circular plate can be then used for a rigid inclusion in a square plate. The values of the equivalent radius of the square plate are determined by the structural stress solutions obtained from finite element analyses. Then the stress intensity factor solutions for spot welds between two square plates of similar material, dissimilar materials, equal thickness and different thicknesses under opening loading condition are investigated. The analytical stress intensity factor solutions based on the analytical structural stress solutions for a rigid inclusion in a square plate with the equivalent radius are compared with the stress intensity factor solutions obtained from finite element analyses. Finally, complete sets of the normalized stress intensity factor solutions for combinations of steel, aluminum and magnesium sheets of different thicknesses and combinations of aluminum and copper sheets of different thicknesses are presented for convenient engineering applications.

In Chapter IV, the structural stress solutions for a rigid inclusion in a square plate under opening and bending loading conditions are investigated. For cross-tension specimens, the closed-form structural stress solutions of Lin and Pan [2, 3] can be expressed as a constant plus a cosine function. However, the distributions of the opening force and constraint moment per unit length along the two opposite outer edges are non-uniform while the closed-form structural stress solutions of Lin and Pan [2, 3] assume

that both the opening force and constraint moment per unit length along the two opposite outer edges are uniformly distributed. The coefficients for the structural stress solutions for a rigid inclusion in a square upper plate of a cross-tension specimen are therefore needed. The equivalent coefficients can be determined by the structural stress solutions at the critical locations obtained from finite element analyses. The numerical out-of-plane shear structural stress solutions are also introduced based on the amplitude of the cosine function of the in-plane structural stress solutions. Then the stress intensity factor solutions for spot welds between square plates of similar material with equal thickness under opening and bending loading conditions are investigated. The analytical stress intensity factor solutions based on the closed-form structural stress solutions for a rigid inclusion in a square plate with the equivalent coefficients are compared with the stress intensity factor solutions obtained from finite element analyses. The fitting coefficients for the stress intensity factor solutions accounting for the flexibility of spot welds are introduced. Finally, the analytical stress intensity factor solutions based on the closed-form structural stress solutions for a rigid inclusion in a square plate with the equivalent and numerical coefficients for the structural stress and the fitting coefficients for the stress intensity factor are compared with the stress intensity factor solutions obtained from finite element analyses.

In chapter V, , the J integral and analytical stress intensity factor solutions for spot welds in the square overlap parts of cross-tension specimens of different thicknesses and materials are developed. First, the analytical structural stress solutions for a rigid inclusion in a square plate under opening and bending loading conditions are reviewed. Then, the J integral and stress intensity factor solutions for spot welds between square

plates are presented in terms of the structural stresses for a strip model. With the available structural stress solutions, the analytical J integral and stress intensity factor solutions can be obtained. The analytical stress intensity factor solutions are selectively compared with the results of three-dimensional finite element analyses for spot welds between square plates under opening and bending loading conditions. Complete sets of the normalized stress intensity factor solutions at the critical locations for combinations of steel, aluminum and magnesium sheets of different thicknesses and combinations of aluminum and copper sheets of different thicknesses are presented for convenient engineering applications.

References

[1] Asim K, Lee J, Pan J. Failure mechanism of laser welds in lap-shear specimens of High Strength Low Alloy (HSLA) steels under cyclic loading conditions. 2010; to be submitted for publication.

[2] Lin PC, Pan J. Closed-form structural stress and stress intensity factor solutions for spot welds under various types of loading conditions. Int J Solids Struct 2008; 45: 3996-4020.

[3] Lin PC, Pan J. Closed-form structural stress and stress intensity factor solutions for spot welds in commonly used specimens. Eng Fract Mech 2008; 75: 5187-5206.

CHAPTER II

STRESS INTENSITY FACTOR SOLUTIONS FOR ESTIMATION OF FATIGUE LIVES OF LASER WELDS IN LAP-SHEAR SPECIMENS

2.1. Introduction

Laser welding has been used more widely in the industry because of its advantages such as narrow heat affected zone, small distortion, and relatively high welding speed. A lap joint is one of common weld joints in laser welding due to its relative less restricted tolerance requirement. Due to the geometry of a lap joint, natural crack tips or notch tips are presented at the edges of the weld bead. Fatigue cracks usually are initiated from the natural crack or notch tips of lap joints. Laser welded components with lap joints are often subjected to cyclic loading conditions. Many researchers investigated the fatigue lives of laser welded lap joints. Hsu and Albright [1] combined a static stress analysis with the Neuber's rule and established a model to calculate the fatigue life from the local stress and strain near the main notch. Wang and Ewing [2] conducted experiments to examine the fatigue strengths of resistance spot welds and laser welds under lap-shear loading conditions. Flavenott et al. [3] performed fatigue tests on laser welded lap joints with various welding parameters such as the weld bead geometry, the gap between the upper and lower sheets and the input energy of laser. Wang [4, 5] correlated the experimental fatigue lives of laser welds with the values of the *J*-integral from finite element computations. Zhang [6] proposed structural stress solutions based on the outer surface strains of laser welded lap joints.

Ono et al. [7] investigated the fatigue strength of laser welded lap joints and correlated the fatigue lives to the maximum stress intensity factor ranges. Terasaki et al. [8] examined the fatigue lives of laser welded lap joints and correlated the experimental results by the stress intensity factor solutions. Kaitanov et al. [9] showed that the fatigue strength of laser welded lap joints depends on the weld width. Cho et al. [10] examined the fatigue strength of laser welded lap joints with consideration of residual stresses obtained from thermo-mechanical finite element analyses. Sonsino et al. [11] examined laser welded tube-tube specimens by multiaxial fatigue theories. Sripichai et al. [12] investigated the fatigue lives of laser welded lap joints of high strength low alloy steel based on closed-form analytical and computational stress intensity factor solutions.

In order to analyze the experimental results for laser welded lap joints under cyclic loading condition, a fracture mechanics approach is adopted here. Stress intensity factor solutions of laser welded lap joints are required for this approach. However, there are no stress intensity factor solutions clearly given as functions of the geometric parameters for laser welded lap joints in the literature. Therefore, stress intensity factor solutions for laser welded lap joints are developed in this investigation for engineering applications. For thin plates and beams, Pook [13] adopted the energy release rate concept to determine stress intensity factor solutions of various configurations with connections based on the simple beam/plate bending theory. Newman and Dowling [14] adopted Pook's global stress intensity factor solutions to develop a fatigue crack growth model to predict the fatigue lives of spot welds. Lin et al. [15] adopted the fatigue crack growth model to model the kinked crack growth near spot welds in various types of specimens and correlated the predicted fatigue lives with the experimental results. Newman and

Dowling [14], Lin et al. [15] and Sripichai et al. [12] assumed the local stress intensity factors for kinked cracks emanating from spot welds and laser welds to be constant for all kink lengths in their fatigue crack growth models. Lin et al. [16, 17] and Tran et al. [18, 19] adopted the local stress intensity factor solutions of Wang and Pan [20] for kinked cracks as functions of the kink length to predict the fatigue lives of aluminum spot friction welds in lap-shear specimens.

Radaj [21] and Radaj and Zhang [22-24] established the foundation to use the structural stresses to determine the stress intensity factors for spot welds under various types of loading conditions. Zhang [25, 26] presented closed-form stress intensity factor solutions at the critical locations of spot welds in various types of specimens based on the analytical stress solutions for a plate with a rigid inclusion under various types of loading conditions, and correlated the solutions with the experimental results. It should be emphasized that the authors mentioned above used the structural stresses to estimate the stress intensity factor solutions at the critical locations of spot welds to correlate with the experimental results under cyclic loading conditions. The structural stress approach appears to be promising to estimate the fatigue lives of weld joints in thin plates. Tran et al. [18, 19] recently used the closed-form analytical structural stress solutions for spot welds to estimate the fatigue lives of aluminum spot friction welds.

In this chapter, fatigue experiments of laser welded lap-shear specimens of Asim et al. [27] are first reviewed. The analytical global stress intensity factor solutions for the main or natural cracks are then derived based on the beam bending theory. Finite element analyses of laser welded lap-shear specimens with different weld widths were carried out to obtain the stress intensity factor solutions of the main cracks for

comparison with the analytical solutions. Based on the analytical stress intensity factor solutions obtained from the beam bending theory and the elasticity theory for two solids with connection, the transition weld width is determined and compared with the computational solutions. Approximate closed-form stress intensity factor solutions based on the results of the finite element analyses in combination with the analytical solutions for a full range of the normalized weld widths are developed for future engineering applications. Next, finite element analyses of laser welded lap-shear specimens with two weld widths were conducted to obtain the local stress intensity factor solutions for kinked cracks as functions of the kink length. The global stress intensity factor solutions and local stress intensity factor solutions for vanishing and finite kinked cracks are then adopted in a fatigue crack growth model to estimate the fatigue lives of the laser welds. Also, a structural stress model based on the beam bending theory is adopted to estimate the fatigue lives of the welds. The fatigue life estimations based on the fatigue crack growth model and the structural stress model are then compared with the experimental results. Finally, conclusions are made.

2.2. Experimental results for laser welds in lap-shear specimens of HSLA steel

The experiment of Asim et al. [27] is first briefly reviewed here. Lap-shear specimens were made by using two 97 mm by 27 mm non-galvanized HSLA sheets with a nominal thickness of 1 mm. The specimens were welded with 6 kW CO_2 laser with a welding speed of 8 m/min. The specimens were then cut into a dog-bone shape. Figures 2.1(a) and 2.1(b) show top and bottom views of a laser welded lap-shear specimen, respectively. The width and length of the uniform narrow part of the dog-bone area is 8

mm and 15 mm, respectively. Two doublers of 50 mm by 27 mm are used to align the applied load to avoid the initial realignment of the specimen under lap-shear loading conditions and to strengthen the gripping holes of the specimen. The lap-shear specimens were tested by using an Instron servo-hydraulic fatigue testing machine with a load ratio $R = 0.2$. The test frequency was 10 Hz. The tests were terminated when specimens either separated or nearly separated. Figure 2.2 shows the experimental results of laser welded lap-shear specimens under cyclic loading conditions. The mechanical properties and hardness across the weld are given in Asim et al. [27] in detail.

Figure 2.3 shows a micrograph of the cross section of a partially failed laser weld in a specimen under the load range of 1,646 N at the fatigue life of 10,129 cycles. The arrows in the figure schematically show the direction of the applied load. As shown in the figure, two fatigue cracks were initiated near the main crack tips on the edges of the laser weld. The two fatigue cracks can be considered as kinked cracks with respect to the main crack tips. The experimental results show that one kinked crack usually becomes dominant and results in the final failure of the specimen. The kink angles are all close to $90°$ based on the micrographs of the cross sections of nearly failed and failed welds.

2.3. Analytical global stress intensity factor solutions

Figure 2.4 shows a schematic of a lap-shear specimen. As shown in the figure, the specimen has the width W, the sheet thickness t, and the length L for the upper and lower sheets. Note that the upper and lower sheets have the same thickness. The specimen has the overlap length V, the width b and the uniform length l for the central portion of the dog-bone area respectively. The width w of the laser weld zone of the

specimen is indicated as the shaded area. The specimen has two doublers with length d. The applied force F is shown as the bold arrows. The elastic beam bending theory is adopted here to derive the analytical stress intensity factor solutions as in Pook [13]. The weld zone is assumed to have the same elastic properties as the base metal. The weld protrusion as shown in Figure 2.3 is not considered in the derivation of the analytical solutions in this chapter. Since the specimen length L and the overlap length V are much larger than the sheet thickness t and the weld width w, the analytical solutions are only expressed in terms of the weld width w, the sheet thickness t, the specimen width b, and the applied force F.

As in Radaj [21], Radaj and Zhang [22-24], Lin et al. [28], and Lin and Pan [29], the load of a lap-shear specimen can be decomposed into statically equivalent symmetric and anti-symmetric loads. Figure 2.5 shows a schematic of the decomposition of the shear load of a lap-shear specimen. Here, the dog-bone area of a lap-shear specimen is modeled as two beams with connection. For the two-beam model shown in Figure 2.5(a), F/b represents the force per unit width of the dog-bone area. The forces per unit width, F/b, are applied along the interfacial surface of the two beams. In Figure 2.5(b), the forces per unit width, F/b, now become the membrane forces per unit width, F/b, and the bending moments per unit width, $Ft/2b$, applied at the middle surface of the upper and lower beams. Both applied membranes forces and bending moments shown in Figure 2.5(b) are statically equivalent to the shear forces of the two beams shown in Figure 2.5(a). The membrane forces and bending moments shown in Figure 2.5(b) can further be decomposed into four types of symmetric and anti-symmetric loading conditions: counter bending (Figure 2.5(c)), central bending (Figure 2.5(d)), tension

(Figure 2.5(e)) and in-plane shear (Figure 2.5(f)). The bending moments per unit width of the counter bending and central bending loading conditions have a magnitude of $Ft/4b$, and the forces per unit width of the tension and in-plane shear loading conditions have a magnitude of $F/2b$.

Three types of loading conditions in Figures 2.5(c), 2.5(d), and 2.5(f) give different opening and shear modes of the main crack. The counter bending loading condition gives mode I (opening mode) loading to the main crack while the central bending and in-plane shear loading conditions give mode II (in-plane shear mode) loading to the main crack. Thus, the K_{I} solution can be derived from the two beams under counter bending conditions (Figure 2.5(c)), while the K_{II} solution can be derived from the two beams under central bending and in-plane shear loading conditions (Figure 2.5(d) and 2.5(f)). Note that the tension loading condition (Figure 2.5(e)) does not give any stress intensity factor solutions. The detailed derivation of the stress intensity factor solutions based on the beam bending theory is presented in Appendix A. From Equation (2.A14) in Appendix A, the stress intensity factor K_{I} solution is determined from the counter bending loading condition as

$$K_{\mathrm{I}} = \frac{\sqrt{3}}{2}\frac{F}{b\sqrt{t}} \tag{2.1}$$

Similarly, from Equation (2.A15) in Appendix A, the stress intensity factor K_{II} solution is determined from the central bending and in-plane shear loading conditions based on the superposition principle as

$$K_{\mathrm{II}} = \frac{F}{b\sqrt{t}} \tag{2.2}$$

Equations (2.1) and (2.2) were derived based on the assumption that the weld width w is large compared to the thickness t of the upper and lower sheets. This assumption will be examined by the results of finite element analyses presented later in the chapter.

When the weld width w becomes small compared to the thickness t, the stress intensity factor solutions should approach to the K_{I} and K_{II} solutions for two semi-infinite solids with connection under shear loading conditions based on the Westergaard stress function in Tada et al. [30]. Figure 2.6 shows a schematic diagram of two semi-infinite solids with connection of the length w under shear loading conditions. The Cartesian coordinate $x-y$ system is also shown. The forces per unit width F/b are applied along the x axis at $x=+\infty$ and $-\infty$ of the upper and lower solids, respectively. The stress intensity factors $K_{\mathrm{II,TPI}}$ and $K_{\mathrm{I,TPI}}$ based on the Westergaard stress function [30] are

$$K_{\mathrm{II,TPI}} = \frac{\sqrt{2}F}{b\sqrt{\pi w}} \tag{2.3}$$

and

$$K_{\mathrm{I,TPI}} = 0 \tag{2.4}$$

As the weld width increases, the $K_{\mathrm{II,TPI}}$ exact solution in Equation (2.3) based on the Westergaard stress function decreases. A transition weld width w_t can be determined when $K_{\mathrm{II,TPI}} = K_{\mathrm{II}}$. Equations (2.2) and (2.3) give the normalized transition weld width of $w_t/t = 2/\pi \approx 0.64$. Note that the normalized transition weld width w_t/t cannot be determined from K_{I} and $K_{\mathrm{I,TPI}}$ since both K_{I} and $K_{\mathrm{I,TPI}}$ are constants. Theoretically speaking, it is possible that when the weld width is larger than w_t, the analytical

solutions in Equations (2.1) and (2.2) are applicable. This has to be validated by the results of the finite element analyses as reported in the following.

2.4. Computational global stress intensity factor solutions

Finite element analyses were carried out in order to obtain the global stress intensity factor solutions as functions of the weld width and to determine the ranges of the weld width where the two sets of the analytical solutions are applicable. Figure 2.7(a) shows a schematic of a two-dimensional finite elemental model of a lap-shear specimen and the boundary conditions. The specimen has the sheet thickness t, the length L, the overlap length V, and the weld width w. Both upper and lower sheets have the same thickness t. The $x-y$ coordinate system is shown in the figure. The left edge has a fixed displacement condition at the middle surface while the right edge has a concentrated force per unit width, F/b, applied at the middle surface in the $+x$ direction. Here, F denotes the applied force and b denotes the width of the central portion of the dog-bone area of the specimen.

The two-dimensional plane-strain finite elemental model has the sheet thickness $t = 1$ mm, length $L = 82$ mm, overlap length $V = 15$ mm and doubler length $d = 35$ mm. The width b of the central portion of the dog-bone area of the specimen used in the model is 8 mm. Here, the weld width w is varied in order to investigate the effect of weld width on the global stress intensity factor solutions. Note that the length L is taken between the left edge and the center of the hole of the upper sheet as shown in Figure 2.1. The displacements of the middle surface of the left edge in the x and y directions are constrained as shown in the figure. Figures 2.7(b) and 2.7(c) show the right part of the

finite element mesh for $w/t = 1$ and a close-up view of the mesh near the right main crack tip, respectively. The weld protrusion of the lower sheet as shown in Figure 2.3 is not modeled in the finite element analyses. The effect of the weld protrusion on the weld failure was investigated in Lee at al. [31] and Asim et al. [27] under quasi-static and cyclic loading conditions, respectively. The weld metal and the base metal are assumed to be linear elastic with the Young's modulus $E = 210$ GPa and the Poisson's ratio $\nu = 0.3$. Second-order quarter point crack-tip elements with collapsed nodes were used to model the $1/\sqrt{r}$ singularity near the crack tip. The commercial finite element program ABAQUS [31] was employed to perform the computation.

Figure 2.8 shows the normalized computational $\overline{K}_{\mathrm{I}}$ and $\overline{K}_{\mathrm{II}}$ solutions, the normalized $\overline{K}_{\mathrm{II,TPI}}$ solution based on the Westergaard stress function, and the normalized $\overline{K}_{\mathrm{I}}$ and $\overline{K}_{\mathrm{II}}$ solutions based on the beam bending theory as functions of the normalize weld width w/t. All solutions shown in Figure 2.8 are normalized by the K_{II} solution based on the beam bending theory in Equation (2.2). As shown in the figure, when the normalized weld width w/t increases, the normalized computational $\overline{K}_{\mathrm{I}}$ and $\overline{K}_{\mathrm{II}}$ solutions approach to the analytical solutions based on the beam bending theory in Equations (2.1) and (2.2). As the normalized weld width w/t decreases, the normalized computational $\overline{K}_{\mathrm{I}}$ and $\overline{K}_{\mathrm{II}}$ solutions approach to the analytical solutions based on the Westergaard stress function in Equations (2.4) and (2.3). When $w/t \geq 2$, the computational K_{II} solution is equal to the analytical K_{II} solution. When $w/t \geq 4$, the computational K_{I} solution is equal to the analytical K_{I} solution. Table 1 lists the normalized computational $\overline{K}_{\mathrm{I}}$ and $\overline{K}_{\mathrm{II}}$ as functions of w/t for future engineering applications.

Due to the small weld width selected in this investigation ($w/t = 1$), the computational K_{I} and K_{II} solutions deviate a bit from the analytical solutions based on the beam bending theory. The value of the normalized global K_{I} is 0.51 and the value of the normalized global K_{II} is 1.03 (both are normalized by K_{I} and K_{II} in Equations (2.1) and (2.2) respectively). Due to the small weld width, the stress singularity due to the crack may cause the stress distribution in the middle portion of the connection of the two beams in Figure 2.5(a) to deviate from the stress distribution derived from the beam bending theory and thus the energy released rate is different from that based on the beam bending theory. Therefore, the computational K_{I} and K_{II} solutions are different from the analytical K_{I} and K_{II} solutions based on the beam bending theory in Equations (2.1) and (2.2). For a large weld width, the effect of the crack tip singularity is only limited to the small regions near the crack tips in the connection region of the two beams and thus the stress distribution in the middle portion agrees with that derived from the beam bending theory far away from the tips.

The computational results shown in Figure 2.8 indicate that the analytical stress intensity factor solutions in Equations (2.1) and (2.2) based on the beam bending theory seem to be able to characterize reasonably well the global stress intensity factors of laser welded lap-shear specimens for $w/t \geq 2$. From the computational results in Figure 2.8, the K_{I} solutions can be approximated by a linear function of w/t for $0 \leq w/t < 2$ as

$$K_{\mathrm{I}} = \frac{\sqrt{3}}{2}\frac{F}{b\sqrt{t}}\frac{w}{2t} \tag{2.5}$$

For $w/t \geq 2$, the K_{I} solutions can be estimated by Equation (2.1) based on the beam bending theory. As shown in Figure 2.8, the K_{II} solutions can be estimated in 3 regions.

The K_{II} solutions can be estimated by Equation (2.3) for $0 \le w/t < 0.37$. For $0.37 \le w/t < 1.12$, the K_{II} solutions can be approximated by a function of w/t as

$$K_{II} = 1.0285\left(\frac{w}{t}\right)^{-0.242}\frac{F}{b\sqrt{t}} \tag{2.6}$$

And for $w/t \ge 1.12$, the K_{II} solutions can be estimated by Equation (2.2) based on the beam bending theory. In summary, the K_I and K_{II} solutions now can be determined by Equations (2.1), (2.2), (2.3), (2.5) and (2.6) for a full range of w/t's.

2.5. Analytical local stress intensity factor solutions for kinked cracks

Figure 2.9 shows a schematic of a main crack and a kinked crack with the kink length a and the kink angle α. Here, K_I and K_{II} represent the global stress intensity factors for the main crack, and k_I and k_{II} represent the local stress intensity factors for the kinked crack. Note that the arrows in the figure represent the positive values of the global and local stress intensity factors K_I, K_{II}, k_I and k_{II}.

For kinked cracks, when the kink length approaches to 0, the local stress intensity factors k_I and k_{II} can be expressed as functions of the kink angle α and the global K_I and K_{II} for the main crack. The local stress intensity factor solutions are given as [33, 34]

$$(k_I)_0 = \frac{1}{4}\left(3\cos\frac{\alpha}{2} + \cos\frac{3\alpha}{2}\right)K_I - \frac{3}{4}\left(\sin\frac{\alpha}{2} + \sin\frac{3\alpha}{2}\right)K_{II} \tag{2.7}$$

$$(k_{II})_0 = \frac{1}{4}\left(\sin\frac{\alpha}{2} + \sin\frac{3\alpha}{2}\right)K_I + \frac{1}{4}\left(\cos\frac{\alpha}{2} + 3\cos\frac{3\alpha}{2}\right)K_{II} \tag{2.8}$$

where $(k_{\mathrm{I}})_0$ and $(k_{\mathrm{II}})_0$ represent the local k_{I} and k_{II} solutions for the kink length a approaching to 0.

2.6. Computational local stress intensity factor solutions for finite kinked cracks

After a kinked crack emanating from the main crack, the local stress intensity factor solutions at the kinked crack tip vary as functions of the kink length. The general trend was shown for spot welds in cup and lap-shear specimens [35, 20]. Here, two-dimensional plane-strain finite element computations were carried out to investigate the local stress intensity factor solutions for kinked cracks with different kink lengths for $w/t = 1$ and 2. Seven normalized kink lengths, namely, $a/t =$ 0.025, 0.05, 0.1, 0.2, 0.3, 0.5 and 0.7 are considered in this investigation.

Figure 2.10(a) again shows a schematic of a two-dimensional finite element model of a lap-shear specimen and the boundary conditions similar to that in Figure 2.7(a). The finite element models are developed for the weld widths of $w = 1$ and 2 mm that correspond to $w/t = 1$ and 2, respectively. The width b of the central portion of the dog-bone area of the specimen remains to be 8 mm. The length L between the right edge and the center of the hole of the upper sheet remains to be 82 mm. Both upper and lower sheets have the same thickness of 1 mm. Both doublers have the same length of 35 mm. The loading and boundary conditions of the specimen are the same as those for the finite element model shown in Figure 2.7(a). In Figure 2.10(a), the thin solid lines indicate the two kinked cracks. The kink angle in this investigation is selected to be $90°$. Figure 2.10(b) and 2.10(c) show the right part of the finite element mesh for $w/t = 1$ and $a/t = 0.2$, and a close-up view of the mesh near the kinked crack tip, respectively.

Figure 2.11 shows the values of $k_{\mathrm{I}}/(k_{\mathrm{I}})_0$ as functions of the normalized kink length a/t for $w/t=1$ and 2. Note that the values of $(k_{\mathrm{I}})_0$ used in the normalizations are based on the analytical global stress intensity factor solutions in Equations (2.1) and (2.2) and Equation (2.7) with the kink angle $\alpha=90°$. Figure 2.11 shows that as the kink length approaches to 0, the value of $k_{\mathrm{I}}/(k_{\mathrm{I}})_0$ appears to approach to the local stress intensity factor solutions, shown as symbols at $a/t=0$, based on Equation (2.7) and the computational K_{I} and K_{II} solutions for the main crack (without kinked cracks). The value of $k_{\mathrm{I}}/(k_{\mathrm{I}})_0$ increases as the kink length increases monotonically. Figure 2.12 shows the values of $|k_{\mathrm{II}}|/(k_{\mathrm{I}})_0$ as functions of the normalized kink length a/t for $w/t=1$ and 2. Note that the local stress intensity factor solutions k_{II} are negative as defined in Figure 2.9 in this investigation. As shown in Figure 2.12, the value of $|k_{\mathrm{II}}|/(k_{\mathrm{I}})_0$ appears to approach to the local stress intensity factor solutions as the kink length approaches 0, shown as symbols at $a/t=0$, based on Equation (2.7) and the computational K_{I} and K_{II} solutions for the main crack (without kinked cracks). As the kink length increases, the value of $|k_{\mathrm{II}}|/(k_{\mathrm{I}})_0$ decreases and appears to approach to 0 for a very large kink length. These normalized values of the local stress intensity factor solutions indicate that the kinked crack growth is under mixed mode I and II loading conditions. However, the kinked cracks are under dominant mode I loading conditions. Table 2.2 and 2.3 list the normalized local stress intensity factor k_{I} and k_{II} solutions, respectively, for $\alpha=90°$, $w/t=1$ and 2 for future engineering applications.

2.7. A fatigue crack growth model

As in Newman and Dowling [14] and Lin et al. [15], the Paris law is adopted to describe the fatigue crack propagation for kinked cracks emanating from the main cracks of laser welds in lap-shear specimens. The Paris law is

$$\frac{da}{dN} = C\left(\Delta k_{eq}(a)\right)^m \tag{2.9}$$

where a is the kink length, N is the life or number of cycles, C and m are material constants, and Δk_{eq} is the range of the equivalent stress intensity factor under mixed mode loading conditions. As shown by the results of finite element analyses in Figures 2.11 and 2.12, the local stress intensity factor k_I and k_{II} solutions for kinked cracks in laser welds can be expressed as functions of the normalized kink length a/t as

$$k_I(a) = f_I \cdot (k_I)_0 \tag{2.10}$$

$$k_{II}(a) = f_{II} \cdot (k_I)_0 \tag{2.11}$$

where f_I and f_{II} are geometric functions which depend on the geometric parameters of the laser welded lap-shear specimens such as the weld width w and the sheet thickness t. The local stress intensity factor k_I and k_{II} solutions as functions of the kink length a can be obtained from the linear interpolation between the normalized local stress intensity factor k_I and k_{II} solutions obtained from the finite element analyses. Since the local stress intensity factor k_I and k_{II} solutions for $0.7 < a/t < 1.0$ were not investigated due to their anticipated very large and small values, respectively, the variations of the local stress intensity factor k_I and k_{II} solutions in this range are assumed to be the same as those for $0.5 < a/t < 0.7$. Since the fatigue crack growth is under local mixed mode I and

II loading conditions, the range of the equivalent stress intensity factor Δk_{eq} can be defined as

$$\Delta k_{\text{eq}}(a) = \sqrt{\Delta k_{\text{I}}(a)^2 + \gamma \Delta k_{\text{II}}(a)^2} \tag{2.12}$$

where γ is an empirical constant to account for the sensitivity of material to mode II loading conditions. For lack of any further information, the value of γ is also taken as 1. By substituting Equation (2.12) into Equation (2.9) and integrating Equation (2.9), the fatigue lives of laser welds in lap-shear specimens can be expressed as

$$N = \frac{1}{C}\left[\int_{0}^{0.025t'} \left[\Delta k_{eq}(a)\right]^{-m} da + \int_{0.025t'}^{0.05t'} \left[\Delta k_{eq}(a)\right]^{-m} da + \ldots + \int_{0.5t'}^{t'} \left[\Delta k_{eq}(a)\right]^{-m} da \right] \tag{2.13}$$

where 0, 0.025, 0.05, …, and 0.5 represent the values of the normalized kink length a/t where the computational local stress intensity solutions are available and and t' is the crack growth distance $(= t/\sin\alpha)$. For $\alpha = 90°$, $t' = t$.

A simplified model with the local stress intensity factors $(k_{\text{I}})_0$ and $(k_{\text{II}})_0$ solutions for the kink length a approaching to 0 is also considered. In this case, as in Newman and Dowling [14] and Lin et al. [15], the ranges of the equivalent local stress intensity factors are assumed to be constant for all kink lengths and assumed to be equal to those for kinked cracks with the vanishing kink length (with a approaching to 0). The fatigue life of a laser weld can then be obtained by substituting Equations (2.7) and (2.8) into Equation (2.9) and integrating Equation (2.9) explicitly as

$$N = \frac{t'}{C\left((\Delta k_{\text{eq}})_0\right)^m} \tag{2.14}$$

where $\left(\Delta k_{eq}\right)_0$ is the range of the equivalent stress intensity factor at the vanishing kink length from Equation (2.12). Note that the stress intensity factor ranges used in Equations (2.9), (2.13) and (2.14) are the stress intensity factor ranges without consideration of the load ratio effect. The load ratio R is 0.2 for the fatigue experiments and it is not expected to have significant effects on the life predictions of these laser welds.

As shown in Figure 2.11, the values of the normalized $k_I/\left(k_I\right)_0$ solutions for $w/t=1$ and 2 almost coincide with each other. As shown in Figure 2.12, the values of the normalized $\left|k_{II}\right|/\left(k_I\right)_0$ are small. The kinked cracks are under mixed mode loading conditions. As indicated in Equation (2.12), the small values of $\Delta\left|k_{II}\right|/\Delta\left(k_I\right)_0$ will not change the effective stress intensity factor ranges significantly. Therefore, the fatigue life estimations will not be significantly dependent on the contributions of Δk_{II}. Figures 2.11 and 2.12 indicate that the analytical global stress intensity factor solutions in Equations (2.1) and (2.2) based on the beam bending theory and the normalized local stress intensity factor solutions (listed in Tables 2.2 and 2.3) can be used to estimate the fatigue lives for laser welds with the weld width as small as $w/t=1$.

2.8. The structural stress model

Here, the beam bending theory is adopted to develop the structural stress model for laser welds in lap-shear specimens. The dog bone area of the beam is modeled as two beams with connection. Figure 2.5(b) shows the equivalent loading of the lap-shear loading of the two-beam model shown in Figure 2.5(a) with the membrane forces per unit

width, F/b, and the bending moments per unit width, $Ft/2b$, applied at the middle surfaces of the upper and lower beams. Both membrane force per unit width, F/b, and bending moment per unit width, $Ft/2b$, contribute to the structural stress at the edge of the weld. The structural stress of the laser weld in lap-shear specimen is

$$\sigma = \frac{F}{tb} + \frac{3F}{tb} \tag{2.15}$$

where that the first term on the right hand side of the equation corresponds to the structural stress subjected to the membrane force per unit width and the second term on the right hand side of the equation corresponds to the structural stress subjected to the bending moment per unit width. By using Equation (2.15) for the structural stress ranges at the edge of the weld bead and the experimental stress-life fatigue data of the HSLA steel, the fatigue lives of laser welds in lap-shear specimens can be estimated.

2.9. Application of the fatigue crack growth and structural stress models

In order to determine the applicability of the fatigue crack growth model based on the global stress intensity factor solutions in Equations (2.1) and (2.2), the fatigue lives based on the fatigue crack growth model with the local stress intensity factor solutions as functions of kink length are estimated and compared with the experimental results. The fatigue lives based on the simplified fatigue crack growth model and structural stress model are also estimated and compared with the experimental results.

Based on the experimental observations, the kink angle α is taken approximately to be $90°$. For HSLA steel, the material constants C and m for the Paris law are chosen for ferrite-pearlite steels as $C = 6.89\times10^{-9}\ \dfrac{\text{mm/cycle}}{\left(\text{MPa}\sqrt{\text{m}}\right)^m}$ and $m = 3$, based on the

micrograph of the cross section of the welds as discussed in Asim et al. [27]. The normalized weld width w/t for the laser welds in lap-shear specimens of Asim et al. [27] is 0.86. Therefore, Equations (2.5) and (2.6) are used to estimate the global stress intensity factor solutions and the fatigue lives of the laser welds. The normalized local stress intensity factor solutions for $w/t = 1$ in Figures 2.11 and 2.12 are used to estimate the fatigue lives of the laser welds since the fatigue cracks grow under dominant mode I loading conditions and the small differences of the local stress intensity factor solutions for $w/t = 1$ and $w/t = 0.86$ should not have significant effects on the fatigue life estimations.

Figure 2.13 shows the experimental results, the fatigue life estimations based on the fatigue crack growth model (Equation (2.13)) with the global stress intensity factor solutions in (Equations (2.5) and (2.6)) and the local stress intensity factor solutions from the finite element analyses for $w/t = 1$, the fatigue life estimations based on the simplified fatigue crack growth model (Equation (2.14)) with the analytical global and local stress intensity factor solutions in Equations (2.5), (2.6), (2.7) and (2.8), and the fatigue life estimations based on the structural stress solution in Equation (2.15). The fatigue life estimations based on the fatigue crack growth model in Equation (2.13) with the global and the local stress intensity factor solutions for $w/t = 0.86$ are in agreement with the experimental results while the fatigue life estimations based on the simplified fatigue crack growth model are higher than the experimental results. The fatigue life estimations based on the structural stress model agree with the experimental results for the larger load ranges but higher than the experimental results for the smaller load ranges.

This may be due to the experimental stress-life fatigue data used in structural stress model take account of plasticity at the low load ranges.

When comparing the simplified fatigue crack growth model (Equation (2.14)) and the fatigue crack growth model with consideration of the local stress intensity factor solutions of kinked cracks as functions of the kink length (Equation (2.13)), the fatigue life estimations based on the fatigue crack growth model in Equation (2.13) are much lower than those based on the simplified model in Equation (2.14). Because the value of the equivalent local stress intensity factor solution increases as the kink length increases, the kinked crack growth is much faster than that estimated by assuming that the equivalent local stress intensity factor is constant and equal to that of the vanishing kink length.

In this investigation, two kinked cracks of the same length emanating from both main cracks are modeled in the finite element analyses to represent the kinked cracks emanating from the laser weld as shown in Figure 2.3, although one kinked crack usually becomes dominant and results in the final failure of the specimen. Finite element analyses for a weld with single kinked crack of different kink lengths were carried out. The results indicate that the local stress intensity factor k_{I} solution is very close to that for a weld with two kinked cracks of the same length as presented earlier. However, the value of the local stress intensity factor k_{II} solution for a weld with single kinked crack is slightly lower than that for a weld with two kinked cracks of the same length. The difference of the k_{II} solutions increases as the kink length increases. But the kinked crack grows under dominant mode I loading conditions. Therefore, the effective stress intensity factor ranges are almost the same for welds with single and two kinked cracks

for a given a/t. Therefore, the fatigue life estimations based on the local stress intensity factor solutions for welds with single and two kinked cracks are almost the same. In summary, the local stress intensity factor solutions for a weld with two kinked cracks are also applicable to a weld with single kinked crack of the same kink length. In this investigation, the residual stresses in the weld, heat affected zone and base metal are not considered for lack of any quantitative information on the residual stresses in this laser welding process. When the residual stress distributions are available, the stress intensity factor solutions due to the residual stresses can be considered for fatigue life estimations within the context of the linear elastic fracture mechanics as in Chien et al. [36].

2.10. Conclusions

Fatigue behavior of laser welds in lap-shear specimens of high strength low alloy (HSLA) steel is investigated based on experimental observations and two fatigue life estimation models. Fatigue experiments of laser welded lap-shear specimens are first reviewed. Analytical stress intensity factor solutions based on the beam bending theory are derived and compared with the analytical solutions for two semi-infinite solids with connection. Finite element analyses of laser welded lap-shear specimens with different weld widths were also conducted to obtain the stress intensity factor solutions. Approximate closed-form stress intensity factor solutions based on the results of the finite element analyses in combination with the analytical solutions based on the beam bending theory and Westergaard stress function for a full range of the normalized weld widths are developed for future engineering applications.

Next, finite element analyses of laser welded lap-shear specimens with two weld widths were conducted to obtain the local stress intensity factor solutions for kinked cracks as functions of the kink length. The computational results indicate that the kinked cracks are under dominant mode I loading conditions and the normalized local stress intensity factor solutions can be used in combination with the global stress intensity factor solutions to estimate fatigue lives of laser welds with the weld width as small as the sheet thickness. The global stress intensity factor solutions and the local stress intensity factor solutions for vanishing and finite kinked cracks are then adopted in the fatigue crack growth model to estimate the fatigue lives. Also, a structural stress model based on the analytical solution is adopted to estimate the fatigue lives of the welds. The fatigue life estimations based on the fatigue crack growth model with the local stress intensity factor solutions as functions of the kink length and the structural stress model are agree well with the experimental results. Note that the structural stress model seems to be more suitable for estimation of fatigue lives at high load ranges.

Appendix A: Derivation of stress intensity factor solutions based on beam bending theory

For linear elastic materials, the stress intensity factor solutions can be derived from the elastic energy release rate G. Under plane strain conditions, the relationship between the elastic energy release rate G and the stress intensity factors can be expressed as

$$G = \frac{K_{\mathrm{I}}^2 + K_{\mathrm{II}}^2}{E'} \tag{2.A1}$$

where $E' = E/\left(1-\nu^2\right)$. Here, E is Young's modulus and ν is Poisson's ratio.

Consider a two-dimensional elastic cracked solid with unit width under load controlled conditions. The increase of the potential energy of the system, $\mathrm{d}\Pi$, can be expressed as

$$\mathrm{d}\Pi = \mathrm{d}U - \mathrm{d}W \tag{2.A2}$$

where $\mathrm{d}U$ is the increase of the elastic strain energy of the system and $\mathrm{d}W$ is the work done by the external force. For linear elastic materials, the increase of the elastic energy stored within the system is half of the work done by the external force. Equation (2.A2) can thus be rewritten as

$$\mathrm{d}\Pi = -\mathrm{d}U \tag{2.A3}$$

Alternatively, the decrease of the potential energy of the system, $-\mathrm{d}\Pi$, can be expressed as the increase of the elastic energy, $\mathrm{d}U$, stored within the system as

$$-\mathrm{d}\Pi = \mathrm{d}U \tag{2.A4}$$

The energy release rate is the decrease of the potential energy per unit crack extension. Therefore for any crack extension $\mathrm{d}x$, the energy release rate G can be expressed as

$$G = \frac{-\mathrm{d}\Pi}{\mathrm{d}x} \tag{2.A5}$$

Combining Equations (2.A1), (2.A4) and (2.A5) gives

$$\frac{\mathrm{d}U}{\mathrm{d}x} = \frac{K_{\mathrm{I}}^2 + K_{\mathrm{II}}^2}{E'} \tag{2.A6}$$

Figure 2.A1(a) shows the right part of the two-beam model shown in Figure 2.5(b). Both beams have the same thickness *t*. Both beams and the connection are assumed to have lengths much larger than the thickness of the beams. In fact, this assumption may not be strictly valid for laser welds where the weld width can be equal to or smaller than

the thickness. For the purpose of illustration, the beam area associated with the crack extension is marked as area B and shown as the dark-shaded area in Figure 2.A1(a). The beam area in front of the extended crack tip is marked as area A and shown as the light-shaded area in Figure 2.A1(a). Finally, the two beams are marked as areas C1 and C2 in Figure 2.A1(a). As shown in Figure 2.5, the loading condition of the right half of the specimen can be decomposed into counter bending, central bending, tension and in-plane shear loading conditions as shown in Figures 2.A1(b), 2.A1(c), 2.A1(d), and 2.A1(e), respectively. In these figures, the areas in front of the extended crack tip, the beam areas associated with the crack extension, and the two beams are marked and shaded similar to those in Figure 2.A1(a). The increase of the elastic energy for the crack extension $\mathrm{d}x$ and the stress intensity factor solution for each of the loading conditions will be discussed in the following.

A1. Stress intensity factor solution under counter bending conditions

Figure 2.A1(b) shows the two-beam model under counter bending conditions. Note that under this loading condition, the loading is symmetric and K_{II} is 0. The bending moments per unit width of $Ft/4b$ are applied at the far ends of beam areas C1 and C2. These applied bending moments cancel each other and there is no bending moment and internal force at the far end of beam area A. Because the elastic energies in the far ends of beam areas A, C1 and C2 do not vary with the position, the increase of the elastic energy per unit width for any crack extension $\mathrm{d}x$ is the increase of the elastic strain energy in beam area B as

$$\mathrm{d}U = \left(2w_{\mathrm{C}} - w_{\mathrm{A}}\right)\cdot \mathrm{d}x \tag{2.A7}$$

where w_C is the elastic strain energy per unit width for each of the two beam areas C1 and C2 and w_A is the elastic strain energy per unit width for beam area A. Here, w_A equals 0. From the elastic strain energy of the beam under plane strain bending conditions, Equation (2.A7) can be expressed as

$$\mathrm{d}U = \frac{3}{4}\frac{F^2}{E'b^2t}\cdot \mathrm{d}x \tag{2.A8}$$

Combining Equations (2.A6) and (2.A8) with $K_{II} = 0$ gives the K_I solution under counter bending conditions as

$$K_{I,B} = \frac{\sqrt{3}}{2}\frac{F}{b\sqrt{t}} \tag{2.A9}$$

A2. Stress intensity factor solution under central bending conditions

Figure 2.A1(c) shows the two-beam model under central bending conditions. In this case, the loading is anti-symmetric and K_I equals 0. The bending moments per unit width, $Ft/4b$, are applied at the far ends of beam areas C1 and C2. However, these applied bending moments cause a bending moment per unit width, $Ft/2b$, at the far end of beam area A. In this case, w_A is no longer equal to 0. From the elastic strain energy of the beam under plane strain bending conditions, Equation (2.A7) can be expressed as

$$\mathrm{d}U = \left(\frac{3}{4}\frac{F^2}{E'b^2t} - \frac{3}{16}\frac{F^2}{E'b^2t}\right)\cdot \mathrm{d}x \tag{2.A10}$$

Combining Equations (2.A6) and (2.A10) with $K_I = 0$ gives the K_{II} solution under counter bending loading conditions as

$$K_{II,CB} = \frac{3}{4}\frac{F}{b\sqrt{t}} \tag{2.A11}$$

A3. Stress intensity factor solution under in-plane shear loading conditions

Figure 2.A1(e) shows the two-beam model under in-plane shear loading conditions. In this case, the loading is anti-symmetric and K_{I} is 0. The membrane forces per unit width, $F/2b$, are applied at the far ends of beam areas C1 and C2. These applied membrane forces cause a bending moment per unit width, $Ft/2b$, at the far end of beam area A. From the elastic strain energy of the beams under axial loading conditions (in areas C1 and C2) and the elastic strain energy of the beam (in area A) under plane strain bending conditions, Equation (2.A7) can be expressed as

$$\mathrm{d}U = \left(\frac{F^2}{4E'b^2t} - \frac{3}{16}\frac{F^2}{E'b^2t} \right) \cdot \mathrm{d}x \tag{2.A12}$$

Combining Equations (2.A6) and (2.A12) with $K_{\mathrm{I}} = 0$ gives the K_{II} solution under in-plane shear loading conditions as

$$K_{\mathrm{II,S}} = \frac{F}{4b\sqrt{t}} \tag{2.A13}$$

A4. Stress intensity factor solution under lap-shear loading conditions

Based on the superposition principle of the linear elasticity, the total stress intensity factor solutions are the combination of the stress intensity factor solutions from the four loading conditions. Note that the tension loading condition as shown in Figure 2.A1(d) does not give any stress intensity factor solution. The K_{I} solution is from the counter bending loading condition as

$$K_{\mathrm{I}} = \frac{\sqrt{3}}{2}\frac{F}{b\sqrt{t}} \tag{2.A14}$$

The K_{II} solution comes from the central bending and in-plane shear loading conditions as

$$K_{II} = \frac{F}{b\sqrt{t}} \tag{2.A15}$$

Acknowledgements

Partial support of this work by the National Science Foundation under grant No. DMI-0456755 is greatly appreciated. The support of Dr. M. Li of TWB (Monroe, MI) to provide the laser welded specimens used in this investigation is also greatly appreciated. In addition, the supported of Dr. P. A. Friedman of Ford Motor Company to provide the stress-life data for the HSLA steel for the estimations of fatigue lives based on the structural stress model is greatly appreciated.

References

[1] Hsu C, Albright CE. Fatigue analysis of laser welded lap joints. Eng Fract Mech 1991; 39: 575-580.

[2] Wang PC, Ewing KM. A comparison of fatigue strengths: Laser beam vs. resistance spot welds. Welding J 1991; 70: 43-7.

[3] Flavenott JF, Deville JP, Diboine A, Cantello M, Gobbi SL. Fatigue resistance of laser welded lap joints of steel sheets. Welding in the World 1993; 31: 12-15.

[4] Wang PC. Calculation of laser beam weld specification for automotive sheet steel. Welding Research Supplement 1993; April: 155-163.

[5] Wang PC. Fracture mechanics parameter for the fatigue resistance of laser welds. Int J Fatigue 1995; 17: 25-34.

[6] Zhang S. Stress in laser welded lap joints determined by outer surface strains. Welding J 2002; 81: 14-18.

[7] Ono M, Kabasawa M, Omura M. Static and fatigue strength of laser-welded lap joints in thin steel sheet. Welding Int 1997; 11: 462-7.

[8] Terasaki T, Sobue T, Kitamura T. Study of fatigue strength of laser welded lap joint. Q J Japan Welding Society 2001; 19: 507-12.

[9] Kaitanov AY, Ozersky AD, Zabelin AM, Kislov VS. Static and fatigue strengths of laser welded overlap joints with controlled penetration. Proc. SPIE 2002; 4644: 116-26.

[10] Cho SK, Yang YS, Son KJ, Kim JY. Fatigue strength in laser welding of the lap joint. Finite Elem Anal Des 2004; 40: 1059-70.

[11] Sonsino CM, Kueppers M, Eibl M, Zhang G. Fatigue strength of laser beam welded thin steel structures under multiaxial loading. Int J Fatigue 2006; 28: 657-62.

[12] Sripichai K, Asim K, Jo WH, Pan J, Li M. Fatigue behavior of laser welds in lap-shear specimens of high strength low alloy (HSLA) steels. SAE Technical Paper No. 2009-01-0028. Warrendale (PA): Society of Automotive Engineers; 2009.

[13] Pook LP. Approximate stress intensity factors obtained from simple plate bending theory. Eng Fract Mech 1979; 12: 505-522.

[14] Newman JA, Dowling NE. A crack growth approach to life prediction of spot-welded lap joints. Fatigue Fract Engrg Mater Struct 1998; 21: 1123-1132.

[15] Lin SH, Pan J, Wung P, Chiang J. A fatigue crack growth model for spot welds under cyclic loading conditions. Int J Fatigue 2006; 28: 792-803.

[16] Lin PC, Pan J, Pan T. Failure modes and fatigue life estimations of spot friction welds in lap-shear specimens of aluminum 6111-T4 sheets. Part 1: Welds made by a concave tool. Int J Fatigue 2008; 30: 74-89.

[17] Lin PC, Pan J, Pan T. Failure modes and fatigue life estimations of spot friction welds in lap-shear specimens of aluminum 6111-T4 sheets. Part 2: Welds made by a flat tool. Int J Fatigue 2008; 30: 90-105.

[18] Tran VX, Pan J, Pan T. Fatigue behavior of aluminum 5754-O and 6111-T4 spot friction welds in lap-shear specimens. Int J Fatigue 2008; 30: 2175-2190.

[19] Tran VX, Pan J, Pan T. Fatigue behavior of spot friction welds in lap-shear and cross-tension specimens of dissimilar aluminum sheets. Int J Fatigue 2010; 32: 1022-1041.

[20] Wang DA, Pan J. A computational study of local stress intensity factor solutions for kinked cracks near spot welds in lap-shear specimens. Int J Solids Struct 2005; 42: 6277-6298.

[21] Radaj D. Stress singularity, notch stress and structural stress at spot –welded joints. Eng Fract Mech 1989; 34: 495-506.

[22] Radaj D, Zhang S. Stress intensity factors for spot welds between plates of unequal thickness. Eng Fract Mech 1991; 39: 391-413.

[23] Radaj D, Zhang S. Simplified formulae for stress intensity factors of spot welds. Eng Fract Mech 1991; 40: 233-236.

[24] Radaj D, Zhang S. Stress intensity factors for spot welds between plate of dissimilar materials. Eng Fract Mech 1992; 42: 233-236.

[25] Zhang S. Stress intensities at spot welds. Int J Fract 1997; 88: 167-185.

[26] Zhang S. Fracture mechanics solutions to spot welds. Int J Fract 2001; 112: 247-75.

[27] Asim K, Lee J, Pan J. Failure mechanism of laser welds in lap-shear specimens of High Strength Low Alloy (HSLA) steels under cyclic loading conditions. 2010; to be submitted for publication.

[28] Lin PC, Wang DA, Pan J. Mode I stress intensity factor solutions for spot welds in lap-shear specimens. Int J Solids Struct 2007; 44: 1013-1037.

[29] Lin PC, Pan J. Closed-form structural stress and stress intensity factor solutions for spot welds in commonly used specimens. Eng Fract Mech 2008; 75: 5187-5206.

[30] Tada H, Paris PC, Irwin GR. The stress analysis of cracks handbook. 3rd edition. New York: ASME Press; 2000.

[31] Lee J, Asim K, Pan J. Modeling of failure mode of laser welds in lap-shear specimens of HSLA steel sheets. 2010; to be submitted for publication.

[32] ABAQUS v6.7 User Manual. Providence, RI: SIMULIA; 2007.

[33] Bilby BA, Cardew GE, Horward IC. Stress intensity factors at the tip of kinked and forked cracks. The fourth international conference on fracture, University of Waterloo, Ontario, June 19-24, 1977; Pergamon Press, NY; 1978; 3A: 197-200.

[34] Cotterell B, Rice JR. Slightly curved or kinked cracks. Int J Fract 1980; 16: 155-169.

[35] Wang DA, Lin SH, Pan J. Stress intensity factor for spot welds and associated kinked cracks in cup specimens. Int J Fatigue 2005; 27: 581-598.

[36] Chien WY, Pan J, Close D, Ho S. Fatigue analysis of crankshaft sections under bending with consideration of residual stresses. Int J Fatigue 2005;27:1-19.

Table 2.1: The normalized global stress intensity factor $\overline{K}_{\mathrm{I}}$ and $\overline{K}_{\mathrm{II}}$ solutions for various normalized weld widths.

w/t	0.125	0.25	0.50	0.64	1.0	2.0	4.0	6.0
$\overline{K}_{\mathrm{I}}$	0.021	0.059	0.165	0.238	0.441	0.815	0.867	0.866
$\overline{K}_{\mathrm{II}}$	2.270	1.632	1.225	1.133	1.033	1.000	1.000	1.000

Table 2.2: The normalized local stress intensity factor $k_{\mathrm{I}}/(k_{\mathrm{I}})_0$ solutions for $\alpha = 90°$, $w/t = 1$ and 2.

a/t	0.025	0.05	0.1	0.2	0.3	0.5	0.7
$w/t = 1$	1.459	1.674	2.039	2.767	3.653	6.724	15.761
$w/t = 2$	1.500	1.702	2.049	2.754	3.634	6.713	15.761

Table 2.3: The normalized local stress intensity factor $|k_{\mathrm{II}}|/(k_{\mathrm{I}})_0$ solutions for $\alpha = 90°$, $w/t = 1$ and 2.

a/t	0.025	0.05	0.1	0.2	0.3	0.5	0.7
$w/t = 1$	0.205	0.180	0.149	0.119	0.102	0.063	0.020
$w/t = 2$	0.298	0.270	0.229	0.169	0.124	0.060	0.017

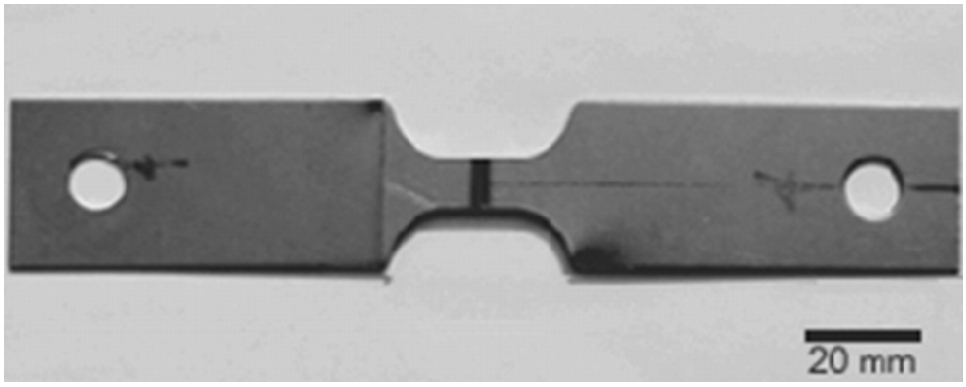

(a)

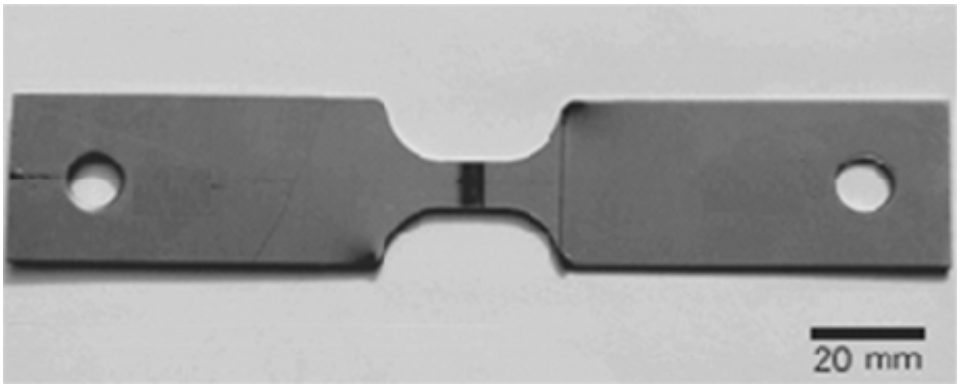

(b)

Figure 2.1. (a) A top view and (b) a bottom view of a laser-welded lap-shear specimen.

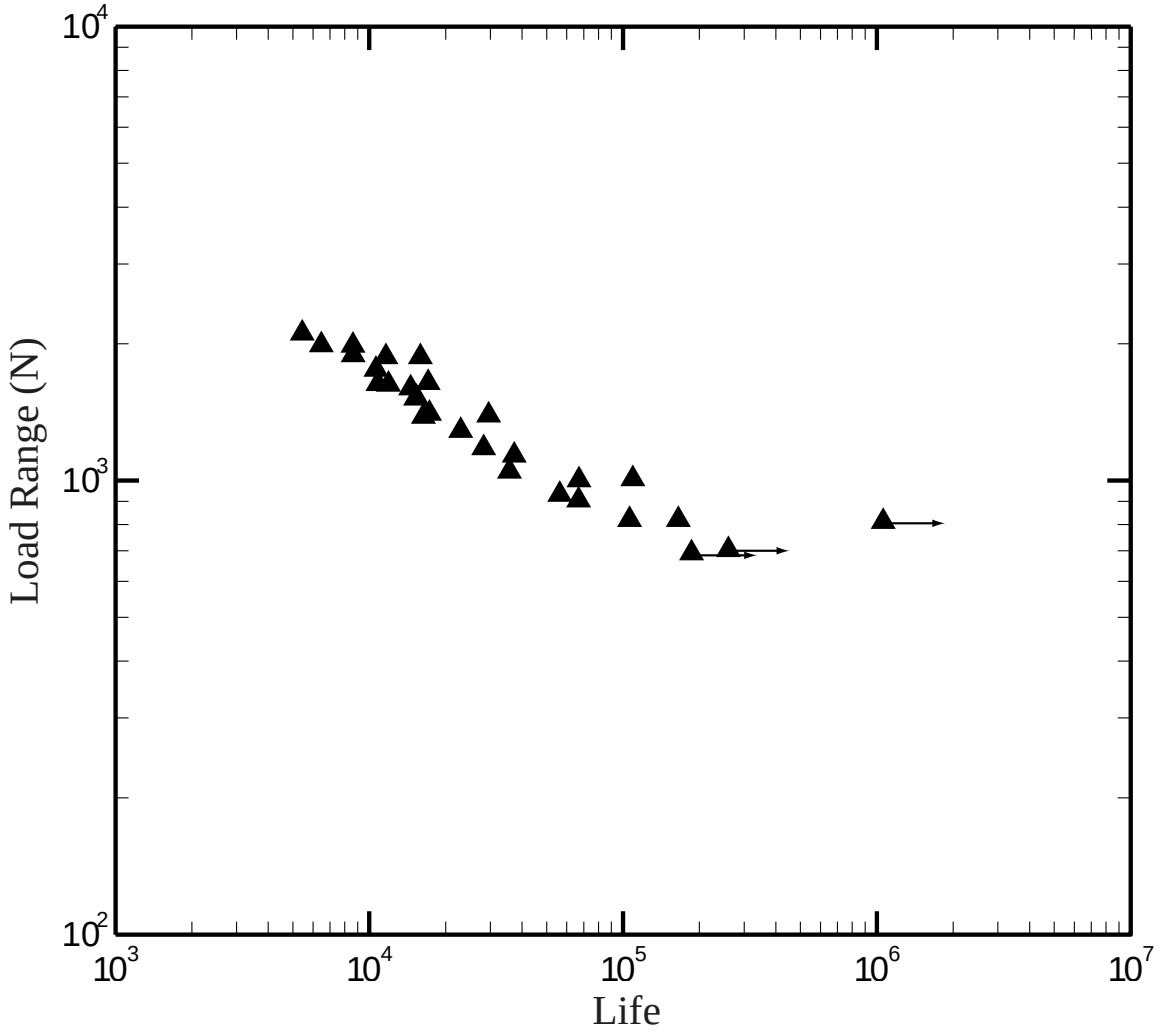

Figure 2.2. The experimental results for laser-welded lap-shear specimens under cyclic loading conditions.

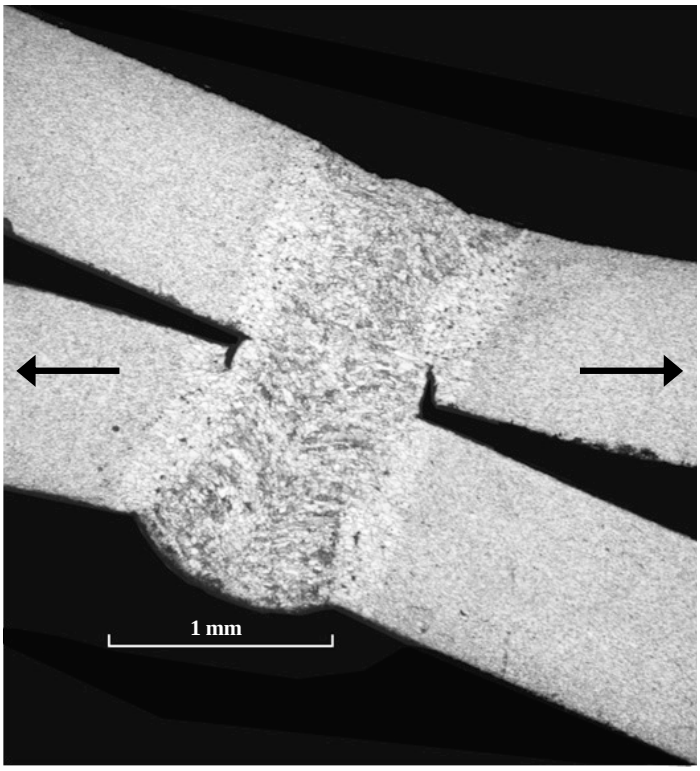

Figure 2.3. A micrograph of a partially failed laser weld.

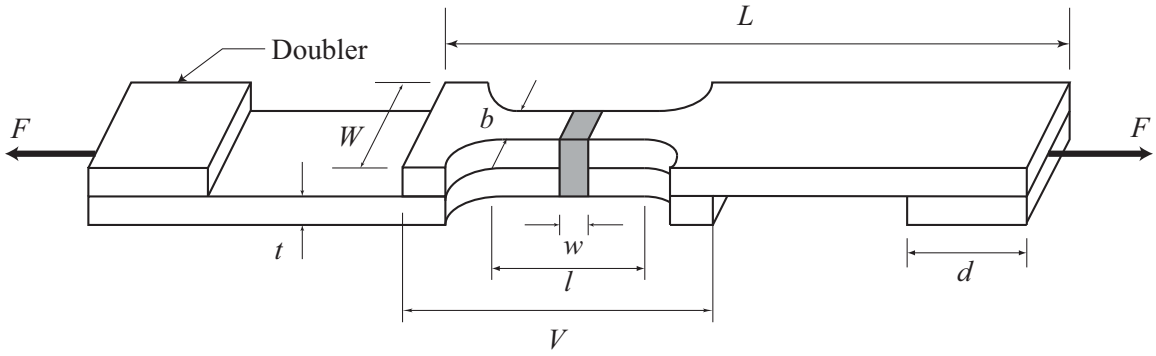

Figure 2.4. A schematic of a lap-shear specimen. The applied force F is shown as the bold arrows.

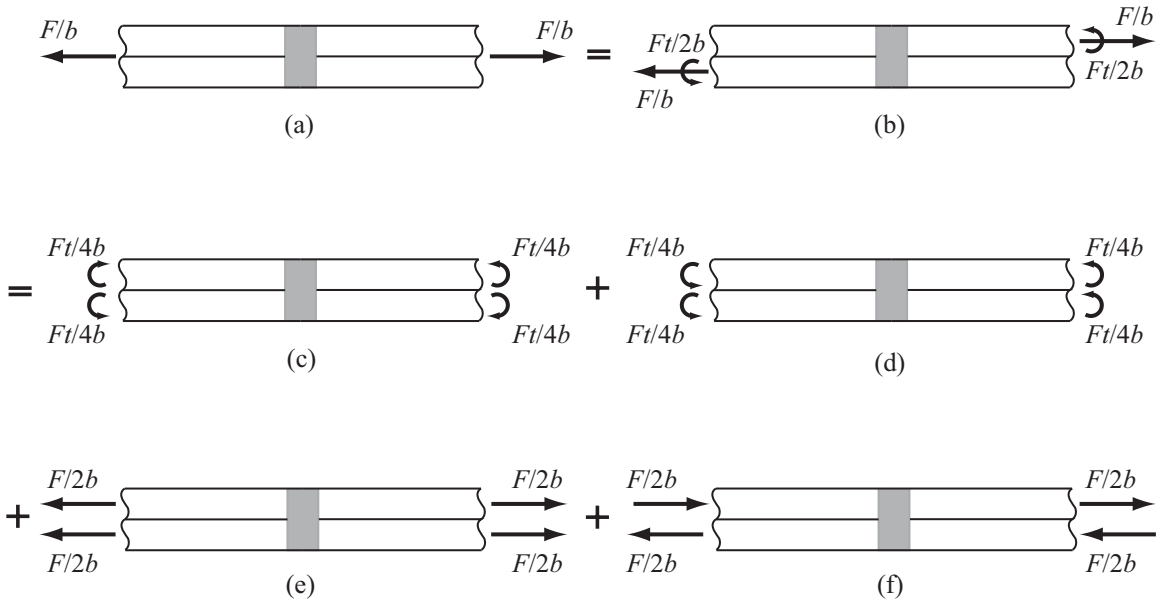

Figure 2.5. A schematic of the decomposition of the shear load of a lap-shear specimen. The weld zone is shown as the shaded area. The two-beam model is subjected to (a) lap-shear loading and (b) equivalent loading of (a). The equivalent loading shown in (b) is decomposed into (c) counter bending, (d) central bending, (e) tension, and (f) in-plane shear loading conditions.

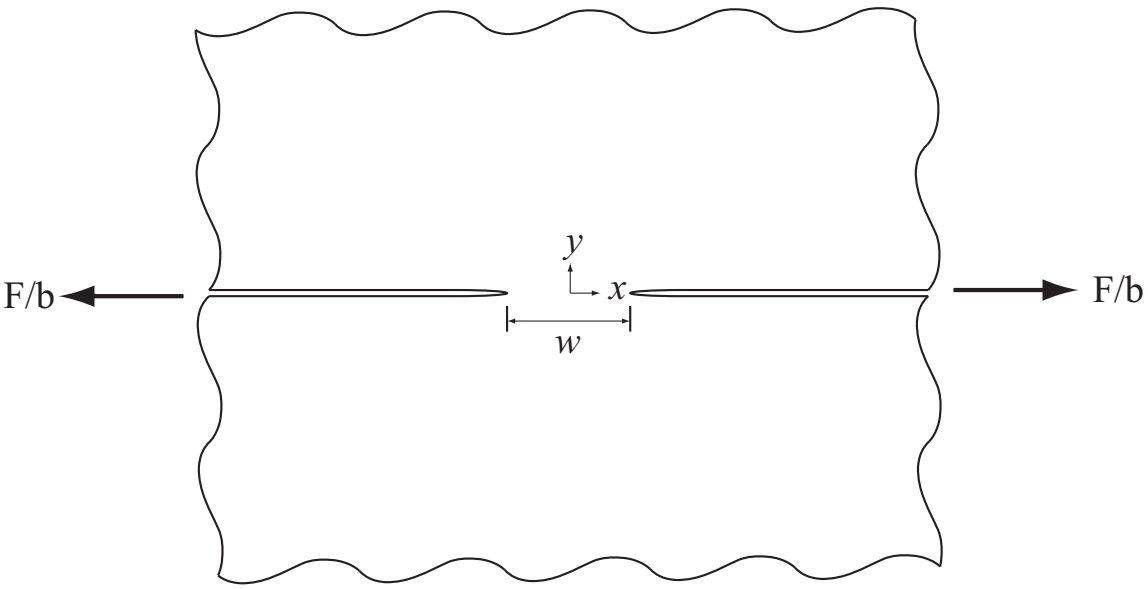

Figure 2.6. A schematic diagram of two semi-infinite solids with connection of the length w. The Cartesian coordinate $x-y$ system is shown. The forces per unit width, F/b, are applied along the x axis at $x=+\infty$ and $-\infty$ of the upper solid and lower solid, respectively.

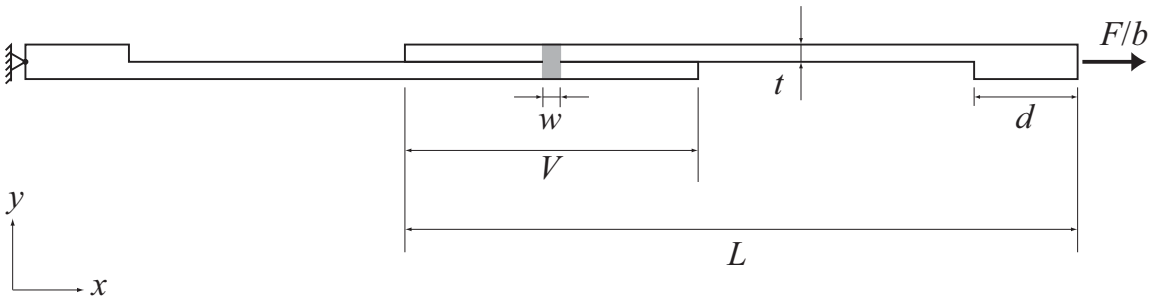

(a)

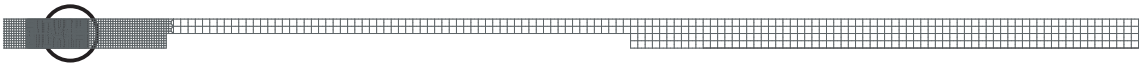

(b)

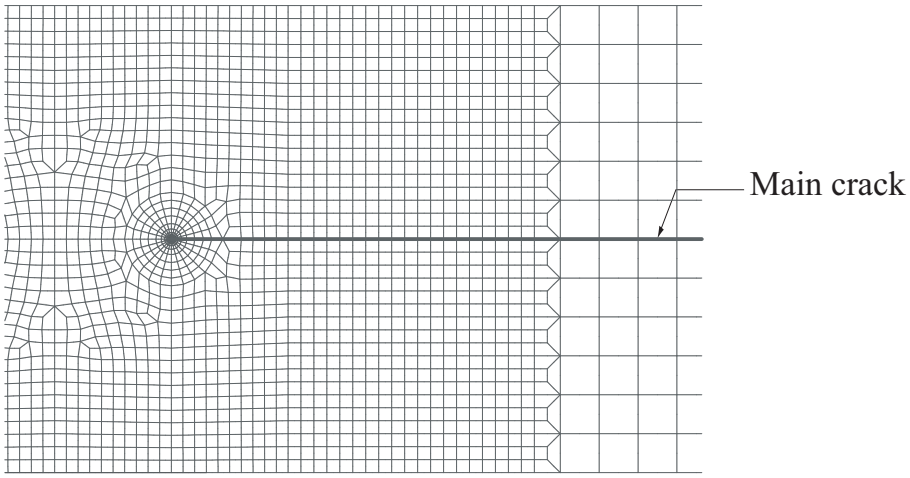

(c)

Figure 2.7. (a) A schematic of a two-dimensional finite elemental model of a lap-shear specimen and the boundary conditions, (b) the right part of the finite element mesh for $w/t = 1$, and (c) a close-up view of the finite element mesh near the main crack tip.

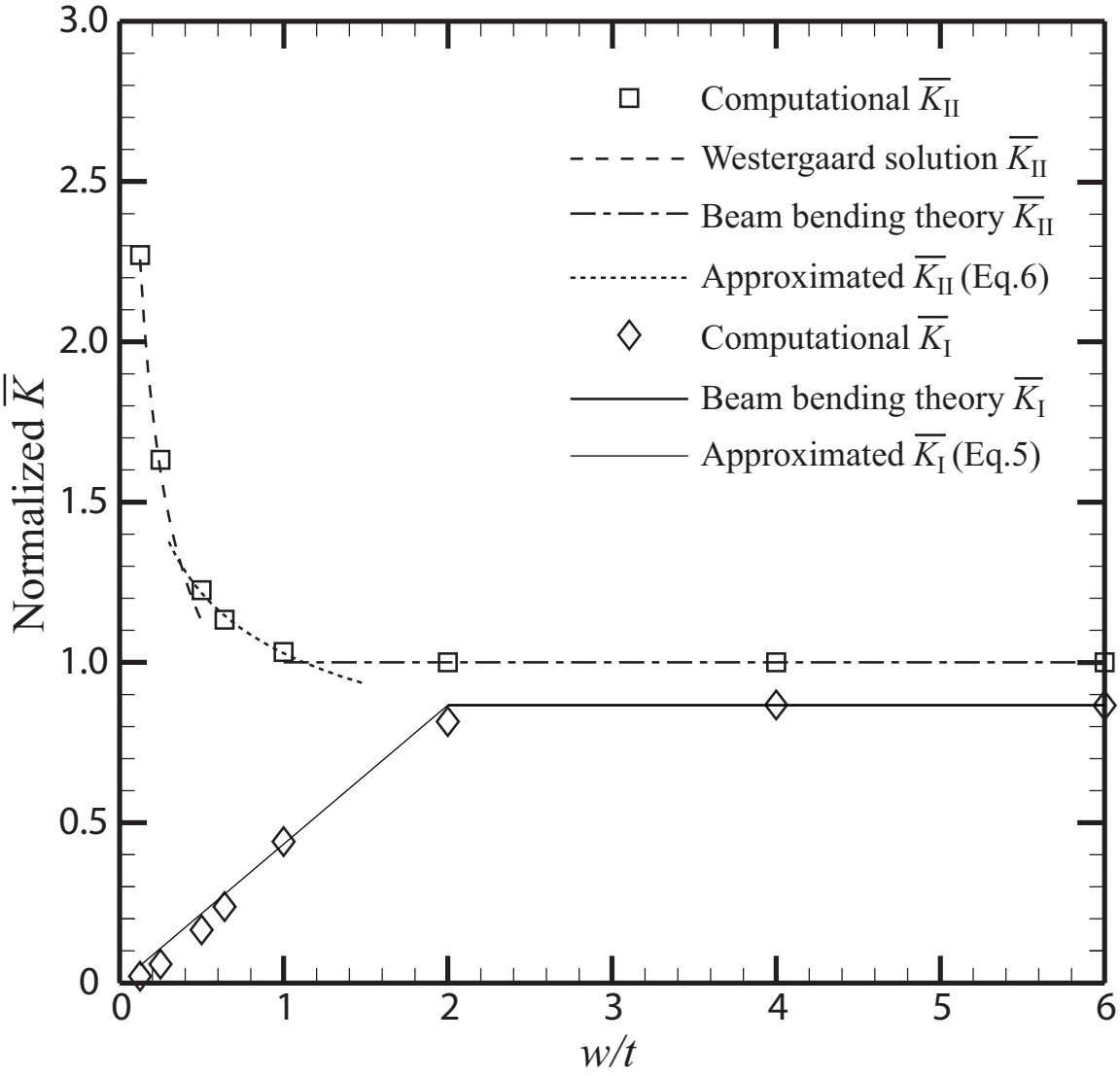

Figure 2.8. The normalized computational and analytical $\overline{K}_I$ and $\overline{K}_{II}$ solutions based on the beam bending theory, the Westergaard stress function and the approximated $\overline{K}_I$ and $\overline{K}_{II}$ solutions based on Equation (2.5) and (2.6) as functions of w/t.

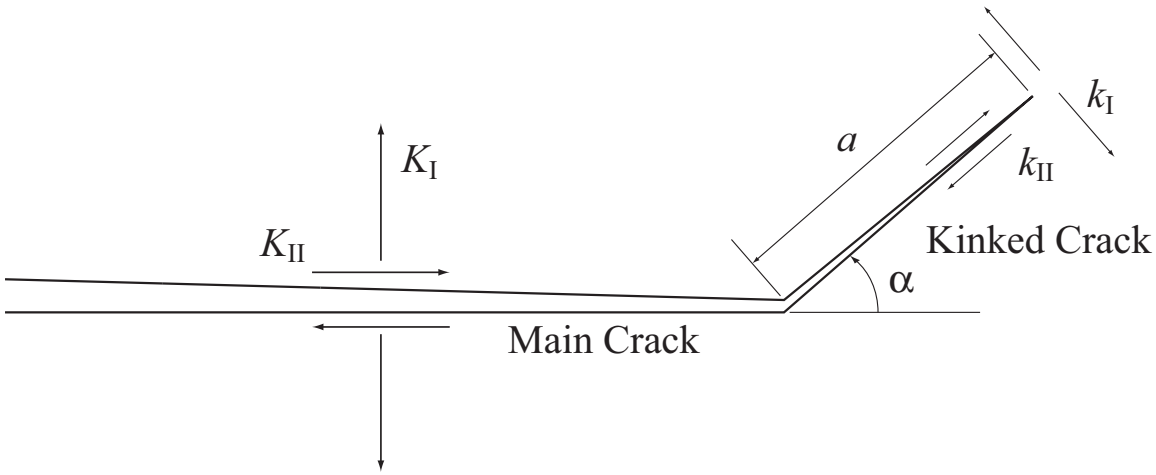

Figure 2.9. A schematic of a main crack and a kinked crack with the kink length a and the kink angle α.

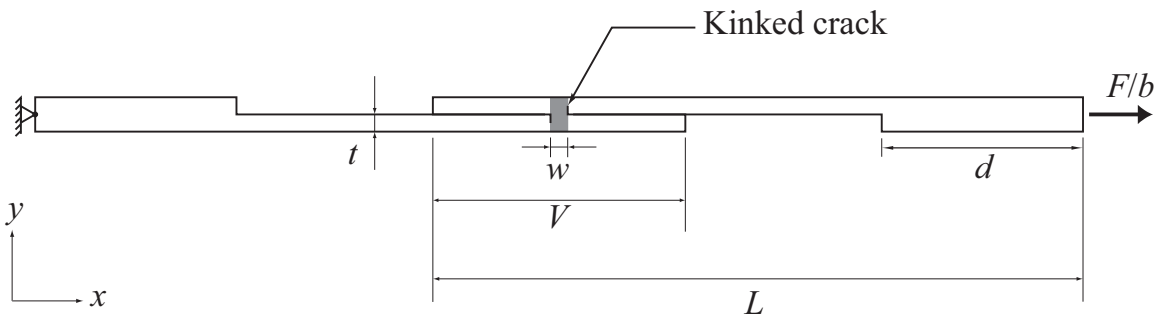

(a)

(b)

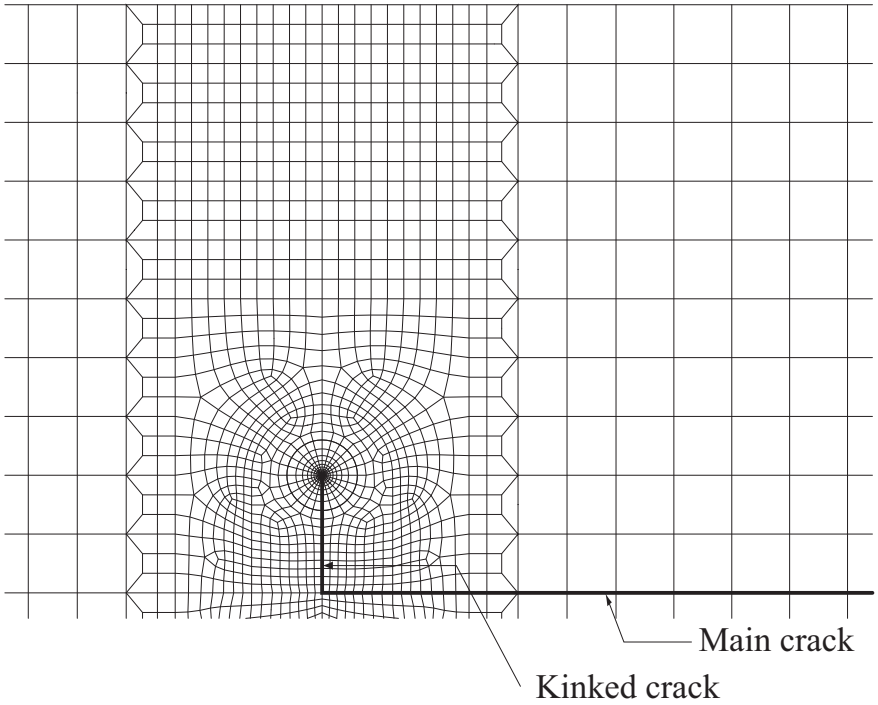

(c)

Figure 2.10. (a) A schematic of a two-dimensional finite elemental model of a lap-shear specimen with two kinked cracks and the boundary conditions, (b) the right part of the finite element mesh for $w/t = 1$ and $a/t = 0.2$, and (c) a close-up view of the finite element mesh near the kinked crack tip.

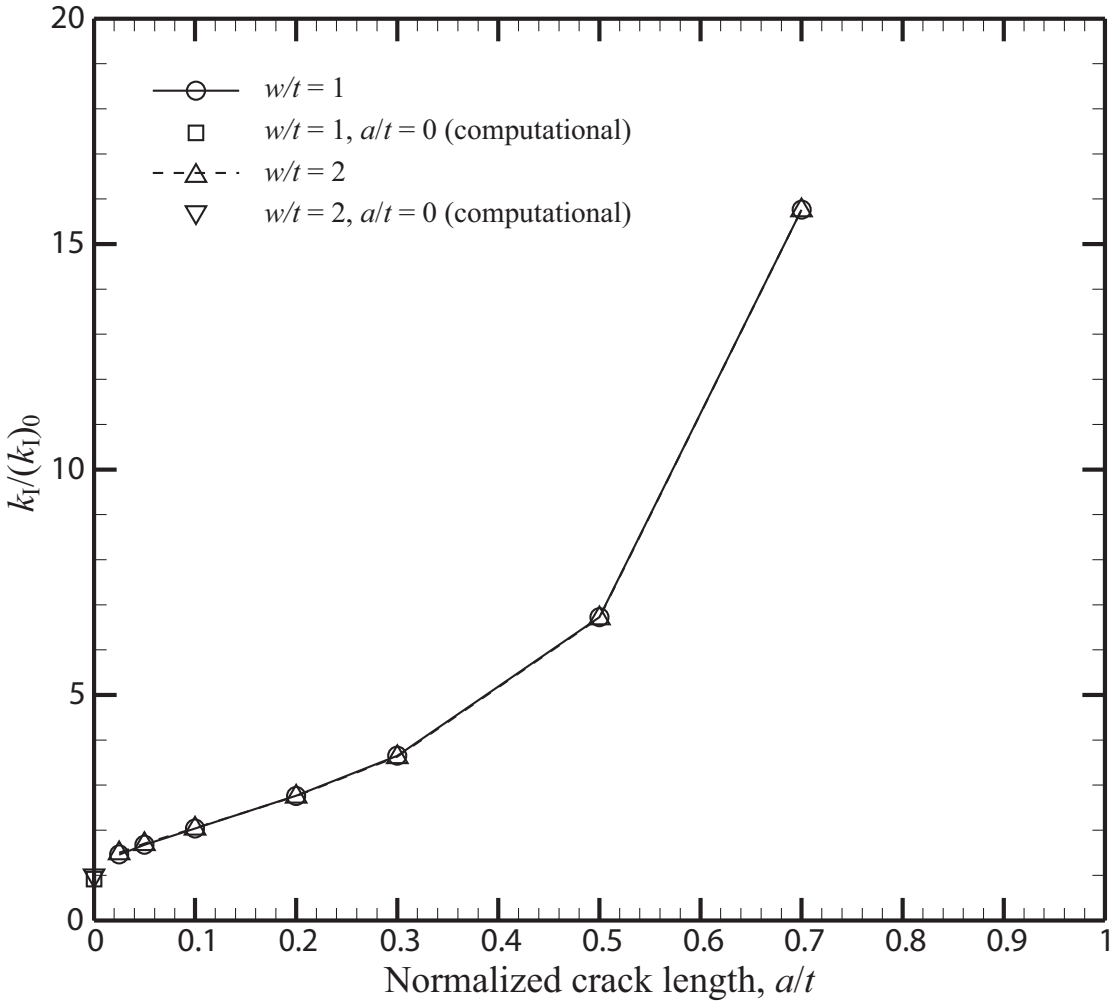

Figure 2.11. The values of $k_{\mathrm{I}}/(k_{\mathrm{I}})_0$ as functions of the normalized kink length a/t for $w/t = 1$ and 2 and $\alpha = 90°$.

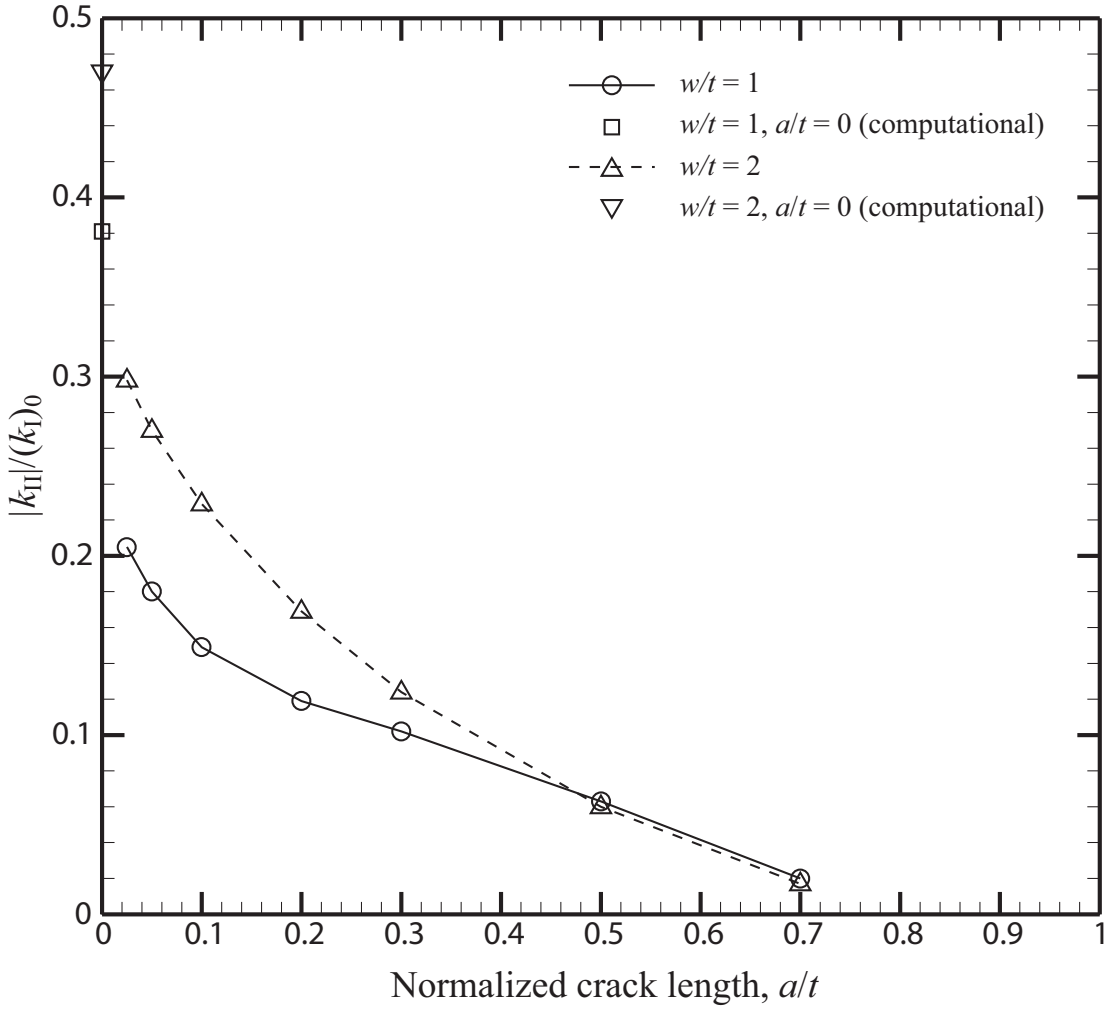

Figure 2.12. The values of $k_{\mathrm{II}}/(k_{\mathrm{I}})_0$ as functions of the normalized kink length a/t for $w/t = 1$ and 2 and $\alpha = 90°$.

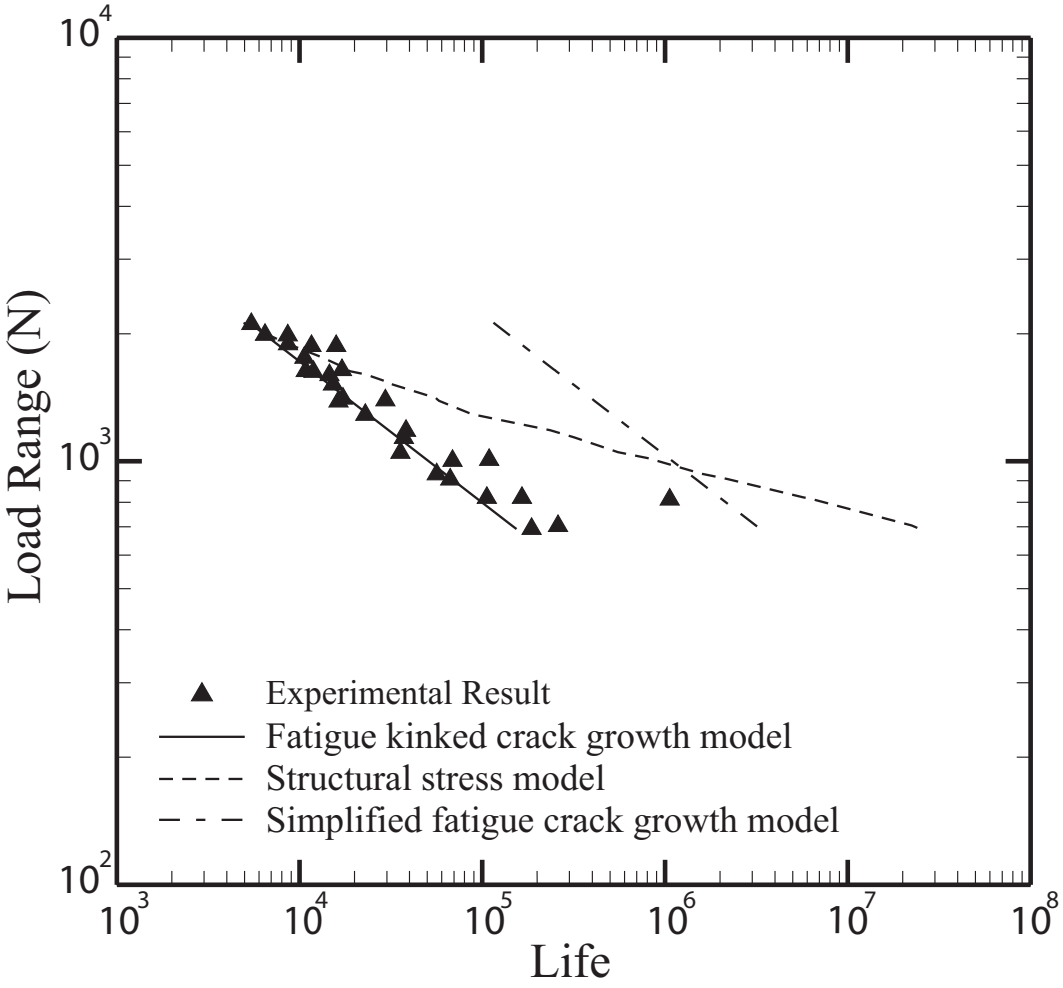

Figure 2.13. The experimental results and the fatigue life estimations based on the fatigue crack growth model, simplified fatigue crack growth model, and the structural stress model.

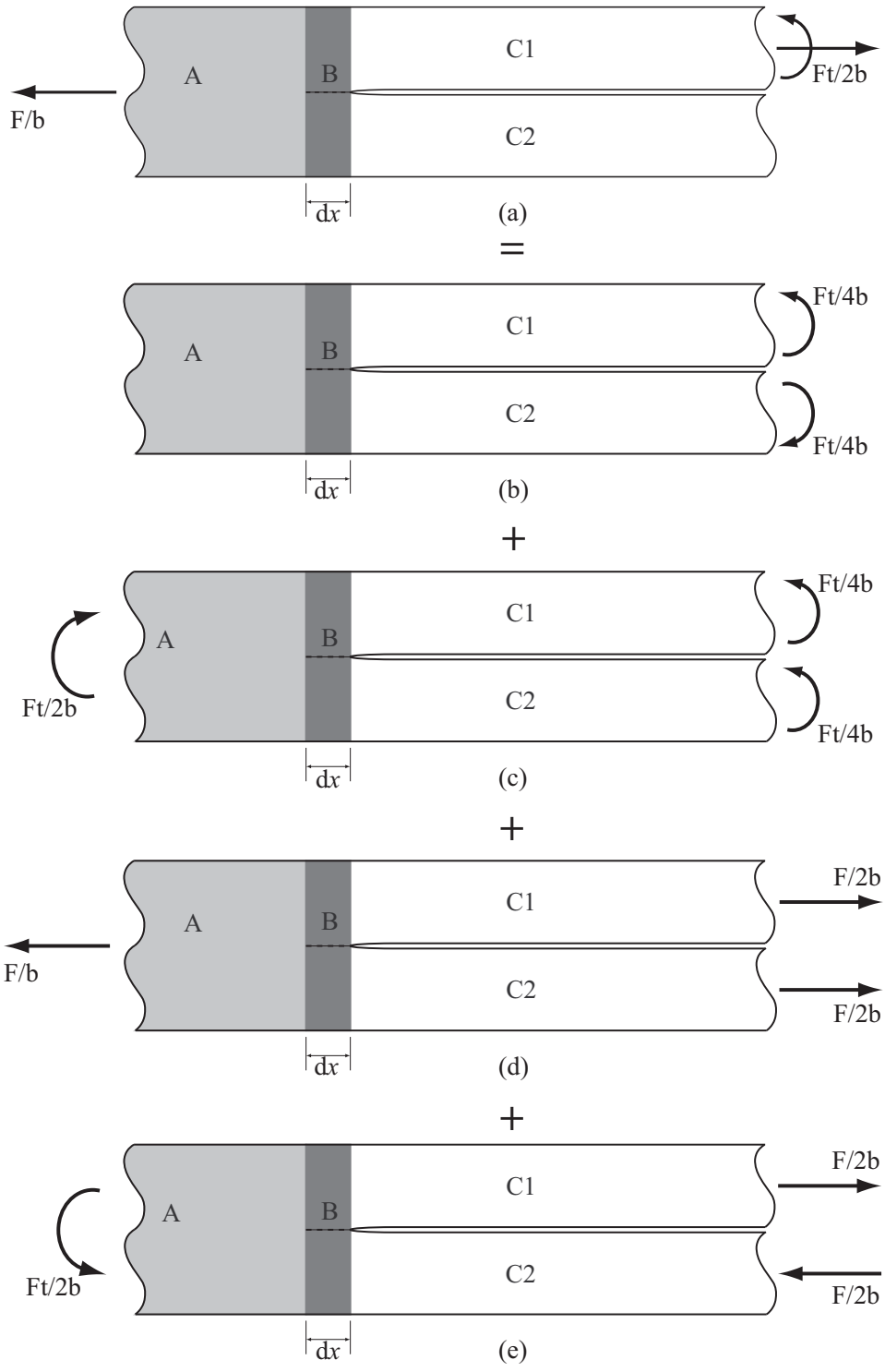

Figure 2.A1. A schematic of the decomposition of the loads for the right part of the two-beam model. The two beams are subjected to (a) equivalent lap-shear loading. The equivalent lap-shear loading shown in (a) is decomposed into (b) counter bending, (c) central bending, (d) tension, and (e) in-plane shear loading conditions.

CHAPTER III

CLOSED-FORM STRUCTURAL STRESS AND STRESS INTENSITY FACTOR SOLUTIONS FOR SPOT WELDS IN SQUARE PLATES UNDER OPENING LOADING CONDITIONS

3.1. Introduction

Resistance spot welding is widely used to join sheet metals in the automotive industry. The fatigue lives of spot welds have been investigated by many researchers. Due to the geometry of spot welds, natural crack tips or notch tips are presented along the nugget circumference. Stress intensity factor solutions for spot welds at the critical locations in various types of specimens have been developed to investigate the fatigue lives of spot welds. Pook [1, 2] gave the maximum stress intensity factors for spot welds in lap-shear, coach-peel specimens, circular plate, and other bending dominant plate and beam configurations. Radaj [3] and Radaj and Zhang [4-6] established the foundation to use the structural stress solutions to determine the stress intensity factor solutions for spot welds. Zhang [7, 8] obtained the stress intensity factor solutions at the critical locations of spot welds in various types of specimens in order to correlate the experimental results of spot welds in these specimens under cyclic loading conditions. Pan and Sheppard [9] investigated the stress intensity factor solutions for both the main cracks and the kinked cracks in lap-shear and modified coach peel specimens by finite element analyses. Wang et al. [10, 11] and Lin et al [12] proposed new stress intensity factor solutions for square-cup and lap-shear specimens and the solutions were validated by their three-dimensional

finite element analyses. Lin and Pan [13, 14] proposed the closed-form structural stress and stress intensity factor solutions for spot welds in various types of specimens.

Pook [2] indicated that for a class of transversely loaded configurations consisting of two thin plates or beams joined over part of their common plane under symmetric loading conditions, the stress intensity factor at a crack tip depends on the bending moment acting to the beam or plate in the vicinity of the crack tip. Wang et al. [10] conducted three-dimensional finite element analyses of circular plates with connection under opening loading conditions. The computational results indicate that the stress intensity factor along the crack front can be correlated very well with the analytical solutions based on the bending moments or the corresponding structural stresses for thin plates with connection. The close-form solutions for thin plates with rigid inclusions under shear, central bending, counter bending, and opening loading conditions were obtained by Muskhelishvili [15], Goland [16], Timoshanko and Woinowsky-Krieger [17], Lin et al. [12] and Lin and Pan [13], respectively. The classical solutions of Muskhelishvili [15], Goland [16], Timoshanko and Woinowsky-Krieger [17] were obtained from the complex variable approach and the Kirchhoff plate theory. The Lin and Pan [13] solutions were obtained from the Airy stress function and the Kirchhoff plate theory.

For the stress intensity factor solutions for spot welds in cross-tension specimens, Lin and Lin [18] indicates that as the effective specimens length increases, the trends of the stress intensity factor solutions based on the closed-form structural stress solutions of Lin and Pan [13] agree quite well with the computational results. However, when the effective length of the specimens is equal to the specimen width, the stress intensity factor solutions based on the closed-form structural stress solutions of Lin and Pan [13]

overestimated the computational result by about 20%. Note that, the structural stress solutions of Lin and Pan [13, 14] are based on the superposition of the solutions for a rigid inclusion in a square plate under opening loading and counter-bending loading conditions. Therefore, the main purpose of this investigation is to determine the source of this 20% overestimation. Furthermore, in order to examine the accuracy of the analytical structural stress and stress intensity factor solutions for spot welds in lap-shear, square-cup, U-shape, cross-tension and coach-peel specimens presented in Lin and Pan [13, 14], it is necessary to first examine carefully the analytical solutions for the square overlap parts of these specimens.

The structural stress and stress intensity factor solutions for spot welds between dissimilar sheets are also quite important. For example, in a modern multi-material vehicle, lightweight materials such as aluminum, magnesium and advanced high strength steel sheets must be joined to the underlying substructure, which is usually composed of the conventional steel. Therefore, the stress intensity factor solutions along the circumference of spot welds between dissimilar sheets are of interest for future vehicle durability considerations. For lithium-ion batteries in electric or hybrid vehicle, electrodes are made of aluminum and copper sheets. Therefore, the stress intensity factor solutions for spot welds between aluminum and copper sheets are also of interest for the durability consideration of lithium-ion batteries. Tran and Pan [19] recently presented analytical stress intensity factor solutions for spot welds in lap-shear specimens of different thicknesses and materials in the normalized form for convenient engineering applications. In this chapter, analytical stress intensity factor solutions for spot welds in

square plates of different thicknesses and materials under opening loading conditions will also be presented in the normalized form for convenient engineering applications.

In this chapter, the structural stress solutions for a rigid inclusion in a square plate under opening loading conditions are first investigated. When the plate with the ratio of the plate width to the rigid inclusion becomes large, the structural stress solutions along the rigid inclusion circumference become uniform. Based on this assumption, the square plate then can be idealized to be a circular plate with an equivalent radius and the analytical structural stress solutions for a rigid inclusion in a circular plate can be then used for a rigid inclusion in a square plate. The values of the equivalent radius of the square plate are determined by the structural stress solutions obtained from finite element analyses. Then the stress intensity factor solutions for spot welds between two square plates of similar material, dissimilar materials, equal thickness and different thicknesses under opening loading condition are investigated. The analytical stress intensity factor solutions based on the analytical structural stress solutions for a rigid inclusion in a square plate with the equivalent radius are compared with the stress intensity factor solutions obtained from finite element analyses. Finally, complete sets of the normalized stress intensity factor solutions for combinations of steel, aluminum and magnesium sheets of different thicknesses and combinations of aluminum and copper sheets of different thicknesses are presented for convenient engineering applications.

3.2. Analytical structural stress solutions for a rigid inclusion in a circular plate

Lin and Pan [13] presented the closed-form structural stress solutions for a rigid inclusion in a finite circular plate under an out-of-plane or opening force F_z with the

boundary conditions of both simply supported and clamped outer edges. Figure 3.1(a) shows schematically an axisymmetric model of a finite circular plate with a simply supported outer edge. The plate has the thickness t and the diameter $2b$. The plate has a rigid inclusion with the diameter $2a$. The inclusion is subjected to an out-of-plane or resultant opening force F_z. The structural stress $\sigma_{ss,axis}$ or the maximum bending stress σ_{rr} along the circumference of the rigid inclusion in the circular plate with a simply supported outer edge based on the Kirchhoff plate theory can be written as [13,14]

$$\sigma_{ss,axis} = \frac{-3F_z\left[\left(a^2-b^2\right)\left(-1+\nu\right)+2b^2\left(1+\nu\right)\ln\left(b/a\right)\right]}{2\pi t^2\left[a^2\left(-1+\nu\right)-b^2\left(1+\nu\right)\right]} \tag{3.1}$$

Figure 3.1(b) shows schematically an axisymmetric model of a finite circular plate with a clamped outer edge. The structural stress $\sigma_{c,axis}$ or the maximum bending stress σ_{rr} along the circumference of the rigid inclusion in the circular plate with a clamped outer edge based on the Kirchhoff plate theory can be written as [13]

$$\sigma_{c,axis} = \frac{-3F_z\left[a^2-b^2+2b^2\ln\left(b/a\right)\right]}{2\pi t^2\left(a^2-b^2\right)} \tag{3.2}$$

3.3. Finite element analyses for a rigid inclusion in a finite circular plate

In order to investigate the structural stress solutions for a rigid inclusion in a square plate and compare to the analytical solutions for a rigid inclusion in a finite circular plate, finite element analyses for a rigid inclusion in a finite circular plate were conducted first in order to investigate the effects of element type and size near the rigid inclusion on the solutions. Figure 3.2(a) shows a schematic of an axisymmetrical finite element model and the boundary conditions along the edge of the rigid inclusion. The z-r coordinate

system is shown in the figure. The origin of the z-r coordinate system is located at the center of the lower surface of the rigid inclusion and the z axis passes the symmetry axis of the axisymmetrical plate. In this model, the rigid inclusion with the radius $a = 3.2\,\text{mm}$ is represented by the roller boundary conditions at $r = a$, as shown in the figure. The lower surface of the plate at $r = a$ is fixed. The boundary conditions at $r = a$ are used to produce the stress solutions that are consistent with the Kirchhoff plate theory. The circular plate has the thickness $t = 0.65\,\text{mm}$ and the diameter $2b = 50.8$ mm and is subjected to the roller boundary conditions and a uniform displacement in the z direction on the upper surface at $r = b$. Figures 3.2(b) – 3.2(g) show the meshes of various axisymmetrical finite element models. Figures 3.2(h) – 3.2(j) show magnified views of the meshes near the circumference of the inclusion for the models shown in Figures 3.2(e) – 3.2(g), respectively. The z-r coordinate systems are shown in the figures and indicate the centers of the axisymmetrical models. In this investigation, the finite elements along the inclusion circumference were selected from the size equal to the plate thickness to the size equal to 1/12 of the plate thickness. The material is assumed to be a linear elastic isotropic material. The Young's modulus E is taken as 207 GPa, and the Poisson's ratio ν is taken as 0.3. The commercial finite element program ABAQUS [20] was employed to perform the computations. The element type is selected to be CAX8R which gives linear distributions of the strains within the element.

Figure 3.3 shows the bending stress σ_{rr} distributions along the thickness direction at $r = a$ from the axisymmetrical finite element models with the clamped boundary condition at $r = b$. The solutions are normalized with the analytical structural stress solution for a rigid inclusion in a finite circular plate with the boundary condition of a

clamped outer edge, $\sigma_{c,axis}$, in Equation (3.2). As shown in the figure, the bending stress σ_{rr} near the lower surface of the axisymmetrical finite element models increases as the element size decreases due to the local effect of the reaction force from the fixed displacement on the lower surface at $r = a$. As shown in the figure, when the finite element size equals to the plate thickness, the stress solution follows the exact linear distribution of the Kirchhoff plate theory. Therefore, the finite element model to investigate the structural stress solution for a rigid inclusion in a square plate was selected to be the model with the element size of the plate thickness along the inclusion circumference since the element selected gives linear distributions of stresses and strains in the thickness direction.

3.4. Finite element analyses for a rigid inclusion in a square plate

For modeling of spot welds in various types of specimens, the square overlap parts of the specimens, which are common to all types of specimens are considered here. Figure 3.4 shows a schematic of two square plates with connection or spot weld. Both plates have the thickness t and the width $2b$. The connection or spot weld is shown as the shaded area and has the diameter $2a$. Both plates are subjected to a uniform out-of-plane or opening displacement along the outer edges as shown schematically as bolded arrows. Points A, B, C and D indicate the critical locations of the connection or spot weld. In order to derive closed-form stress intensity factor solutions for spot welds between square plates, the analytical structural stress solutions for a rigid inclusion in a square plate are needed. Here, finite element analyses for a rigid inclusion in a square plate were carried out in order to investigate the applicability of the analytical structural stress solutions for

a rigid inclusion in a circular plate. Figure 3.5(a) shows a schematic of a half three-dimensional finite element model for a square plate with a rigid inclusion. The boundary conditions along the boundary of the central hole (rigid inclusion) and the applied out-of-plane displacement to the upper surfaces of the outer square edges are also shown. Figure 3.5(b) shows a schematic of a half three-dimensional finite element model for a square plate with a rigid inclusion. The boundary conditions along the boundary of the central hole (rigid inclusion), the applied out-of-plane displacement to the upper surfaces of the outer square edges and the roller boundary conditions on the outer square edges are also shown. For both cases, the x-y-z coordinate system is shown and the origin of the coordinates is located at the center of the lower surface of the rigid inclusion of the square plate. In these models, the rigid inclusion with the radius $a = 3.2$ mm was replaced with a hole and the roller boundary conditions at $r = a$, as shown in the figures. The square plate has the thickness $t = 0.65$ mm and different values of the width $2b$. The square plate is subjected to a uniform displacement in the z direction along the upper surfaces of the outer edges. Five ratios of the plate width to the rigid inclusion diameter, namely, b/a = 3, 5.91, 7.94, 10 and 15 are considered in this investigation. Figure 3.5(c) shows the finite element mesh of a quarter three-dimensional finite element model for b/a = 7.94. The x-y-z coordinate system is again shown and the origin is located at the center of the lower surface of the rigid inclusion of the square plate. Due to the symmetry, only a quarter of the model was considered. The material is assumed to be a linear elastic isotropic material. The Young's modulus E is taken as 207 GPa, and the Poisson's ratio ν is taken as 0.3. The commercial finite element program ABAQUS [20] was employed to perform the computations.

Figure 3.6 shows the normalized structural stress distributions, or the maximum bending stress distributions along the circumference of the rigid inclusion for the ratios of the plate width to the rigid inclusion diameter, *b/a* , of 3, 5.91 and 7.94. The structural stress solutions are expressed as functions of the orientation angle θ from the x axis to the y axis in the counter-clockwise sense. The computational structural stress solutions are normalized by the computational structural stress solution at the critical location of $\theta = 0$. As shown in Figure 3.6, when the square plate with a rigid inclusion with the ratio of the plate width to the rigid inclusion diameter, *b/a* , is large as 5.91, the structural stress solutions along the circumference of the rigid inclusion are almost uniform. Therefore, the analytical structural stress solutions for a rigid inclusion in a circular plate now can be used to approximate the structural stress solutions for a rigid inclusion in a square plate for large ratios of *b/a* . Based on the analytical structural stress solutions for a rigid inclusion in a circular plate in Equations (3.1) and (3.2), the structural stress solutions for a rigid inclusion in a square plate with simply supported outer edges can be written as [13, 14]

$$\sigma_{ss,square} = \frac{-3F\left[\left(a^2 - b'^2\right)\left(-1+\nu\right) + 2b'^2\left(1+\nu\right)\ln\left(b'/a\right)\right]}{2\pi t^2\left[a^2\left(-1+\nu\right) - b'^2\left(1+\nu\right)\right]} \tag{3.3}$$

where F is the total opening force acting on the outer edges of the square plate and b' is the equivalent radius for the equivalent circular plate model, where the structural stress for a rigid inclusion in a square plate with the width $2b$ equals that for a rigid inclusion in a circular plate with the diameter $2b'$. Similarly, the structural stress solutions for a rigid inclusion in a square plate with clamped outer edges can be written as [13]

$$\sigma_{c,square} = \frac{-3F\left[a^2 - b'^2 + 2b'^2\ln\left(b'/a\right)\right]}{2\pi t^2\left(a^2 - b'^2\right)} \tag{3.4}$$

Figure 3.7 shows the values of the normalized equivalent radius b'/b as functions of the ratio of the plate width to the rigid inclusion diameter, b/a, for a rigid inclusion in a square plate with both simply supported and clamped boundary conditions along the outer edges. Lin and Pan [14] proposed the equivalent radius $b' = 2b/\sqrt{\pi}$ based on an area equivalence rule. The normalized solution of $2/\sqrt{\pi}$ (= 1.128) based on the area equivalence rule is shown as a thin line in Figure 3.7. Table 3.1 lists the values of the normalized equivalent radius b'/b for various ratios of b/a for convenient engineering applications. For both simply supported and clamped boundary conditions along the outer edges, as the ratio of the plate width to the rigid inclusion diameter increases, the equivalent radius seem to reach the values of 0.838 and 1.056, respectively. These values of the equivalent radius correspond to the square plate with the two boundary conditions along the outer edges with the rigid inclusion diameter decreasing to 0. The solutions based on the area equivalent rule apparently overestimate the value of b'/b for both boundary conditions especially for the simply supported boundary conditions along the outer edges by as much as 35%. Based on the computational results in Figure 3.7, the equivalent radius of a square plate with a rigid inclusion with simply supported outer edges can be approximated as a function of b/a as

$$\frac{b'}{b} = 0.838 + 0.4877e^{-0.3513(b/a)} \tag{3.5}$$

Similarly, the equivalent radius of a square plate with a rigid inclusion with clamped outer edges can be approximated as a function of b/a as

$$\frac{b'}{b} = 1.056 + 0.3814e^{-0.6165(b/a)} \tag{3.6}$$

The approximate equivalent radius from Equations (3.5) and (3.6) are also shown as a line and dotted line in Figure 3.7, respectively.

3.5. Analytical stress intensity factor solutions for spot welds between square plates of equal thickness

Stress intensity factor solutions for spot welds in various types of specimens were obtained from the structural stress solutions in [3-8]. Analytical stress intensity factor solutions for spot welds between square plates of equal thickness under opening loading conditions, as shown in Figure 3.4, were proposed in [10, 13] based on the structural stress solutions for a rigid inclusion in a square plate with the equivalent radius b' based on the area equivalence rule. For spot welds between square plates of the same material and equal thickness with simply supported outer edges, the stress intensity factor K_{I} solution can be written as [13, 14],

$$K_{\mathrm{I,ss}} = \frac{\sqrt{t}\sigma_{ss,square}}{\sqrt{3}} = \frac{-\sqrt{3}F\left[\left(a^2 - b'^2\right)\left(-1+\nu\right) + 2b'^2\left(1+\nu\right)\ln\left(b'/a\right)\right]}{2\pi t^{3/2}\left[a^2\left(-1+\nu\right) - b'^2\left(1+\nu\right)\right]} \tag{3.7}$$

Similarly, the stress intensity factor K_{I} solution for spot welds between square plates of the same material and equal thickness with clamped outer edges can be written as [10, 13],

$$K_{\mathrm{I,c}} = \frac{\sqrt{t}\sigma_{c,square}}{\sqrt{3}} = \frac{-\sqrt{3}F\left[a^2 - b'^2 + 2b'^2\ln\left(b'/a\right)\right]}{2\pi t^{3/2}\left(a^2 - b'^2\right)} \tag{3.8}$$

Now, with the computational results presented earlier in this chapter, the values of b'/b in Equations (3.5) and (3.6) should be used.

3.6. Finite element analyses for spot welds between square plates of equal thickness

Finite element analyses for spot welds between square plates of equal thickness were conducted in order to investigate the applicability of the solutions of the equivalent radius in Equations (3.5) and (3.6) to estimate the stress intensity factor solutions for spot welds. Figure 3.8(a) shows a schematic of a three-dimensional finite element model of two square plates with connection and simply supported outer edges. Figure 3.8(b) shows a schematic of a three-dimensional finite element model of two square plates with connection and clamped outer edges. For both cases, the x-y-z coordinate system is shown and the origin of the coordinates is located at the center of the connection of the two square plates. Both plates have the equal thickness $t = 0.65\,\text{mm}$ and various values of the width $2b$. The connection or spot weld has the diameter of $2a = 6.4\,\text{mm}$. The lower surfaces of the outer edges of the lower plates are fixed. The upper plates are subjected to a uniform out-of-plane displacement in the z direction along the upper surfaces of the outer edges. Five ratios of the plate width to the connection diameter, namely, b/a = 3, 5.91, 7.94, 10 and 15, are considered in this investigation. Figures 3.8(c) and 3.8(d) show a quarter of a three-dimensional finite element model for b/a = 7.94 and a close-up view of the mesh near the crack front. The x-y-z coordinate system is shown and the origin of the coordinates is located at the center of the connection of the square plates. Due to the symmetry, only a quarter of the model was considered. The material is assumed to be a linear elastic isotropic material. The Young's modulus E is taken as 207 GPa, and the Poisson's ratio ν is taken as 0.3. The commercial finite element program ABAQUS [20] was employed to perform the

computations. Brick elements C3D20R with quarter point nodes and collapsed nodes along the crack front are adopted to model the $1/\sqrt{r}$ singularity near the crack front.

Figure 3.9 shows the normalized stress intensity factor K_{I} solutions for spot welds between square plates with various ratios of the plate width to the connection diameter, b/a. In this figure, the K_{I} solutions are normalized by the analytical K_{I} solutions for spot welds between square plates with simply supported and clamped outer edges obtained from Equations (3.7) and (3.8) and the equivalent radius b' listed in Table 3.1. The normalized computational K_{I} solutions for spot welds between square plates with simply supported and clamped outer edges are shown as circle and square symbols in Figure 3.9, respectively. The applicability of the equivalent radius b' based on the area equivalence rule on the stress intensity factor K_{I} solutions is also investigated. The normalized analytical K_{I} solutions for spot welds between square plates with simply supported and clamped outer edges obtained from Equations (3.7) and (3.8) and the equivalent radius b' based on the area equivalence rule are shown as triangle and diamond symbols in Figure 3.9, respectively. As shown in Figure 3.9, the computational K_{I} solutions are agree quite well with the analytical solutions obtained from Equations (3.7) and (3.8) based on the equivalent radius b' listed in Table 3.1 for large ratios of b/a. As shown in Figure 3.6 earlier, the structural stress solutions for a rigid inclusion in a square plate deviate from the analytical solutions for a rigid inclusion in a circular plate as the value of b/a decreases to 3 due to the effects of the boundary of the square plate. Therefore, it is not unreasonable that the analytical K_{I} solutions for both simply supported and clamped outer edges underestimate the K_{I} solutions by 3 to 7% based on

the equivalent radius b' listed in Table 3.1 for b/a equal to 3 as shown in Figure 3.9. However, the analytical K_{I} solution based on the equivalent radius b' of the area equivalence rule just happens to agree well with the computational K_{I} solutions for b/a equal to 3 under the clamped outer edge conditions. The most important result from this investigation is that when the area equivalent rule is used for the stress intensity factor solutions in Lin and Pan [14] for the square overlap part of cross-tension specimens, the stress intensity factor solutions can be overestimated by more than 15% under the opening loading conditions. It should be mentioned that the structural stress solutions for a rigid inclusion in a square plate with simply supported outer edges are the main contribution for the structural stress and stress intensity factor solutions for spot welds in cross-tension specimens.

3.7. Analytical stress intensity factor solutions for spot welds between square plates of different thicknesses and materials

Generally, two square plates with connection do not necessarily have equal thickness or the same material. Figure 3.10 shows a schematic of two square plates with connection or spot weld. Both plates have the width $2b$. The upper plate has the thickness t_u and the lower plate has the thickness t_l. The connection or spot weld is shown as the shaded area and has the diameter $2a$. Both plates are subjected to a uniform out-of-plane or opening displacement along the outer edges as shown schematically as bolded arrows. Points A, B, C and D indicate the critical locations of the connection or spot weld. The material of the upper plate and lower plate can be either identical or dissimilar. Figure 3.4 shows the special case that the thickness of the upper

and lower plates are equal ($t_u = t_l = t$) and the upper and lower plates are made of identical material.

For the general case of spot welds between square plates of different thicknesses and materials under opening loading conditions as shown in Figure 3.10, the analytical stress intensity factor solutions can be determined from the analytical structural stress solutions for a rigid inclusion in a square plate. Figure 3.11(a) shows a two-dimensional model of two infinite strips of different thicknesses and materials with connection under plane strain conditions. As shown in Figure 3.11(a), the radial stress σ_{rr} and the shear stress $\sigma_{r\theta}$ along the circumference of a rigid inclusion in a plate are used to represent the normal structural stresses, σ_x^u and σ_x^l, and the shear structural stresses, τ_{xz}^u and τ_{xz}^l, for the strip model with respect to the Cartesian coordinate system as shown in the figure. Figure 3.11(b) shows the front and side views of the left part of the strip model near the crack tip with the linearly distributed structural stresses through the thickness based on the Kirchhoff plate theory. The strip model can be used to represent the cross section perpendicular to the crack front along the spot weld or the connection circumference. The two strips are assumed to be linear elastic isotropic materials with the Young's modulus E_u and Poisson's ratio ν_u for the upper strip material, and the Young's modulus E_l and Poisson's ratio ν_l for the lower strip material. The upper strip has the thickness t_u and the lower strip has the thickness t_l. The normal stresses σ_{ui}, σ_{uo}, σ_{li} and σ_{lo} represent the normal stresses σ_x at the inner (*i*) and outer (*o*) surfaces of the upper (*u*) and lower (*l*) strips, respectively. The shear stresses τ_{ui}, τ_{uo}, τ_{li} and τ_{lo} represent the shear stresses τ_{xz} at the inner (*i*) and outer (*o*) surfaces of the upper (*u*) and

lower (*l*) strips, respectively. Based on the strip model, Zhang [21] derived the in-plane J integral, J_{xy}, based on the in-plane normal stresses as

$$J_{xy} = \frac{t_u}{6\left[1+2\eta\delta\left(2+3\delta+2\delta^2\right)+\eta^2\delta^4\right]E'_u}$$
$$\times\left[\left(1+\eta\delta+3\eta\delta^2+3\eta\delta^3\right)\sigma_{ui}^2+\eta^2\left(3+3\delta+\delta^2+\eta\delta^2\right)\sigma_{li}^2\right.$$
$$-\eta\left(3+\delta+\eta\delta^2+3\eta\delta^3\right)\sigma_{ui}\sigma_{li}+\left(1+\eta\delta\right)\left(\sigma_{uo}+\eta\delta\sigma_{lo}\right)^2$$
$$\left.+\left(1-2\eta\delta-3\eta\delta^2\right)\left(\sigma_{ui}\sigma_{uo}+\eta\delta\sigma_{ui}\sigma_{lo}\right)-\eta\left(3+2\delta-\eta\delta^2\right)\left(\sigma_{uo}\sigma_{li}+\eta\delta\sigma_{li}\sigma_{lo}\right)\right] \quad (3.9)$$

where δ is the thickness ratio and η is the modulus ratio. δ and η are defined as

$$\delta = \frac{t_u}{t_l} \quad (3.10)$$

and

$$\eta = \frac{E'_u}{E'_l} \quad (3.11)$$

Under plane strain conditions, E'_u and E'_l are defined as

$$E'_u = \frac{E_u}{\left(1-\nu_u^2\right)} \quad (3.12a)$$

and

$$E'_l = \frac{E_l}{\left(1-\nu_l^2\right)} \quad (3.12b)$$

Based on the in-plane part of the J integral solution of the strip model and the analytical solutions for interface cracks of Suo and Hutchison [22], Zhang [21] derived the stress intensity factor K_1 and K_2 solutions in terms of the structural stresses σ_{ui}, σ_{uo}, σ_{li} and σ_{lo} of the upper and lower plates as

$$K_1 = \frac{\cosh(\pi\varepsilon)\sqrt{t_u}}{2\sqrt{3(1+\eta)(1+4\eta\delta+6\eta\delta^2+3\eta\delta^3)(1+\tan^2\omega)}}\times$$

$$\left\{\left[\frac{(1+4\eta\delta+9\eta\delta^2+6\eta\delta^3)\tan\omega}{\sqrt{1+2\eta\delta(2+3\delta+2\delta^2)+\eta^2\delta^4}}-\sqrt{3}\right]\sigma_{ui}\right.$$

$$-\left[\frac{(1+4\eta\delta+3\eta\delta^2)\tan\omega}{\sqrt{1+2\eta\delta(2+3\delta+2\delta^2)+\eta^2\delta^4}}+\sqrt{3}\right]\sigma_{uo}$$

$$+\eta\left[\frac{\delta(1-2\eta\delta-3\eta\delta^2)\tan\omega}{\sqrt{1+2\eta\delta(2+3\delta+2\delta^2)+\eta^2\delta^4}}+\sqrt{3}(2+\delta)\right]\sigma_{li}$$

$$\left.-\eta\delta\left[\frac{(1+4\eta\delta+3\eta\delta^2)\tan\omega}{\sqrt{1+2\eta\delta(2+3\delta+2\delta^2)+\eta^2\delta^4}}+\sqrt{3}\right]\sigma_{lo}\right\} \qquad (3.13)$$

$$K_2 = \frac{\cosh(\pi\varepsilon)\sqrt{t_u}}{2\sqrt{3(1+\eta)(1+4\eta\delta+6\eta\delta^2+3\eta\delta^3)(1+\tan^2\omega)}}\times$$

$$\left\{\left[\frac{1+4\eta\delta+9\eta\delta^2+6\eta\delta^3}{\sqrt{1+2\eta\delta(2+3\delta+2\delta^2)+\eta^2\delta^4}}+\sqrt{3}\tan\omega\right]\sigma_{ui}\right.$$

$$-\left[\frac{1+4\eta\delta+3\eta\delta^2}{\sqrt{1+2\eta\delta(2+3\delta+2\delta^2)+\eta^2\delta^4}}-\sqrt{3}\tan\omega\right]\sigma_{uo}$$

$$+\eta\left[\frac{\delta(1-2\eta\delta-3\eta\delta^2)}{\sqrt{1+2\eta\delta(2+3\delta+2\delta^2)+\eta^2\delta^4}}-\sqrt{3}(2+\delta)\tan\omega\right]\sigma_{li}$$

$$\left.-\eta\delta\left[\frac{1+4\eta\delta+3\eta\delta^2}{\sqrt{1+2\eta\delta(2+3\delta+2\delta^2)+\eta^2\delta^4}}-\sqrt{3}\tan\omega\right]\sigma_{lo}\right\} \qquad (3.14)$$

In Equations (3.13) and (3.14), ε is the bimaterial constant which is defined as

$$\varepsilon = \frac{1}{2\pi}\ln\frac{\kappa_u/G_u+1/G_l}{\kappa_l/G_l+1/G_u} \qquad (3.15)$$

where G_u is the shear modulus of the upper plate and G_l is the shear modulus of the lower plate. Under the plane strain conditions, the constants κ_u and κ_l are defined as

$$\kappa_u = 3 - 4\nu_u \tag{3.16a}$$

and

$$\kappa_l = 3 - 4\nu_l \tag{3.16b}$$

In Equations (3.13) and (3.14), ω is the angular quantity which can be found in Suo and Hutchinson [22]. The angular quantity ω is a function of the thickness ratio δ and the Dundurs parameters α and β which are defined as

$$\alpha = \frac{\xi(\kappa_l + 1) - (\kappa_u + 1)}{\xi(\kappa_l + 1) + (\kappa_u + 1)} \tag{3.17}$$

$$\beta = \frac{\xi(\kappa_l - 1) - (\kappa_u - 1)}{\xi(\kappa_l + 1) + (\kappa_u + 1)} \tag{3.18}$$

where ξ is the shear modulus ratio which is defined as

$$\xi = \frac{G_u}{G_l} \tag{3.19}$$

For square plates under opening loading conditions, the normal stresses σ_{ui} and σ_{li} are the structural stresses in Equation (3.3) and (3.4) for simply supported and clamped outer edges, respectively. For square plates under opening loading conditions, $\sigma_{uo} = -\sigma_{ui}$ and $\sigma_{lo} = -\sigma_{li}$. In order to examine the analytical and computational results for both similar and dissimilar material cases, the values of the in-plane J integral, J_{xy}, are obtained and compared. The J_{xy} integral is defined for interface cracks between dissimilar materials as

$$J_{xy} = \frac{K_1^2 + K_2^2}{\cosh^2(\pi\varepsilon)E^*} \tag{3.20}$$

where E^* is defined as

$$\frac{1}{E^*} = \frac{1}{2}\left(\frac{1}{E'_u} + \frac{1}{E'_l}\right) \tag{3.21}$$

According to Equation (3.20), an equivalent K_{eq} can be defined as

$$K_{eq} = \sqrt{K_1^2 + K_2^2} = \sqrt{J_{xy}\cosh^2(\pi\varepsilon)E^*} \tag{3.22}$$

For the similar material case, Equation (3.20) becomes

$$J_{xy} = \frac{K_I^2 + K_{II}^2}{E'} \tag{3.23}$$

where

$$E' = \frac{E}{(1-\nu^2)} \tag{3.24}$$

The equivalent K_{eq} in Equation (3.22) becomes

$$K_{eq} = \sqrt{K_I^2 + K_{II}^2} = \sqrt{J_{xy}E'} \tag{3.25}$$

The value of K_{eq} are also obtained analytically and computationally for comparison.

The values of the Dundurs parameters α and β, bimaterial constant ε, modulus ratios η and ξ, and angular quantity ω (in degree) for dissimilar materials of combinations between magnesium (Mg), aluminum (Al), and steel (Fe) sheets and combinations of aluminum (Al) and copper (Cu) sheets with $\delta = 1$ and $\delta = 0.5$ are listed in Tables 3.2a and 3.2b, respectively. For the notations of the material combinations shown in Tables 3.2a and 3.2b such as Mg/Al, Mg represents the upper sheet material and Al represents the lower sheet material. In this investigation, the Young's modulus and

Poisson's ratio for magnesium (Mg) are taken as 45 GPa and 0.35, respectively. The Young's modulus and Poisson's ratio for aluminum (Al) are taken as 68.9 GPa and 0.33, respectively. The Young's modulus and Poisson's ratio for steel (Fe) are taken as 207 GPa and 0.3, respectively. The Young's modulus and Poisson's ratio for copper (Cu) are taken as 110 GPa and 0.34, respectively. Note that K_1 and K_2 are the stress intensity factor solutions for interface cracks between dissimilar materials. When the upper and lower sheet materials are identical, the K_1 and K_2 solutions in Equations (3.13) and (3.14) become the conventional K_I and K_{II} solutions, respectively. For similar material, $\alpha = \beta = \varepsilon = 0$ and $\eta = \xi = 1$, $\omega = 49.1°$ for $\delta = 1$ and $\omega = 49.8°$ for $\delta = 0.5$.

In order to assess the significance of the out-of-plane shear stress intensity factor solution K_{III}, the out-of-plane shear stress along the circumference of a rigid inclusion in a square plate under opening loading conditions was investigated. Figure 3.12 shows the normalized out-of-plane shear stresses distributions along the circumference of the rigid inclusion for the ratios of the plate width to the rigid inclusion diameter, b/a, of 3, 5.91 and 7.94. The out-of-plane shear stress solutions are expressed as functions of the orientation angle θ from the x axis to the y axis in the counter-clockwise sense. The computational out-of-plane shear stress solutions are normalized by the computational in-plane structural stress solution at the critical location of $\theta = 0$. As shown in the figure, for the large ratio $b/a = 7.94$, the out-of-plane shear structural stresses are very small and can be neglected when compare to the in-plane structural stresses. Thus, for the square specimens under opening loading conditions, the out-of-plane shear stress intensity factor K_{III} solutions are assumed to be very small and neglected when compare to the in-plane stress intensity factor K_I, K_{II}, K_1 and K_2 solutions.

3.8. Finite element analyses for spot welds between square plates of different thicknesses and materials

Finite element analyses for spot welds between square plates of different thicknesses and materials were conducted in order to investigate the applicability of the stress intensity factor solutions for interface cracks in Equations (3.13) and (3.14) based on the equivalent radius listed in Table 3.1 to estimate the stress intensity factor solutions. For a spot weld between square plates of equal thickness and dissimilar materials, the three-dimensional finite element model and the boundary conditions as shown in Figure 3.8 for the ratio of $b/a = 7.94$ was also used in the computation for the dissimilar material case here. For a spot weld between square plates of unequal thicknesses, three-dimensional finite element models and the boundary conditions are shown in Figure 3.13. The finite element models were used for computations for both similar and dissimilar material cases. Figure 3.13(a) shows a schematic of a three-dimensional finite element model of two square plates of unequal thicknesses with connection and simply supported outer edges. Figure 3.13(b) shows a schematic of a three-dimensional finite element model of two square plates of unequal thicknesses with connection and clamped outer edges. For both cases, the x-y-z coordinate system is shown and the origin of the coordinates is located at the center of the connection interface of the two square plates. The upper plate has the thickness $t_u = 0.65$ mm and the lower plate has the thickness $t_l = 1.30$ mm. Both plates have the width $2b = 50.8$ mm. The connection has the diameter of $2a = 6.4$ mm. The lower surfaces of the outer edges of the lower plates are fixed. The upper plates are subjected to a uniform out-of-plane displacement in the z direction along the upper

surfaces of the outer edges. Figures 3.13(c) and 3.13(d) show a quarter of the three-dimensional finite element model and a close-up view of the mesh near the crack front. The x-y-z coordinate system is shown and the origin of the coordinates is located at the center of the connection interface of the square plates. Due to the symmetry, only a quarter of the model was considered.

For the similar material case, the material is assumed to be a linear elastic isotropic material. The Young's modulus and Poisson's ratio are taken as 207 GPa and 0.3 for steel (Fe), respectively. For the dissimilar material case, the smallest or largest modulus ratio for all material combinations as mentioned early is the combination of magnesium and steel sheets. For this combination, the upper sheet is selected to be Mg and the lower sheet is selected to be Fe to give the smallest or largest stiffness ratio between the upper and lower sheets. The Young's modulus and Poisson's ratio for magnesium (Mg) are taken as 45 GPa and 0.35, respectively. For the dissimilar material case with equal thickness, the upper sheet is selected to be Mg and the lower sheet is selected to be Fe. The commercial finite element program ABAQUS [20] was employed to perform the computations. Brick elements C3D20R with quarter point nodes and collapsed nodes along the crack front are adopted to model the singularity near the crack front.

Tables 3.3a and 3.3b list the normalized J_{xy}, K_{eq}, K_I, K_{II}, K_1 and K_2 solutions for the ratio of the plate width to the spot weld diameter, b/a = 7.94 for the similar and dissimilar material cases. The computational J_{xy}, K_{eq}, K_I, K_{II}, K_1 and K_2 solutions were normalized by the analytical J_{xy}, K_{eq}, K_{I} and K_1 solutions obtained from Equations (3.3), (3.4), (3.9), (3.13) and (3.14) for spot welds between square plates with simply supported and clamped outer edges. As listed in Table 3.3, the computational J_{xy}

and K_{eq} solutions are agree quite well with the corresponding analytical solutions obtained from Equations (3.3), (3.4), (3.9) and (3.13) based on the equivalent radius b' listed in Table 3.1. For all cases except the similar material case with equal thickness, the computational K_{II} or K_2 solutions are much lower than the K_{I} or K_1 solutions obtained from the computations and Equations (3.3), (3.4) and (3.13) based on the equivalent radius b' in Table 3.1 indicating that spot welds are under mode I dominant conditions. For all cases except the similar material case with equal thickness, the computational K_{I} and K_1 solutions are slightly larger than those of the corresponding analytical solutions and the computational K_{II} and K_2 solutions are smaller than those of the corresponding analytical solutions. Based on the values of the J_{xy} and K_{eq} solutions listed in Tables 3.3a and 3.3b for the selected thickness and material combinations, the in-plane J_{xy} and the equivalent stress intensity factor solutions in Equations (3.3), (3.4), (3.9) and (3.15) with the equivalent radius b' can be used to determined the in-plane J_{xy} and the equivalent stress intensity factor solutions for spot welds between square plates under opening loading conditions with the maximum error of less than 1%. However, when the analytical K_{eq} solutions are decomposed into the K_{I} and K_{II} solutions or K_1 and K_2 solutions based on Equations (3.13) and (3.14), the errors can be as large as 5% for the dominant K_{I} or K_1 solutions. The results indicate that the decomposition of the J_{xy} integral into either K_{I} and K_{II} or K_1 and K_2 based on the interpolated values of ω from Zhang [21] or Suo and Hutchinson [22] may not be accurate enough. However, the

dominant K_1 or K_1 solutions are still quite acceptable for engineering applications when K_{eq} is used to for fatigue life estimations.

3.9. Normalized stress intensity factor solutions for spot welds between square plates of different thicknesses and materials

As discussed earlier, the results of three-dimensional finite element analyses selectively confirmed the accuracy of the analytical stress intensity factor solutions for spot welds between square plates of different thicknesses and materials. However, the stress intensity factor solutions from the combinations of Equations (3.3) and (3.4) and Equations (3.13) and (3.14) are in general quite complex. The stress intensity factor solutions for spot welds between square plates of identical material ($\eta = 1$) and different thicknesses can be written in the normalized forms as

$$K_I = g_{kI}\left(\frac{b}{a}, \delta\right)\frac{F}{t_u\sqrt{t_u}} \tag{3.26}$$

$$K_{II} = g_{kII}\left(\frac{b}{a}, \delta\right)\frac{F}{t_u\sqrt{t_u}} \tag{3.27}$$

where g_{kI} and g_{kII} are the dimensionless geometric functions of b/a and δ. For spot welds between square plates of different thicknesses and materials, the stress intensity factor solutions can be written in the normalized forms as

$$K_1 = g_{k1}\left(\frac{b}{a}, \delta, \eta\right)\frac{F}{t_u\sqrt{t_u}} \tag{3.28}$$

$$K_2 = g_{k2}\left(\frac{b}{a}, \delta, \eta\right)\frac{F}{t_u\sqrt{t_u}} \tag{3.29}$$

where g_{k1} and g_{k2} are the dimensionless geometric functions b/a, δ and η.

Figure 3.14 shows the geometric functions g_{kI}^{SS}, g_{kII}^{SS}, g_{kI}^{C}, and g_{kII}^{C} for spot welds between square plates of identical material ($\eta = 1$) with $\delta = 1$ and $\delta = 0.5$ as functions of b/a for simply supported and clamped outer edges. The superscript *SS* and *C* denote the simply supported and clamped outer edges, respectively. The computational geometric functions g_{kI}^{SS}, g_{kII}^{SS}, g_{kI}^{C}, and g_{kII}^{C} are shown as symbols in Figure 3.14. As mention earlier, the computational geometric functions agree very well with the geometric functions obtained from the analytical solutions in Equations (3.3), (3.4), (3.13) and (3.14) with the approximate equivalent radius b' in Equations (3.5) and (3.6). As the lower plate thickness increases (for the case of $\delta = 0.5$), the K_{II} solutions increase because the difference of the structural stresses between the upper and lower plates increases while the K_I solutions decrease. The results of the finite element analyses for selected values of b/a and η are shown as symbols.

Figures 3.15, 3.16, 3.17, and 3.18 shows the geometric functions g_{k1}^{SS}, g_{k2}^{SS}, g_{k1}^{C}, and g_{k2}^{C} for spot welds between square plates of dissimilar materials between magnesium and steel, between aluminum and steel, between magnesium and aluminum, and between aluminum and copper with different thicknesses respectively. Figures 3.15(a), 3.16(a), 3.17(a) and 3.18(a) show geometric functions g_{k1}^{SS} and g_{k2}^{SS} for Mg/Fe, Al/Fe, Mg/Al and Al/Cu welds in square plates with simply supported outer edges, respectively, for $\delta = 1$ and $\delta = 0.5$ as functions of b/a. The computational g_{k1}^{SS} and g_{k2}^{SS} are shown as symbols in Figure 3.15(a). As listed in Tables 3.2a and 3.2b, the values of the modulus ratio η for Mg/Fe, Al/Fe, Mg/Al and Al/Cu welds are 0.23, 0.34, 0.66, and 0.62, respectively. As

mention earlier, selected computational geometric functions agree well with the geometric functions obtained from the analytical solutions in Equations (3.3), (3.4), (3.13) and (3.14)with the approximate equivalent radius b' in Equations (3.5) and (3.6). As shown in these figures, the trends of the K_1 and K_2 solutions for these four types of welds are quite similar. The results in Figures 3.15(a), 3.16(a), 3.17(a) and 3.18(a) also indicate that, as the thickness of the lower plates increase, the K_1 solutions decrease while the K_2 solutions increase. As shown in these figures, the K_1 solutions barely increase with the increase of η. However, the K_2 solutions decrease significantly with the increase of η. As η increases, the decreases and increases of K_1 and K_2 solutions increase as the lower plates become thicker.

Figures 3.15(b), 3.16(b), 3.17(b) and 3.18(b) show geometric functions g_{k1}^{C}, and g_{k2}^{C} for Mg/Fe, Al/Fe, Mg/Al and Al/Cu welds in square plates with clamped outer edges, respectively, for $\delta = 1$ and $\delta = 0.5$ as functions of b/a. The computational g_{k1}^{C}, and g_{k2}^{C} are shown as symbols in Figure 3.15(b). As mention earlier, selected computational geometric functions agree well with the geometric functions obtained from the analytical solutions in Equations (3.3), (3.4), (3.13) and (3.14) with the approximate equivalent radius b' in Equations (3.5) and (3.6). As shown in these figures, the trends of the K_1 and K_2 solutions for these four types of welds are quite similar to those of simply supported outer edges in Figures 3.15(a), 3.16(a), 3.17(a) and 3.18(a). Note that the K_1 and K_2 solutions for clamped outer edges are lower than those for simply supported outer edges.

Figures 3.15(c), 3.16(c), 3.17(c) and 3.18(c) show geometric functions g_{k1}^{SS} and g_{k2}^{SS} for Fe/Mg, Fe/Al, Al/Mg and Cu/Al welds in square plates with simply supported outer edges, respectively, for $\delta = 1$ and $\delta = 0.5$ as functions of b/a. As listed in Tables 3.2a and 3.2b, the values of the modulus ratio η for Fe/Mg, Fe/Al, Al/Mg and Cu/Al welds are 4.43, 2.94, 1.51, and 1.61, respectively. As shown in these figures, the trends of the K_1 and K_2 solutions for these four types of welds are quite similar. The results in Figures 3.15(c), 3.16(c), 3.17(c) and 3.18(c) also indicate that, as the thickness of the lower plates increase, the K_1 solutions decrease while the K_2 solutions increase. As shown in these figures, the K_1 solutions barely increase with the increase of η. However, the K_2 solutions decrease significantly with the increase of η. As η increases, the decreases and increases of K_1 and K_2 solutions increase as the lower plates become thicker. Note that, for $\delta = 1$, the K_I solutions for Fe/Mg, Fe/Al, Al/Mg and Cu/Al welds are equal to those for Mg/Fe, Al/Fe, Mg/Al and Al/Cu, respectively. Note that the K_2 solutions for $\delta = 1$ have negative values.

Figures 3.15(d), 3.16(d), 3.17(d) and 3.18(d) show geometric functions g_{k1}^{C}, and g_{k2}^{C} for Fe/Mg, Fe/Al, Al/Mg and Cu/Al welds in square plates with clamped outer edges, respectively, for $\delta = 1$ and $\delta = 0.5$ as functions of b/a. As shown in these figures, the trends of the K_1 and K_2 solutions for these four types of welds are quite similar to those for simply supported outer edges in Figures 3.15(c), 3.16(c), 3.17(c) and 3.18(c). Note that the values of K_1 and K_2 solutions for clamped outer edges are lower than those for simply supported outer edges.

3.10. Conclusions

Closed-form structural stress and stress intensity factor solutions for spot welds in square plates under opening loading conditions are investigated here. First, the existing analytical axisymmetric solutions for a rigid inclusion in a circular plate with simply supported and clamped outer edges are reviewed. Then the results of axisymmetrical finite element analyses for a rigid inclusion in a circular plate are presented. The results indicate that the finite element model with one element across the plate thickness is an appropriate model to investigate the structural stress solutions for a rigid inclusion in a square plate to avoid the local effect of the reaction force due to the constraint applied to the rigid inclusion. Next, the results of three-dimensional finite element analyses for a rigid inclusion in a square plate with simply supported and clamped outer edges are presented. The results indicate that, as the ratio of the plate width to the rigid inclusion diameter becomes large about 6, the structural stress solutions along the circumference of the rigid inclusion become almost uniform. Approximate equivalent radius solutions are then determined in order to use the analytical structural stress solutions for a rigid inclusion in a circular plate to calculate the structural stress solutions along the circumference of the rigid inclusion in a square plate. Then, the results of three-dimensional finite element analyses for spot welds between square plates of different thicknesses and materials are presented. The results indicate that the computational stress intensity factor solutions agree well with those based on the structural stress solutions with the equivalent radius. Based on the closed-form structural stress solutions, complete sets of the normalized stress intensity factor solutions for spot welds between square plates of different thicknesses and materials under opening loading conditions are

presented for combinations of steel, aluminum and magnesium sheets and combinations of aluminum and copper sheets for convenient engineering applications.

Reference

[1] Pook LP. Fracture mechanics analysis of the fatigue behaviour of spot welds. Int J Fract 1975; 11: 173-176.

[2] Pook LP. Approximate stress intensity factors obtained from simple plate bending theory. Eng Frac Mech 1979; 12: 505-522.

[3] Radaj D. Stress singularity, notch stress and structural stress at spot–welded joints. Eng Fract Mech 1989; 34: 495-506.

[4] Radaj D, Zhang S. Stress intensity factors for spot welds between plates of unequal thickness. Eng Fract Mech 1991; 39: 391-413.

[5] Radaj D, Zhang S. Simplified formulae for stress intensity factors of spot welds. Eng Fract Mech 1991; 40: 233-236.

[6] Radaj D, Zhang S. Stress intensity factors for spot welds between plate of dissimilar materials. Eng Fract Mech 1992; 42: 233-236.

[7] Zhang S. Stress intensities at spot welds. Int J Fract 1997; 88: 167-185.

[8] Zhang S. Fracture mechanics solutions to spot welds. Int J Fract 2001; 112: 247-75.

[9] Pan N, Sheppard SD. Stress intensity factors in spot welds. Eng Frac Mech 2003; 70: 671-684.

[10] Wang DA, Lin SH, Pan J. Stress intensity factors for spot welds and associated kinked cracks in cup specimens. Int J Fatigue 2005; 27: 581-598.

[11] Wang DA, Lin PC, Pan J. Geometric functions of stress intensity factor solutions for spot welds in lap-shear specimens. Int J Solids Struct 2005; 42: 6299-6318.

[12] Lin PC, Wang DA, Pan J. Mode I stress intensity factor solutions for spot welds in lap-shear specimens. Int J Solids Struct 2007; 44: 1013-1037.

[13] Lin PC, Pan J. Closed-form structural stress and stress intensity factor solutions for spot welds under various types of loading conditions. Int J Solids Struct 2008; 45: 3996-4020.

[14] Lin PC, Pan J. Closed-form structural stress and stress intensity factor solutions for spot welds in commonly used specimens. Eng Fract Mech 2008; 75: 5187-5206.

[15] Muskhelishvili NI. Some Basic Problems of the Mathematical Theory of Elasiticiy. Noordhoff, Groningen; 1953

[16] Goland M. The influence of the shape and rigidity of an elastic inclusion of the transverse flexure of thin plates. J App Mech 1943; A-69-A-75.

[17] Timoshenko S, Woinowsky-Krieger S. Theory of Plate and Shells, 2nd ed. McGrow-Hill, NY; 1959.

[18] Lin PC, Lin ZL. Geometric functions of stress intensity factor solutions for spot welds in cross-tension specimens. To be submitted.

[19] Tran VX, Pan J. Analytical stress intensity factor solutions for resistance and friction stir spot welds in lap-shear specimens of different materials and thicknesses. Eng Frac Mech 2010; 77: 2611-2639.

[20] ABAQUS v6.7 User Manual. Providence, RI: SIMULIA; 2007.

[21] Zhang S. Stress intensities derived from stresses around a spot welds. Int J Fract 1999; 99: 239-257.

[22] Suo Z, Hutchinson JW. Interface crack between two elastic layers. Int J Fract 1990; 43: 1-18.

Table 3.1. The normalized equivalent radius b'/b for various ratios of the plate width to the rigid inclusion diameter, b/a.

b/a	3	5.91	7.94	10	15
b'/b, simply supported	1.006	0.894	0.866	0.852	0.838
b'/b, clamped	1.123	1.074	1.063	1.059	1.056

Table 3.2a. The values of interface crack parameters between magnesium (Mg), aluminum (Al), and steel (Fe) sheets.

Spot weld	α	β	ε	η	ξ	δ	ω
Mg/Al	-0.203	-0.038	0.012	0.663	0.643	1.0	49.37
						0.5	50.05
Al/Fe	-0.493	-0.117	0.037	0.340	0.325	1.0	51.05
						0.5	51.81
Mg/Fe	-0.632	-0.136	0.044	0.225	0.209	1.0	51.30
						0.5	52.19
Al/Mg	0.203	0.038	-0.012	1.508	1.554	1.0	49.00
						0.5	49.88
Fe/Al	0.493	0.117	-0.037	2.942	3.074	1.0	48.00
						0.5	49.90
Fe/Mg	0.632	0.136	-0.044	4.436	4.777	1.0	48.52
						0.5	50.92

Table 3.2b. The values of interface crack parameters between aluminum (Al) and copper (Cu) sheets.

Spot weld	α	β	ε	η	ξ	δ	ω
Al/Cu	-0.233	-0.064	0.020	0.62	0.63	1.0	50.36
						0.5	50.98
Cu/Al	0.233	0.064	-0.020	1.61	1.58	1.0	48.05
						0.5	49.21

Table 3.3a. The normalized in-plane J integral and stress intensity factor solutions J_{xy}, K_{eq}, K_I and K_{II} for the ratio of the plate width to the spot weld diameter, b/a =7.94.

Nomalized K	Similar material, $\delta = 1.0$		Similar material, $\delta = 0.5$	
	Simply supported	clamped	Simply supported	clamped
$J_{xy}^{FEM} / J_{xy}^{SS}$	0.990	1.019	0.985	1.016
$K_{eq}^{FEM} / K_{eq}^{SS}$	0.995	1.009	0.992	1.008
K_I^{FEM} / K_I^{SS}	0.995	1.009	1.000	1.018
K_{II}^{FEM} / K_I^{SS}	-	-	0.427	0.427
K_{II}^{SS} / K_I^{SS}	-	-	0.447	0.447

Table 3.3b. The normalized in-plane J integral and stress intensity factor solutions J_{xy}, K_{eq}, K_1 and K_2 for the ratio of the plate width to the spot weld diameter, b/a =7.94.

Nomalized K	Mg/Fe, $\delta = 1$		Mg/Fe, $\delta = 0.5$	
	Simply supported	clamped	Simply supported	clamped
$J_{xy}^{FEM} / J_{xy}^{SS}$	1.009	1.016	1.010	1.013
$K_{eq}^{FEM} / K_{eq}^{SS}$	1.004	1.008	1.005	1.006
K_1^{FEM} / K_1^{SS}	1.013	1.020	1.033	1.040
K_2^{FEM} / K_1^{SS}	0.291	0.286	0.573	0.565
K_2^{SS} / K_1^{SS}	0.318	0.322	0.617	0.619

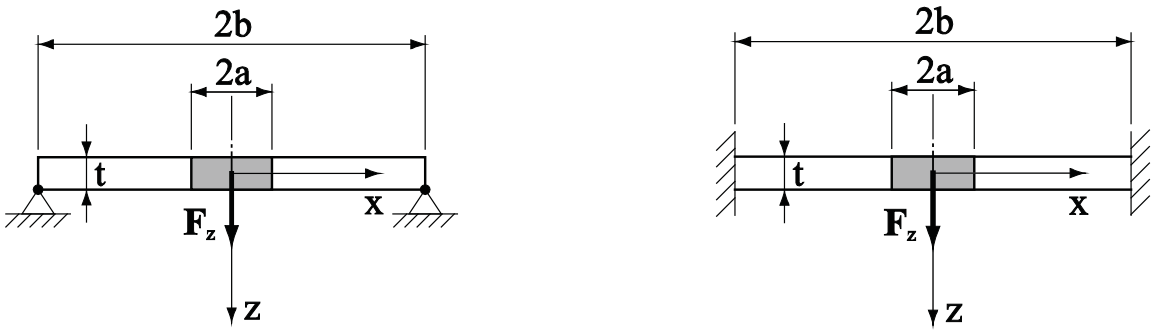

Figure 3.1. A plate with a rigid inclusion subject to an out-of-plane or an opening force to the inclusion and with (a) a clamped outer edge and (b) a simply supported outer edge.

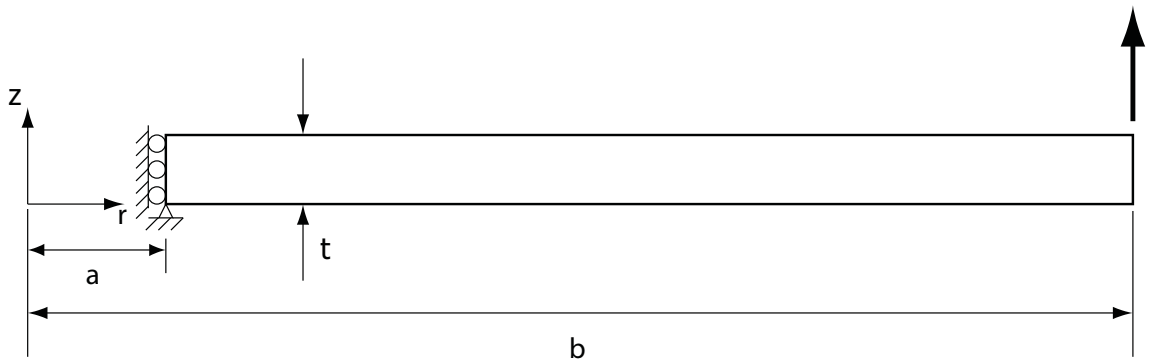

(a)

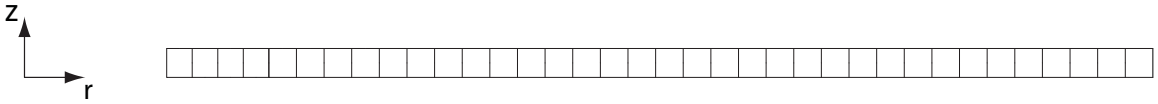

(b)

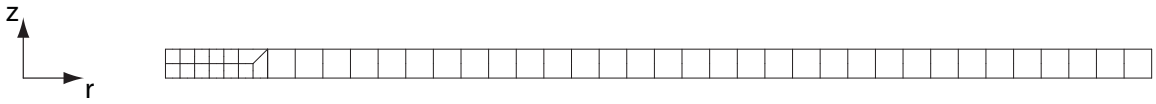

(c)

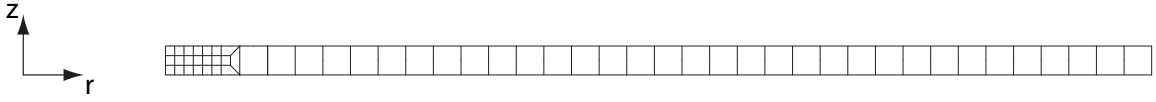

(d)

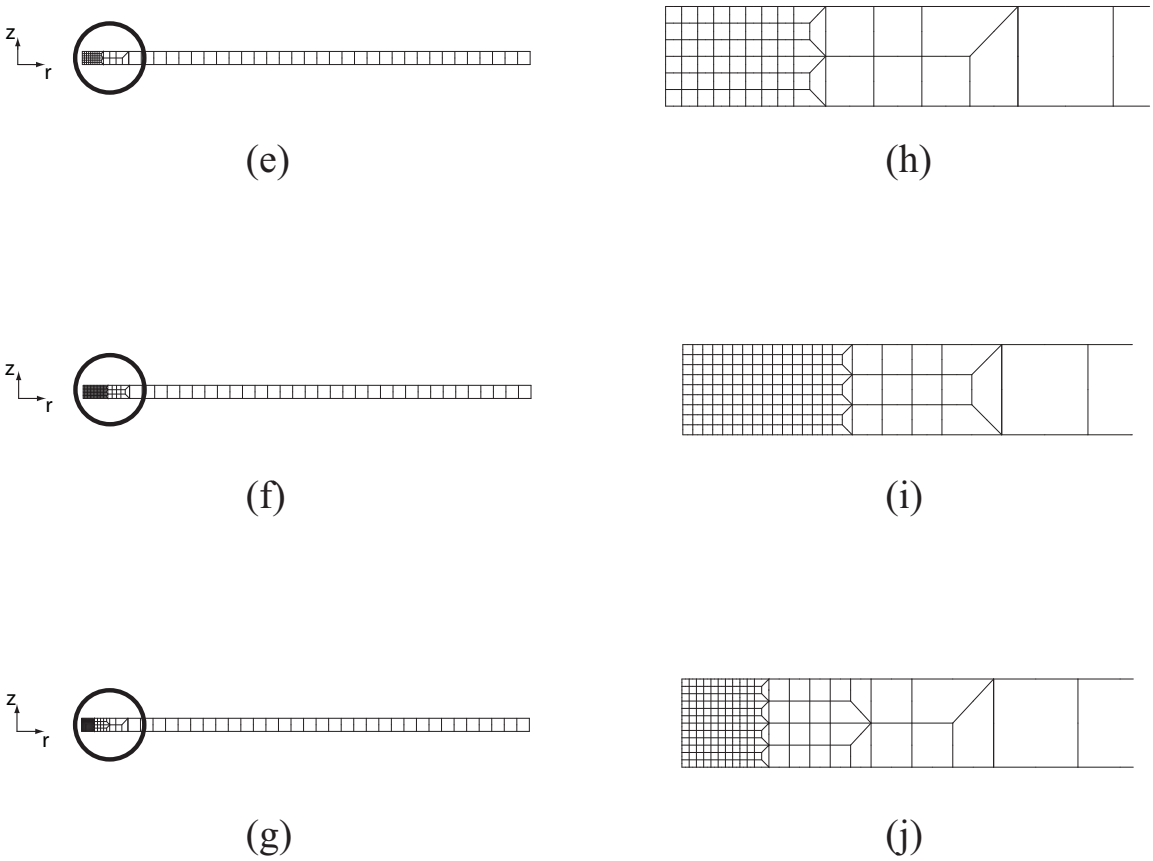

Figure 3.2. (a) A schematic of an axisymmetrical finite element model and the boundary conditions, (b) – (g) meshes of various axisymmetrical finite element models, and (h) – (j) close-up views of the finite element models in (e) – (g), respectively.

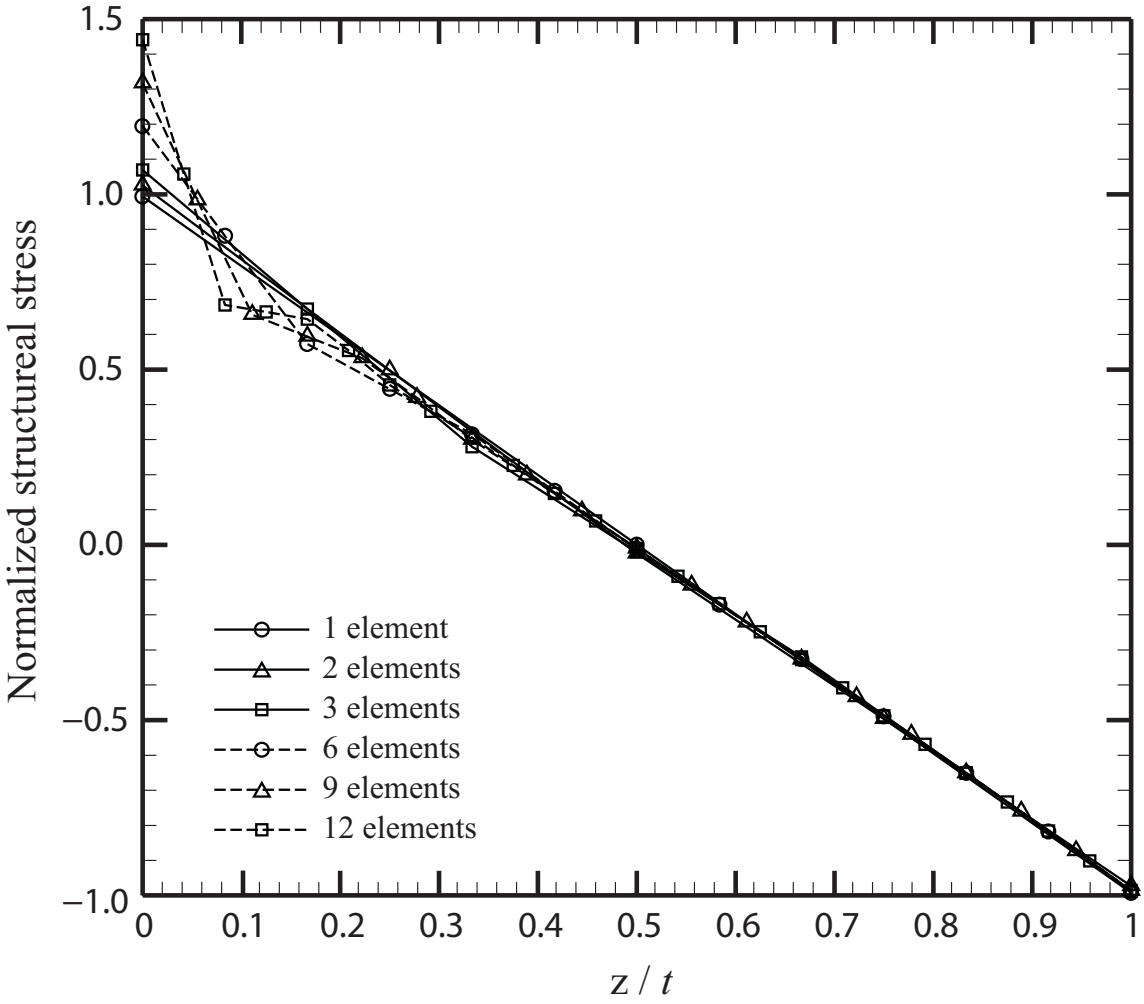

Figure 3.3. The bending stress σ_{rr} distributions along the thickness direction at $r = a$ from various axisymmetrical finite element analyses.

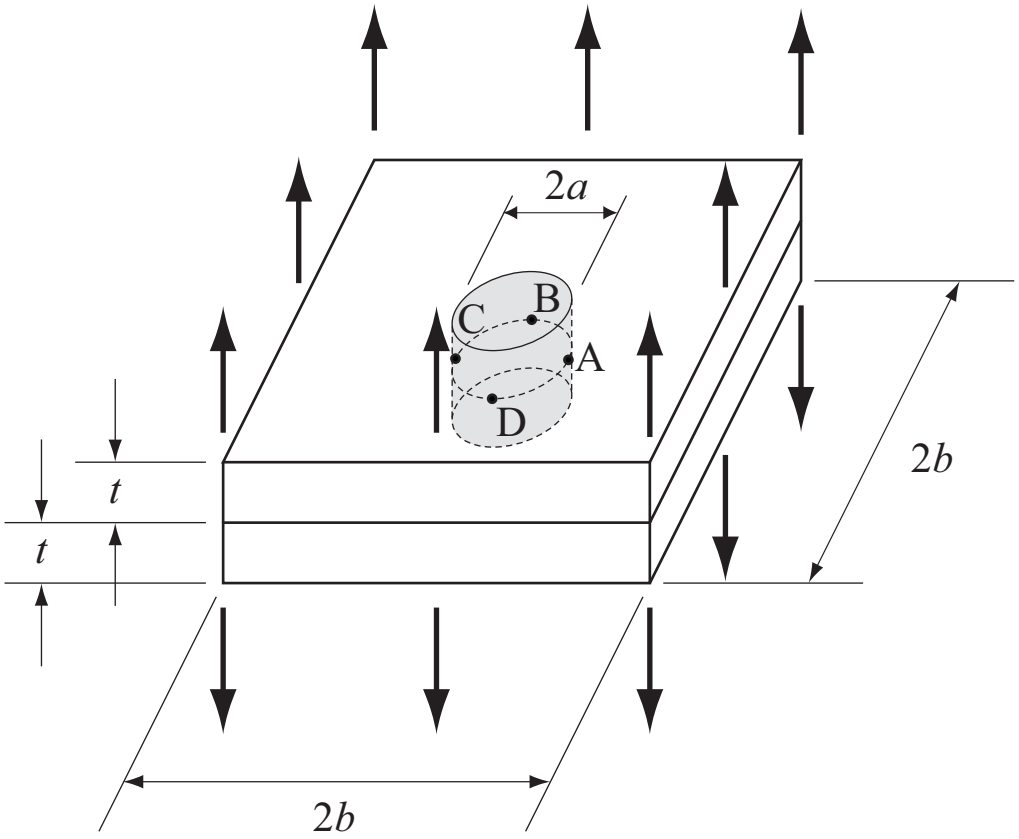

Figure 3.4. A schematic of two square plates of equal thickness with connection or spot weld subject to a uniform out-of-plane or opening displacement along the outer edges.

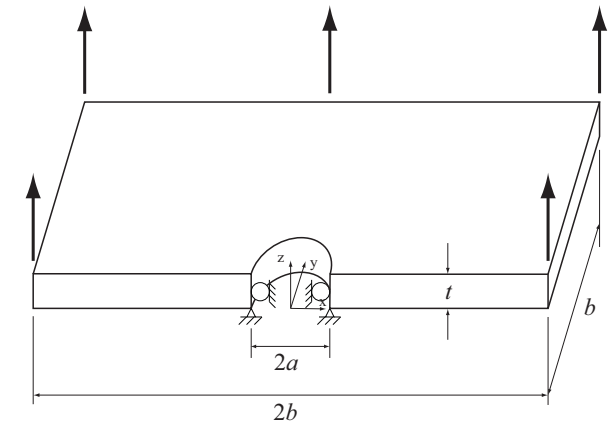

(a)

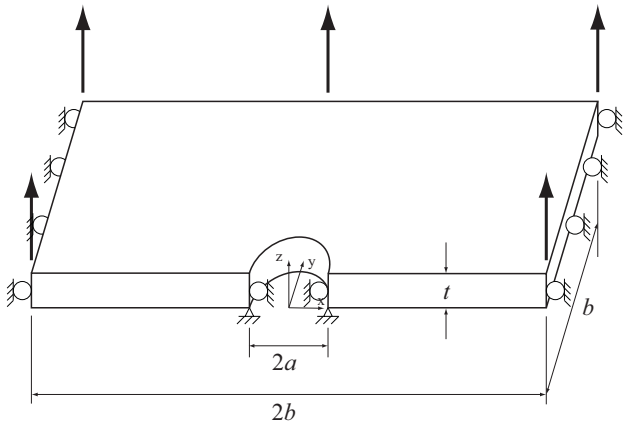

(b)

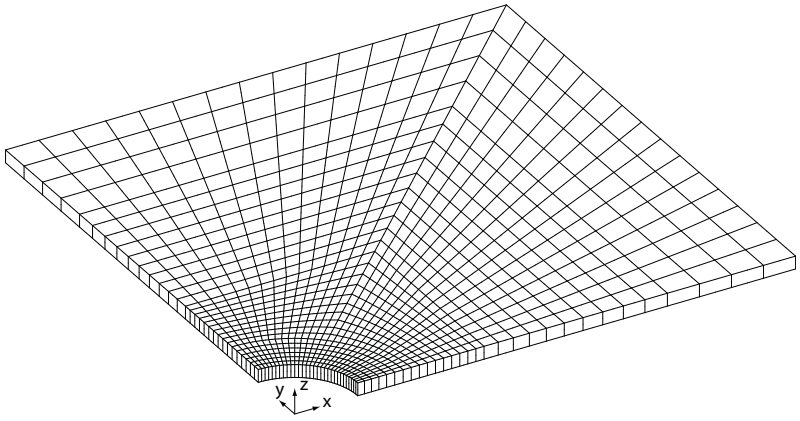

(c)

Figure 3.5. Schematics of a three-dimensional finite element model of a square plate with a rigid inclusion under a uniform displacement and with (a) simply supported and (b) clamped outer edges. (c) A three dimensional finite element model for $b/a = 7.94$.

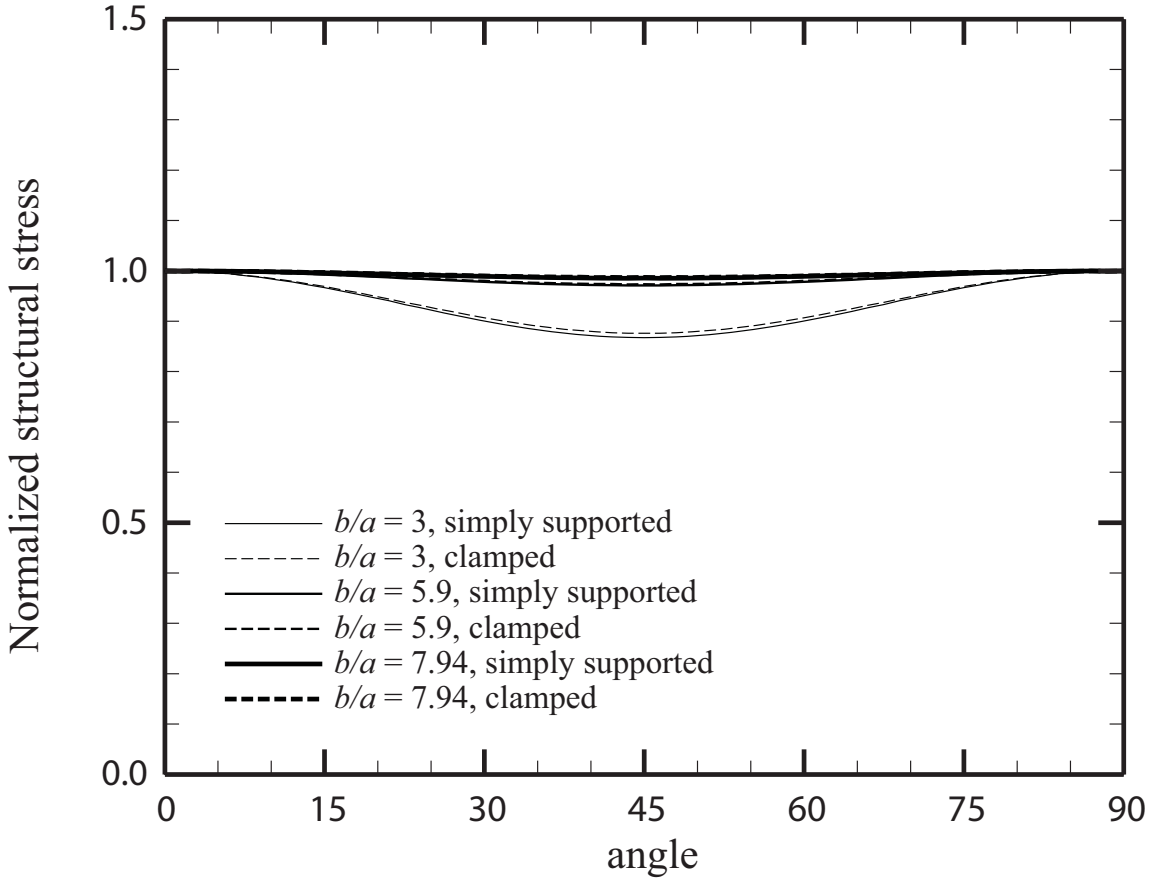

Figure 3.6. The normalized structural stress distributions along the circumference of a rigid inclusion for selected ratios of the plate width to the rigid inclusion diameter, b/a.

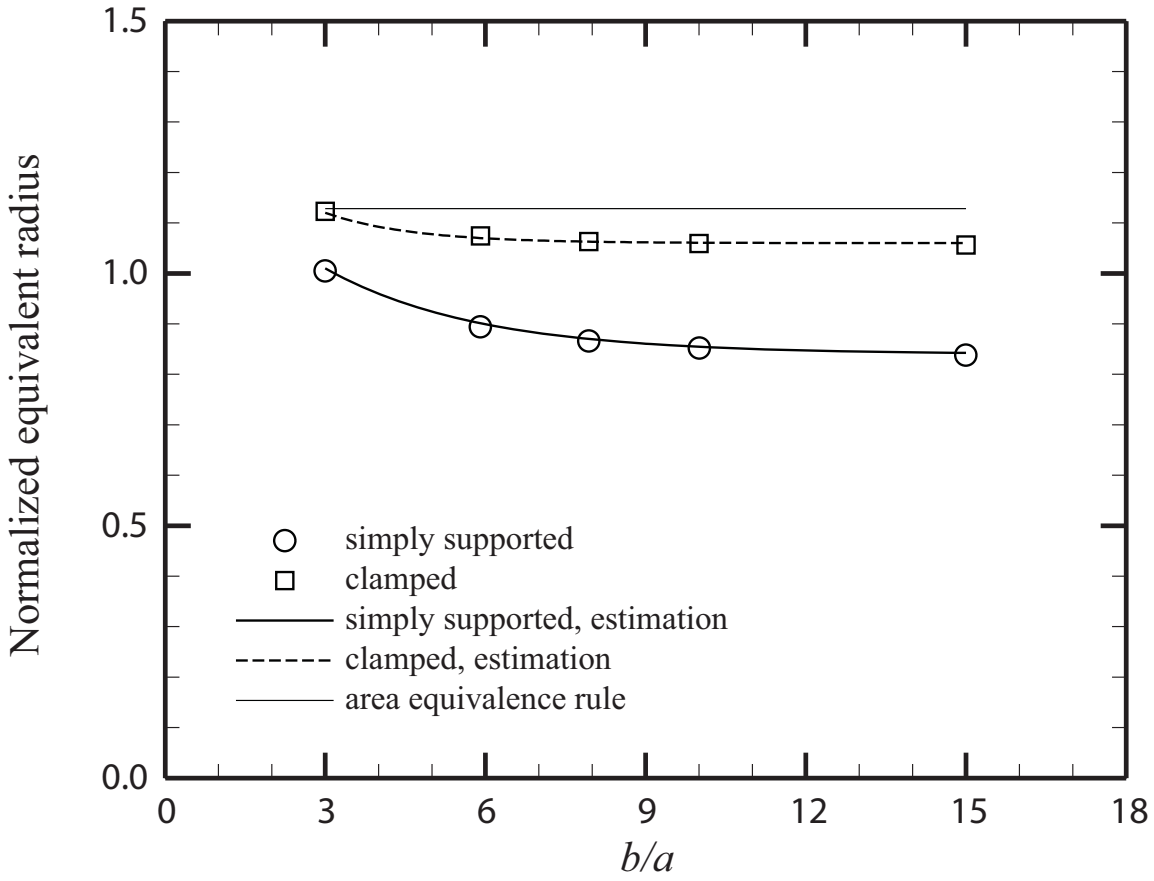

Figure 3.7. The values of the normalized equivalent radius b'/b as functions of the ratio of the plate width to the rigid inclusion diameter, b/a.

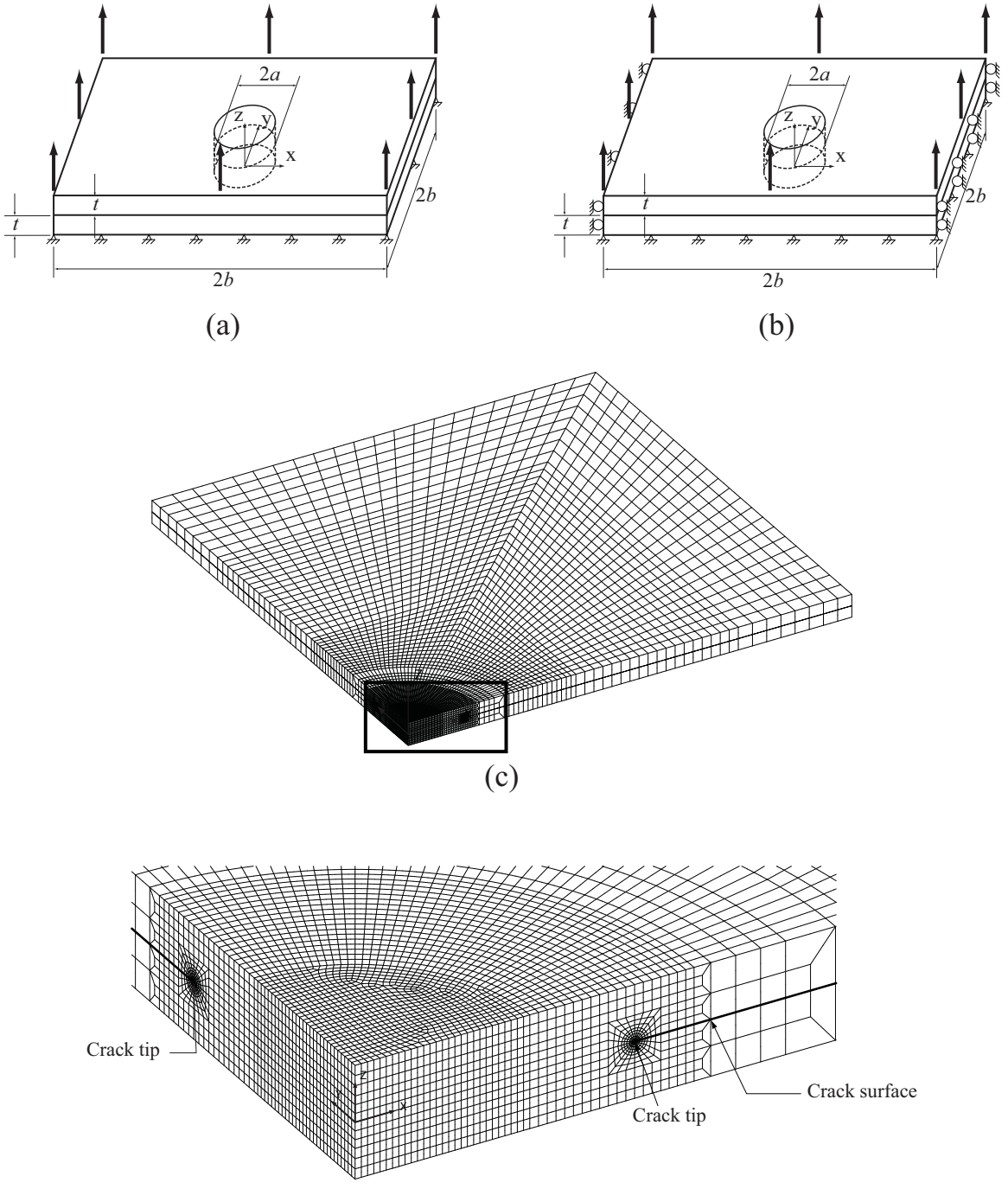

Figure 3.8. Schematics of a three-dimensional finite element model of two square plates of equal thickness with connection under a uniform applied displacement and with (a) simply supported and (b) clamped outer edges. (c) A three-dimensional finite element model for $b/a = 7.94$ and (d) a close-up view of the mesh near the crack front for the model in (c).

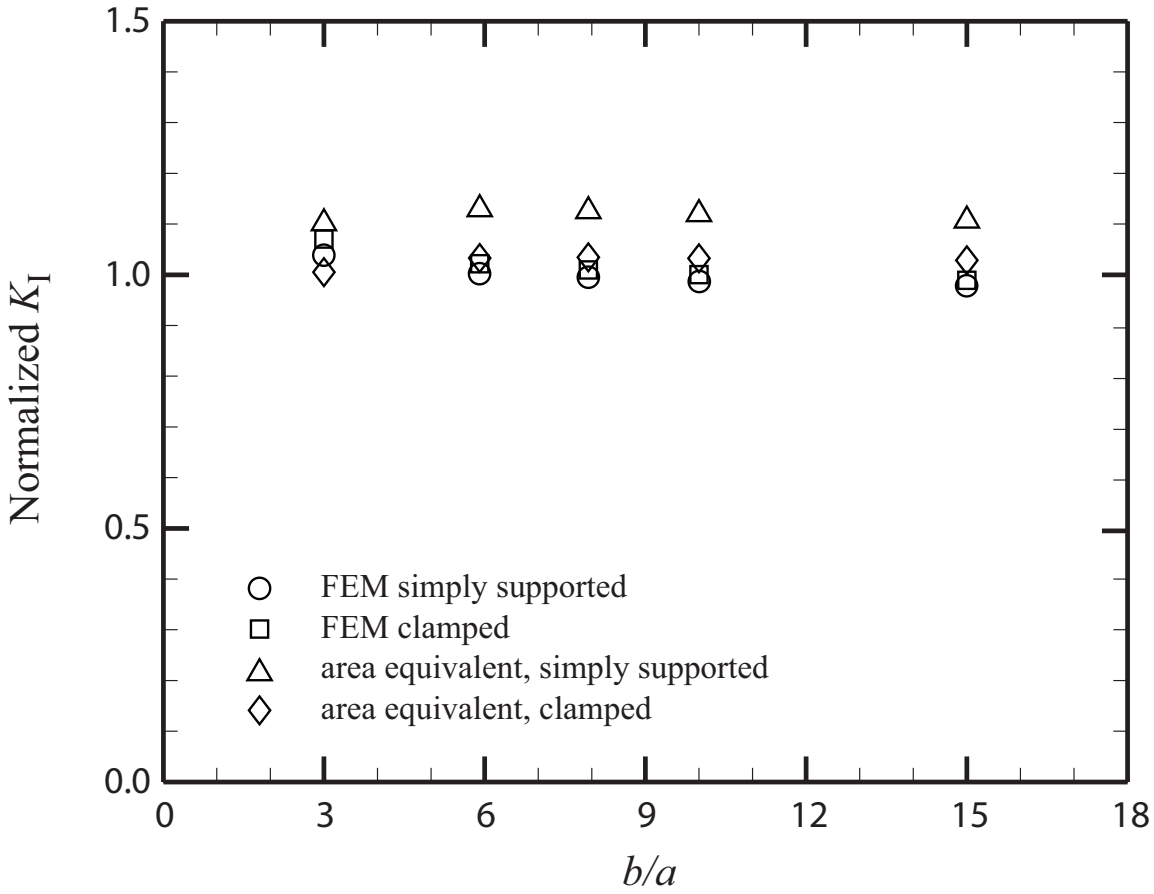

Figure 3.9. The normalized stress intensity factor K_I solutions for various ratios of the plate width to the connection diameter, b/a.

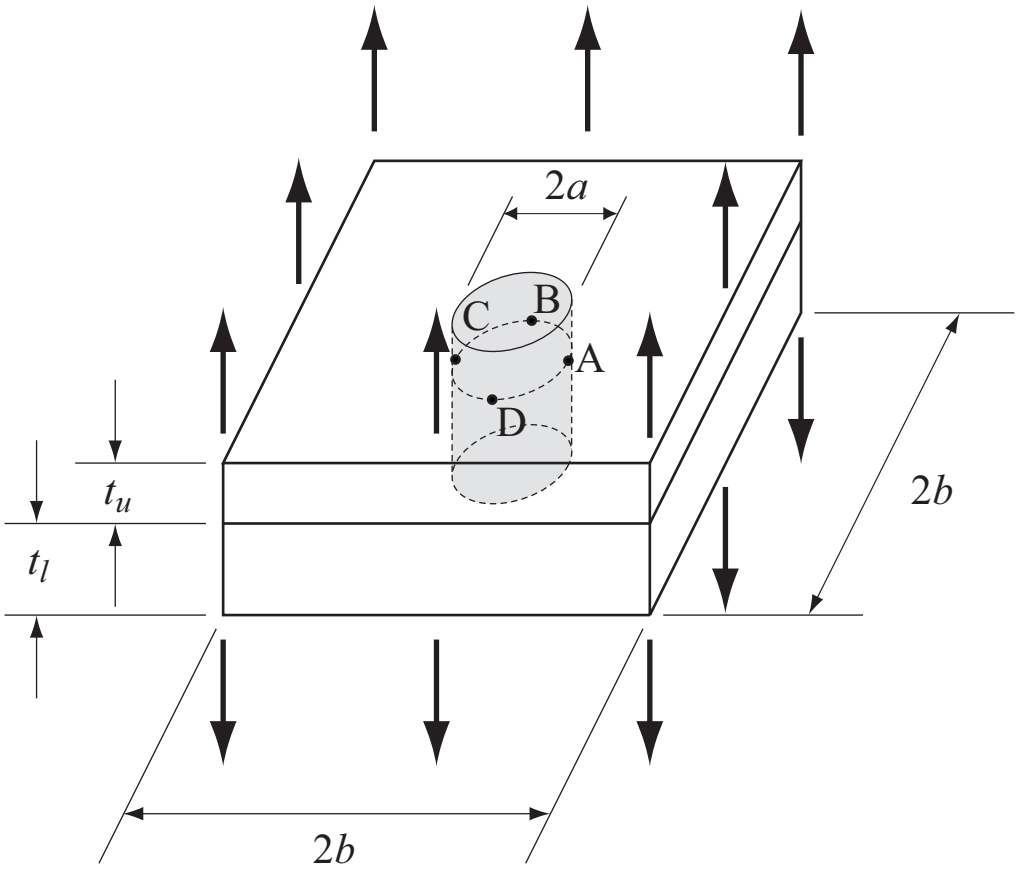

Figure 3.10. A schematic of two square plates of unequal thickness with connection or spot weld subject to a uniform out-of-plane or opening displacement along the outer edges.

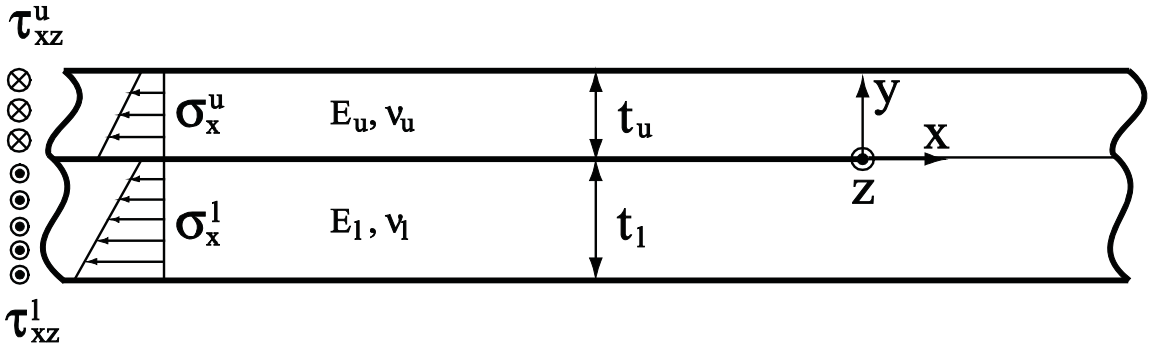

(a)

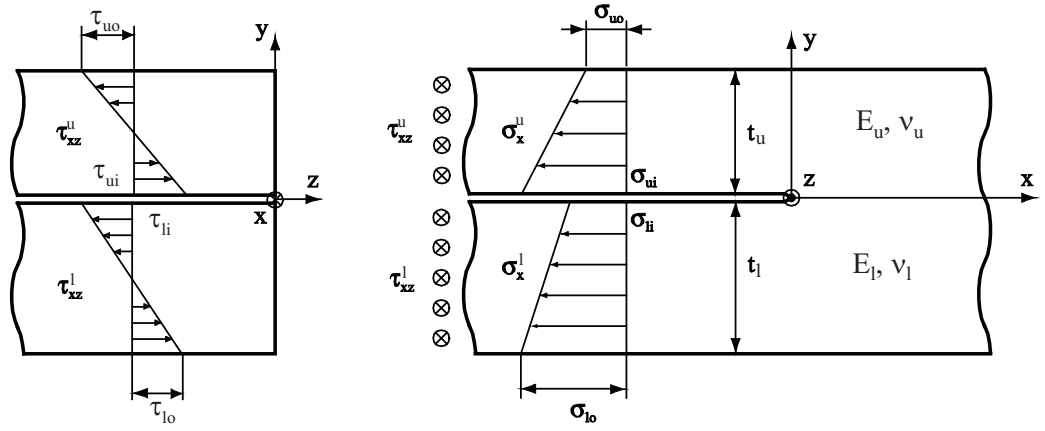

(b)

Figure 3.11. (a) A two-dimensional model of two infinite strips made of different thicknesses and materials with connection under plane strain conditions and (b) the front and side views of the left half of the strip model near the crack tip.

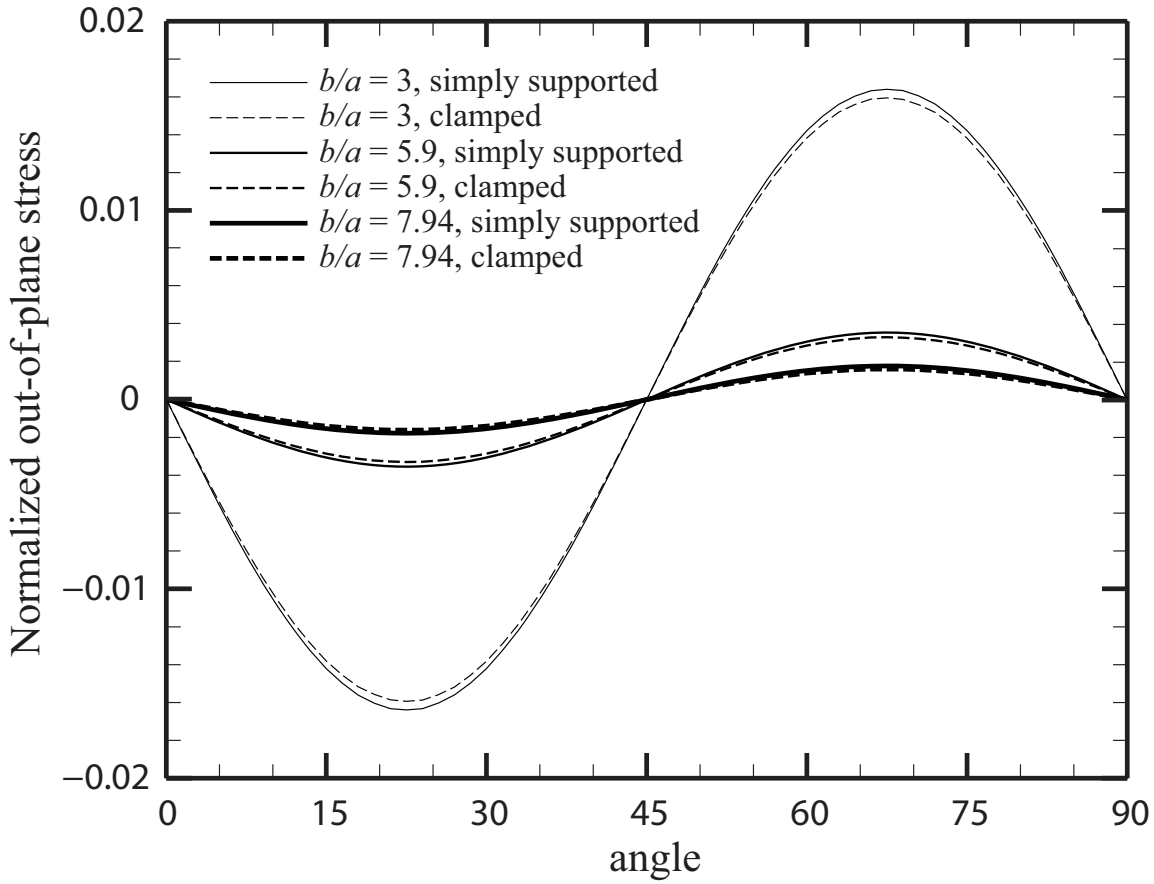

Figure 3.12. The normalized out-of-plane shear stress distributions along the circumference of a rigid inclusion in a square plate for selected ratios of the plate width to the rigid inclusion diameter, b/a .

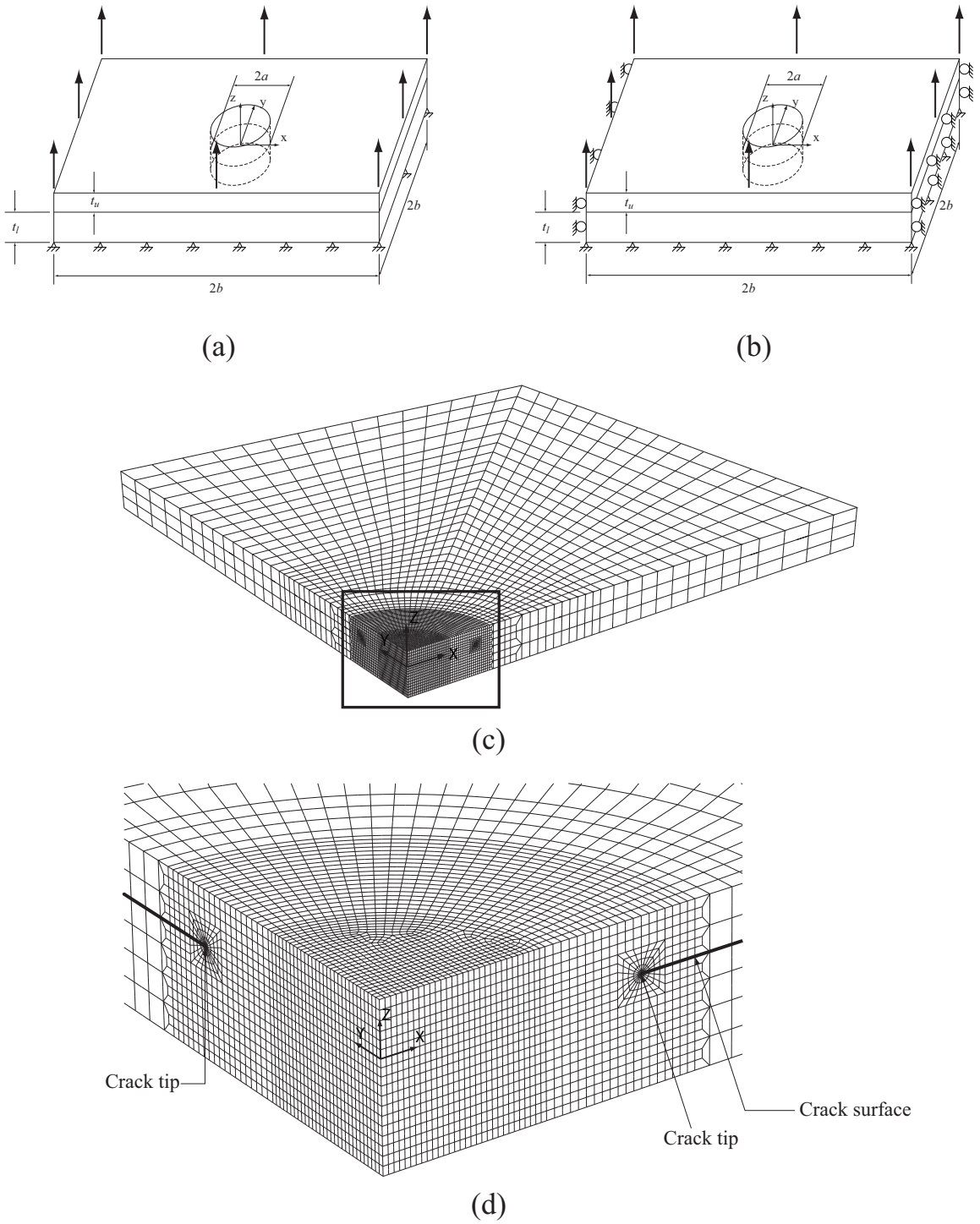

Figure 3.13. Schematics of a three-dimensional finite element model of two square plates of unequal thicknesses with connection under a uniform applied displacement and with (a) simply supported and (b) clamped outer edges. (c) A three-dimensional finite element model for $b/a = 7.94$ and $\delta = 0.5$ and (d) a close-up view of the mesh near the crack front for the model in (c).

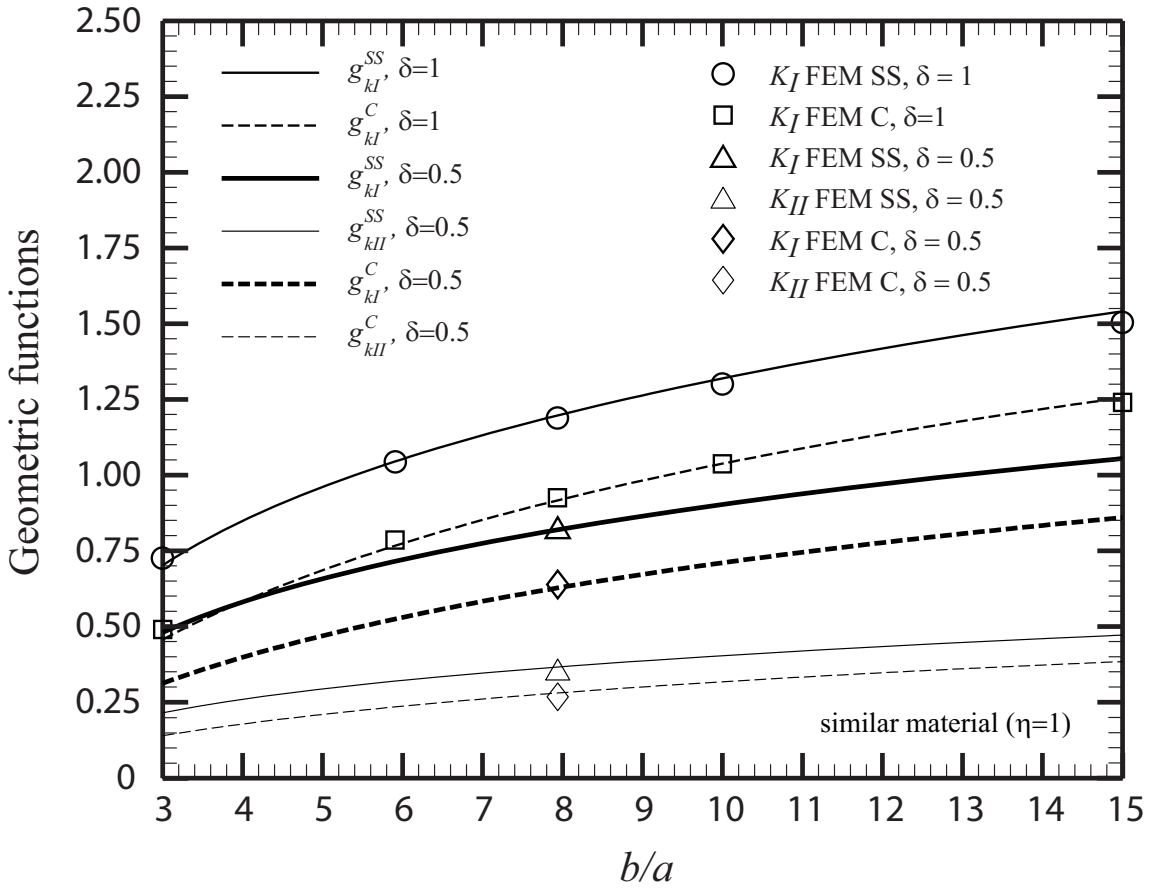

Figure 3.14. The geometric functions g_{kI}^{SS}, g_{kII}^{SS}, g_{kI}^{C}, and g_{kII}^{C} for spot welds in square plates of identical material for $\delta = 1$ and $\delta = 0.5$ as functions of b/a. The computational solutions are shown as symbols.

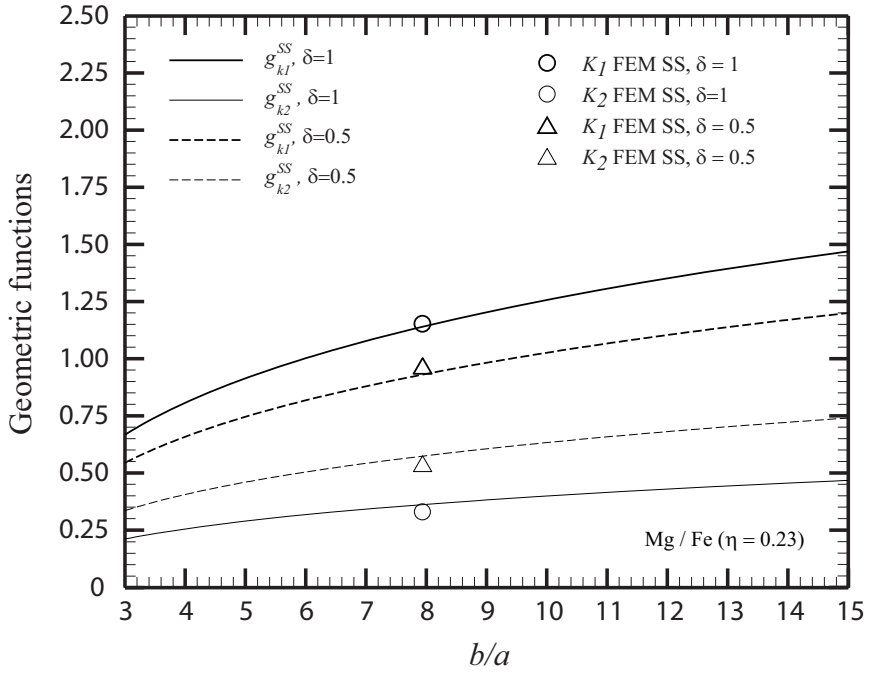
Geometric functions
b/a
g^{SS}_{k1}, δ=1
g^{SS}_{k2}, δ=1
g^{SS}_{k1}, δ=0.5
g^{SS}_{k2}, δ=0.5
K_1 FEM SS, δ = 1
K_2 FEM SS, δ=1
K_1 FEM SS, δ = 0.5
K_2 FEM SS, δ = 0.5
Mg / Fe (η = 0.23)

(a)

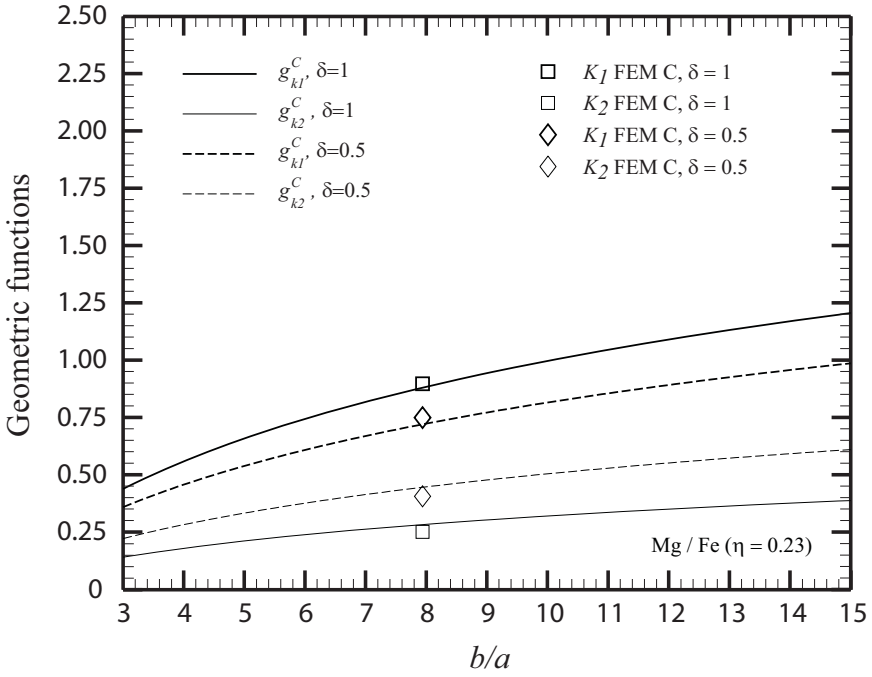
Geometric functions
b/a
g^{C}_{k1}, δ=1
g^{C}_{k2}, δ=1
g^{C}_{k1}, δ=0.5
g^{C}_{k2}, δ=0.5
K_1 FEM C, δ = 1
K_2 FEM C, δ = 1
K_1 FEM C, δ = 0.5
K_2 FEM C, δ = 0.5
Mg / Fe (η = 0.23)

(b)

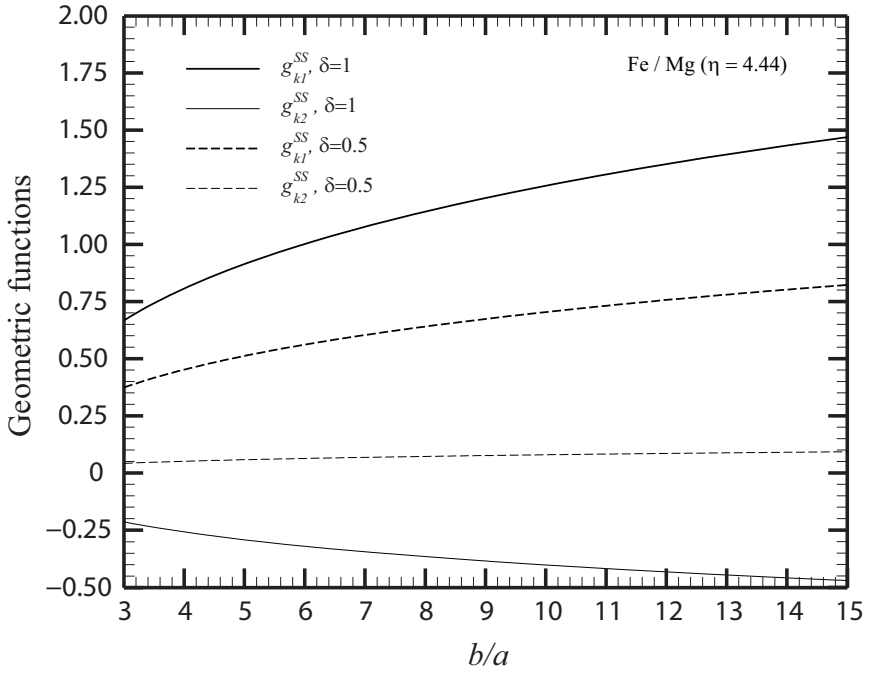

(c)

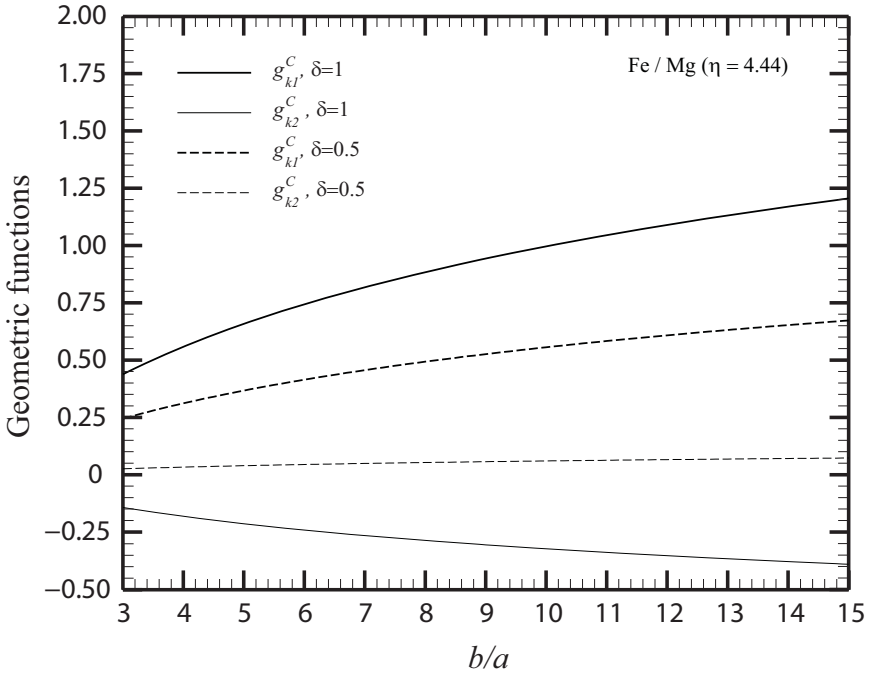

(d)

Figure 3.15. The geometric functions (a) g_{k1}^{SS} and g_{k2}^{SS} for Mg/Fe welds, (b) g_{k1}^{C} and g_{k2}^{C} for Mg/Fe welds, (c) g_{k1}^{SS} and g_{k2}^{SS} for Fe/Mg welds and (d) g_{k1}^{C} and g_{k2}^{C} for Fe/Mg welds with $\delta = 1$ and $\delta = 0.5$ as functions of b/a. The computational solutions were shown as symbols.

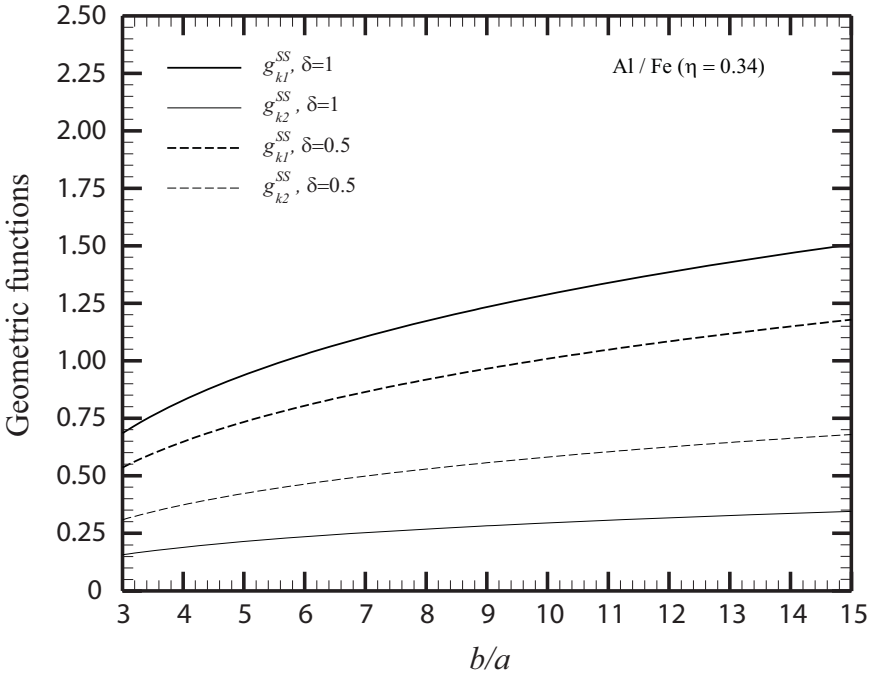
Geometric functions
b/a
Al / Fe (η = 0.34)
g_{k1}^{SS}, δ=1
g_{k2}^{SS}, δ=1
g_{k1}^{SS}, δ=0.5
g_{k2}^{SS}, δ=0.5

(a)

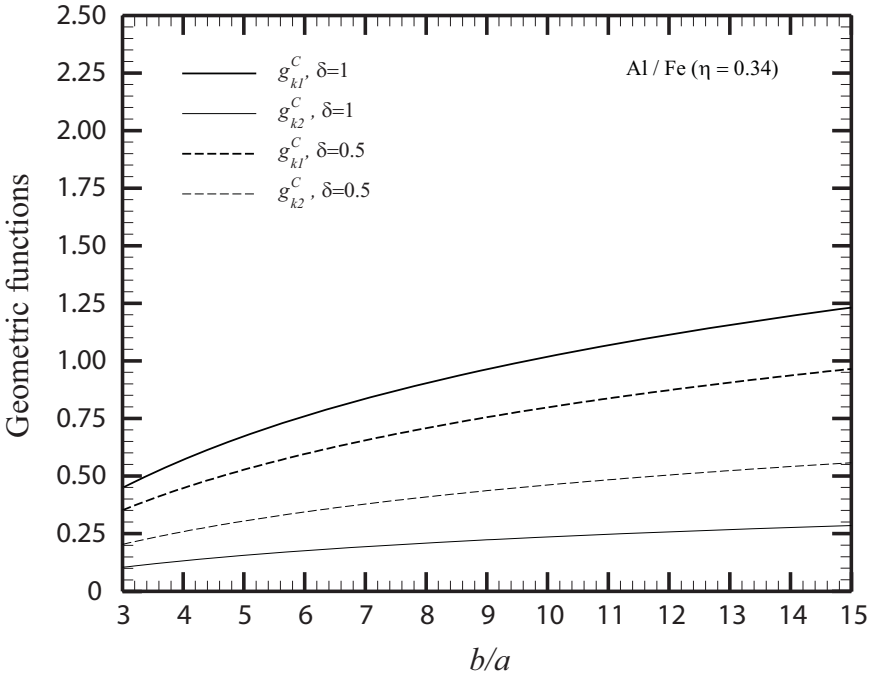
Geometric functions
b/a
Al / Fe (η = 0.34)
g_{k1}^{C}, δ=1
g_{k2}^{C}, δ=1
g_{k1}^{C}, δ=0.5
g_{k2}^{C}, δ=0.5

(b)

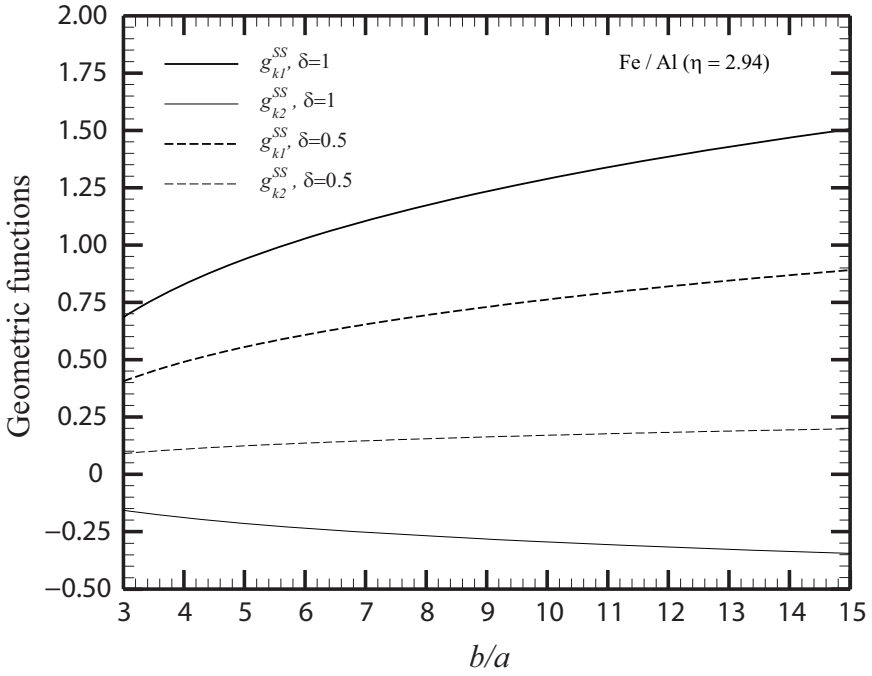

(c)

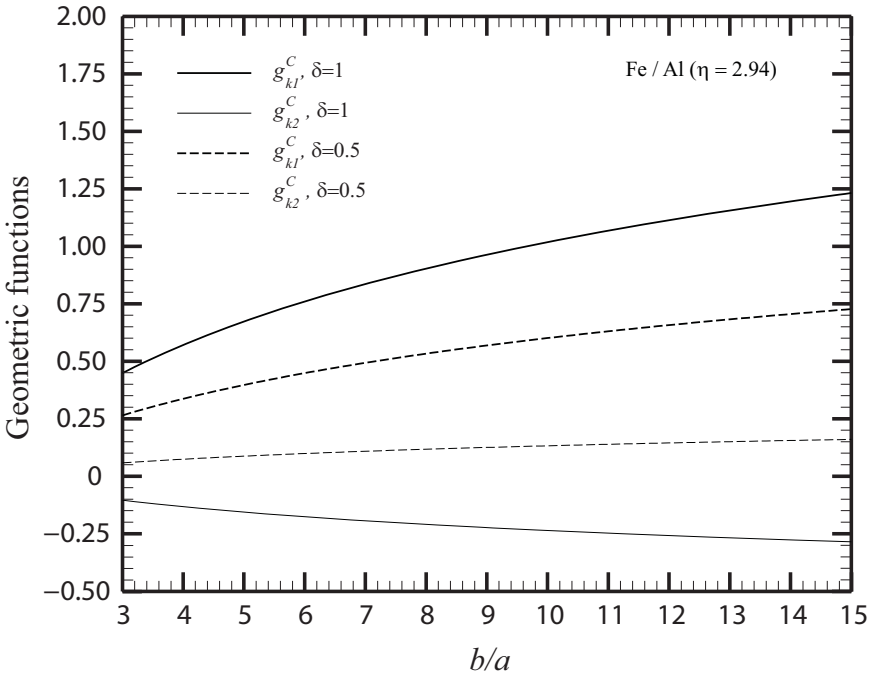

(d)

Figure 3.16. The geometric functions (a) g_{k1}^{SS} and g_{k2}^{SS} for Al/Fe welds, (b) g_{k1}^{C} and g_{k2}^{C} for Al/Fe welds, (c) g_{k1}^{SS} and g_{k2}^{SS} for Fe/Al welds and (d) g_{k1}^{C} and g_{k2}^{C} for Fe/Al welds with $\delta = 1$ and $\delta = 0.5$ as functions of b/a.

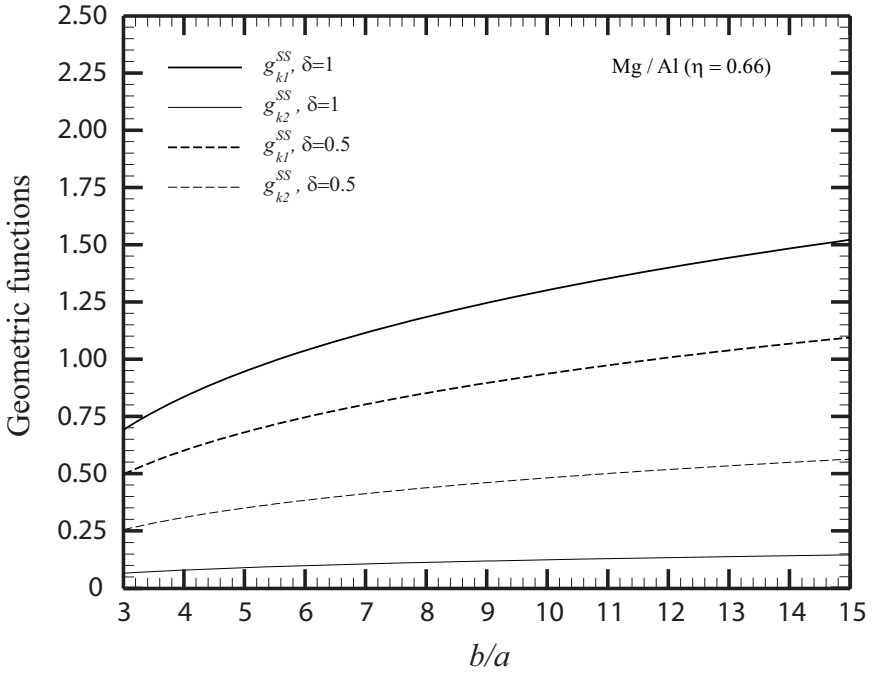
Mg / Al (η = 0.66)
g_{k1}^{SS}, δ=1
g_{k2}^{SS}, δ=1
g_{k1}^{SS}, δ=0.5
g_{k2}^{SS}, δ=0.5
Geometric functions
b/a

(a)

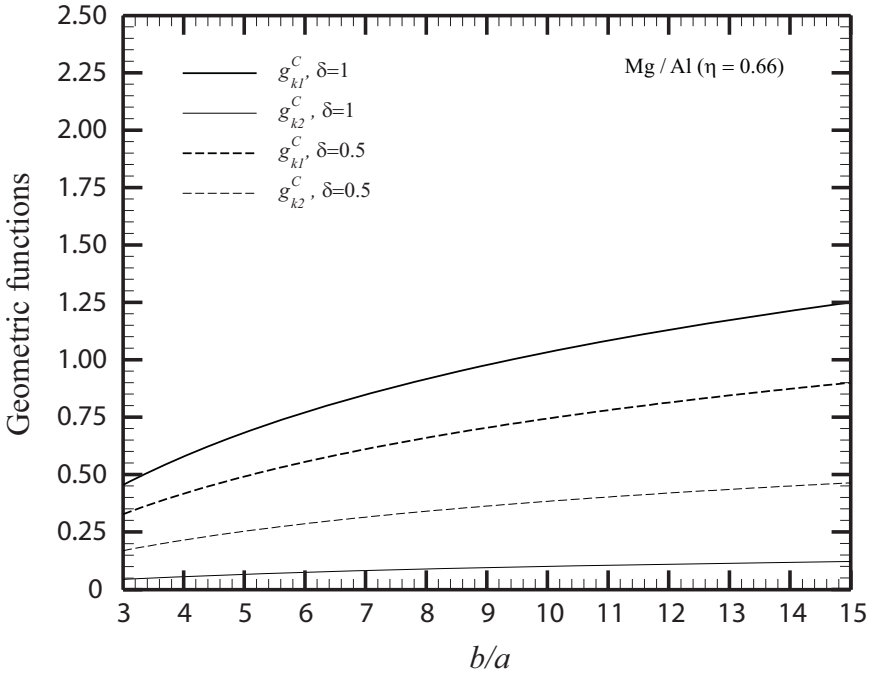
Mg / Al (η = 0.66)
g_{k1}^{C}, δ=1
g_{k2}^{C}, δ=1
g_{k1}^{C}, δ=0.5
g_{k2}^{C}, δ=0.5
Geometric functions
b/a

(b)

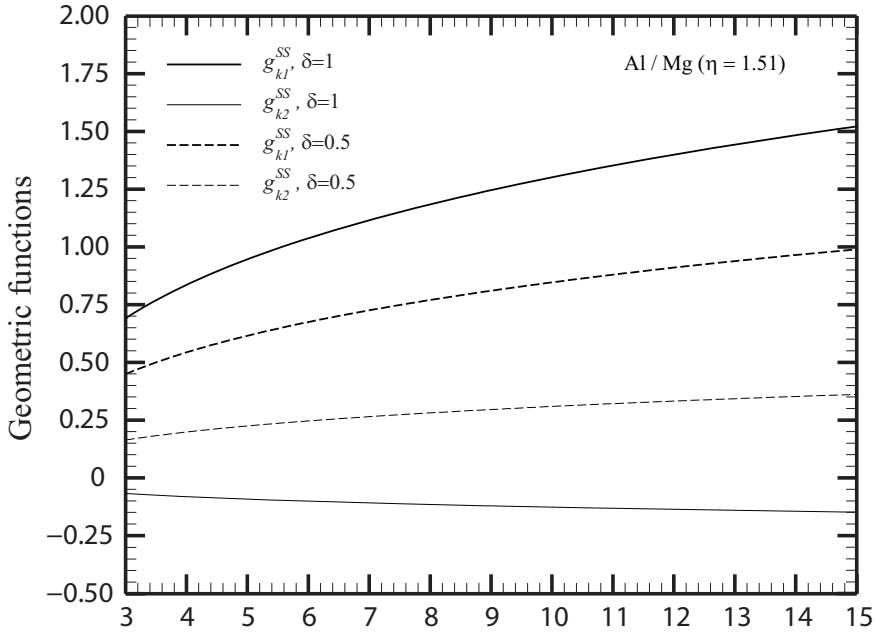

(c)

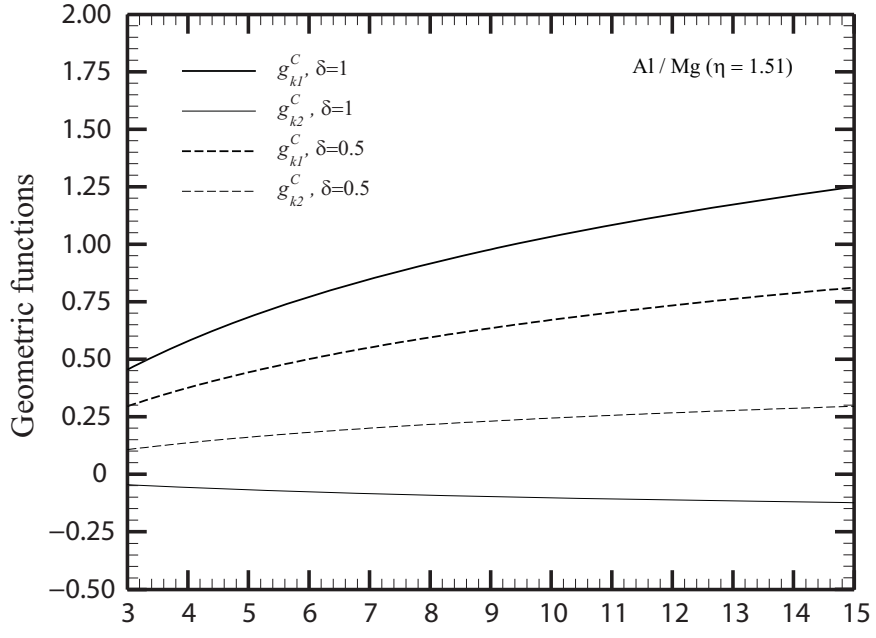

(d)

Figure 3.17. The geometric functions (a) g_{k1}^{SS} and g_{k2}^{SS} for Mg/Al welds, (b) g_{k1}^{C} and g_{k2}^{C} for Mg/Al welds, (c) g_{k1}^{SS} and g_{k2}^{SS} for Al/Mg welds and (d) g_{k1}^{C} and g_{k2}^{C} for Al/Mg welds with $\delta = 1$ and $\delta = 0.5$ as functions of b/a.

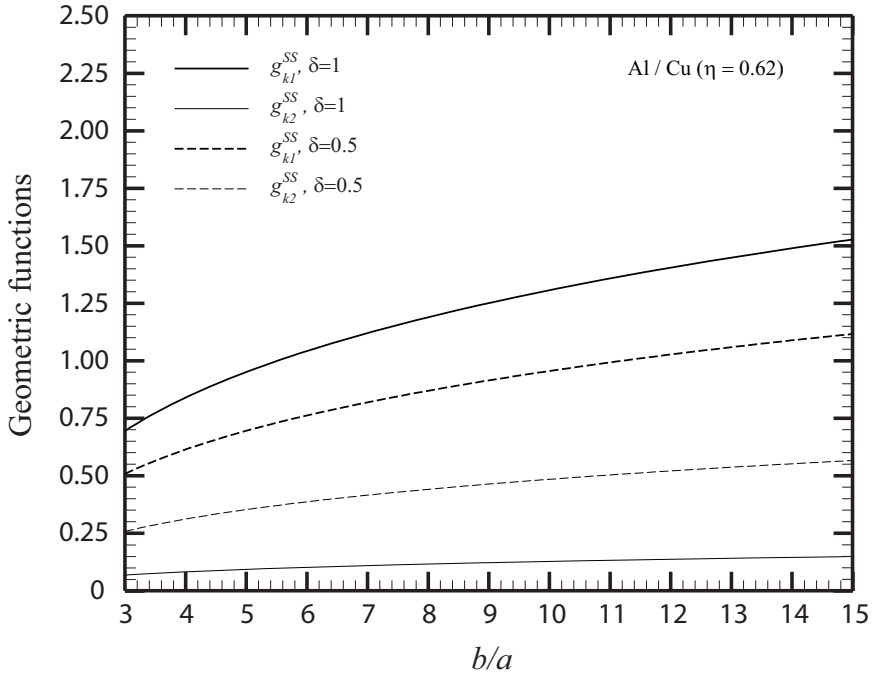
Geometric functions
b/a
Al / Cu (η = 0.62)
g_{k1}^{SS}, δ=1
g_{k2}^{SS}, δ=1
g_{k1}^{SS}, δ=0.5
g_{k2}^{SS}, δ=0.5

(a)

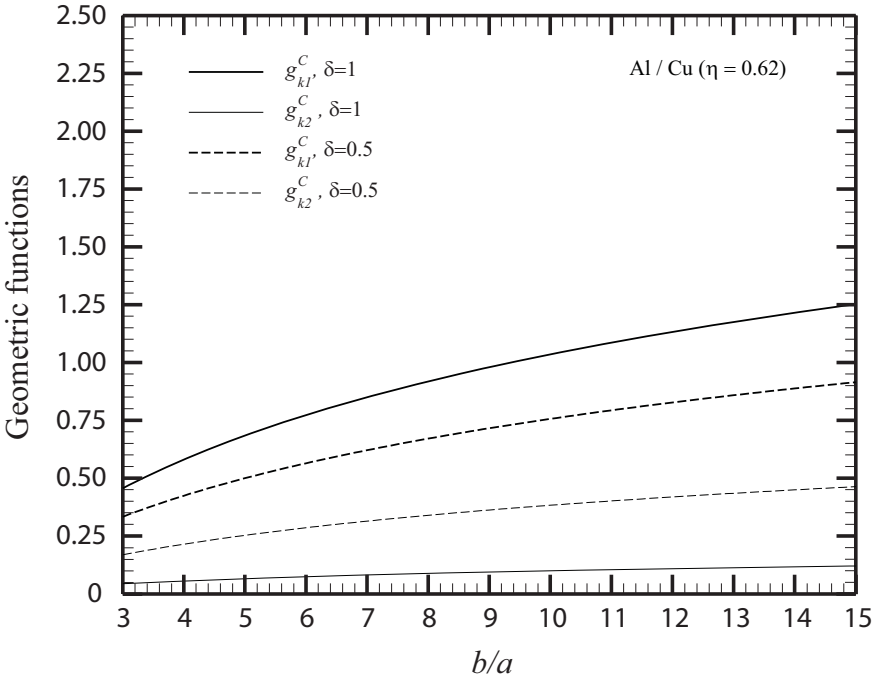
Geometric functions
b/a
Al / Cu (η = 0.62)
g_{k1}^{C}, δ=1
g_{k2}^{C}, δ=1
g_{k1}^{C}, δ=0.5
g_{k2}^{C}, δ=0.5

(b)

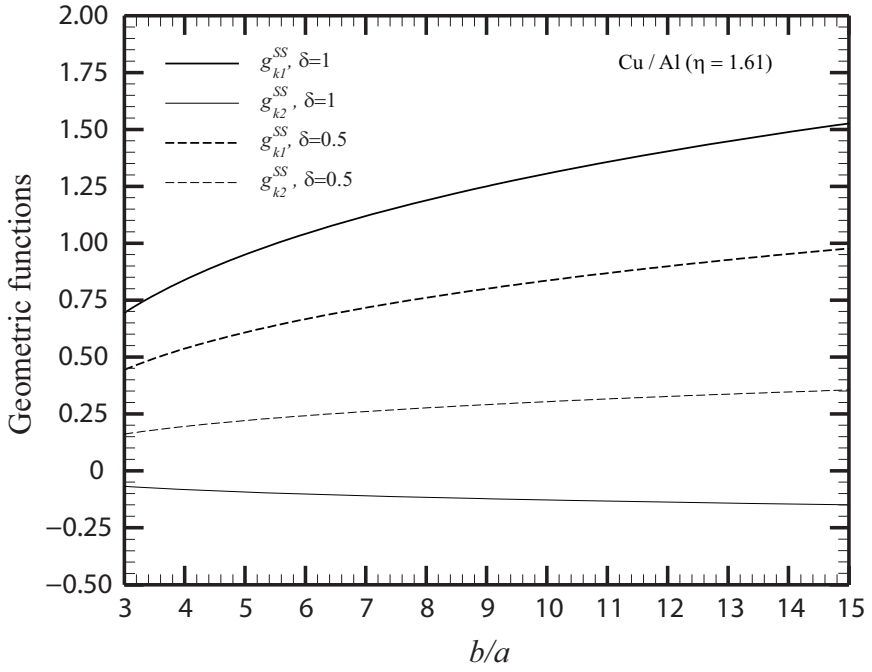

(c)

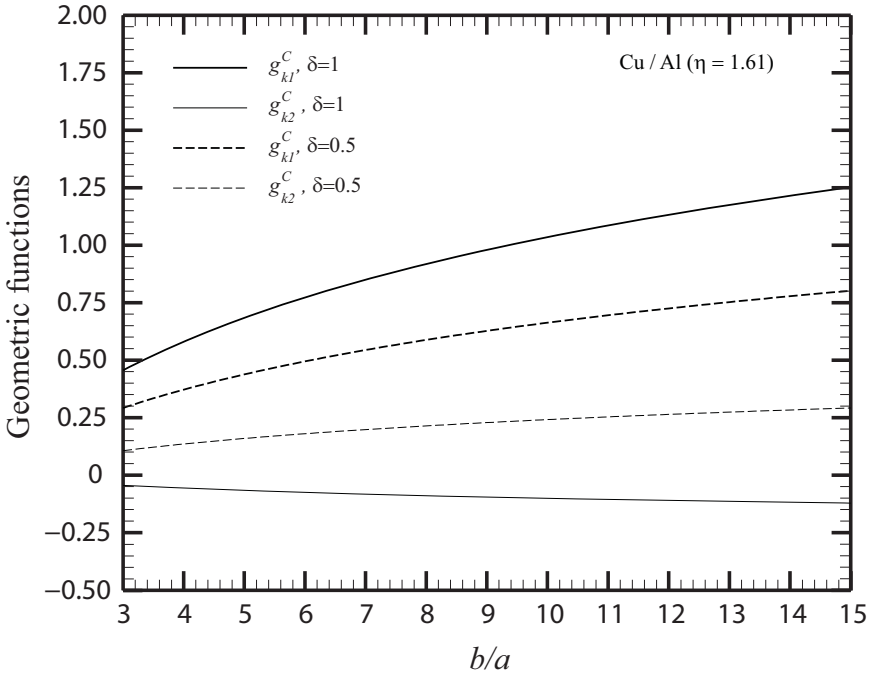

(d)

Figure 3.18. The geometric functions (a) g_{k1}^{SS} and g_{k2}^{SS} for Al/Cu welds, (b) g_{k1}^{C} and g_{k2}^{C} for Al/Cu welds, (c) g_{k1}^{SS} and g_{k2}^{SS} for Cu/Al welds and (d) g_{k1}^{C} and g_{k2}^{C} for Cu/Al welds with $\delta = 1$ and $\delta = 0.5$ as functions of b/a.

CHAPTER IV

CLOSED-FORM STRUCTURAL STRESS AND STRESS INTENSITY FACTOR SOLUTIONS FOR SPOT WELDS IN SQUARE OVERLAP PARTS OF CROSS-TENSION SPECIMENS

4.1. Introduction

Resistance spot welding is widely used to join sheet metals in the automotive industry. The fatigue lives of spot welds have been investigated by many researchers. Due to the geometry of spot welds, natural crack tips or notch tips are presented along the nugget circumference. Stress intensity factor solutions for spot welds at the critical locations in various types of specimens have been developed to investigate the fatigue lives of spot welds. Pook [1, 2] gave the maximum stress intensity factors for spot welds in lap-shear, coach-peel specimens, circular plate, and other bending dominant plate and beam configurations. Radaj [3] and Radaj and Zhang [4-6] established the foundation to use the structural stress solutions to determine the stress intensity factor solutions for spot welds. Zhang [7, 8] obtained the stress intensity factor solutions at the critical locations of spot welds in various types of specimens in order to correlate the experimental results of spot welds in these specimens under cyclic loading conditions. Pan and Sheppard [9] investigated the stress intensity factor solutions for both the main cracks and the kinked cracks in lap-shear and modified coach peel specimens by finite element analyses. Wang et al. [10, 11] and Lin et al [12] proposed new stress intensity factor solutions for square-

cup and lap-shear specimens and the solutions were validated by their three-dimensional finite element analyses. Lin and Pan [13, 14] proposed the closed-form structural stress and stress intensity factor solutions for spot welds in various types of specimens.

Pook [2] indicated that for a class of transversely loaded configurations consisting of two thin plates or beams joined over part of their common plane under symmetric loading conditions, the stress intensity factor at a crack tip depends on the bending moment acting to the beam or plate in the vicinity of the crack tip. Wang et al. [10] conducted three-dimensional finite element analyses of circular plates with connection under opening loading conditions. The computational results indicate that the stress intensity factor along the crack front can be correlated very well with the analytical solutions based on the bending moments or the corresponding structural stresses for thin plates with connection. The close-form solutions for thin plates with rigid inclusions under shear, central bending, counter bending, and opening loading conditions were obtained by Muskhelishvili [15], Goland [16], Timoshanko and Woinowsky-Krieger [17], Lin et al. [12] and Lin and Pan [13], respectively. The classical solutions of Muskhelishvili [15], Goland [16], Timoshanko and Woinowsky-Krieger [17] were obtained from the complex variable approach and the Kirchhoff plate theory. The Lin and Pan [13] solutions were obtained from the Airy stress function and the Kirchhoff plate theory.

For the stress intensity factor solutions for spot welds in cross-tension specimens, Lin and Lin [18] indicates that as the effective specimens length increases, the trends of the stress intensity factor solutions based on the closed-form structural stress solutions of Lin and Pan [13] agree quite well with the computational results. However, when the effective length of the specimens is equal to the specimen width, the stress intensity

factor solutions based on the closed-form structural stress solutions of Lin and Pan [13] overestimated the computational result by about 20%. Note that, the structural stress solutions of Lin and Pan [13, 14] are based on the superposition of the solutions for a rigid inclusion in a square plate under opening loading and counter-bending loading conditions. Therefore, the main purpose of this investigation is to determine the source of this 20% overestimation. Furthermore, in order to examine the accuracy of the analytical structural stress and stress intensity factor solutions for spot welds in lap-shear, square-cup, U-shape, cross-tension and coach-peel specimens presented in Lin and Pan [13, 14], it is necessary to first examine carefully the analytical solutions for the square overlap parts of these specimens. Ultimately, closed-form structural stress and stress intensity factor solutions for spot welds in cross-tension specimens will be provided for researchers to avoid three-dimensional finite element analyses.

In this chapter, the structural stress solutions for a rigid inclusion in a square plate under opening and bending loading conditions are investigated. Figure 4.1(a) shows a schematic of a cross-tension specimen. The specimen has the thickness t and the width $2b$. The spot weld is shown as the light shaded area and has the diameter $2a$. The overlapped part of the specimen is marked by dashed lines. The dark shaded area shows the area clamped by fixtures and subjects to a uniform out-of-plane displacement. Since the parts of the sheets clamped by the fixtures have no contribution to the bending moment applied to the spot weld, the length of the central effective portion is therefore denoted as the effective specimen length $2l$. For cross-tension specimens shown in Figure 4.1(a), the closed-form structural stress solutions of Lin and Pan [13, 14] can be expressed as a constant plus a cosine function. However, the distributions of the opening

force and constraint moment per unit length along the two opposite outer edges are non-uniform while the closed-form structural stress solutions of Lin and Pan [13, 14] assume that both the opening force and constraint moment per unit length along the two opposite outer edges are uniformly distributed. The coefficients for the structural stress solutions for a rigid inclusion in a square upper plate of a cross-tension specimen are therefore needed. The equivalent coefficients can be determined by the structural stress solutions at the critical locations obtained from finite element analyses. The numerical out-of-plane shear structural stress solutions are also introduced based on the amplitude of the cosine function of the in-plane structural stress solutions. Then the stress intensity factor solutions for spot welds between square plates of similar material with equal thickness under opening and bending loading conditions are investigated. The analytical stress intensity factor solutions based on the closed-form structural stress solutions for a rigid inclusion in a square plate with the equivalent coefficients are compared with the stress intensity factor solutions obtained from finite element analyses. The fitting coefficients for the stress intensity factor solutions accounting for the flexibility of spot welds are introduced. Finally, the analytical stress intensity factor solutions based on the closed-form structural stress solutions for a rigid inclusion in a square plate with the equivalent and numerical coefficients for the structural stress and the fitting coefficients for the stress intensity factor are compared with the stress intensity factor solutions obtained from finite element analyses.

4.2. Analytical structural stress solution for a rigid inclusion in a square plate

Lin and Pan [13, 14] presented closed-form structural stress solutions for spot welds in cross-tension and U-shape specimens. The solutions are based on the superposition of the structural stress solutions for a rigid inclusion in a square plate based on the Kirchhoff plate theory. When the specimen effective length reduces to the specimen width ($2l = 2b$), cross-tension specimens in Figure 4.1(a) can be modeled as two square plates with connection or spot weld subjected to a uniform out-of-plane displacement as shown in Figure 4.1(b). Figure 4.1(b) shows a schematic of two square plates with connection or spot weld. Both plates have the equal thickness t and the width $2b$. The connection or spot weld is shown as the shaded area and has the diameter $2a$. Both plates are subjected to a uniform out-of-plane displacement along the two opposite outer edges and shown schematically as bolded arrows. Point A, B, C and D indicate the critical locations of the connection or spot weld.

Figure 4.2 shows a schematic of a top view of the connection or spot weld (idealized as a rigid inclusion) in the upper plate of the specimen with the cylindrical and Cartesian coordinate systems centered at the center of the upper half of the spot weld. The critical locations of points A, B, C and D are 0°, 180°, 90° and 270° with respect to the x axis, respectively. The critical locations of points A, B, C and D can also be seen in Figure 4.1(b). The orientation angle θ represents the angular location along the circumference of the spot weld. Note that the angle θ is measured from the x axis to y axis in counter-clockwise sense.

For spot welds between square plates under opening and bending loading conditions, the structural stress solutions of the upper and lower plates can be approximately decomposed into three types of loads according to the superposition principle. Figure 4.3

shows the decomposition of the loads of the square overlap part of a cross-tension specimen. Model A represents a spot weld in the square overlap part of a cross-tension specimen. Both upper and lower plates are subjected to uniform opening force per unit length $\tilde{F}$ and uniform constraint moment per unit length $\tilde{M}_{\mathrm{c}}$. Model B represents the upper half of model A. In model B, F represents the resultant opening forces applied to the center of circular interfacial of the spot weld. The forces and moments in model B can be approximately decomposed into three types of loads: counter bending (model C), opening (model D) and cross opening / closing (model E) that can be approximated as a twisting loading condition. For a rigid inclusion in a square plate under counter bending loading condition, the uniformly distributed constraint moment $\tilde{M}_{\mathrm{c}}$ for the constrained outer edges of the square plate can be expressed as (Lin and Pan [13,14]),

$$\tilde{M}_{\mathrm{c}} = \frac{F\left[a^2 - b'^2 + 2a^2 \ln\left(b'/a\right)\right]}{4\pi\left(a^2 - b'^2\right)} \tag{4.1}$$

The structural stress solutions for a rigid inclusion in a finite square plate under counter bending loading condition can be expressed as (Lin and Pan [13,14]),

$$\sigma_{\mathrm{CB}} = \frac{3\tilde{M}_{\mathrm{c}}}{t^2 XY}\left[2b^2 X + 4Y\left(a^4 b^4 + b^8\right)\cos 2\theta\right] \tag{4.2}$$

Where b' is the equivalent radius for the equivalent circular plate model with the simply supported outer edges. θ is the angle from the x axis to the y axis in the counter-clockwise sense. Note that the equivalent radius b' presented in Sripichai and Pan [19] are listed in Table 4.1 and are used here. The approximate equivalent radius presented in Sripichai and Pan [19] is expressed as

$$\frac{b'}{b} = 0.838 + 0.4877e^{-0.3513(b/a)} \tag{4.3}$$

and

$$X = (-1+\nu)\left(a^4 + b^4\right)^2 - 4a^2b^6(1+\nu) \tag{4.4}$$

$$Y = a^2(-1+\nu) - b^2(1+\nu) \tag{4.5}$$

For the opening loading condition in model D, the structural stress solutions for a rigid inclusion in a finite square plate can be express as (Lin and Pan [13,14]),

$$\sigma_{\mathrm{O}} = \frac{-3F\left[\left(a^2 - b'^2\right)(-1+\nu) + 2b'^2(1+\nu)\ln(b'/a)\right]}{2\pi t^2\left[a^2(-1+\nu) - b'^2(1+\nu)\right]} \tag{4.6}$$

For the cross opening / closing condition approximated as a twisting loading condition in model E, the structural stress solutions for a rigid inclusion in a finite square plate can be expressed as (Lin and Pan [13,14]),

$$\sigma_{\mathrm{TW}} = \frac{-24\tilde{M}_{x'y'}}{t^2 X'}\left[a^4\left(b/\sqrt{2}\right)^4 + \left(b/\sqrt{2}\right)^8\right]\cos 2\theta \tag{4.7}$$

where $\tilde{M}_{x'y'} = F/16$ is the uniform distributed twisting moment and

$$X' = -\left[a^4 + \left(b/\sqrt{2}\right)^4\right]^2(1-\nu) - 4a^2\left(b/\sqrt{2}\right)^6(1+\nu) \tag{4.8}$$

Note that, the analytical out-of-plane shear stress is zero for all of models C, D and E.

4.3. Finite element analyses for a rigid inclusion in a square plate

Here, finite element analyses for a rigid inclusion in a square plate under opening and bending loading conditions were carried out in order to investigate the applicability of the closed-form structural stress solutions of Lin and Pan [13,14]. Figure 4.4(a) shows a schematic of a half three-dimensional finite element model for a square plate with a rigid inclusion. The boundary conditions along the boundary of the central hole (rigid inclusion), the applied out-of-plane displacement to the upper surfaces of the two

opposite outer edges and the roller boundary conditions on the two opposite outer edges or constrained outer edges are also shown. The x-y-z coordinate system is shown and the origin of the coordinates is located at the center of the lower surface of the rigid inclusion of the square plate. In this model, the rigid inclusion with the radius $a = 3.2$ mm is replaced with a hole and the roller boundary conditions at $r = a$ is shown in the figure. The square plate has the thickness $t = 0.65$ mm and different values of the width $2b$. The square plate is subjected to a uniform out-of-plane displacement in the z direction along the upper surfaces of the two opposite outer edges. Five ratios of the plate width to the rigid inclusion diameter, namely, b/a = 3, 5.91, 7.94, 10 and 15 are considered in this investigation. Figure 4.4(b) shows the finite element mesh of a quarter three-dimensional finite element model for b/a = 7.94. The x-y-z coordinate system is again shown and the origin of the coordinates is located at the center of the lower surface of the rigid inclusion of the square plate. Due to the symmetry, only a quarter of the model was considered. The material is assumed to be a linear elastic isotropic material. The Young's modulus E is taken as 207 GPa, and the Poisson's ratio ν is taken as 0.3. The commercial finite element program ABAQUS [20] was employed to perform the computations. Here, the model to investigate the structural stress solutions for a rigid inclusion in a square plate was selected with the element size of the plate thickness along the inclusion circumference since the element selected gives linear distributions of stresses and strains in the thickness direction as mentioned in Sripichai and Pan [19].

Figure 4.5 shows the distributions of the opening force or the transverse shear force per unit length, F_z, along the plate width of the constrained outer edges. The computational opening forces per unit length, F_z, are normalized by the uniform opening

forces per unit length $\tilde{F}$ based on the assumption that the total opening forces are distributed uniformly along the constrained outer edges. As shown in Figure 4.5, the computational opening forces per unit length are non-uniform along the plate width and the opening forces per unit length are maximum at the center of the constrained outer edges. Figure 4.6 shows the distributions of the constraint moment per unit length, M_x, along the plate width of the constrained outer edges. The computational constraint moments per unit length M_x are normalized by the uniform constraint moments per unit length $\tilde{M}_c$ in Equation (4.1). As shown in Figure 4.6, the computational constraint moments per unit length are non-uniform along the plate width and the constraint moments per unit length are maximum at the center of the constrained outer edges. Due to the non-uniform distributions of the opening force and constraint moment per unit length, the coefficients are introduced to account for the non-uniform distributions in order to use the closed-form structural stress solutions of Lin and Pan [13, 14] to approximate the structural stress solutions in cross-tension specimens. Figure 4.7 shows the normalized structural stress or the maximum bending stress distributions along the circumference of the rigid inclusion for the ratios of the plate width to the rigid inclusion diameter, *b/a*, of 3, 5.91 and 7.94. The structural stress solutions are expressed as functions of the orientation angle θ from the x axis to the y axis in the counter-clockwise sense. The computational structural stress solutions are normalized by the computational structural stress solutions at the critical location of $\theta = 0$. Based on the normalized structural stress solutions along the circumference of the rigid inclusion in Figure 4.7, the structural stress solutions can be expressed as

$$\sigma = G + H\cos 2\theta \tag{4.9}$$

where G is the constant term of the structural stress solutions and can be expressed in the closed-form as

$$G = A + B \tag{4.10}$$

Similarly, H is the amplitude of the cosine function of the structural stress solutions and can be expressed in the closed-form as

$$H = C + D \tag{4.11}$$

Where

$$A = \frac{-3F\left[\left(a^2 - b'^2\right)\left(-1+\nu\right) + 2b'^2\left(1+\nu\right)\ln\left(b'/a\right)\right]}{2\pi t^2\left[a^2\left(-1+\nu\right) - b'^2\left(1+\nu\right)\right]} \tag{4.12}$$

$$B = \frac{3p_c\tilde{M}_c}{t^2 XY}\left[2b^2 X\right] \tag{4.13}$$

$$C = \frac{3p_c\tilde{M}_c}{t^2 XY}\left[4Y\left(a^4 b^4 + b^8\right)\right] \tag{4.14}$$

$$D = \frac{-24q_c\tilde{M}_{x'y'}}{t^2 X'}\left[a^4\left(b/\sqrt{2}\right)^4 + \left(b/\sqrt{2}\right)^8\right] \tag{4.15}$$

Note that p_c and q_c are the equivalent coefficients accounting for the non-uniform distributions of the opening force and constraint moment per unit length. The equivalent coefficients p_c and q_c can be determined from the computational structural stress solutions at the critical locations ($\theta = 0^\circ$ and $\theta = 90^\circ$) and Equations (4.9) – (4.15). Figure 4.8 shows the values of the equivalent coefficients p_c and q_c as functions of the ratio of the plate width to the rigid inclusion diameter, b/a. Table 4.1 lists the values of the equivalent coefficients p_c and q_c for various b/a for convenient engineering applications. As the ratio of the plate width to the rigid inclusion diameter increases, the equivalent coefficients p_c and q_c seem to reach the values of 1.126 and 1.031,

respectively. Based on the results in Figure 4.8, the equivalent coefficient p_c can be approximated as a function of b/a as

$$p_c = 1.126 + 1.4955e^{-0.3672(b/a)} \tag{4.16}$$

Similarly, the equivalent coefficient q_c can be approximated as a function of b/a as

$$q_c = 1.031 + 2.2150e^{-0.3878(b/a)} \tag{4.17}$$

The approximate equivalent coefficients p_c and q_c from Equations (4.16) and (4.17) are also shown as a line and dotted line in Figure 4.8, respectively. From the definition of the equivalent coefficients p_c and q_c in Equations (4.13) – (4.15), the constraint moment $p_c\tilde{M}_c$ can be viewed as the equivalent constraint moment accounting for the non-uniform distribution of the constraint moment per unit length. Similarly, the twisting moment $q_c\tilde{M}_{x'y'}$ can be viewed as the equivalent uniformly distributed twisting moment accounting for the non-uniform distribution of the opening force per unit length.

Figure 4.9 shows the normalized out-of-plane shear stress distributions along the circumference of the rigid inclusion for the ratios of the plate width to the rigid inclusion diameter, b/a, of 3, 5.91 and 7.94. The out-of-plane shear stress solutions are expressed as functions of the orientation angle θ from the x axis to the y axis in the counter-clockwise sense. The computational out-of-plane shear stress solutions are normalized by the computational in-plane structural stress solutions at the critical location of $\theta = 0$. As shown in Figure 4.9, the out-of-plane shear stress solutions can be expressed as

$$\tau = c_\tau H \sin 2\theta \tag{4.18}$$

Where c_τ is the numerical coefficient for the out-of-plane shear stress solution. Figure 4.10 shows the numerical coefficient c_τ for the out-of-plane shear stress solution as a function of the ratio of the plate width to the rigid inclusion diameter, b/a. As the ratio of the plate width to the rigid inclusion diameter, b/a, increases, the numerical coefficient c_τ for the out-of-plane shear stress solution seems to reach the value of -0.111. Table 4.1 also lists the values of the numerical coefficient c_τ for various b/a for convenient engineering applications. Based on the results in Figure 4.10, the numerical coefficient c_τ for the out-of-plane shear stress solution can be approximated as a function of b/a as

$$c_\tau = -0.111 - 0.0263e^{-0.5538(b/a)} \tag{4.19}$$

The approximate numerical coefficient c_τ for the out-of-plane shear stress solution is shown as a line in Figure 4.10.

The computational results indicate that the out-of-plane shear stress exist at the circumference of the rigid inclusion while the closed-form structural stress solutions of Lin and Pan [13,14] based on the Kirchhoff plate theory give no out-of-plane shear stress along the circumference of the rigid inclusion. This could be the main reason that the closed-form structural stress solutions of Lin and Pan [13, 14] need the equivalent coefficients p_c and q_c for the structural stress solutions since the closed-form solutions based on the Kirchhoff plate theory do not give the shear stress that occurs along the circumference of the rigid inclusion.

4.4. Analytical stress intensity factor solutions for spot welds between square plates of equal thickness

Stress intensity factor solutions of spot welds in various types of specimens were obtained from the structural stress solutions in [3-8]. Analytical stress intensity factor solutions for spot welds between square plates of equal thickness under opening and bending loading conditions, as shown in Figure 4.1(b), were proposed in [13, 14] based on the structural stress solutions for a rigid inclusion in a square plate with the equivalent radius b' based on the area equivalence rule. Figure 4.11(a) shows a two-dimensional model of two infinite strips of same thickness and material with connection under plane strain conditions. As shown in Figure 4.11(a), the radial stress σ_{rr} and the shear stress $\sigma_{r\theta}$ along the circumference of a rigid inclusion in a plate are used to represent the normal structural stresses, σ_x^u and σ_x^l, and the shear structural stresses, τ_{xz}^u and τ_{xz}^l, for the strip model with respect to the Cartesian coordinate system as shown in the figure. Figure 4.11(b) shows the front and side views of the left part of the strip model near the crack tip with the linearly distributed structural stresses through the thickness based on the Kirchhoff plate theory. The strip model can be used to represent the cross section perpendicular to the crack front along the spot weld or the connection circumference. The two strips are assumed to be linear elastic isotropic materials with the Young's modulus E and Poisson's ratio ν. Both upper and lower strips has the thickness t. The normal stresses σ_{ui}, σ_{uo}, σ_{li} and σ_{lo} represent the normal stresses σ_x at the inner (*i*) and outer (*o*) surfaces of the upper (*u*) and lower (*l*) strips, respectively. The shear stresses τ_{ui}, τ_{uo}, τ_{li} and τ_{lo} represent the shear stresses τ_{xz} at the inner (*i*) and outer (*o*) surfaces of the upper (*u*) and lower (*l*) strips, respectively. For square plates under opening and

bending loading conditions, the normal stresses σ_{ui} and σ_{li} are the structural stresses obtained from Equation (4.9). The shear stresses τ_{ui} and τ_{li} are the shear stresses obtained from Equation (4.18). Note that the structural stress solutions of the lower plate can be derived by substituting $\theta+\pi/2$ for θ in Equations (4.9) and (4.18). For square plates under opening and bending loading conditions, $\sigma_{uo}=-\sigma_{ui}$, $\sigma_{lo}=-\sigma_{li}$, $\tau_{uo}=-\tau_{ui}$ and $\tau_{lo}=-\tau_{li}$. Thus the stress intensity factor K_{I} solution for spot welds between square plates of equal thickness under opening and bending loading conditions can be simplified as (Lin and Pan [13,14] and Tran and Pan [21])

$$K_{\mathrm{I}}=\frac{\sqrt{3t}}{12}\left(\sigma_{ui}-\sigma_{uo}+\sigma_{li}-\sigma_{lo}\right)=\frac{\sqrt{t}}{\sqrt{3}}G \tag{4.20}$$

Similarly, the stress intensity factor K_{II} solution for spot welds between square plates of equal thickness under opening and bending loading conditions can be simplified as (Lin and Pan [13,14] and Tran and Pan [21])

$$K_{\mathrm{II}}=\frac{\sqrt{t}}{4}\left(\sigma_{ui}-\sigma_{li}\right)=\frac{\sqrt{t}}{2}H\cos 2\theta \tag{4.21}$$

The stress intensity factor K_{III} solution of for spot welds between square plates of equal thickness under opening and bending loading conditions can be calculated from the out-of-plane J integral, J_{III}. The detailed derivation of the out-of-plane J integral and stress intensity factor K_{III} solutions is presented in Appendix. Based on Equation (4.A12) in Appendix, the stress intensity factor K_{III} solutions can be simplified as

$$K_{\mathrm{III}}=\sqrt{\frac{t}{24}\left(\tau_{ui}+\tau_{li}\right)^2+6\left(\tau_{ui}^2+\tau_{li}^2\right)}=\frac{\sqrt{t}}{\sqrt{2}}c_{\tau}H\sin 2\theta \tag{4.22}$$

From the analytical K_{I} and K_{II} solutions, the contribution of each type of loads (i.e. opening, counter bending, and twisting) to the analytical K_{I} and K_{II} solutions can be investigated by examining the ratios of the structural stresses for each type of loads to the total structural stresses. From Equation (4.20), the analytical K_{I} solution of the opening loading condition can be expressed as

$$K_{\mathrm{I,O}} = \frac{\sqrt{3t}}{12}\left(\sigma_{ui} - \sigma_{uo} + \sigma_{li} - \sigma_{lo}\right)_O = \frac{\sqrt{t}}{\sqrt{3}}A \tag{4.23}$$

where the subscript O denotes the opening condition and the subscript O outside the bracket denotes the structural stresses σ_{ui}, σ_{uo}, σ_{li} and σ_{lo} of the opening loading condition in Equation (4.6). Similarly, the analytical K_{I} solution of the counter bending loading condition can be expressed as

$$K_{\mathrm{I,CB}} = \frac{\sqrt{3t}}{12}\left(\sigma_{ui} - \sigma_{uo} + \sigma_{li} - \sigma_{lo}\right)_{CB} = \frac{\sqrt{t}}{\sqrt{3}}B \tag{4.24}$$

where the subscript CB denotes the counter bending loading condition and the subscript CB outside the bracket denotes the structural stresses σ_{ui}, σ_{uo}, σ_{li} and σ_{lo} of the counter bending loading condition in Equation (4.2). From Equations (4.20), (4.23) and (4.24), the contribution of the opening loading condition to the analytical K_{I} solution can be expressed as

$$\frac{K_{\mathrm{I,O}}}{K_{\mathrm{I}}} = \frac{A}{G} \tag{4.25}$$

and the contribution of the counter bending loading condition to the analytical K_{I} solution can be expressed as

$$\frac{K_{\mathrm{I,CB}}}{K_{\mathrm{I}}} = \frac{B}{G} \tag{4.26}$$

From Equation (4.21) the analytical K_{II} solution of the counter bending loading condition can be expressed as

$$K_{\mathrm{II,CB}} = \frac{\sqrt{t}}{4}\left(\sigma_{ui} - \sigma_{li}\right)_{CB} = \frac{\sqrt{t}}{2} C \cos 2\theta \tag{4.27}$$

where the subscript CB denotes the counter bending loading condition and the subscript CB outside the bracket denotes the structural stresses σ_{ui}, σ_{uo}, σ_{li} and σ_{lo} of the counter bending loading condition in Equation (4.2). Similarly, the analytical K_{II} solution of the twisting loading condition can be expressed as

$$K_{\mathrm{II,TW}} = \frac{\sqrt{t}}{4}\left(\sigma_{ui} - \sigma_{li}\right)_{TW} = \frac{\sqrt{t}}{2} D \cos 2\theta \tag{4.28}$$

where the subscript TW denotes the twisting loading condition and the subscript TW outside the bracket denotes the structural stresses σ_{ui}, σ_{uo}, σ_{li} and σ_{lo} of the twisting loading condition in Equation (4.7). From Equations (4.21), (4.27) and (4.28), the contribution of the counter bending loading condition to the analytical K_{II} solution can be expressed as

$$\frac{K_{\mathrm{II,CB}}}{K_{\mathrm{II}}} = \frac{C}{H} \tag{4.29}$$

and the contribution of the twisting loading condition to the analytical K_{II} solution can be expressed as

$$\frac{K_{\mathrm{II,TW}}}{K_{\mathrm{II}}} = \frac{D}{H} \tag{4.30}$$

Tables 4.2a and 4.2b list the contributions of the opening, counter bending and twisting loading conditions to the analytical K_{I} and K_{II} solutions based on the equivalent radius b' presented in Sripichai and Pan [19] and the equivalent radius b' based on the area equivalence rule, respectively. Both solutions are based on the values of the equivalent coefficients p_{c} and q_{c} equal to 1. As listed in Tables 4.2a and 4.2b, the opening loading condition contributes to the analytical K_{I} solution approximately 120 to 115%, while the counter bending loading condition reduces the analytical K_{I} solution by 20 to 15% approximately. For the analytical K_{II} solution, the twisting loading condition contributes more to the analytical K_{II} solution while the counter bending loading condition reduces the analytical K_{II} solution. Table 4.3a lists a comparison of the structural stress solutions in Equations (4.10) – (4.15) based on the equivalent radius b' of Sripichai and Pan [19] (as listed in Table 4.1) without the equivalent coefficients p_{c} and q_{c} ($p_{\mathrm{c}}=1$ and $q_{\mathrm{c}}=1$) and the original closed-form structural stress solutions of Lin and Pan [14] with the equivalent radius b' based on the area equivalence rule. Table 4.3b lists a comparison of the structural stress solutions in Equations (4.10) – (4.15) based on the equivalent radius b' of Sripichai and Pan [19] with the equivalent coefficients p_{c} and q_{c} listed in Table 4.1 and the original closed-form structural stress solutions of Lin and Pan [13, 14] with the equivalent radius b' based on the area equivalence rule. The subscript *area* denotes the structural stress solutions based on the area equivalence rule without the equivalent coefficients p_{c} and q_{c} or the original closed-form structural stress solutions of Lin and Pan [13, 14]. As listed in Table 4.3, the equivalent radius b' has more influence on the analytical K_{I} solution than the equivalent coefficient p_{c} since

most of the contribution of the analytical K_{I} solution comes from the opening loading condition. The equivalent radius b' presented in Sripichai and Pan [19] reduced the analytical K_{I} solution from the analytical K_{I} solution based on the closed-form structural stress solutions of Lin and Pan [13, 14], which is based on the area equivalence rule, by 10 to 13%. The equivalent coefficient p_{c} reduced the analytical K_{I} solution from the analytical K_{I} solution based on the closed-form structural stress solutions of Lin and Pan [14] further by only 2 to 5%. With the combination of the equivalent radius b' presented in Sripichai and Pan [19] and the equivalent coefficient p_{c}, the analytical K_{I} solution in Equation (4.20) can be significantly less than the analytical K_{I} solution based on the original closed-form structural stress solution of Lin and Pan [13, 14] by 10 to 20% for large ratios of b/a .

For the analytical K_{II} solution, the equivalent radius b' has less influence on the analytical K_{II} solution since most of the contribution of the analytical K_{II} solution comes from the twisting loading condition which does not depend on the equivalent radius b' as listed in Table 4.3a. The equivalent radius b' presented in Sripichai and Pan [19] increases the analytical K_{II} solution from the analytical K_{II} solution based on the closed-form structural stress solutions of Lin and Pan [13, 14] by 2 to 9%, due to the decrease of the structural stress of the counter bending loading condition. The equivalent coefficient p_{c}, which increases the equivalent constraint moment per unit length of the counter bending loading condition, increases the structural stress of the counter bending loading condition. This results in reduction of the analytical K_{II} solution. However, the equivalent coefficient q_{c} increases the structural stress of the twisting loading condition

and thus increases the analytical K_{II} solution. With the combination of the equivalent radius b' presented in Sripichai and Pan [19] and the equivalent coefficients p_c and q_c, the analytical K_{II} solution in Equation (4.21) can be more or less than the analytical K_{II} solution based on the original closed-form structural stress solution of Lin and Pan [13, 14] by 10% for large ratios of b/a .

4.5. Finite element analyses for spot welds between square plates of equal thickness

Finite element analyses for spot welds between square plates of equal thickness under opening and bending loading conditions were conducted in order to investigate the applicability of the structural stress solutions with the equivalent coefficients to estimate the stress intensity factor solutions for spot welds. Figure 4.12(a) shows a schematic of a three-dimensional finite element model of two square plates with connection and the roller boundary conditions on the two opposite outer edges of the upper and lower plates. The x-y-z coordinate system is shown and the origin of the coordinates is located at the center of the connection of the two square plates. Both plates have the equal thickness $t = 0.65$ mm and different values of the width $2b$. The connection or spot weld has the diameter of $2a = 6.4$ mm. The lower surfaces of the two opposite outer edges of the lower plates are fixed. The upper plates are subjected to a uniform out-of-plane displacement in the z direction along the upper surfaces of the two opposite outer edges. Five ratios of the plate width to the connection diameter, namely, b/a = 3, 5.91, 7.94, 10 and 15, are considered in this investigation. Figures 4.12(b) and 4.12(c) show a quarter of a three-dimensional finite element model for b/a = 7.94 and a close-up view of the mesh near the crack front. The x-y-z coordinate system is shown and the origin of

the coordinates is located at the center of the connection of the square plates. Due to the symmetry, only a quarter of the model was considered. The material is assumed to be a linear elastic isotropic material. The Young's modulus E is taken as 207 GPa, and the Poisson's ratio ν is taken as 0.3. The commercial finite element program ABAQUS [20] was employed to perform the computations. Brick elements C3D20R with quarter point nodes and collapsed nodes along the crack front are adopted to model the $1/\sqrt{r}$ singularity near the crack front.

Figure 4.13 shows the normalized stress intensity factor K_{I} and K_{II} solutions at the critical location of point A for spot welds between square plates with various ratios of the plate width to the connection diameter, b/a. The stress intensity factor K_{I} and K_{II} solutions are normalized by the analytical stress intensity factor K_{I} solutions at the critical location of point A obtained from Equation (4.20) with the equivalent coefficients listed in Table 4.1. The normalized computational K_{I} and K_{II} solutions for spot welds between square plates are shown as circle and thin line circle symbols in Figure 4.13, respectively. As shown in Figure 4.13, the analytical stress intensity factor K_{I} solutions obtained from Equation (4.20) with the equivalent coefficients p_{c} and q_{c} listed in Table 4.1 agree well with the computational K_{I} solutions except for the ratio of the plate width to the connection diameter of $b/a = 3$. At the small ratio of the plate width to the connection diameter, b/a, the effect of the outer edges may be significant and cause the deviation of the computational K_{I} solutions from the analytical K_{I} solutions. The analytical stress intensity factor K_{II} solutions at the critical location of point A obtained from Equation (4.21) with the equivalent coefficients p_{c} and q_{c} listed in Table 4.1 for

various ratios of the plate width to the connection diameter, *b/a* , are also shown in the figure. The analytical K_{II} solutions are also normalized by the analytical K_I solutions at the critical location of point A obtained from Equation (4.20) with the equivalent coefficients listed in Table 4.1. The normalized analytical K_{II} solutions are shown as thin line square symbols in Figure 4.13. For the stress intensity factor K_{II} solutions, the computational K_{II} solutions have significantly lower values than the analytical K_{II} solutions obtained from Equation (4.21) with the equivalent coefficients p_c and q_c listed in Table 4.1 as shown in Figure 4.13. The applicability of the approximate equivalent coefficients p_c and q_c in Equations (4.16) and (4.17) are also investigated. The normalized analytical stress intensity factor K_I and K_{II} solutions at the critical location of point A obtained from Equations (4.20) and (4.21) with the equivalent coefficients p_c and q_c in Equations (4.16) and (4.17) are also shown in Figure 4.13. These stress intensity factors solutions are also normalized by the analytical stress intensity factor K_I solutions at the critical location of point A obtained from Equation (4.20) with the equivalent coefficients p_c and q_c listed in Table 4.1. The normalized analytical K_I and K_{II} solutions obtained from Equations (4.20) and (4.21) with the approximate equivalent coefficients p_c and q_c are shown as triangle and thin line triangle symbols in Figure 4.13, respectively. As shown in Figure 4.13, the analytical stress intensity factor K_I and K_{II} solutions based on the approximate equivalent coefficients agree very well with the analytical K_I and K_{II} solutions with the equivalent coefficients listed in Table 4.1.

Figure 4.14 shows the stress intensity factor K_{III} solutions at the angle of $45°$ from the critical location of point A in the counter-clockwise sense for spot welds between square plates and the analytical stress intensity factor K_{III} solutions at the angle of $45°$ from the critical location of point A in the counter-clockwise sense obtained from Equation (4.22) with the equivalent and numerical coefficients p_{c}, q_{c}, and c_{τ} listed in Table 4.1. The applicability of the approximate numerical coefficient c_{τ} for the out-of-plane shear stress solution in Equation (4.19) is also investigated here. The normalized analytical stress intensity factor K_{III} solutions at the angle of $45°$ from the critical location of point A in the counter-clockwise sense obtained from Equation (4.22) with the approximate equivalent radius in Equation (4.3) and the approximate equivalent and numerical coefficients p_{c}, q_{c}, and c_{τ} in Equations (4.16), (4.17) and (4.19) are also shown in Figure 4.14. The computational and analytical K_{III} solutions were normalized by the analytical K_{I} solutions at the critical location of point A obtained from Equation (4.20) with the equivalent coefficients listed in Table 4.1. As shown in Figure 4.14, the values of the computational K_{III} solutions are higher than those of the analytical K_{III} solutions obtained from Equation (4.22) with the equivalent and numerical coefficients p_{c}, q_{c}, and c_{τ} listed in Table 4.1. The analytical K_{III} solutions obtained from Equation (4.22) and the equivalent and numerical coefficients p_{c}, q_{c}, and c_{τ} listed in Table 4.1 and from Equations (4.16), (4.17) and (4.19) agree very well with each other. The main reason that the computational K_{II} solutions are lower than the analytical K_{II} solutions and the computational K_{III} solutions are higher than the analytical K_{III} solutions may come from the flexibility of the connection of the two square plates. The investigation of

the effect of the flexibility of the rigid inclusion to the structural stress solutions was also carried out. As the rigid inclusion become more flexible, with the Young's modulus E equal to that of the plate material, the stress amplitude H of the structural stress obtained from Equation (4.9) decreases while the magnitude of the out-of-plane shear stress increases. These result in decreasing of K_{II} solution and increasing of K_{III} solution. Thus the fitting coefficients for the stress intensity factor solutions accounting for the flexibility of the connection are needed. Figure 4.15 shows the values of the fitting coefficients k_{cII} and k_{cIII} as functions of the ratio of the plate width to the connection diameter, b/a. The fitting coefficients k_{cII} and k_{cIII} are determined from the computational and analytical stress intensity factor K_{II} and K_{III} solutions and can be expressed as,

$$k_{\mathrm{cII}} = \frac{K_{\mathrm{II,FEM}}}{K_{\mathrm{II,SS}}} \tag{4.31}$$

where $K_{\mathrm{II,FEM}}$ is the computational stress intensity factor K_{II} solution and $K_{\mathrm{II,SS}}$ is the analytical stress intensity factor K_{II} solution obtained from Equation (4.21) with the equivalent coefficients p_{c} and q_{c} listed in Table 4.1. Similarly, the fitting coefficient k_{cIII} can be expressed as,

$$k_{\mathrm{cIII}} = \frac{K_{\mathrm{III,FEM}}}{K_{\mathrm{III,SS}}} \tag{4.32}$$

where $K_{\mathrm{III,FEM}}$ is the computational stress intensity factor K_{III} solution and $K_{\mathrm{III,SS}}$ is the analytical stress intensity factor K_{III} solution obtained from Equation (4.22) with the equivalent and numerical coefficients p_{c}, q_{c}, and c_{τ} listed in Table 4.1. Table 4.4 lists

the values of the fitting coefficients k_{cII} and k_{cIII} for various ratios of b/a for convenient engineering applications. As the ratio of the plate width to the connection diameter increases, the fitting coefficients k_{cII} and k_{cIII} seem to reach the limiting values of 0.565 and 2.768, respectively. Based on the results in Figure 4.15, the fitting coefficients k_{cII} and k_{cIII} accounting for the flexibility of the connection can be approximated as functions of b/a as

$$k_{cII} = 0.565 - 0.1417e^{-0.3473(b/a)} \tag{4.33}$$

$$k_{cIII} = 2.768 + 0.3058e^{-0.3260(b/a)} \tag{4.34}$$

In order to determine the applicability of the fitting coefficients k_{cII} and k_{cIII}, the distributions of the stress intensity factor K_I, K_{II} and K_{III} solutions for a selected value of b/a were investigated. The fitting coefficients k_{cII} and k_{cIII} are applied to the structural stress solutions. Then, the stress intensity factor solutions based on the structural stress solutions with the fitting coefficients are calculated. From the definitions of the fitting coefficients k_{cII} and k_{cIII} in Equations (4.31) and (4.32), the in-plane structural stress solutions for a rigid inclusion in a square plate with the fitting coefficients can be expressed as,

$$\sigma_{eff} = G + k_{cII} H \cos 2\theta \tag{4.35}$$

Similarly, the out-of-plane shear structural stress solutions for a rigid inclusion in a square plate with the fitting coefficients can be expressed as,

$$\tau_{eff} = c_\tau k_{cIII} H \sin 2\theta \tag{4.36}$$

By applying the structural stress solutions with the fitting coefficients in Equations (4.35) and (4.36) to the analytical stress intensity factor K_{I} solution in Equation (4.20), the analytical K_{I} solution based on the structural stress solution with the fitting coefficients can be simplified as (Lin and Pan [13, 14] and Tran and Pan [21])

$$K_{\mathrm{I,kc}} = \frac{\sqrt{3t}}{12}\left(\sigma_{ui} - \sigma_{uo} + \sigma_{li} - \sigma_{lo}\right)_{,eff} = \frac{\sqrt{t}}{\sqrt{3}}G \tag{4.37}$$

Where the normal stresses $\sigma_{ui,eff}$, $\sigma_{uo,eff}$, $\sigma_{li,eff}$ and $\sigma_{lo,eff}$ are based on the structural stress solution with the fitting coefficients in Equation (4.35). Similarly, the analytical stress intensity factor K_{II} solution based on the structural stress solutions with the fitting coefficients can be simplified as (Lin and Pan [13, 14] and Tran and Pan [21])

$$K_{\mathrm{II,kc}} = \frac{\sqrt{t}}{4}\left(\sigma_{ui} - \sigma_{li}\right)_{,eff} = \frac{\sqrt{t}}{2}k_{\mathrm{cII}}H\cos 2\theta \tag{4.38}$$

The analytical stress intensity factor K_{III} solution based on the out-of-plane shear structural stress solutions with the fitting coefficients can be simplified as

$$K_{\mathrm{III,kc}} = \sqrt{\frac{t}{24}\left(\tau_{ui} + \tau_{li}\right)^2_{,eff} + 6\left(\tau^2_{ui,eff} + \tau^2_{li,eff}\right)} = \frac{\sqrt{t}}{\sqrt{2}}c_{\tau}k_{\mathrm{cIII}}H\sin 2\theta \tag{4.39}$$

Where the shear stresses $\tau_{ui,eff}$ and $\tau_{li,eff}$ represent the shear stress τ_{xz} with the fitting coefficients at the interface of the upper (*u*) and lower (*l*) strips based on Equation (4.36), respectively.

Figure 4.16 shows the distributions of the normalized computational and analytical stress intensity factor K_{I}, K_{II} and K_{III} solutions, and the analytical stress intensity factor $K_{\mathrm{I,kc}}$, $K_{\mathrm{II,kc}}$ and $K_{\mathrm{III,kc}}$ solutions based on the structural stress solutions with the fitting coefficients along the circumference of the spot weld for $b/a = 7.94$. All the stress

intensity factor solutions are normalized by the analytical stress intensity factor K_{I} solution at the critical location of point A obtained from Equation (4.20) with the equivalent coefficients p_{c} and q_{c} listed in Table 4.1 without the fitting coefficient k_{cII} ($k_{\mathrm{cII}}=1$). As shown in Figure 4.16, the analytical stress intensity factor K_{I} and $K_{\mathrm{I,kc}}$ solutions agree very well with the computational K_{I} solutions. The fitting coefficient k_{cII} has no effect on the analytical K_{I} solutions as can be seen in Equation (4.37). For the stress intensity factor K_{II} solutions, the analytical stress intensity factor $K_{\mathrm{II,kc}}$ solutions agree very well with the computational K_{II} solutions while the analytical K_{II} solution has the same distribution along the circumference of spot weld as the computational K_{II} solutions but with a higher amplitude. Similarly, the analytical stress intensity factor $K_{\mathrm{III,kc}}$ solutions agree very well with the computational K_{III} solutions while the analytical K_{III} solution has the same distribution along the circumference of spot weld as the computational K_{III} solution but with a lower amplitude. The applicability of the approximate equivalent, numerical and fitting coefficients p_{c}, q_{c}, c_{τ}, k_{cII}, and k_{cIII} in Equations (4.16), (4.17), (4.19), (4.33) and (4.34) were also investigated. Figure 4.17 shows the distributions of the normalized computational and analytical stress intensity factor K_{I}, K_{II} and K_{III} solutions, and the analytical stress intensity factor $K_{\mathrm{I,kc}}$, $K_{\mathrm{II,kc}}$ and $K_{\mathrm{III,kc}}$ solutions based on the structural stress solutions with the fitting coefficients along the circumference of the spot weld for $b/a=7.94$. All the stress intensity factor solutions are normalized by the analytical K_{I} solution at the critical location of point A obtained from Equation (4.20) with the equivalent coefficients p_{c} and

q_c listed in Table 4.1. Noted that the normalized analytical stress intensity factor K_I, K_{II}, K_{III}, $K_{I,kc}$, $K_{II,kc}$ and $K_{III,kc}$ solutions are based on the approximate equivalent radius b' in Equation (4.3) and the approximate equivalent, numerical and fitting coefficients p_c, q_c, c_τ, k_{cII}, and k_{cIII} in Equations (4.16), (4.17), (4.19), (4.33) and (4.34). As shown in Figure 4.17, the analytical stress intensity factor K_I and $K_{I,kc}$ solutions based on the approximate equivalent and fitting coefficients agree very well with the computational K_I solutions. For the stress intensity factor K_{II} solutions, the analytical $K_{II,kc}$ solutions based on the approximate equivalent and fitting coefficients also agree very well with the computational K_{II} solutions while the analytical K_{II} solutions based on the approximate equivalent coefficients are similar to the analytical stress intensity factor K_{II} solutions based on the equivalent coefficients listed in Table 4.1. Similarly, the analytical stress intensity factor $K_{III,kc}$ solutions based on the approximate equivalent, numerical and fitting coefficients agrees very well with the computational K_{III} solutions while the analytical K_{III} solutions are similar to the analytical K_{III} solutions based on the equivalent and numerical coefficients listed in Table 4.1. In conclusion, the approximate equivalent, numerical and fitting coefficients p_c, q_c, c_τ, k_{cII}, and k_{cIII} in Equations (4.16), (4.17), (4.19), (4.33) and (4.34) can be used to determine the K_I, K_{II} and K_{III} solutions quite well.

4.6. Conclusions

Closed-form structural stress and stress intensity factor solutions for spot welds in square overlap parts of cross-tension specimens are systematically examined and

presented here. First, the closed-form analytical solutions for a rigid inclusion in a square plate of Lin and Pan are reviewed. Then the results of three-dimensional finite element analyses for a rigid inclusion in a square plate under opening and bending loading conditions are presented. The results indicate that, the structural stress solutions obtained from finite element analyses can be expressed as a constant plus a cosine function. The results of the opening force and constraint moment per unit length along the constrained outer edges indicates that the distributions of the opening force and constraint moment per unit length are non-uniform. The equivalent coefficients for the structural stress solutions for a rigid inclusion in a square plate are introduced in order to use the closed-form structural stress solutions of Lin and Pan to calculate the structural stress solutions along the circumference of the rigid inclusion in a square plate. The computational out-of-plane shear structural stress solution is also investigated. Due to the fact that the closed-form solutions based on the Kirchhoff plate theory are unable to capture the out-of-plane shear structural stress solution for a rigid inclusion in a square plate under opening and bending loading conditions, the numerical out-of-plane shear structural stress solution is introduced based on the amplitude of the cosine function of the in-plane structural stress solutions. The numerical coefficient for the out-of-plane shear structural stress solution is also presented for selected values of b/a. Then, the results of three-dimensional finite element analyses for spot welds between square plates of similar material with equal thickness are presented. The results indicate that the computational stress intensity factor K_{I} solutions agree well with those based on the structural stress solutions with the equivalent coefficients. However, the computational stress intensity factor K_{II} solutions are lower than those based on the structural stress solutions with the

equivalent coefficients. The computational stress intensity factor K_{III} solutions are higher than those based on the in-plane structural stress solutions with the equivalent and numerical coefficients. These may come from the flexibility of the spot welds between square plates under opening and bending loading conditions. The fitting coefficients for the stress intensity factor solutions are then introduced. The computational stress intensity factor K_{II} and K_{III} solutions agree well with those based on the closed-form structural stress solutions with the equivalent and numerical coefficients for the structural stress and the fitting coefficients for the stress intensity factor.

Appendix: Derivation of the out-of-plane J integral and stress intensity factor solutions

Here, the strip model of Radaj and Zhang [4-6] is adopted to derive the out-of-plane J integral and stress intensity factor solutions for spot welds between square plates under opening and bending loading conditions. The strip model in Figure 4.11 is considered here. Figure 4.A1(a) shows a crack along the interface of the upper and lower plates. A Cartesian coordinate system is shown in the figure and the origin of the coordinates is located at the crack tip. The J integral is defined as [22]

$$J = \int_{\Gamma} (Wn_x - T_i \frac{\partial u_i}{\partial x}) ds \qquad (i = x, y, z) \tag{4.A1}$$

where Γ represents a contour in counter-clockwise sense from the lower crack face to the upper crack face, ds represents the differential arc length of the contour Γ, n_x represents the x component of the unit outward normal **n** to the differential arc length ds, T_i $(=\sigma_{ij} n_j)$ represent the components of the traction vector **T** on the differential arc

length ds, and u_i represent the components of the displacement vector **u**. In Equation (4.A1), the strain energy W is defined as

$$W = \int_o^{\varepsilon_{ij}} \sigma_{ij} d\varepsilon_{ij} \qquad (i = x, y, z) \tag{4.A2}$$

Figure 4.A1(b) shows the front and side views of the left part of the strip model near the crack tip with the linearly distributed out-of-plane shear stresses. Note that only the out-of-plane shear stresses are shown here due to the interest of the out-of-plane J integral, J_{III}, and stress intensity factor K_{III} solutions. As shown in Figure 4.A1(b), line $\overline{ABCDEF}$ is considered as the contour Γ for the J intergral. The integrals along lines $\overline{BC}$ and $\overline{DE}$ are zero because n_x and T_i are zero. Therefore, for a linear elastic isotropic material with the shear modulus G in Figure 4.11, the J integral can be written as

$$J = -\left(\int_{\overline{AB}} W dy + \int_{\overline{CD}} W dy + \int_{\overline{EF}} W dy\right) \tag{4.A3}$$

where the strain energy densities W for a linear elastic isotropic material can be expressed as

$$W = \frac{1-\nu^2}{2E}\sigma_x^2 + \frac{\tau_{xz}^2}{2G} \tag{4.A4}$$

For the out-of-plane J integral, only the portion contributed from the out-of-plane shear stress, $\frac{\tau_{xz}^2}{2G}$, are of interest here.

As shown in Figure 4.A1(b), . The shear stresses τ_{ui}, τ_{uo}, τ_{li} and τ_{lo} represent the shear stresses τ_{xz} at the inner (*i*) and outer (*o*) surfaces of the upper (*u*) and lower (*l*) strips, respectively. For square plates under opening and bending loading conditions,

$\tau_{uo} = -\tau_{ui}$ and $\tau_{lo} = -\tau_{li}$. It should be noted that the out-of-plane shear stress for line $\overline{CD}$ in the weld nugget are required to balance the out-of-plane bending moments induced by the distribution of the out-of-plane shear stresses for lines $\overline{AB}$ and $\overline{EF}$. In Figure 4.A1(b), the shear stress τ_{xz}^{*} represents the required out-of-plane shear stress for line $\overline{CD}$.

Figure 4.A2 shows the decomposition process of the out-of-plane shear stresses τ_{xz} of model A into those of models F and G. Model F represents a strip model subjected to a linearly distributed out-of-plane shear strain γ which has the maximum value γ_o at the outer surfaces of the upper and lower plates. The linearly distributed shear strain γ is the linearly distributed out-of-plane shear strain on the right end of the strips of model A. The equilibrium condition in the z direction gives

$$G\gamma_o = \frac{1}{4}\left(\tau_{ui} - \tau_{li}\right) \tag{4.A5}$$

In Model G, the shear stresses τ'_{uo}, τ'_{ui}, τ'_{li} and τ'_{lo} on the left end of the inner (*i*) and outer (*o*) surfaces of the upper (*u*) and lower (*l*) strips, respectively, can be expressed as

$$\tau'_{uo} = -\frac{3}{4}\tau_{ui} - \frac{1}{4}\tau_{li} \tag{4.A6}$$

$$\tau'_{ui} = \tau_{ui} \tag{4.A7}$$

$$\tau'_{li} = \tau_{li} \tag{4.A8}$$

$$\tau'_{lo} = -\frac{1}{4}\tau_{ui} - \frac{3}{4}\tau_{li} \tag{4.A9}$$

Note that the J_{III} solution for Model F based on Equations (4.A3) – (4.A4) is zero.

Based on the linearly distributed out-of-plane shear stresses in Model G, the J_{III} solution for Model G or Model A based on Equations (4.A3) – (4.A4) can be derived as

$$J_{III} = \frac{1}{2G}\left[\frac{t}{24}\left(\tau_{ui} + \tau_{li}\right)^2 + 6\left(\tau_{ui}^2 + \tau_{li}^2\right)\right] \tag{4.A10}$$

For the out-of-plane shear part of the strip model, the out-of-plane J integral, J_{III}, is related to the stress intensity factor K_{III} solution as

$$J_{III} = \frac{K_{III}^2}{2G} \tag{4.A11}$$

The stress intensity factor K_{III} solution can be obtained from Equations (4.A10) – (4.A11) as

$$K_{III} = \sqrt{\frac{t}{24}\left(\tau_{ui} + \tau_{li}\right)^2 + 6\left(\tau_{ui}^2 + \tau_{li}^2\right)} \tag{4.A12}$$

Reference

[1] Pook LP. Fracture mechanics analysis of the fatigue behaviour of spot welds. Int J Fract 1975; 11: 173-176.

[2] Pook LP. Approximate stress intensity factors obtained from simple plate bending theory. Eng Frac Mech 1979; 12: 505-522.

[3] Radaj D. Stress singularity, notch stress and structural stress at spot–welded joints. Eng Fract Mech 1989; 34: 495-506.

[4] Radaj D, Zhang S. Stress intensity factors for spot welds between plates of unequal thickness. Eng Fract Mech 1991; 39: 391-413.

[5] Radaj D, Zhang S. Simplified formulae for stress intensity factors of spot welds. Eng Fract Mech 1991; 40: 233-236.

[6] Radaj D, Zhang S. Stress intensity factors for spot welds between plate of dissimilar materials. Eng Fract Mech 1992; 42: 233-236.

[7] Zhang S. Stress intensities at spot welds. Int J Fract 1997; 88: 167-185.

[8] Zhang S. Fracture mechanics solutions to spot welds. Int J Fract 2001; 112: 247-75.

[9] Pan N, Sheppard SD. Stress intensity factors in spot welds. Eng Frac Mech 2003; 70: 671-684.

[10] Wang DA, Lin SH, Pan J. Stress intensity factors for spot welds and associated kinked cracks in cup specimens. Int J Fatigue 2005; 27: 581-598.

[11] Wang DA, Lin PC, Pan J. Geometric functions of stress intensity factor solutions for spot welds in lap-shear specimens. Int J Solids Struct 2005; 42: 6299-6318.

[12] Lin PC, Wang DA, Pan J. Mode I stress intensity factor solutions for spot welds in lap-shear specimens. Int J Solids Struct 2007; 44: 1013-1037.

[13] Lin PC, Pan J. Closed-form structural stress and stress intensity factor solutions for spot welds under various types of loading conditions. Int J Solids Struct 2008; 45: 3996-4020.

[14] Lin PC, Pan J. Closed-form structural stress and stress intensity factor solutions for spot welds in commonly used specimens. Eng Fract Mech 2008; 75: 5187-5206.

[15] Muskhelishvili NI. Some Basic Problems of the Mathematical Theory of Elasiticiy. Noordhoff, Groningen; 1953

[16] Goland M. The influence of the shape and rigidity of an elastic inclusion of the transverse flexure of thin plates. J App Mech 1943; A-69-A-75.

[17] Timoshenko S, Woinowsky-Krieger S. Theory of Plate and Shells, 2nd ed. McGrow-Hill, NY; 1959.

[18] Lin PC, Lin ZL. Geometric functions of stress intensity factor solutions for spot welds in cross-tension specimens. To be submitted.

[19] Sripichai K, Pan J. Closed-form structural stress and stress intensity factor solutions for spot welds in square plates under opening loading conditions. To be submitted

[20] ABAQUS v6.7 User Manual. Providence, RI: SIMULIA; 2007.

[21] Tran VX, Pan J. Analytical stress intensity factor solutions for resistance and friction stir spot welds in lap-shear specimens of different materials and thicknesses. Eng Frac Mech 2010; 77: 2611-2639.

[22] Rice JR. A path independent integral and the approximate analysis of strain concentration by notches and cracks. J App Mech 1968; 35: 379-386.

Table 4.1. The normalized equivalent radius b'/b, the equivalent coefficients p_c and q_c, and the fitting coefficient c_τ for various ratios of the plate width to the rigid inclusion diameter, b/a.

b/a	3	5.91	7.94	10	15
b'/b	1.006	0.894	0.866	0.852	0.838
p_c	1.617	1.278	1.201	1.162	1.126
q_c	1.722	1.241	1.132	1.079	1.031
c_τ	-0.116	-0.112	-0.111	-0.111	-0.111

Table 4.2a. The contributions of the opening, counter bending, and twisting loading conditions to the K_I and K_{II} solutions based on the closed-form structural stress solutions of Lin and Pan [13, 14] with the equivalent radius of Sripichai and Pan [19] without the equivalent coefficients p_c and q_c.

b/a	K_I solution		K_{II} solution	
	Opening A/G	Counter bending B/G	Counter bending C/H	Twisting D/H
3	1.26	-0.26	-1.98	2.98
5.91	1.21	-0.21	-1.91	2.91
7.94	1.19	-0.19	-1.82	2.82
10	1.18	-0.18	-1.78	2.78
15	1.15	-0.15	-1.75	2.75

Table 4.2b. The contributions of the opening, counter bending, and twisting loading conditions to the K_I and K_{II} solutions based on the original closed-form structural stress solutions of Lin and Pan [13, 14] with the area equivalence rule.

b/a	K_I solution		K_{II} solution	
	Opening A/G	Counter bending B/G	Counter bending C/H	Twisting D/H
3	1.25	-0.25	-2.34	3.34
5.91	1.19	-0.19	-2.16	2.16
7.94	1.17	-0.17	-1.99	1.99
10	1.16	-0.16	-1.90	1.90
15	1.14	-0.14	-1.81	1.81

Table 4.3a. A comparison of the structural stress solutions based on the closed-form solutions of Lin and Pan [13, 14] with the equivalent radius of Sripichai and Pan [19] without the equivalent coefficients p_c and q_c, and the original closed-form structural stress solutions of Lin and Pan [13, 14] with the area equivalence rule.

b/a	K_I solution			K_{II} solution		
	Opening A/A_{area}	Counter bending B/B_{area}	Combined G/G_{area}	Counter bending C/C_{area}	Twisting D/D_{area}	Combined H/H_{area}
3	0.91	0.95	0.90	0.95	1.00	1.12
5.91	0.88	0.96	0.87	0.96	1.00	1.09
7.94	0.89	0.97	0.87	0.97	1.00	1.06
10	0.89	0.98	0.88	0.98	1.00	1.04
15	0.90	0.99	0.89	0.99	1.00	1.02

Table 4.3b. A comparison of the structural stress solutions based on the closed-form solutions of Lin and Pan [13, 14] with the equivalent radius of Sripichai and Pan [19] and the equivalent coefficients p_c and q_c, and the original closed-form structural stress solutions of Lin and Pan [13, 14] with the area equivalence rule.

b/a	K_I solution			K_{II} solution		
	Opening A/A_{area}	Counter bending B/B_{area}	Combined G/G_{area}	Counter bending C/C_{area}	Twisting D/D_{area}	Combined H/H_{area}
3	0.91	1.53	0.75	1.53	1.72	2.16
5.91	0.88	1.23	0.82	1.23	1.24	1.27
7.94	0.89	1.17	0.84	1.17	1.13	1.06
10	0.89	1.14	0.85	1.14	1.08	0.97
15	0.90	1.11	0.87	1.11	1.03	0.89

Table 4.4. The fitting coefficients k_{cII} and k_{cIII} for various ratios of the plate width to the connection diameter, *b/a*.

b/a	3	5.91	7.94	10	15
k_{cII}	0.520	0.556	0.561	0.563	0.565
k_{cIII}	2.875	2.794	2.783	2.774	2.768

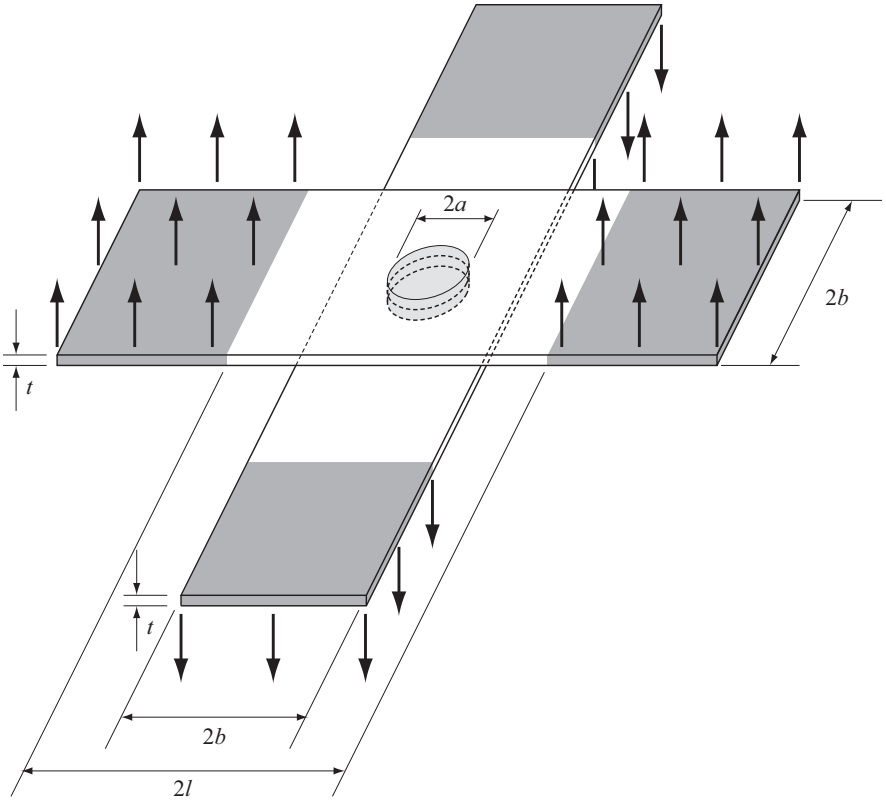

(a)

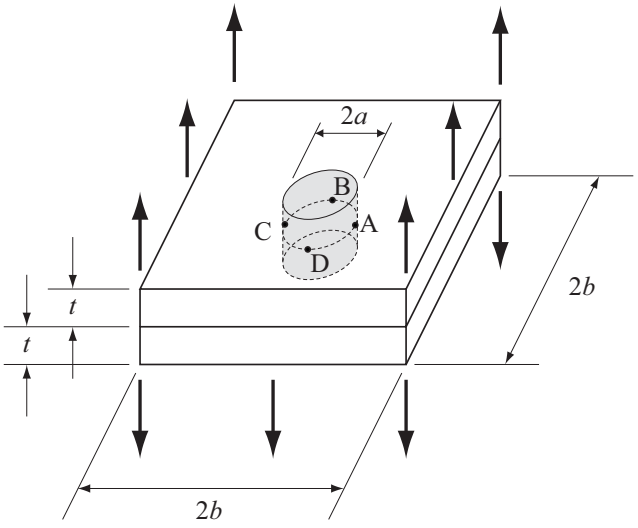

(b)

Figure 4.1. (a) A schematic of a cross-tension specimen and (b) a schematic of two square plates with connection or spot weld under opening and bending loading conditions.

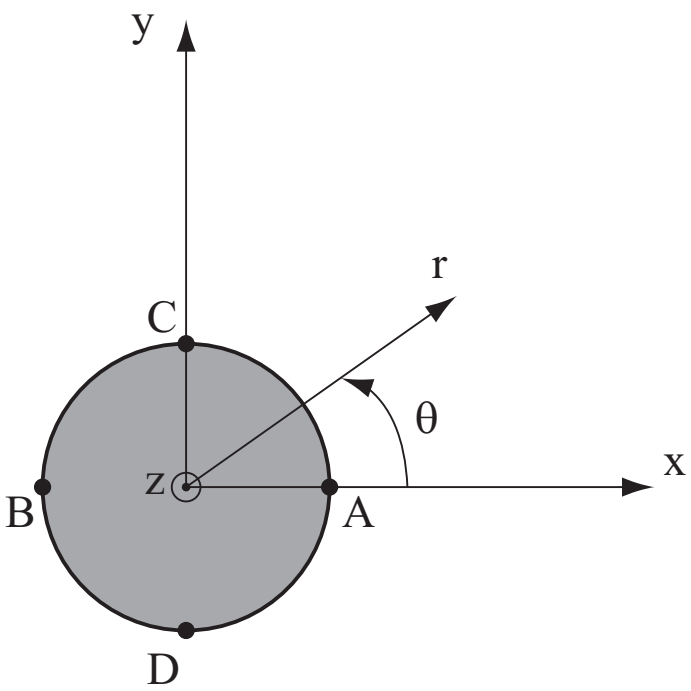

Figure 4.2. A schematic of a top view of the connection or spot weld (idealized as a rigid inclusion) in the upper plate of the specimen.

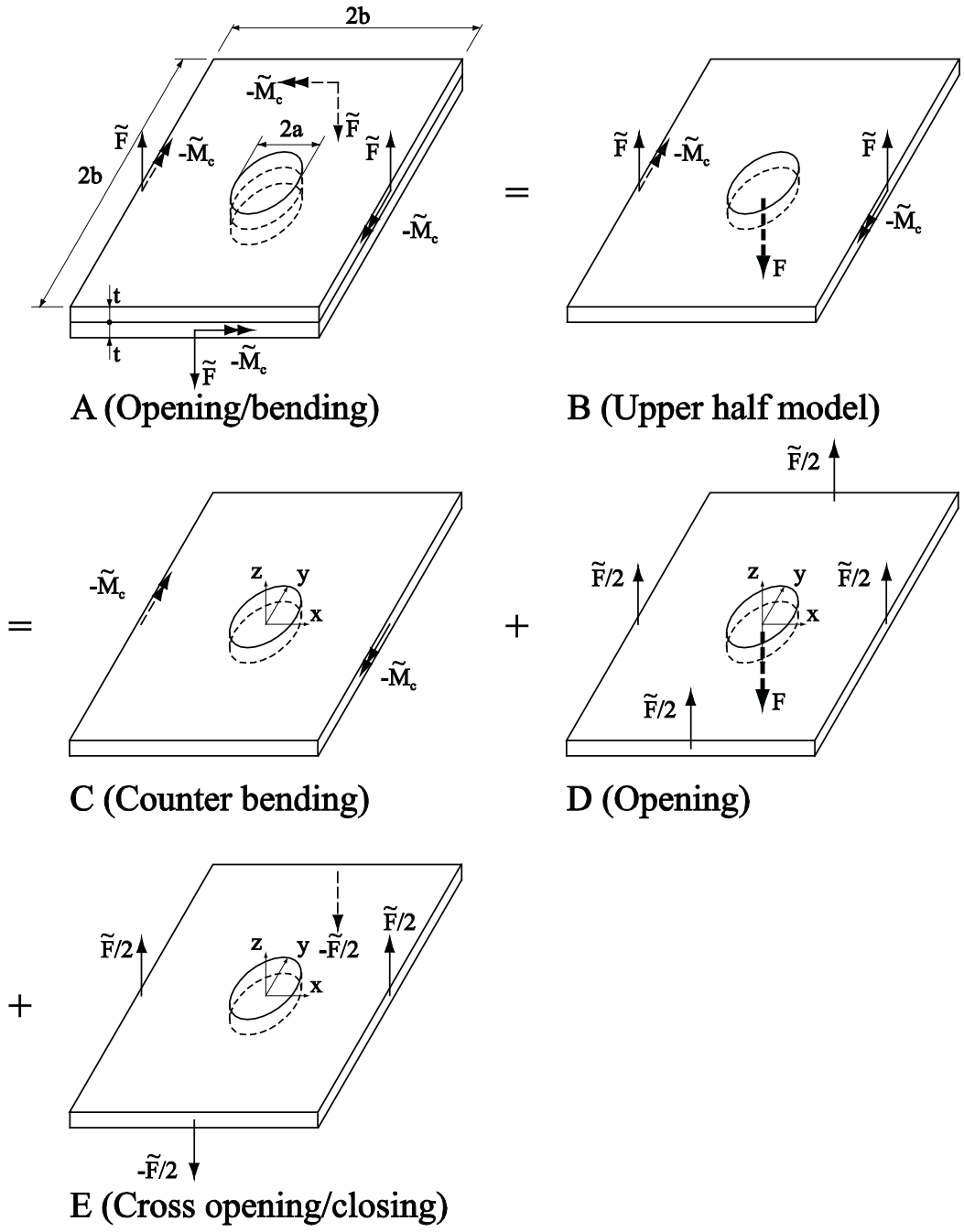

Figure 4.3. Decomposition of the load of a cross-tension specimen. Model A represent a spot weld in the central square part of a cross-tension specimen under opening loading conditions. Model B represents the upper half of model A. The forces of model B are approximately decomposed into three types of loads: counter bending (model C), opening (model D), and cross opening / closing (model E).

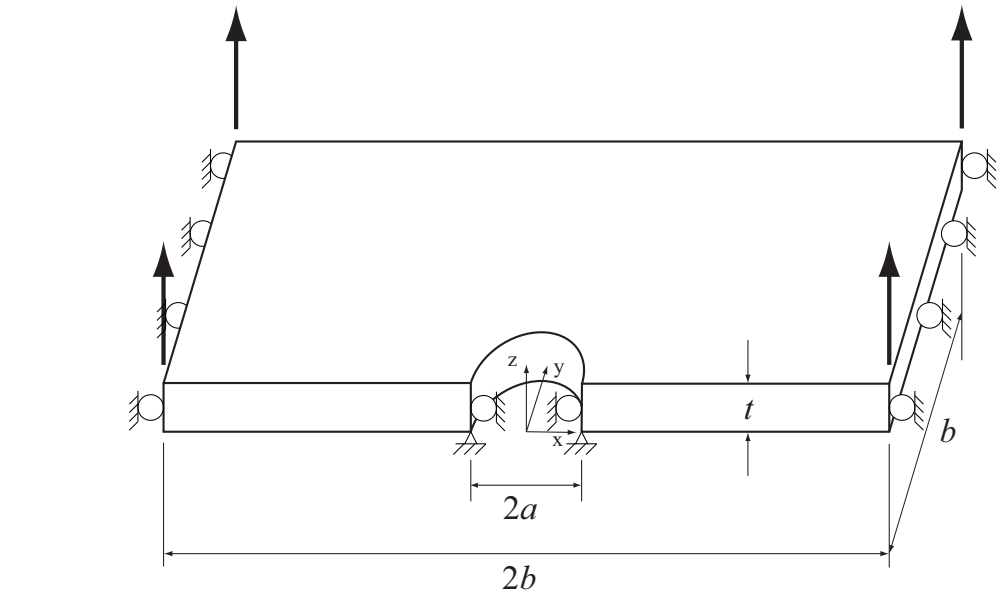

(a)

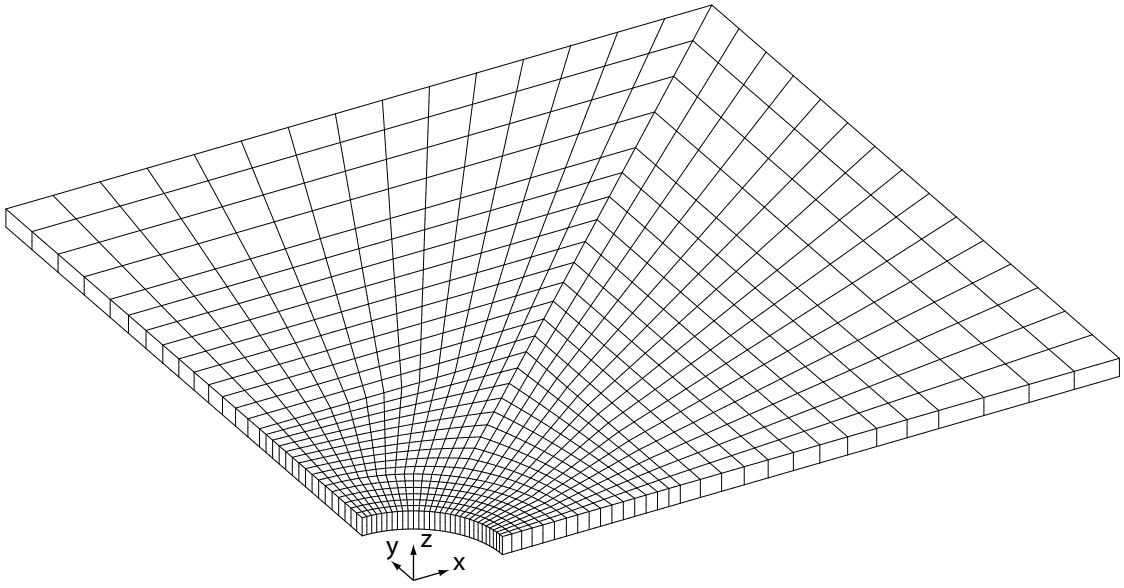

(b)

Figure 4.4. (a) A schematic of a three-dimensional finite element model of a square plate with a rigid inclusion under a uniform out-of-plane displacement and the roller boundary conditions at the two opposite outer edges. (b) A mesh of a three-dimensional finite element model for $b/a = 7.94$.

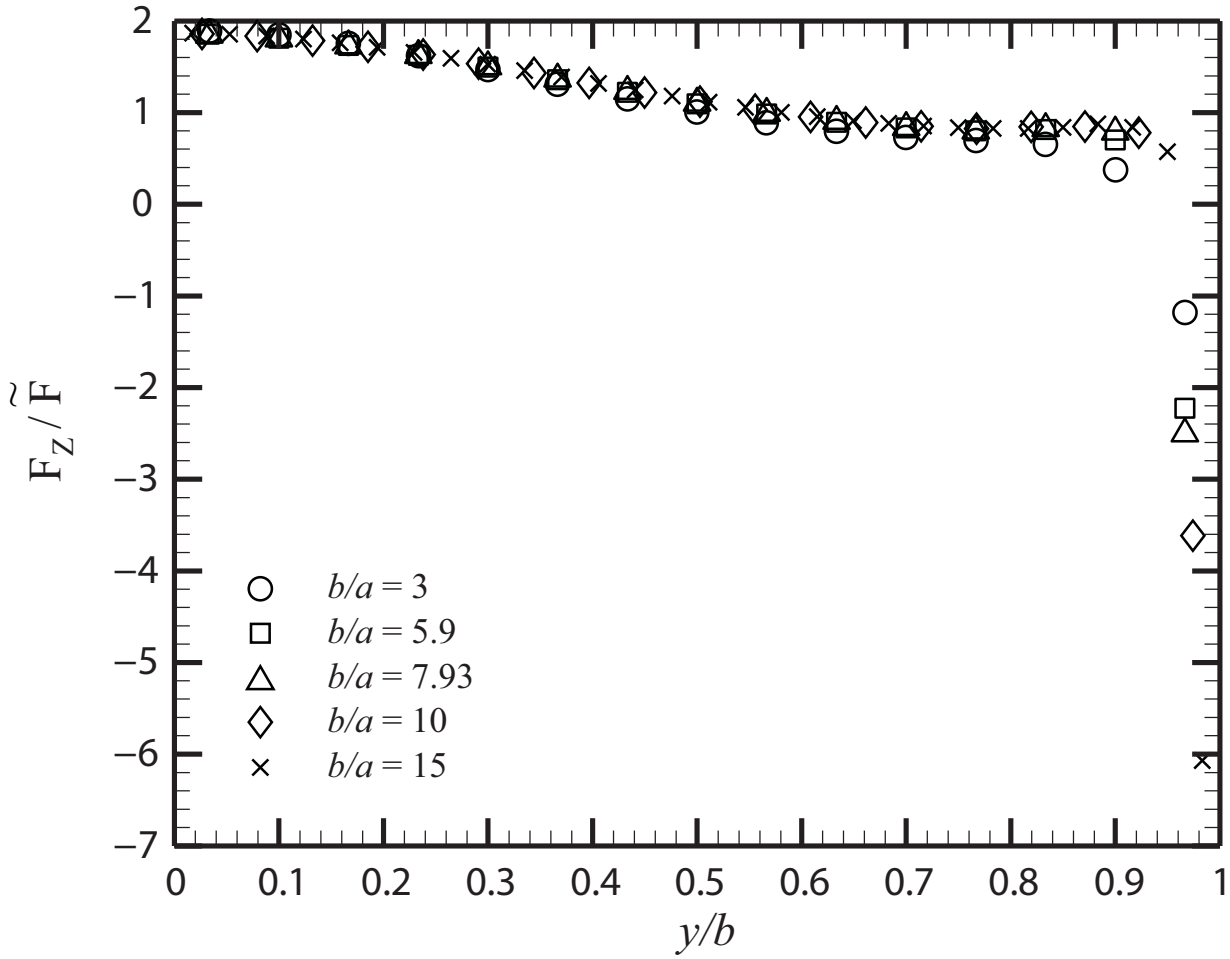

Figure 4.5. The distributions of the opening force per unit length along the width of the square plate with a rigid inclusion.

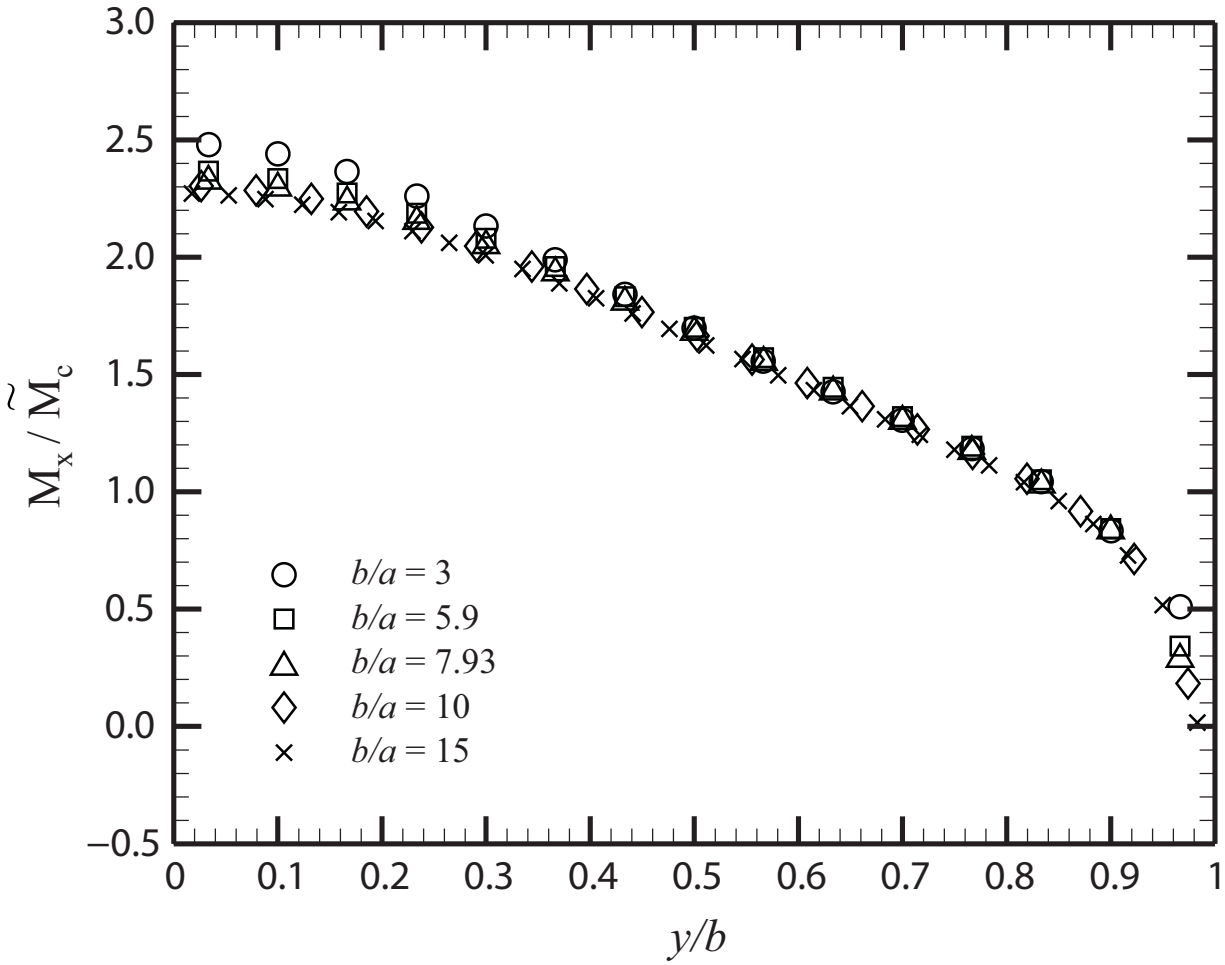

Figure 4.6. The distributions of the constraint moment per unit length along the width of the square plate with a rigid inclusion.

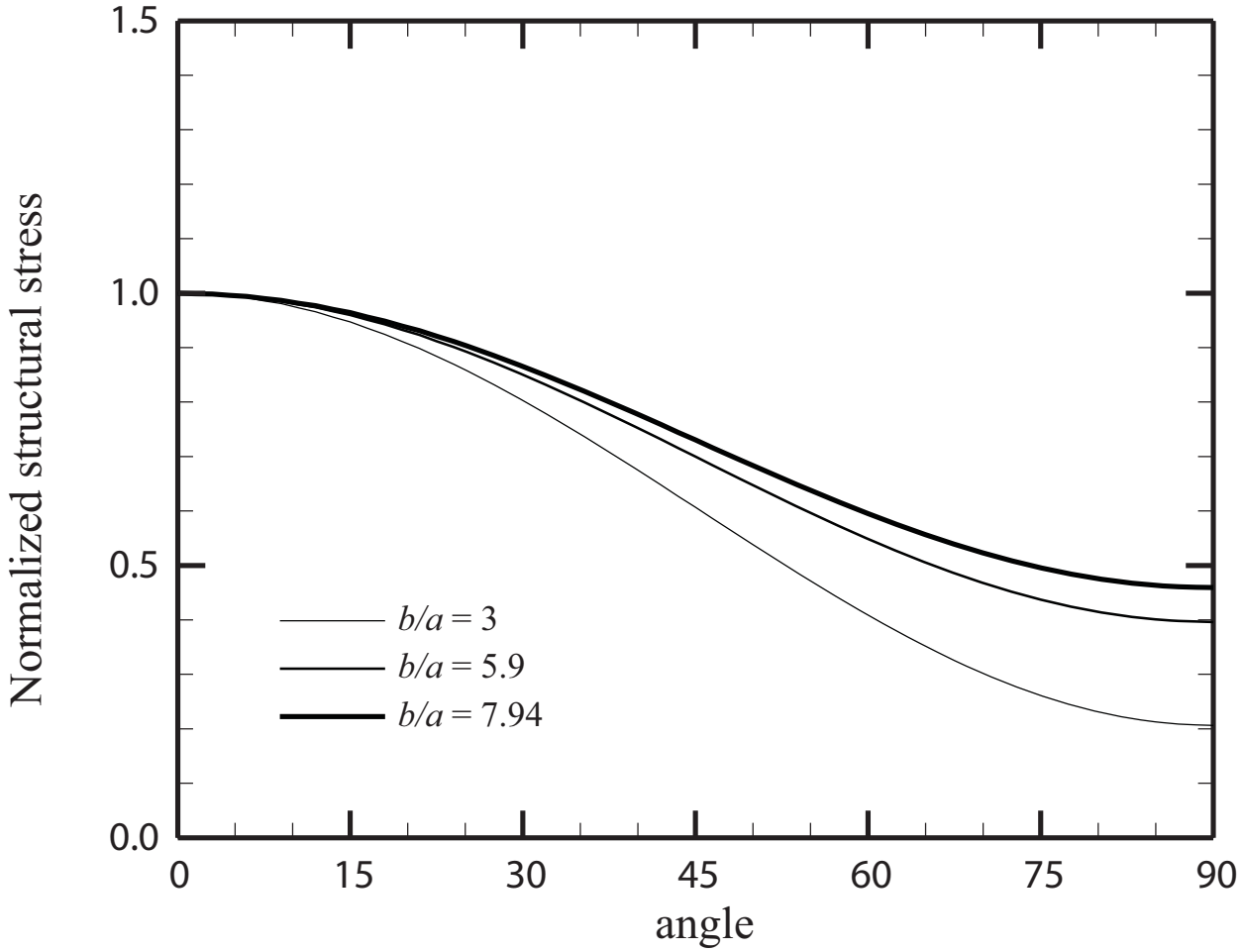

Figure 4.7. The normalized structural stress distributions along the circumference of a rigid inclusion for selected ratios of the plate width to the rigid inclusion diameter, b/a .

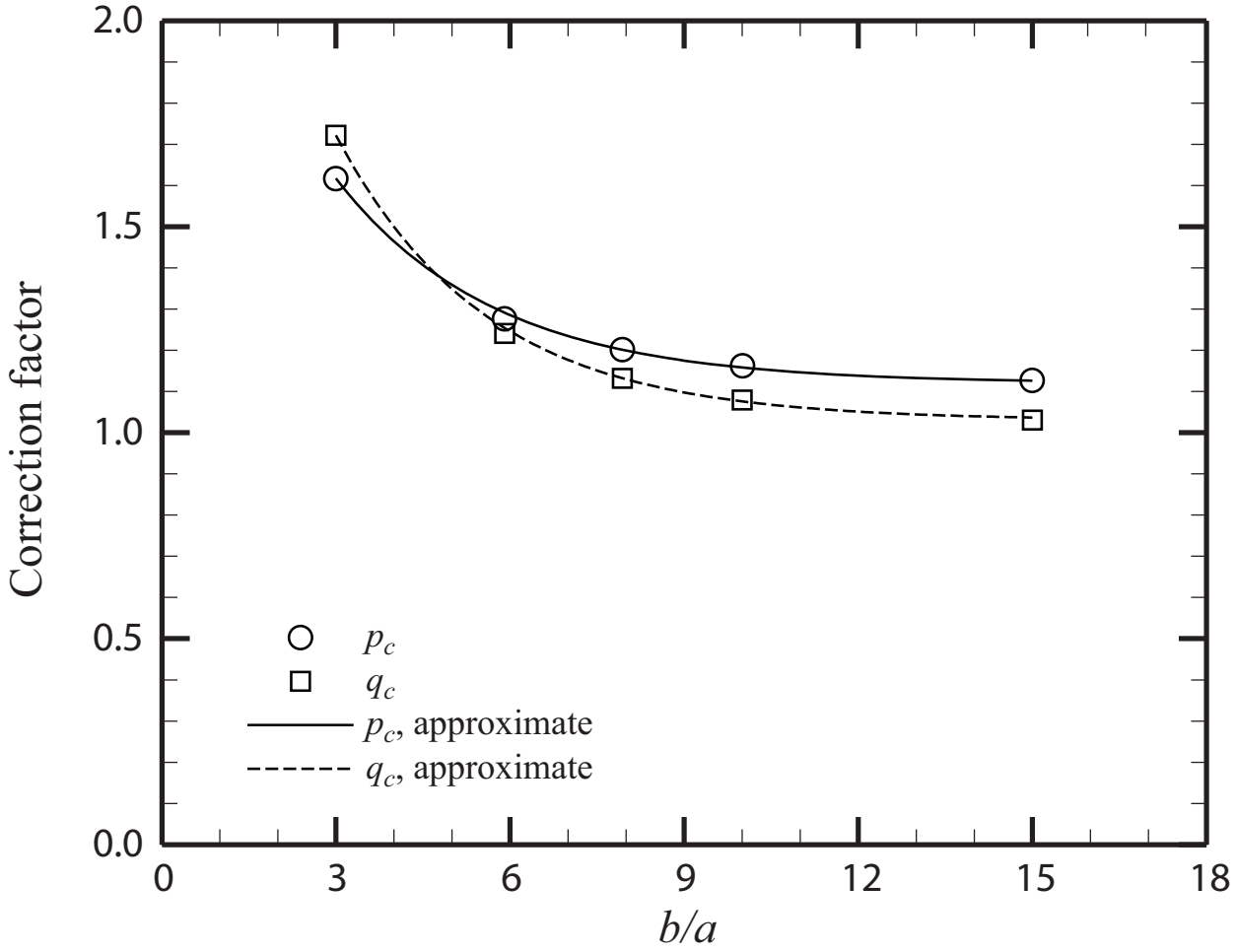

Figure 4.8. The values of the equivalent coefficients p_c and q_c as functions of the ratio of the plate width to the rigid inclusion diameter, b/a.

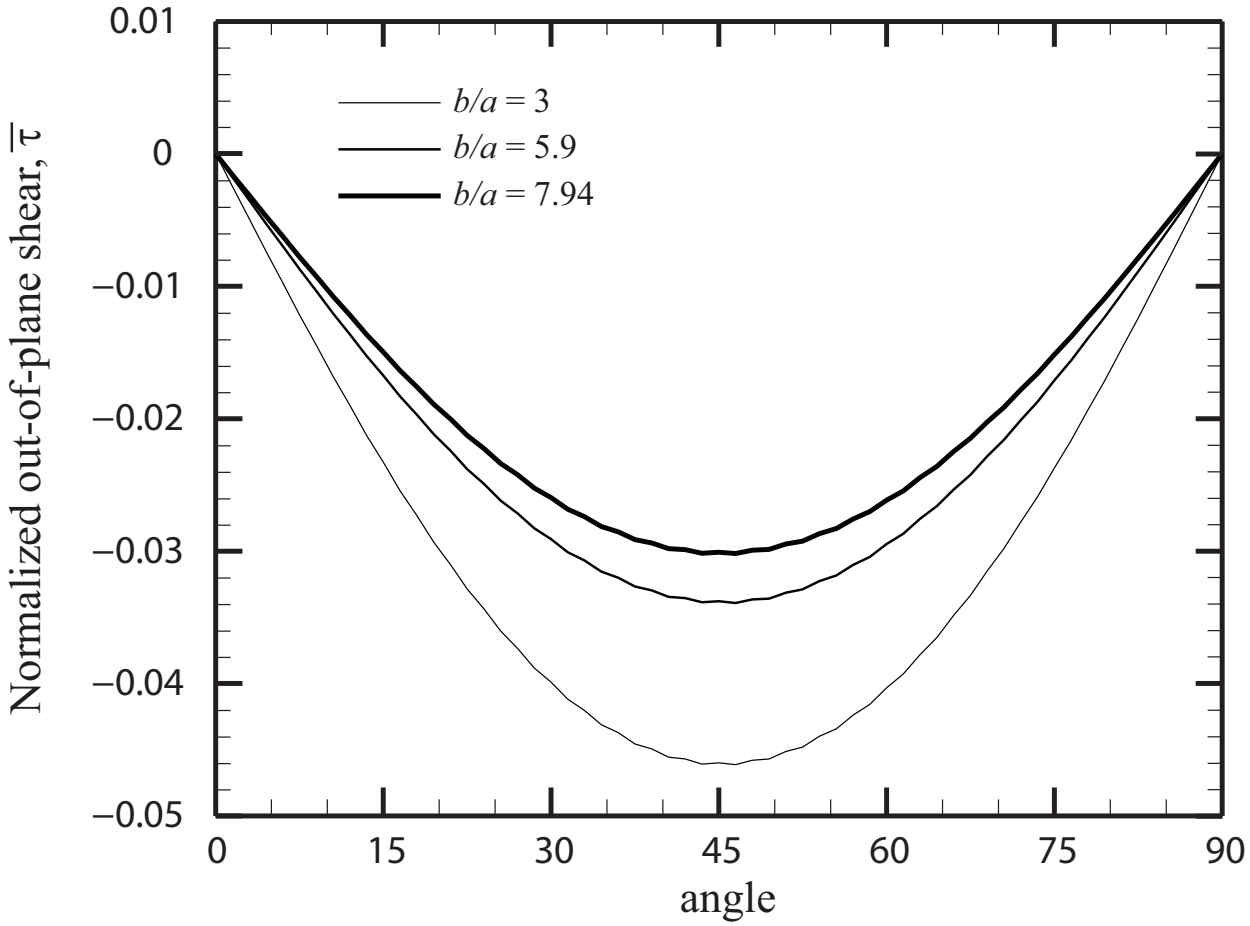

Figure 4.9. The normalized out-of-plane shear stress distributions along the circumference of a rigid inclusion for selected ratios of the plate width to the rigid inclusion diameter, b/a .

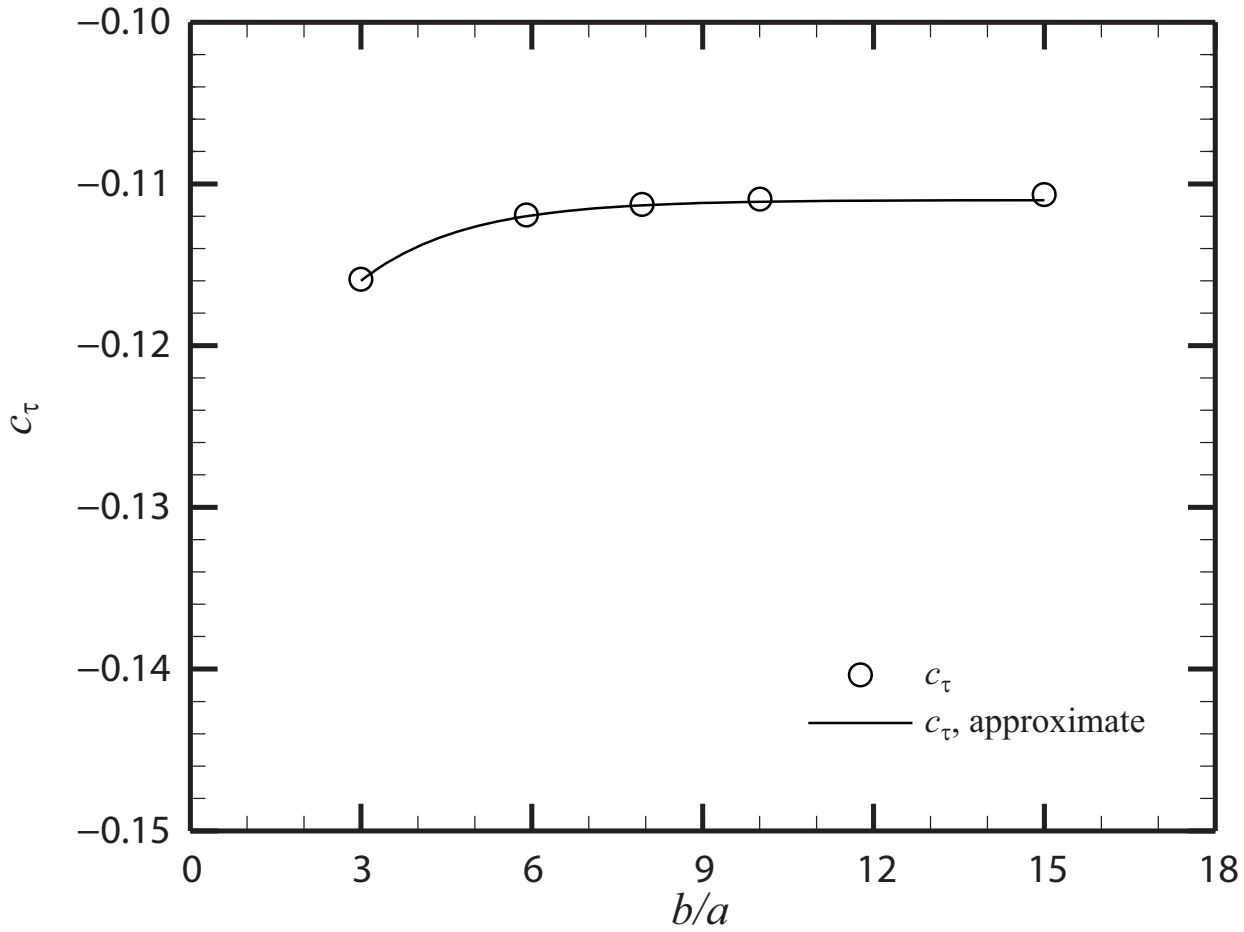

Figure 4.10. The numerical coefficient c_τ as a function of the ratio of the plate width to the rigid inclusion diameter, b/a.

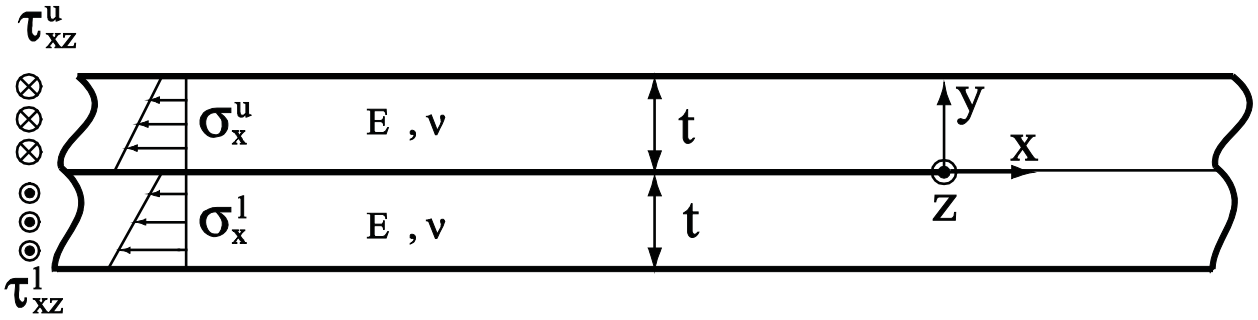

(a)

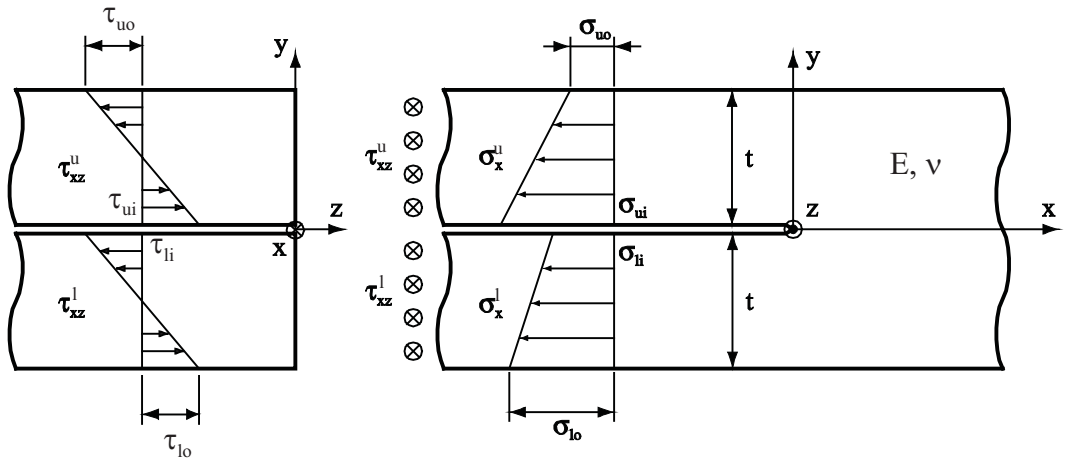

(b)

Figure 4.11. (a) A two-dimensional model of two infinite strips made of same thickness and material with connection under plane strain conditions and (b) the front and side views of the left half of the strip model near the crack tip.

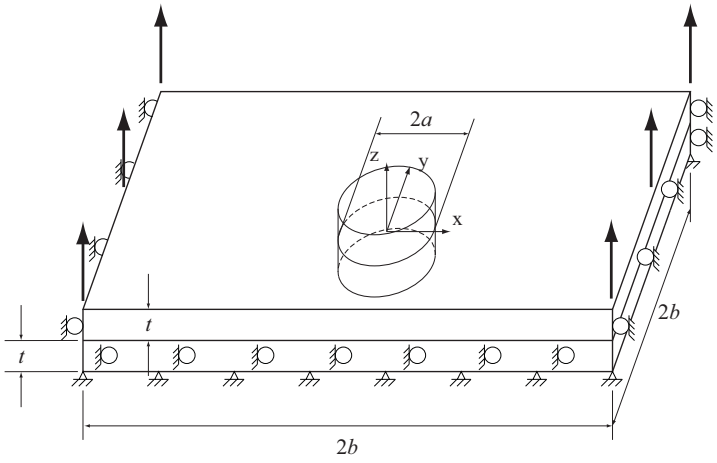

(a)

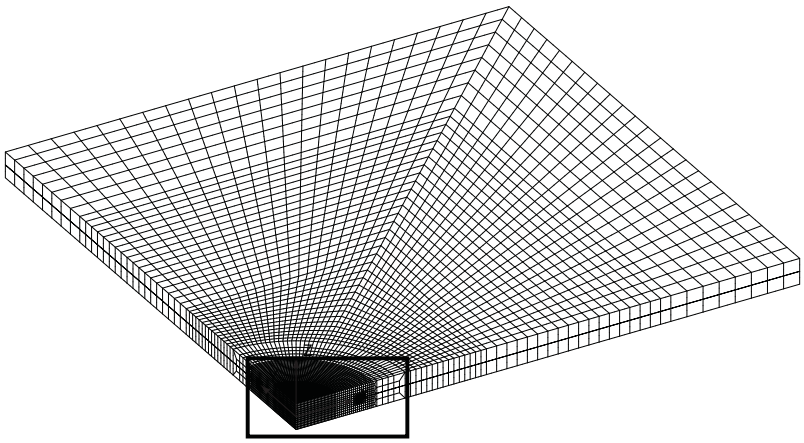

(b)

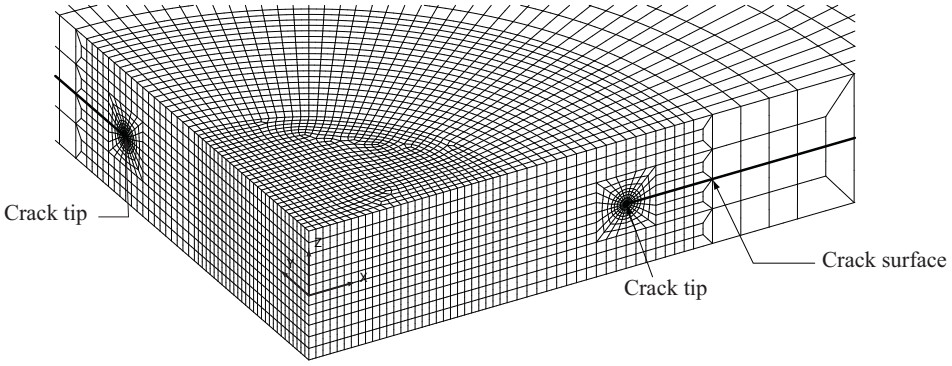

(c)

Figure 4.12. (a) A schematic of a three-dimensional finite element model of two square plates with connection under a uniform applied displacement and the roller boundary conditions. (b) A mesh of a three dimensional finite element model for $b/a = 7.94$ and (c) a close-up view of the mesh near the main crack front for model in (b).

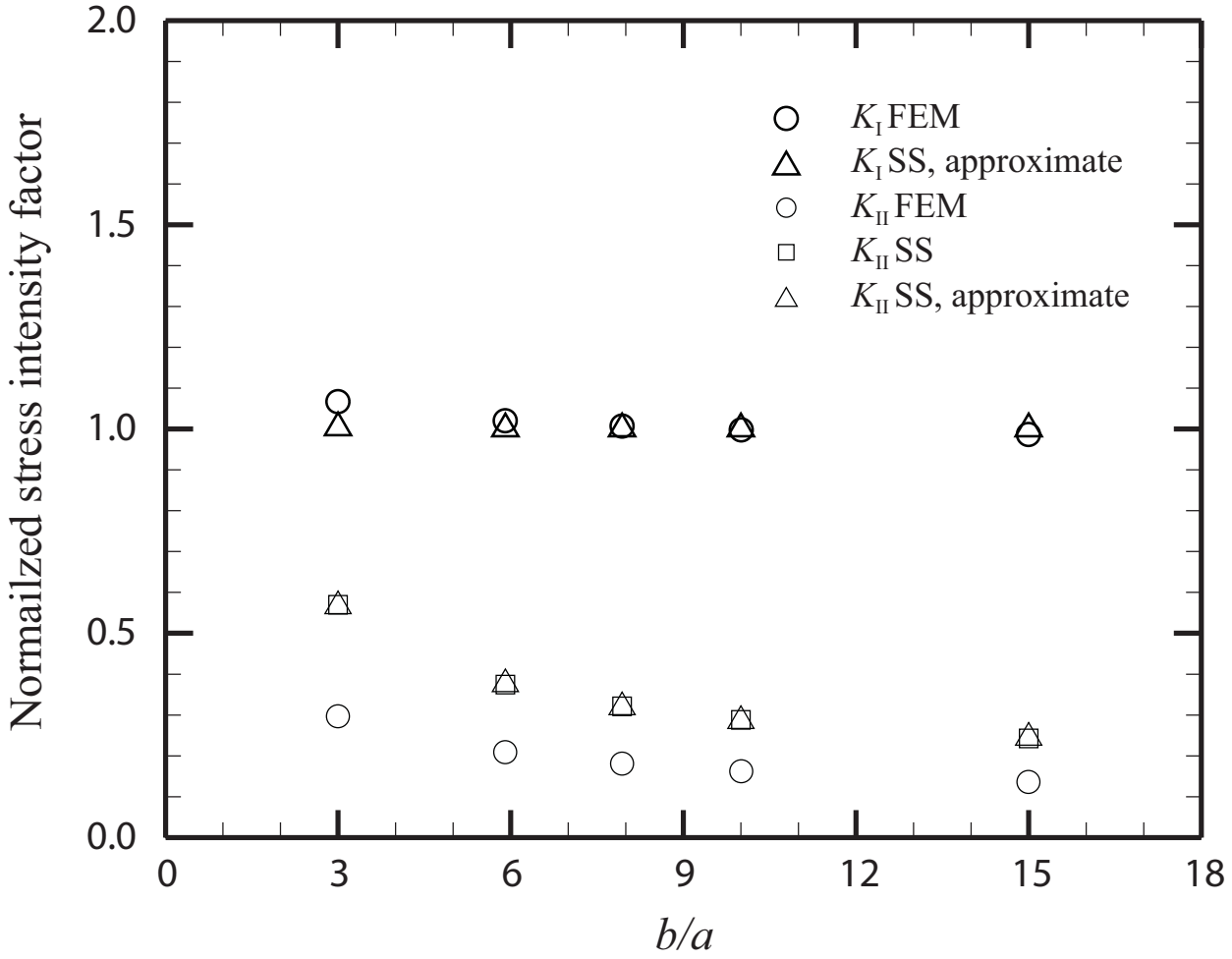

Figure 4.13. The normalized stress intensity factor K_{I} and K_{II} solutions at the critical location point A for various ratios of the plate width to the connection diameter, b/a .

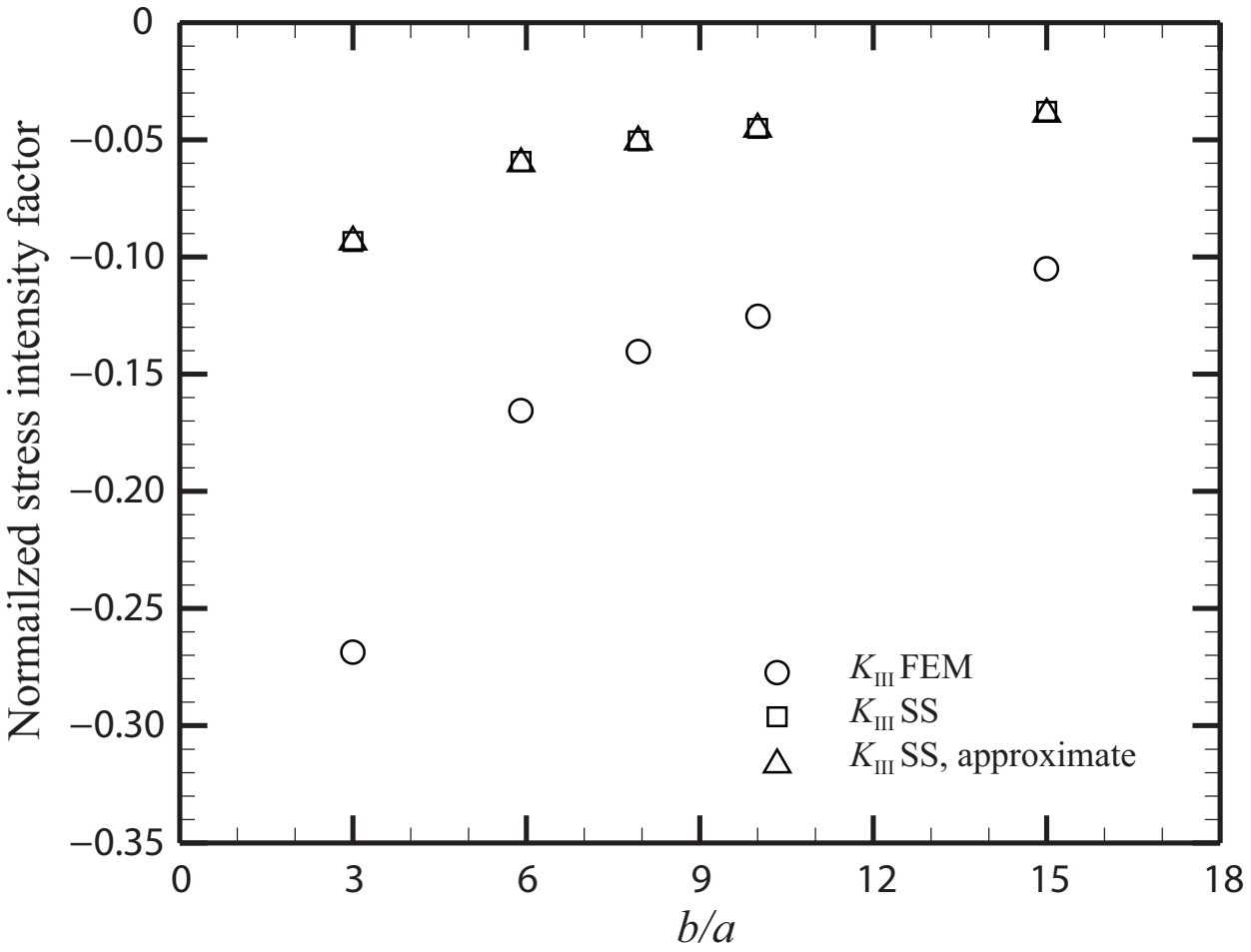

Figure 4.14. The normalized stress intensity factor K_{III} solutions at the angle of 45° from the critical location point A for various ratios of the plate width to the connection diameter, b/a .

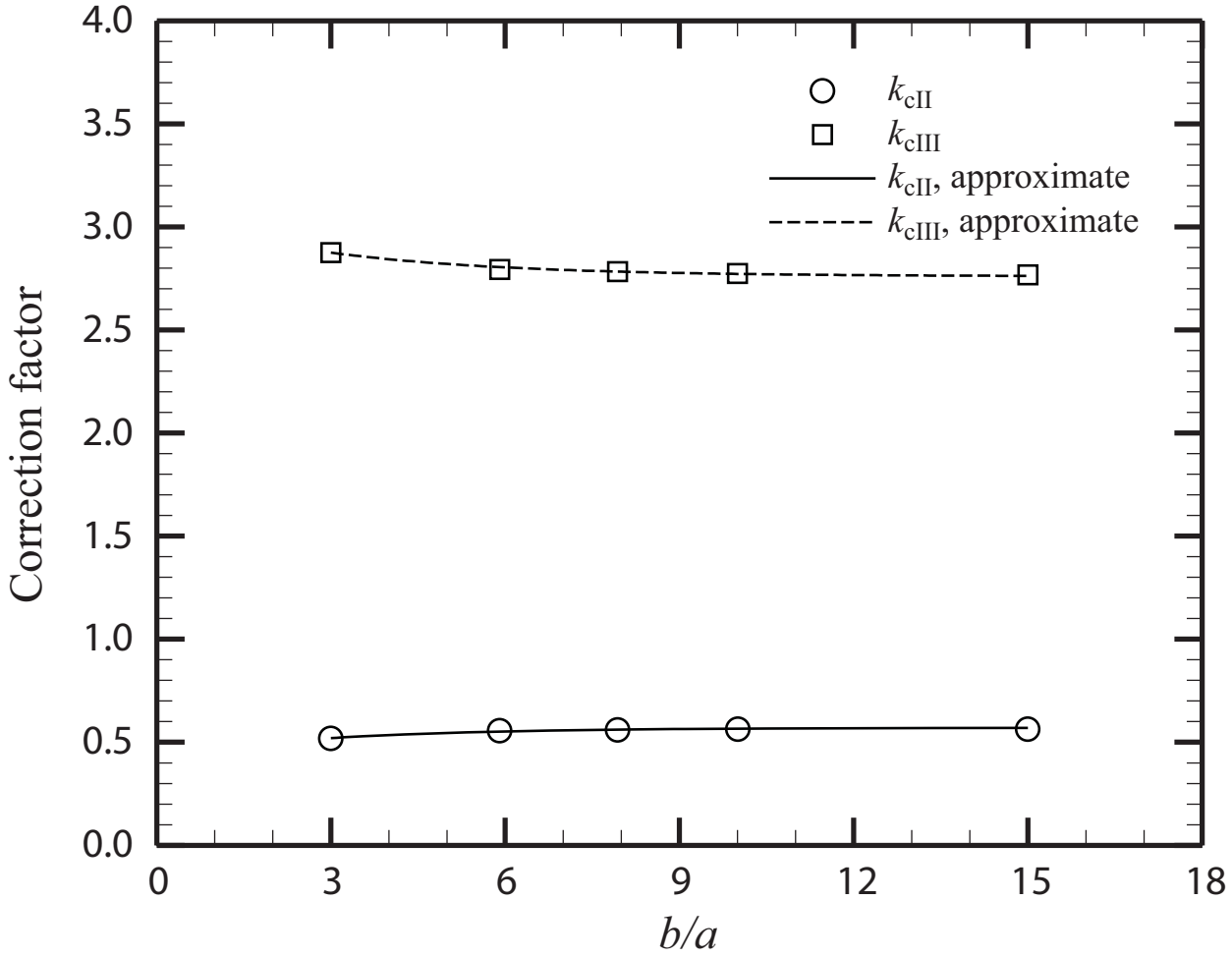

Figure 4.15. The values of the fitting coefficients k_{cII} and k_{cIII} for the stress intensity factor solutions accounting for the flexibility of the spot welds as functions of the ratio of the plate width to the connection diameter, b/a.

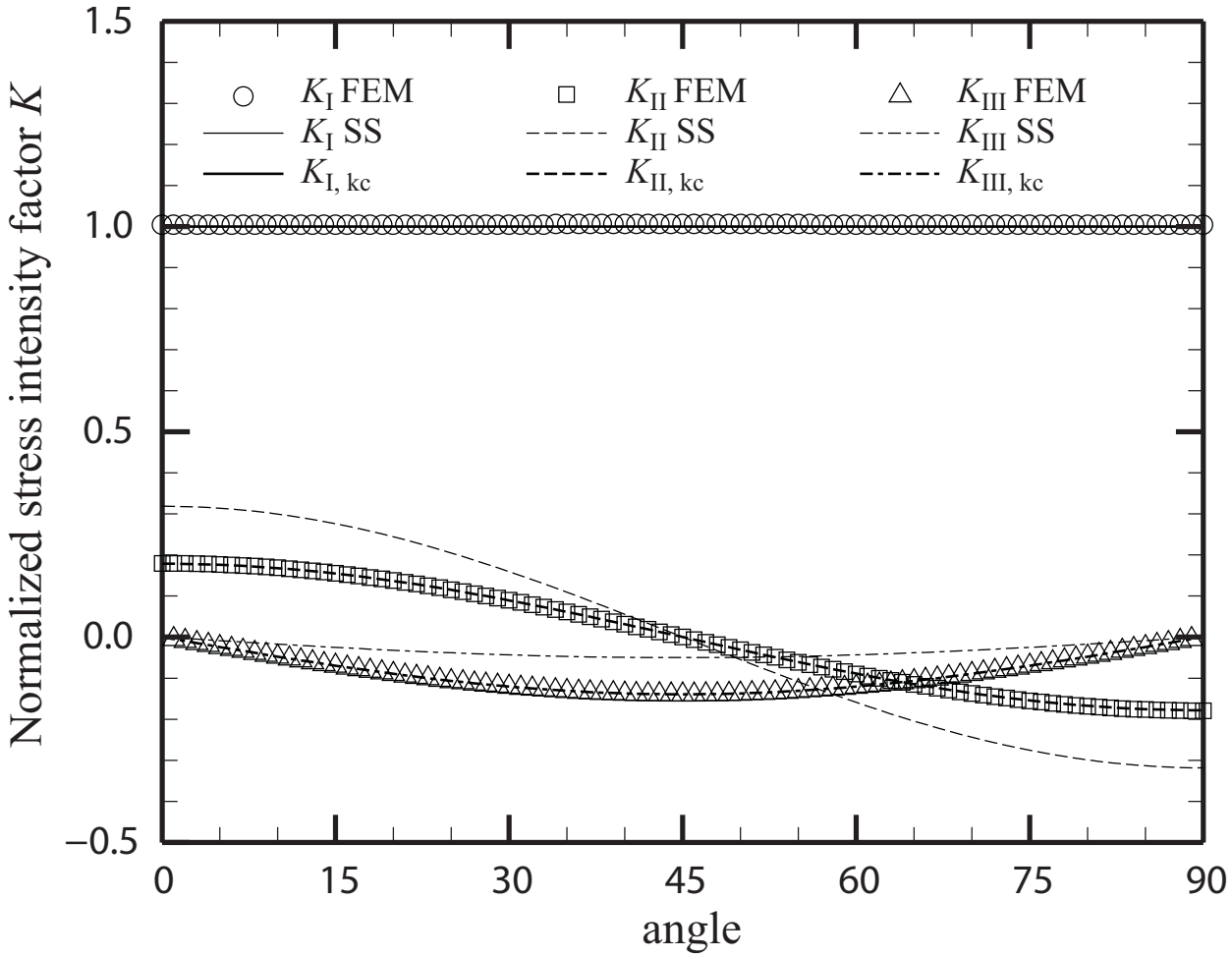

Figure 4.16. The distributions of the normalized computational and analytical stress intensity factor K_{I}, K_{II} and K_{III} solutions, and the analytical stress intensity factor $K_{\mathrm{I,kc}}$, $K_{\mathrm{II,kc}}$ and $K_{\mathrm{III,kc}}$ solutions based on the structural stress solutions with the fitting coefficients for $b/a = 7.94$. The values of the equivalent, numerical and fitting coefficients are listed in Table 1 and Table 4, respectively.

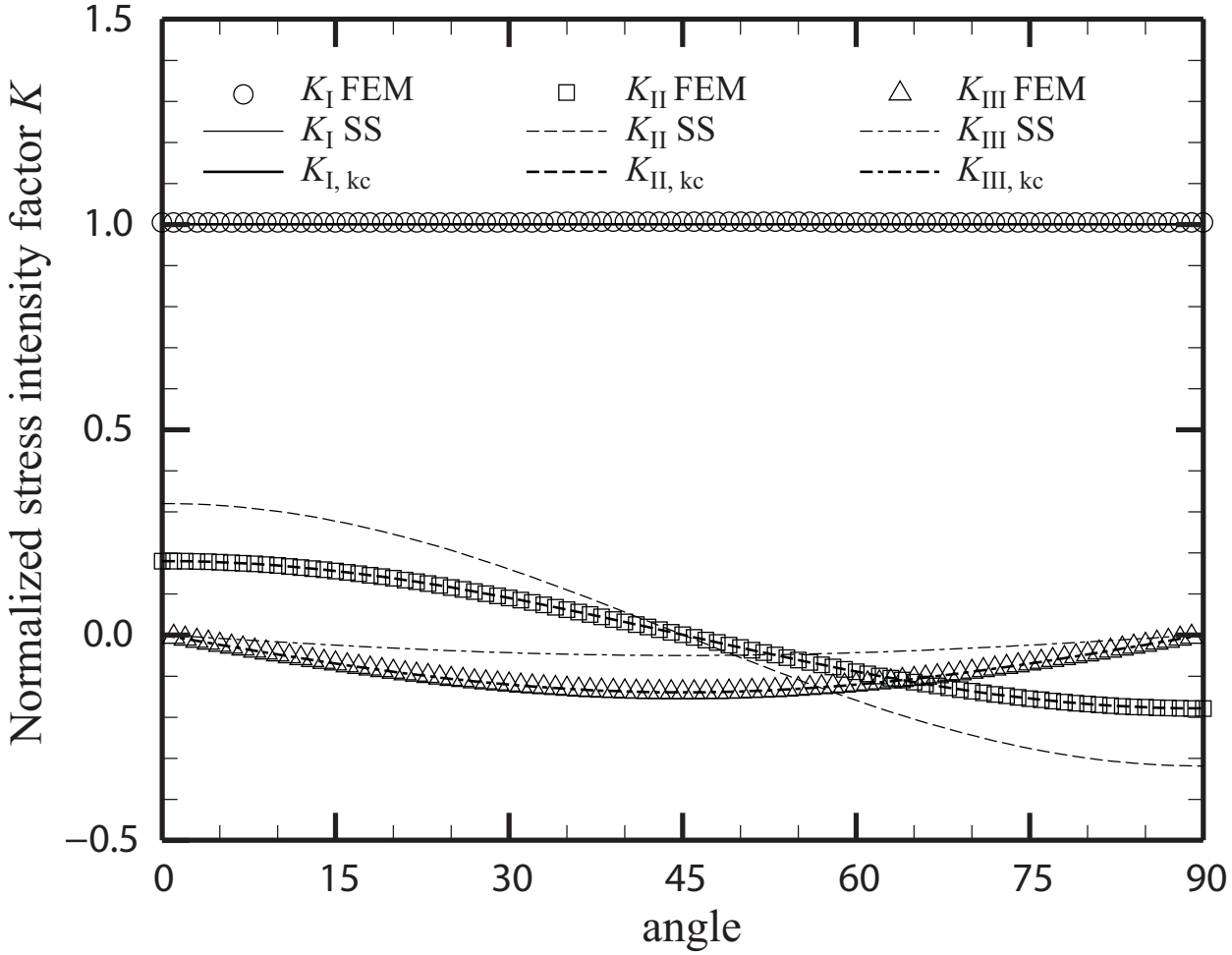

Figure 4.17. The distributions of the normalized computational and analytical stress intensity factor K_{I}, K_{II} and K_{III} solutions, and the analytical stress intensity factor $K_{\mathrm{I,kc}}$, $K_{\mathrm{II,kc}}$ and $K_{\mathrm{III,kc}}$ solutions based on the structural stress solutions with the fitting coefficients for $b/a = 7.94$. The equivalent, numerical and fitting coefficients and the equivalent radius are based on the approximate equations.

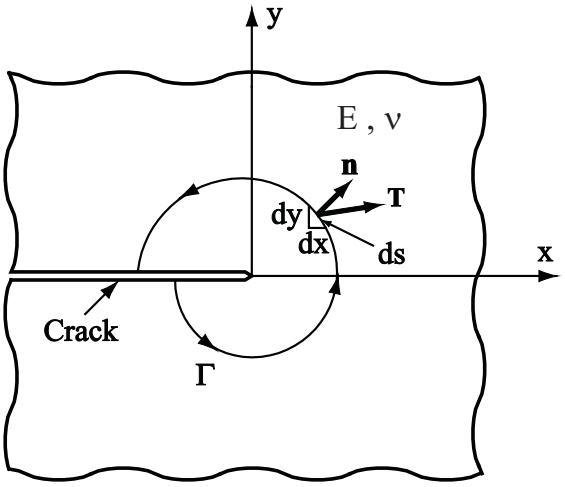

(a)

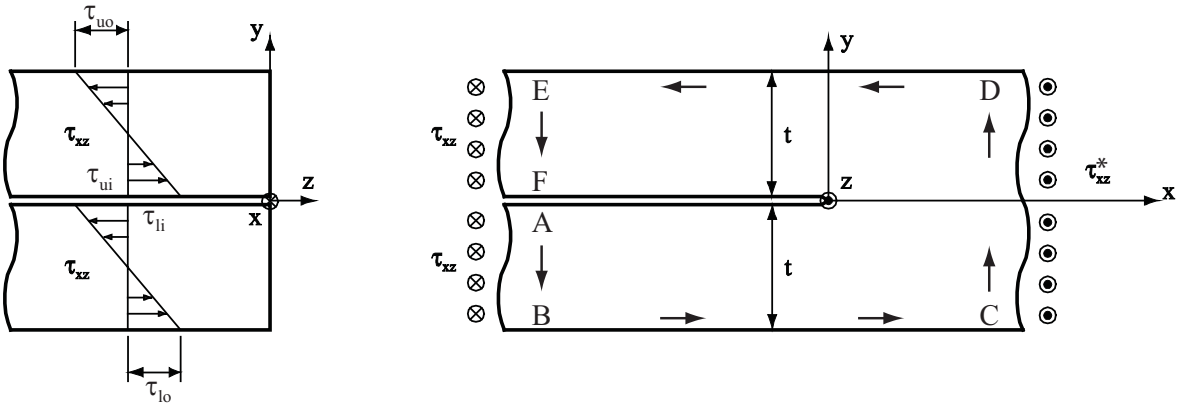

(b)

Figure 4.A1. (a) A crack with contour Γ surrounding a crack tip and (b) the front and side views of the left part of the strip model near the crack tip.

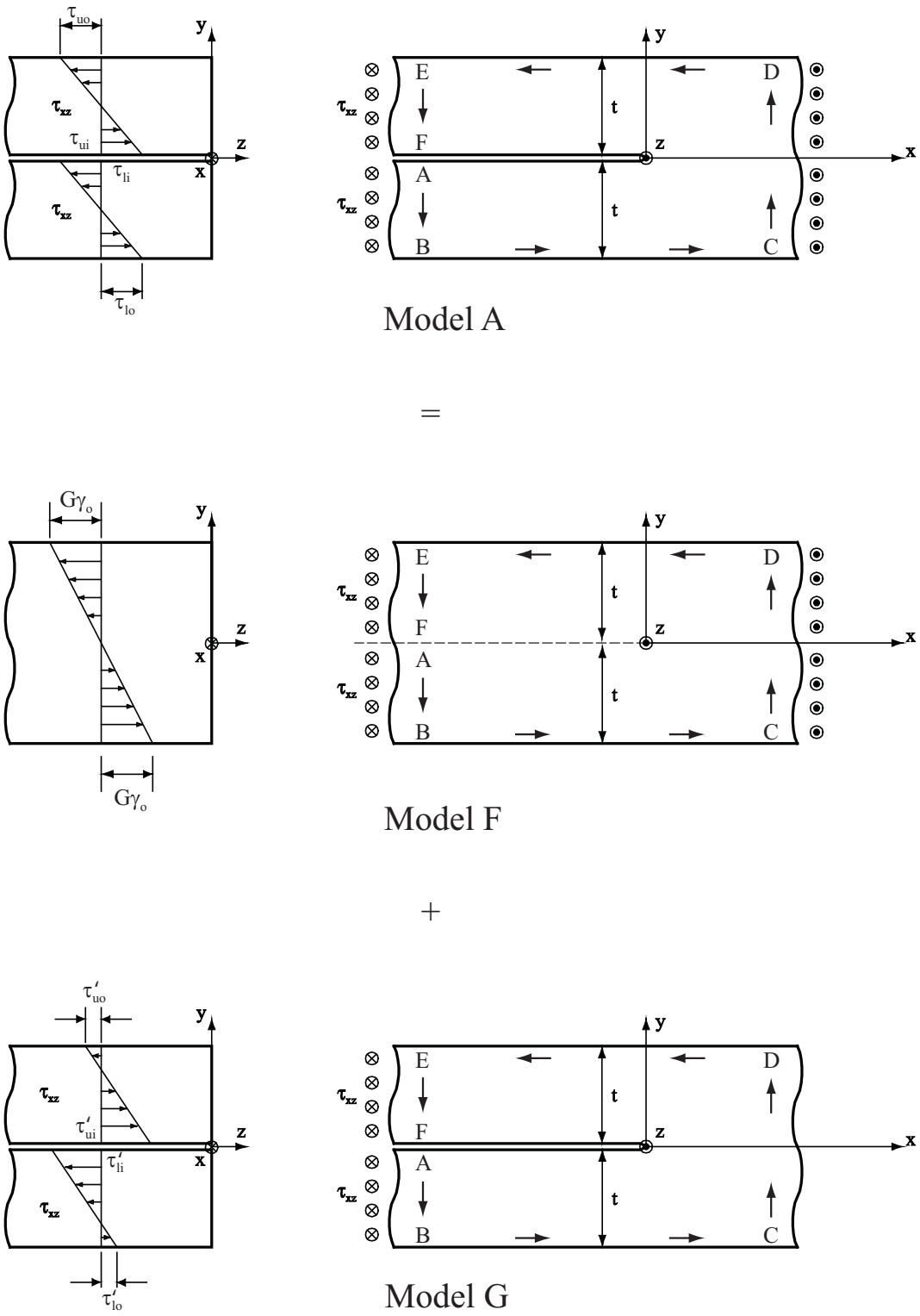

Figure 4.A2. The decomposition of the out-of-plane shear stress distribution of a strip model. Model A represents a spot weld under an out-of-plane shear loading condition. The out-of-plane shear loading condition of model A is decomposed into the loading conditions of models F and G.

CHAPTER V

STRESS INTENSITY FACTOR SOLUTIONS FOR SPOT WELDS IN SQUARE OVERLAP PARTS OF CROSS-TENSION SPECIMENS OF DIFFERENT THICKNESSES AND MATERIALS

5.1. Introduction

Resistance spot welding is widely used to join sheet metals in the automotive industry. The fatigue lives of spot welds have been investigated by many researchers. Due to the geometry of spot welds, natural crack tips or notch tips are presented along the nugget circumference. Stress intensity factor solutions for spot welds at the critical locations in various types of specimens have been developed to investigate the fatigue lives of spot welds. Pook [1, 2] gave the maximum stress intensity factors for spot welds in lap-shear, coach-peel specimens, circular plate, and other bending dominant plate and beam configurations. Radaj [3] and Radaj and Zhang [4-6] established the foundation to use the structural stress solutions to determine the stress intensity factor solutions for spot welds. Zhang [7, 8] obtained the stress intensity factor solutions at the critical locations of spot welds in various types of specimens in order to correlate the experimental results of spot welds in these specimens under cyclic loading conditions. Pan and Sheppard [9] investigated the stress intensity factor solutions for both the main cracks and the kinked cracks in lap-shear and modified coach peel specimens by finite element analyses. Wang et al. [10, 11] and Lin et al [12] proposed new stress intensity factor solutions for square-

cup and lap-shear specimens and the solutions were validated by their three-dimensional finite element analyses. Lin and Pan [13, 14] proposed the closed-form structural stress and stress intensity factor solutions for spot welds in various types of specimens.

Pook [2] indicated that for a class of transversely loaded configurations consisting of two thin plates or beams joined over part of their common plane under symmetric loading conditions, the stress intensity factor at a crack tip depends on the bending moment acting to the beam or plate in the vicinity of the crack tip. Wang et al. [10] conducted three-dimensional finite element analyses of circular plates with connection under opening loading conditions. The computational results indicate that the stress intensity factor along the crack front can be correlated very well with the analytical solutions based on the bending moments or the corresponding structural stresses for thin plates with connection. The close-form solutions for thin plates with rigid inclusions under shear, central bending, counter bending, and opening loading conditions were obtained by Muskhelishvili [15], Goland [16], Timoshanko and Woinowsky-Krieger [17], Lin et al. [12] and Lin and Pan [13], respectively. The classical solutions of Muskhelishvili [15], Goland [16], Timoshanko and Woinowsky-Krieger [17] were obtained from the complex variable approach and the Kirchhoff plate theory. The Lin and Pan [13] solutions were obtained from the Airy stress function and the Kirchhoff plate theory.

For the stress intensity factor solutions for spot welds in cross-tension specimens, Lin and Lin [18] indicates that as the effective specimens length increases, the trends of the stress intensity factor solutions based on the closed-form structural stress solutions of Lin and Pan [13] agree quite well with the computational results. However, when the effective length of the specimens is equal to the specimen width, the stress intensity

factor solutions based on the closed-form structural stress solutions of Lin and Pan [13] overestimated the computational result by about 20%. Note that, the structural stress solutions of Lin and Pan [13, 14] are based on the superposition of the solutions for a rigid inclusion in a square plate under opening loading and counter-bending loading conditions. Therefore, the main purpose of this investigation is to determine the source of this 20% overestimation. Furthermore, in order to examine the accuracy of the analytical structural stress and stress intensity factor solutions for spot welds in lap-shear, square-cup, U-shape, cross-tension and coach-peel specimens presented in Lin and Pan [13, 14], it is necessary to first examine carefully the analytical solutions for the square overlap parts of these specimens.

The structural stress and stress intensity factor solutions for spot welds between dissimilar sheets are also quite important. For example, in a modern multi-material vehicle, lightweight materials such as aluminum, magnesium and advanced high strength steel sheets must be joined to the underlying substructure, which is usually composed of the conventional steel. Therefore, the stress intensity factor solutions along the circumference of spot welds between dissimilar sheets are of interest for future vehicle durability considerations. For lithium-ion batteries in electric or hybrid vehicle, electrodes are made of aluminum and copper sheets. Therefore, the stress intensity factor solutions for spot welds between aluminum and copper sheets are also of interest for the durability consideration of lithium-ion batteries. Tran and Pan [19] recently presented analytical stress intensity factor solutions for spot welds in lap-shear specimens of different thicknesses and materials in the normalized form for convenient engineering applications. In this chapter, analytical stress intensity factor solutions for spot welds in

square plates of different thicknesses and materials under opening loading conditions will also be presented in the normalized form for convenient engineering applications.

In this chapter, the J integral and analytical stress intensity factor solutions for spot welds in the square overlap parts of cross-tension specimens of different thicknesses and materials are developed. First, the analytical structural stress solutions for a rigid inclusion in a square plate under opening and bending loading conditions are reviewed. Then, the J integral and stress intensity factor solutions for spot welds between square plates are presented in terms of the structural stresses for a strip model. With the available structural stress solutions, the analytical J integral and stress intensity factor solutions can be obtained. The analytical stress intensity factor solutions are selectively compared with the results of three-dimensional finite element analyses for spot welds between square plates under opening and bending loading conditions. Complete sets of the normalized stress intensity factor solutions at the critical locations for combinations of steel, aluminum and magnesium sheets of different thicknesses and combinations of aluminum and copper sheets of different thicknesses are presented for convenient engineering applications.

5.2. Analytical structural stress solution for a rigid inclusion in a square plate

Lin and Pan [13, 14] presented closed-form structural stress solutions for spot welds in cross-tension and U-shape specimens. The solutions are based on the superposition of the structural stress solutions for a rigid inclusion in a square plate based on the Kirchhoff plate theory. Figure 5.1(a) shows a schematic of a cross-tension specimen of unequal thicknesses. The upper sheet of the specimen has the thickness t_u and the lower sheet of

the specimen has the thickness t_l. Both upper and lower sheets have the width $2b$. The spot weld is shown as the light shaded area and has the diameter $2a$. The overlapped part of the specimen is marked by dashed lines. The dark shaded area shows the area clamped by fixtures and subjected to a uniform out-of-plane displacement. Since the parts of the sheets clamped by the fixtures have no contribution to the bending moment applied to the spot weld, the length of the central effective portion is therefore denoted as the effective specimen length $2l$. When the specimen effective length reduces to the specimen width ($2l = 2b$), cross-tension specimens in Figure 5.1(a) can be modeled as two square plates with connection or spot weld subjected to a uniform out-of-plane displacement as shown in Figure 5.1(b). Figure 5.1(b) shows a schematic of two square plates with connection or spot weld. Both plates have the width $2b$. The upper plate has the thickness t_u and the lower plate has the thickness t_l. The connection or spot weld is shown as the shaded area and has the diameter $2a$. Both plates are subjected to a uniform out-of-plane or opening displacement along the two opposite outer edges as shown schematically as bolded arrows. Points A, B, C and D indicate the critical locations of the connection or spot weld. The material of the upper plate and lower plate can be either identical or dissimilar.

Lin and Pan [13, 14] treated the spot weld in a cross-tension specimen as a rigid inclusion and assumed that the inclusion is perfectly bonded to the neighboring plate materials in the derivations of the closed-form structural stress solutions. Figure 5.2 shows a schematic of a top view of the connection or spot weld (idealized as a rigid inclusion) in the upper plate of the specimen with the cylindrical and Cartesian coordinate systems centered at the center of the upper half of the spot weld. The critical

locations of points A, B, C and D are 0°, 180°, 90° and 270° with respect to the x axis, respectively. The critical locations of points A, B, C and D can also be seen in Figure 5.1(b). The orientation angle θ represents the angular location along the circumference of the spot weld. Note that the angle θ is measured from the x axis to y axis in counter-clockwise sense.

For spot welds between square plates under opening and bending loading conditions, the structural stress solutions of the upper and lower plates can be approximately decomposed into three types of loads according to the superposition principle (Lin and Pan [13, 14]). Figure 5.3 shows the decomposition of the loads of the square overlap part of a cross-tension specimen. Model A represents a spot weld in the square overlap part of a cross-tension specimen. Both upper and lower plates are subjected to uniform opening force per unit length $\tilde{F}$ and uniform constraint moment per unit length $\tilde{M}_{\mathrm{c}}$. Model B represents the upper half of model A. In model B, F represents the resultant opening forces applied to the center of circular interfacial of the spot weld. The forces and moments in model B can be approximately decomposed into three types of loads: counter bending (model C), opening (model D) and cross opening / closing (model E) that can be approximated as a twisting loading condition. Based on the closed-form structural stress solutions of Lin and Pan [13, 14], Sripichai and Pan [20] presented the structural stress solution for a rigid inclusion under opening and bending loading conditions as

$$\sigma = G + H\cos 2\theta \tag{5.1}$$

where G is the constant term of the structural stress solutions and can be expressed in the closed-form as

$$G = A + B \tag{5.2}$$

Similarly, H is the amplitude of the cosine function of the structural stress solutions and can be expressed in the closed-form as

$$H = C + D \tag{5.3}$$

$$A = \frac{-3F\left[\left(a^2 - b'^2\right)\left(-1+\nu\right) + 2b'^2\left(1+\nu\right)\ln\left(b'/a\right)\right]}{2\pi t^2\left[a^2\left(-1+\nu\right) - b'^2\left(1+\nu\right)\right]} \tag{5.4}$$

$$B = \frac{3p_c\tilde{M}_c}{t^2XY}\left[2b^2X\right] \tag{5.5}$$

$$C = \frac{3p_c\tilde{M}_c}{t^2XY}\left[4Y\left(a^4b^4 + b^8\right)\right] \tag{5.6}$$

$$D = \frac{-24q_c\tilde{M}_{x'y'}}{t^2X'}\left[a^4\left(b/\sqrt{2}\right)^4 + \left(b/\sqrt{2}\right)^8\right] \tag{5.7}$$

where $\tilde{M}_c$ in Equations (5.5) and (5.6) is the uniformly distributed constraint moment for the constrained outer edges of the square plate and can be expressed as (Lin and Pan [13,14])

$$\tilde{M}_c = \frac{F\left[a^2 - b'^2 + 2a^2\ln\left(b'/a\right)\right]}{4\pi\left(a^2 - b'^2\right)} \tag{5.8}$$

$\tilde{M}_{x'y'} = F/16$ is the uniform distributed twisting moment in Lin and Pan [14]. b' is the equivalent radius for the equivalent circular plate model with the simply supported outer edges presented in Sripichai and Pan [21]. The values of the normalized equivalent radius b'/b for various ratios of b/a are listed in Table 5.1. The equivalent radius can be approximated as a function of b/a as (Sripichai and Pan [21])

$$\frac{b'}{b} = 0.838 + 0.4877e^{-0.3513(b/a)} \tag{5.9}$$

p_c and q_c are the equivalent coefficients for the structural stress solutions accounting for the non-uniform distributions of the opening force and constraint moment per unit length presented in Sripichai and Pan [20]. The values of the equivalent coefficients p_c and q_c for various ratios of b/a are also listed in Table 5.1. The equivalent coefficients p_c and q_c can be approximated as functions of b/a as (Sripichai and Pan [20])

$$p_c = 1.126 + 1.4955e^{-0.3672(b/a)} \tag{5.10}$$

$$q_c = 1.031 + 2.2150e^{-0.3878(b/a)} \tag{5.11}$$

X, Y and X' are defined as

$$X = (-1+\nu)\left(a^4 + b^4\right)^2 - 4a^2b^6(1+\nu) \tag{5.12}$$

$$Y = a^2(-1+\nu) - b^2(1+\nu) \tag{5.13}$$

$$X' = -\left[a^4 + \left(b/\sqrt{2}\right)^4\right]^2 (1-\nu) - 4a^2\left(b/\sqrt{2}\right)^6(1+\nu) \tag{5.14}$$

The computational in-plane and out-of-plane structural stress solutions in Sripichai and Pan [20] indicate that the out-of-plane shear structural stresses exist at the circumference of the rigid inclusion while the structural stress solutions of Lin and Pan [13,14] based on the Kirchhoff plate theory give no out-of-plane shear stress at the circumference of the rigid inclusion. Based on the amplitude H of the cosine function of the in-plane structural stress solutions, the out-of-plane shear structural stress solution can be expressed as (Sripichai and Pan [20])

$$\tau = c_\tau H \sin 2\theta \tag{5.15}$$

Where c_τ is the numerical coefficient for the out-of-plane shear stress solution. The values of the numerical coefficient c_τ for various ratios of b/a are also listed in Table

5.1. The numerical coefficient c_τ can be approximated as a function of b/a as (Sripichai and Pan [20])

$$c_\tau = -0.111 - 0.0263e^{-0.5538(b/a)} \tag{5.16}$$

Based on the stress intensity factor solutions obtained from three-dimensional finite analyses for spot welds in the square overlap parts of cross-tension specimens of similar material with equal thickness, Sripichai and Pan [20] presented the structural stress solutions with the fitting coefficients for K solutions accounting for the flexibility of spot welds. The in-plane structural stress and out-of-plane shear structural stress solutions with the fitting coefficients can be expressed, respectively, as

$$\sigma_{eff} = G + k_{\mathrm{cII}} H \cos 2\theta \tag{5.17}$$

$$\tau_{eff} = c_\tau k_{\mathrm{cIII}} H \sin 2\theta \tag{5.18}$$

k_{cII} and k_{cIII} are the fitting coefficients for the stress intensity factor solutions accounting for the flexibility of spot welds. The values of the fitting coefficients k_{cII} and k_{cIII} for various ratios of b/a are listed in Table 5.2. The fitting coefficients k_{cII} and k_{cIII} can be approximated as functions of b/a as (Sripichai and Pan [20])

$$k_{\mathrm{cII}} = 0.565 - 0.1417e^{-0.3473(b/a)} \tag{5.19}$$

$$k_{\mathrm{cIII}} = 2.768 + 0.3058e^{-0.3260(b/a)} \tag{5.20}$$

5.3. Analytical J integral and stress intensity factor solutions for spot welds between two square plates of different thicknesses and materials.

Here, the strip model of Radaj and Zhang [4-6] is adopted to derive the J integral and stress intensity factor solutions for spot welds between square plates of different

thicknesses and materials under opening and bending loading conditions as in Lin and Pan [13] and Tran and Pan [19]. Figure 5.4 shows a two-dimensional model of two infinite strips of different thicknesses and materials with connection under plane strain conditions. The strip model can be used to represent the cross section perpendicular to the crack front along the weld nugget or the connection circumference. The two strips are assumed to be linear elastic isotropic materials with the Young's modulus E_u and Poisson's ratio ν_u for the upper strip material, and the Young's modulus E_l and Poisson's ratio ν_l for the lower strip material. The upper strip has the thickness t_u and the lower strip has the thickness t_l. As shown in Figure 5.4, the radial stress σ_{rr} and the shear stress $\sigma_{r\theta}$ along the circumference of a rigid inclusion in a plate are used to represent the normal structural stresses, σ_x^u and σ_x^l, and the shear structural stresses, τ_{xz}^u and τ_{xz}^l, for the strip model with respect to the Cartesian coordinate system as shown in the figure.

Figure 5.5(a) shows a crack along the interface of the upper and lower plates. A Cartesian coordinate system is shown in the figure and the origin of the coordinates is located at the crack tip. The J integral is defined as [22]

$$J = \int_{\Gamma} (Wn_x - T_i \frac{\partial u_i}{\partial x}) ds \qquad (i = x, y, z) \tag{5.21}$$

where Γ represents a contour in counter-clockwise sense from the lower crack face to the upper crack face, ds represents the differential arc length of the contour Γ, n_x represents the x component of the unit outward normal **n** to the differential arc length ds, T_i $(= \sigma_{ij} n_j)$ represent the components of the traction vector **T** on the differential arc

length ds, and u_i represent the components of the displacement vector **u**. In Equation (5.21), the strain energy W is defined as

$$W = \int_o^{\varepsilon_{ij}} \sigma_{ij} d\varepsilon_{ij} \qquad (i = x, y, z) \tag{5.22}$$

Figure 5.5(b) shows the front and side views of the left part of the strip model and the linearly distributed structural stresses through the thickness based on the Kirchhoff plate theory. As shown in Figure 5.5(b), line $\overline{ABCDEFG}$ is considered as the contour Γ for the J intergral. The integrals along lines $\overline{BC}$ and $\overline{EF}$ are zero because n_x and T_i are zero. For the integrals along lines $\overline{AB}$, $\overline{CD}$, $\overline{DE}$ and $\overline{FG}$, the contributions of the in-plane shear stress τ_{xy} are taken to be zero as in Radaj and Zhang [4]. Therefore, for linear elastic isotropic materials, the J integral can be written as

$$J = -\left(\int_{\overline{AB}} W_l dy + \int_{\overline{CD}} W_l dy + \int_{\overline{DE}} W_u dy + \int_{\overline{FG}} W_u dy\right) \tag{5.23}$$

where the strain energy densities W_u and W_l for linear elastic isotropic materials can be expressed as

$$W_u = \frac{1-\nu^2}{2E_u}\sigma_x^2 + \frac{\tau_{xz}^2}{2G_u} \tag{5.24a}$$

and

$$W_l = \frac{1-\nu^2}{2E_l}\sigma_x^2 + \frac{\tau_{xz}^2}{2G_l} \tag{5.24b}$$

Here, E_u and E_l are the Young's modulus for the upper (u) and lower (l) plates materials, respectively. G_u and G_l are the shear modulus for the upper (u) and lower (l) plates materials, respectively.

As in Figure 5.5(b), the normal stresses σ_x^u and σ_x^l, and the shear stresses τ_{xz}^u and τ_{xz}^l represent the structural stresses for the upper (*u*) and lower (*l*) strips, respectively. The normal stresses σ_{ui}, σ_{uo}, σ_{li} and σ_{lo} represent the normal stresses σ_x^u and σ_x^l at the inner (*i*) and outer (*o*) surfaces of the upper (*u*) and lower (*l*) strips, respectively. The shear stresses τ_{ui}, τ_{uo}, τ_{li} and τ_{lo} represent the shear stresses τ_{xz}^u and τ_{xz}^l at the inner (*i*) and outer (*o*) surfaces of the upper (*u*) and lower (*l*) strips, respectively. It should be noted that the normal stresses and out-of-plane shear stresses for line $\overline{CD}$ and $\overline{DE}$ in the weld nugget are required to balance the in-plane and out-of-plane bending moments induced by the distributions of the normal stresses and out-of-plane shear stresses for lines $\overline{AB}$ and $\overline{FG}$. In Figure 5.5(b), the normal stresses σ_{ui}^*, σ_{uo}^*, σ_{li}^* and σ_{lo}^* and shear stresses τ_{ui}^*, τ_{uo}^*, τ_{li}^* and τ_{lo}^* represent the required normal stresses and out-of-plane shear stress for line $\overline{DE}$ and $\overline{CD}$ at the inner (*i*) and outer (*o*) surfaces of the upper (*u*) and lower (*l*) strips, respectively.

The in-plane part of the J integral solution related to the in-plane normal stresses, J_{xy}, was derived by Zhang [23] as

$$
\begin{aligned}
J_{xy} &= \frac{t_u}{6\left[1+2\eta\delta\left(2+3\delta+2\delta^2\right)+\eta^2\delta^4\right]E_u'} \\
&\times\Big[\left(1+\eta\delta+3\eta\delta^2+3\eta\delta^3\right)\sigma_{ui}^2+\eta^2\left(3+3\delta+\delta^2+\eta\delta^2\right)\sigma_{li}^2 \\
&-\eta\left(3+\delta+\eta\delta^2+3\eta\delta^3\right)\sigma_{ui}\sigma_{li}+\left(1+\eta\delta\right)\left(\sigma_{uo}+\eta\delta\sigma_{lo}\right)^2 \\
&+\left(1-2\eta\delta-3\eta\delta^2\right)\left(\sigma_{ui}\sigma_{uo}+\eta\delta\sigma_{ui}\sigma_{lo}\right)-\eta\left(3+2\delta-\eta\delta^2\right)\left(\sigma_{uo}\sigma_{li}+\eta\delta\sigma_{li}\sigma_{lo}\right)\Big]
\end{aligned}
\tag{5.25}
$$

where δ is the thickness ratio and η is the modulus ratio. δ and η are defined as

$$\delta = \frac{t_u}{t_l} \tag{5.26}$$

and

$$\eta = \frac{E'_u}{E'_l} \tag{5.27}$$

Under plane strain conditions, E'_u and E'_l are defined as

$$E'_u = \frac{E_u}{\left(1-\nu_u^2\right)} \tag{5.28a}$$

and

$$E'_l = \frac{E_l}{\left(1-\nu_l^2\right)} \tag{5.28b}$$

Note that the strip model here is assumed to be under plane strain conditions. The out-of-plane J intergral, J_3 or J_{III}, is derived here. The detailed derivation of the out-of-plane J intergral is shown in the appendix. From Equation (5.A8) in Appendix, the J_3 or J_{III} solution can be expressed as

$$J_3 = \frac{t_u j_3}{6G_u} \tag{5.29}$$

where

$$j_3 = \left(\tau_{ui} - \xi\delta C_{j1}C_{j2}\right)^2 + \frac{\xi}{\delta}\left(\tau_{li} - C_{j1}C_{j2}\right)^2 + 3C_{j1}^2\left\{\xi^2\left(\delta C_{j2} - C_{j3}\right)^2 + \frac{\xi}{\delta}\left(C_{j2} + C_{j3}\right)^2\right\} \tag{5.30}$$

$$C_{j1} = \frac{\tau_{ui}\delta^2 - \tau_{li}}{\left(\xi\delta^2+1\right)^2 + 4\xi\left(\delta^3+\delta^2+\delta\right)} \tag{5.31}$$

$$C_{j2} = \xi\delta + 1 \tag{5.32}$$

$$C_{j3} = 1 - \xi\delta^2 \tag{5.33}$$

ξ is the shear modulus ratio defined as

$$\xi = \frac{G_u}{G_l} \tag{5.34}$$

The total J integral solution for the strip model shown in Figure 5.5(b) is obtained from Equations (5.25) and (5.29) as

$$J = J_{xy} + J_3 = J_{xy} + J_{III} \tag{5.35}$$

Under plane strain conditions, for an interface crack between two dissimilar linear elastic isotropic materials, the J integral is related to the stress intensity factor K_1, K_2 and K_3 as

$$J = \frac{K_1^2 + K_2^2}{\cosh^2(\pi\varepsilon)E^*} + \frac{K_3^2}{2G^*} \tag{5.36}$$

where E^* and G^* are defined as

$$\frac{1}{E^*} = \frac{1}{2}\left(\frac{1}{E_u'} + \frac{1}{E_l'}\right) \tag{5.37}$$

$$\frac{1}{G^*} = \frac{1}{2}\left(\frac{1}{G_u} + \frac{1}{G_l}\right) \tag{5.38}$$

ε is the bimaterial constant defined as

$$\varepsilon = \frac{1}{2\pi}\ln\frac{\kappa_u/G_u + 1/G_l}{\kappa_l/G_l + 1/G_u} \tag{5.39}$$

An equivalent K_{eq} can also be defined as

$$K_{eq} = \sqrt{K_1^2 + K_2^2} = \sqrt{J_{xy}\cosh^2(\pi\varepsilon)E^*} \tag{5.40}$$

Based on the in-plane part of the J integral, J_{xy}, for the strip model and the analytical solutions for interface cracks of Suo and Hutchison [24], Zhang [23] derived the stress

intensity factor K_1 and K_2 solutions in terms of the structural stresses σ_{ui}, σ_{uo}, σ_{li} and σ_{lo} of the upper and lower plates as

$$K_1 = \frac{\cosh(\pi\varepsilon)\sqrt{t_u}}{2\sqrt{3(1+\eta)(1+4\eta\delta+6\eta\delta^2+3\eta\delta^3)(1+\tan^2\omega)}}\times$$

$$\left\{\left[\frac{(1+4\eta\delta+9\eta\delta^2+6\eta\delta^3)\tan\omega}{\sqrt{1+2\eta\delta(2+3\delta+2\delta^2)+\eta^2\delta^4}}-\sqrt{3}\right]\sigma_{ui}\right.$$

$$-\left[\frac{(1+4\eta\delta+3\eta\delta^2)\tan\omega}{\sqrt{1+2\eta\delta(2+3\delta+2\delta^2)+\eta^2\delta^4}}+\sqrt{3}\right]\sigma_{uo}$$

$$+\eta\left[\frac{\delta(1-2\eta\delta-3\eta\delta^2)\tan\omega}{\sqrt{1+2\eta\delta(2+3\delta+2\delta^2)+\eta^2\delta^4}}+\sqrt{3}(2+\delta)\right]\sigma_{li}$$

$$\left.-\eta\delta\left[\frac{(1+4\eta\delta+3\eta\delta^2)\tan\omega}{\sqrt{1+2\eta\delta(2+3\delta+2\delta^2)+\eta^2\delta^4}}+\sqrt{3}\right]\sigma_{lo}\right\} \qquad (5.41)$$

$$K_2 = \frac{\cosh(\pi\varepsilon)\sqrt{t_u}}{2\sqrt{3(1+\eta)(1+4\eta\delta+6\eta\delta^2+3\eta\delta^3)(1+\tan^2\omega)}}\times$$

$$\left\{\left[\frac{1+4\eta\delta+9\eta\delta^2+6\eta\delta^3}{\sqrt{1+2\eta\delta(2+3\delta+2\delta^2)+\eta^2\delta^4}}+\sqrt{3}\tan\omega\right]\sigma_{ui}\right.$$

$$-\left[\frac{1+4\eta\delta+3\eta\delta^2}{\sqrt{1+2\eta\delta(2+3\delta+2\delta^2)+\eta^2\delta^4}}-\sqrt{3}\tan\omega\right]\sigma_{uo}$$

$$+\eta\left[\frac{\delta(1-2\eta\delta-3\eta\delta^2)}{\sqrt{1+2\eta\delta(2+3\delta+2\delta^2)+\eta^2\delta^4}}-\sqrt{3}(2+\delta)\tan\omega\right]\sigma_{li}$$

$$\left.-\eta\delta\left[\frac{1+4\eta\delta+3\eta\delta^2}{\sqrt{1+2\eta\delta(2+3\delta+2\delta^2)+\eta^2\delta^4}}-\sqrt{3}\tan\omega\right]\sigma_{lo}\right\} \qquad (5.42)$$

Under the plane strain conditions, the constants κ_u and κ_l are defined as

$$\kappa_u = 3 - 4\nu_u \tag{5.43a}$$

and

$$\kappa_l = 3 - 4\nu_l \tag{5.43b}$$

In Equations (5.41) and (5.42), ω is the angular quantity which can be found in Suo and Hutchinson [24]. The angular quantity ω is a function of the thickness ratio δ and the Dundurs parameters α and β which are defined as

$$\alpha = \frac{\xi(\kappa_l + 1) - (\kappa_u + 1)}{\xi(\kappa_l + 1) + (\kappa_u + 1)} \tag{5.44}$$

$$\beta = \frac{\xi(\kappa_l - 1) - (\kappa_u - 1)}{\xi(\kappa_l + 1) + (\kappa_u + 1)} \tag{5.45}$$

Based on the out-of-plane part of the J integral solution, J_3, the stress intensity factor K_3 solution can be expressed as,

$$K_3 = \sqrt{\frac{2t_u}{3(\xi + 1)} j_3} \tag{5.46}$$

For square plates under opening and bending loading conditions, the normal stresses σ_{ui} and σ_{li} are the structural stresses obtained from Equation (5.1). The shear stresses τ_{ui} and τ_{li} are the shear stresses obtained from Equation (5.15). Note that the structural stress solutions of the lower plate can be derived by substituting $\theta + \pi/2$ for θ in Equations (5.1) and (5.15). For square plates under opening and bending loading conditions, $\sigma_{uo} = -\sigma_{ui}$, $\sigma_{lo} = -\sigma_{li}$, $\tau_{uo} = -\tau_{ui}$ and $\tau_{lo} = -\tau_{li}$. Note that, for the structural stress solutions of the upper plates, σ_{ui} and τ_{ui}, $t = t_u$ and $\nu = \nu_u$ in Equations (5.1) –

(5.7) and (5.12) – (5.14). For the structural stress solutions of the lower plates, σ_{li} and τ_{li}, $t = t_l$ and $\nu = \nu_l$ in Equations (5.1) – (5.7) and (5.12) – (5.14).

The values of the Dundurs parameters α and β, bimaterial constant ε, modulus ratios η and ξ, and angular quantity ω (in degree) for dissimilar materials of combinations between magnesium (Mg), aluminum (Al), and steel (Fe) sheets and combinations of aluminum (Al) and copper (Cu) sheets with $\delta = 1$ and $\delta = 0.5$ are listed in Tables 5.3a and 5.3b, respectively. For the notations of the material combinations shown in Tables 5.3a and 5.3b such as Mg/Al, Mg represents the upper sheet material and Al represents the lower sheet material. In this investigation, the Young's modulus and Poisson's ratio for magnesium (Mg) are taken as 45 GPa and 0.35, respectively. The Young's modulus and Poisson's ratio for aluminum (Al) are taken as 68.9 GPa and 0.33, respectively. The Young's modulus and Poisson's ratio for steel (Fe) are taken as 207 GPa and 0.3, respectively. The Young's modulus and Poisson's ratio for copper (Cu) are taken as 110 GPa and 0.34, respectively. Note that K_1 and K_2 are the stress intensity factor solutions for interface cracks between dissimilar materials. When the upper and lower sheet materials are identical ($\eta = \xi = 1$), Equation (5.36) becomes

$$J = \frac{K_I^2 + K_{II}^2}{E'} + \frac{K_{III}^2}{2G} \tag{5.47}$$

The K_1, K_2 and K_3 solutions in Equations (5.41), (5.42) and (5.46) become the conventional K_I, K_{II} and K_{III} solutions, respectively. For similar material, $\alpha = \beta = \varepsilon = 0$ and $\eta = \xi = 1$, $\omega = 49.1°$ for $\delta = 1$ and $\omega = 49.8°$ for $\delta = 0.5$.

5.4. Finite element analyses for spot welds between square plates of different thicknesses and materials

Finite element analyses for spot welds between square plates of different thicknesses and materials were conducted in order to investigate the applicability of the stress intensity factor solutions for interface cracks in Equations (5.41), (5.42) and (5.46) based on the structural stress solutions in Equations (5.1) – (5.7) and (5.15), and the structural stress solutions with the fitting coefficients in Equations (5.17) and (5.18) to estimate the stress intensity factor solutions. Figure 5.6(a) shows a schematic of a three-dimensional finite element model of two square plates with connection and roller boundary conditions on the two opposite outer edges of the upper and lower plates. The x-y-z coordinate system is shown and the origin of the coordinates is located at the center of the connection of the two square plates. Both plates have the equal thickness $t = 0.65\,\text{mm}$ and the width $2b = 50.8$. The connection or spot weld has the diameter of $2a = 6.4\,\text{mm}$. The lower surfaces of the two opposite outer edges of the lower plates are fixed. The upper plate was subjected to a uniform out-of-plane displacement in the z direction along the upper surfaces of the two opposite outer edges. Figures 5.6(b) and 5.6(c) show a quarter of a three-dimensional finite element model for $b/a = 7.94$ and a close-up view of the mesh near the crack front. The x-y-z coordinate system is shown and the origin of the coordinates is located at the center of the connection of the square plates. The three-dimensional finite element model and the boundary conditions shown in Figure 5.6 was used in the computations for spot welds between square plates of equal thickness for both similar and dissimilar materials cases. Due to the symmetry, only a quarter of the model was considered

For a spot weld between square plates of unequal thicknesses, a three-dimensional finite element model and the boundary conditions are shown in Figure 5.7. The finite element model was used for computations for both similar and dissimilar material cases. Figure 5.7(a) shows a schematic of a three-dimensional finite element model of two square plates of unequal thicknesses with connection and roller boundary conditions on the two opposite outer edges of the upper and lower plates. The x-y-z coordinate system is shown and the origin of the coordinates is located at the center of the connection interface of the two square plates. The upper plate has the thickness $t_u = 0.65$ mm and the lower plate has the thickness $t_l = 1.30$ mm. Both plates have the width $2b = 50.8$ mm. The connection has the diameter of $2a = 6.4$ mm. The lower surfaces of the outer edges of the lower plates are fixed. The upper plates are subjected to a uniform out-of-plane displacement in the z direction along the upper surfaces of the two opposite outer edges. Figures 5.7(b) and 5.7(c) show a quarter of the three-dimensional finite element model and a close-up view of the mesh near the crack front. The x-y-z coordinate system is shown and the origin of the coordinates is located at the center of the connection interface of the square plates. Due to the symmetry, only a quarter of the model was considered.

For the similar material case, the material is assumed to be a linear elastic isotropic material. The Young's modulus and Poisson's ratio are taken as 207 GPa and 0.3 for steel (Fe), respectively. For the dissimilar material case, three types of combinations of magnesium, aluminum and steel sheets are considered here: Mg/Fe (where the upper sheet is selected to be Mg and the lower sheet is selected to Fe), Al/Fe (where the upper sheet is selected to be Al and the lower sheet is selected to Fe) and Mg/Al (where the

upper sheet is selected to be Mg and the lower sheet is selected to Al). The Young's modulus and Poisson's ratio for magnesium (Mg) are taken as 45 GPa and 0.35, respectively. The Young's modulus and Poisson's ratio for aluminum (Al) are taken as 68.9 GPa and 0.33, respectively. The Young's modulus and Poisson's ratio for steel (Fe) are taken as 207 GPa and 0.3, respectively. The commercial finite element program ABAQUS [25] was employed to perform the computations. Brick elements C3D20R with quarter point nodes and collapsed nodes along the crack front are adopted to model the singularity near the crack front.

Tables 5.4a, 5.4b, 5.4c and 5.4d list the normalized J_{xy}, K_{eq}, K_I, K_{II}, K_1 and K_2 solutions at the critical locations (points A and B) for the ratio of the plate width to the spot weld diameter, b/a = 7.94 for the similar and dissimilar material cases. The computational J_{xy}, K_{eq}, K_I, K_{II}, K_1 and K_2 solutions were normalized by the analytical J_{xy}, K_{eq}, K_{I} and K_1 solutions at the critical locations (points A and B) obtained from Equations (5.1), (5.25), (5.40) and (5.41). Tables 5.5a, 5.5b, 5.5c and 5.5d list the normalized J_{xy}, K_{eq}, K_I, K_{II}, K_1 and K_2 solutions at the critical locations (points A and B) obtained from Equations (5.25), (5.40), (5.41) and (5.42) based on the structural stress solutions with the fitting coefficients in Equation (5.17) for the ratio of the plate width to the spot weld diameter, b/a = 7.94 for the similar and dissimilar material cases. The superscript *kc* denotes the analytical J_{xy}, K_{eq}, K_I, K_{II}, K_1 and K_2 solutions based on the structural stress solutions with the fitting coefficients in Equation (5.17). The analytical J_{xy}, K_{eq}, K_I, K_{II}, K_1 and K_2 solutions based on the structural stress solutions with the fitting coefficients in Equation (5.17) were normalized by the

analytical J_{xy}, K_{eq}, K_{I} and K_1 solutions at the critical locations (points A and B) obtained from Equations (5.1), (5.25), (5.40) and (5.41). As listed in Table 4, the computational J_{xy} and K_{eq} solutions agree quite well with the corresponding analytical solutions obtained from Equations (5.1), (5.25) and (5.40). For all cases, the computational K_{II} or K_2 solutions are much lower than the K_{I} or K_1 solutions obtained from the computations and Equation (5.41) based on the structural stress solutions in Equation (5.1) indicating that spot welds are under mode I dominant conditions. The computational K_{I} and K_1 solutions at the critical location of point A are slightly larger than those of the corresponding analytical solutions based on the structural stress solutions in Equation (5.1). The computational K_{II} and K_2 solutions at critical location of point A are smaller than those of the corresponding analytical solutions based on the structural stress solutions in Equation (5.1). For the stress intensity factor solutions at the critical location of point B, the computational K_{I} and K_1 solutions at the critical location of point B are lower than the corresponding analytical solutions based on the structural stress solutions in Equation (5.1) for most cases. The computational K_{II} and K_2 solutions at critical location of point B are larger than those of the corresponding analytical solutions based on the structural stress solutions in Equation (5.1).

For all cases except the similar material with equal thickness case, the computational J_{xy} and K_{eq} solutions agree with the analytical J_{xy} and K_{eq} solutions based on the structural stress solutions obtained from Equation (5.1) better than the analytical J_{xy} and K_{eq} solutions based on the structural stress solutions with the fitting coefficients in Equation (5.17) as listed in Tables 5.4 and 5.5. For all cases except the similar material

with equal thickness case, the computational K_{I} and K_1 solutions at the critical location of point A are much larger than those of the corresponding analytical solutions based on the structural stress solutions with the fitting coefficients in Equation (5.17). The computational K_{I} and K_1 solutions at the critical location of point B are much smaller than those of the corresponding analytical solutions based on the structural stress solutions with the fitting coefficients in Equation (5.17). For all cases, the computational K_{II} and K_2 solutions at critical locations (point A and B) agree with the corresponding analytical solutions based on the structural stress solutions with the fitting coefficients in Equation (5.17) than those based on the structural stress solutions in Equation (5.1).

Figures 5.8(a), 5.9(a), 5.10(a) and 5.11(a) show the distributions of the normalized computational and analytical stress intensity factor K_{I}, K_{II}, K_{III}, K_1, K_2 and K_3 solutions along the circumference of the spot weld. The subscript *,kc* denotes the analytical stress intensity factor K_{I}, K_{II}, K_{III}, K_1, K_2 and K_3 solutions based on the structural stress solutions with the fitting coefficients in Equation (5.17). The computational and analytical stress intensity factors K_{I}, K_{II}, K_{III}, K_1, K_2 and K_3 solutions were normalized by the analytical K_{I} and K_1 solutions at the critical location of point A based on the structural stress solutions obtained from Equation (5.1). As shown in Figures 5.9(a), 5.10(a) and 5.11(a), the computational K_{I} and K_1 solutions agree with the analytical K_{I} and K_1 solutions based on the structural stress solutions obtained from Equation (5.1) better than the analytical K_{I} and K_1 solutions based on the structural stress solutions with the fitting coefficients obtained from Equation (5.17). For similar material with equal thickness case, the computational K_{I} solutions agree with the

analytical K_{I} solutions based on the structural stress solutions obtained from Equation (5.1) and the analytical K_{I} solutions based on the structural stress solutions with the fitting coefficients obtained from Equation (5.17) since the fitting coefficients k_{cII} and k_{cIII} have no influence on the analytical K_{I} solutions as mentioned in Sripichai and Pan [20]. For the stress intensity factor K_{II} and K_2 solutions, the computational K_{II} and K_2 solutions agree with the analytical K_{II} and K_2 solutions based on the structural stress solutions with the fitting coefficients obtained from Equation (5.17) better than the analytical K_{II} and K_2 solutions based on the structural stress solutions obtained from Equation (5.1) as shown in Figures 5.8(a), 5.9(a), 5.10(a) and 5.11(a). For all cases except the similar material with equal thickness case, the computational K_{III} and K_3 solutions are larger than the analytical K_{III} and K_3 solutions based on the structural stress solutions obtained from Equation (5.1) but smaller than the analytical K_{III} and K_3 solutions based on the structural stress solutions with the fitting coefficients obtained from Equation (5.17). For both similar and dissimilar materials with equal thickness cases, the computational K_{III} and K_3 solutions agree with the analytical K_{III} and K_3 solutions based on the structural stress solutions with the fitting coefficients obtained from Equation (5.17) better than the analytical K_{III} and K_3 solutions based on the structural stress solutions obtained from Equation (5.1). For both similar and dissimilar materials with unequal thicknesses cases, the computational K_{III} and K_3 solutions agree with the analytical K_{III} and K_3 solutions based on the structural stress solutions obtained

from Equation (5.1) better than the analytical K_{III} and K_3 solutions based on the structural stress solutions with the fitting coefficients obtained from Equation (5.17).

Figures 5.8(b), 5.9(b), 5.10(b) and 5.11(b) show the distributions of the normalized computational and analytical equivalent stress intensity factor solutions, K_{eq}, along the circumference of the spot weld. The computational and analytical K_{eq} solutions were normalized by the analytical K_{eq} solutions at the critical location of point A obtained from Equations (5.25) and (5.40) based on the structural stress solutions in Equation (5.1). As shown in the figures, the computational K_{eq} solutions agree with the analytical K_{eq} solutions based on the structural stress solutions in Equation (5.1) better than the analytical K_{eq} solutions based on the structural stress solutions with the fitting coefficients in Equation (5.17). The analytical K_{eq} solutions based on the structural stress solutions with the fitting coefficients in Equation (5.17) has the same distribution along the circumference of the spot weld as the analytical K_{eq} solutions based on the structural stress solutions in Equation (5.1) but with a lower amplitude.

Based on the values of the J_{xy} and K_{eq} solutions listed in Tables 5.4 for the selected thickness and material combinations, the in-plane J_{xy} and the equivalent stress intensity factor solutions in Equations (5.25) and (5.40) based on the structural stress solutions in Equation (5.1) can be used to determined the in-plane J_{xy} and the equivalent stress intensity factor solutions for spot welds between square plates under opening and bending loading conditions with the maximum error of less than 4%. However, when the analytical K_{eq} solutions are decomposed into the K_{I} and K_{II} solutions or K_1 and K_2

solutions based on Equations (5.41) and (5.42), the errors can be as large as 7% for the dominant K_{I} or K_1 solutions. The results indicate that the decomposition of the J_{xy} integral into either K_{I} and K_{II} or K_1 and K_2 based on the interpolated values of ω from Zhang [23] or Suo and Hutchinson [24] may not be accurate enough. However, the dominant K_{I} or K_1 solutions are still quite acceptable for engineering applications when K_{eq} is used for fatigue life estimations. Based on the values of the J_{xy} and K_{eq} solutions listed in Tables 5.4 and 5.5 for the selected thickness and material combinations, the error of the in-plane J_{xy} and the equivalent stress intensity factor solutions in Equations (5.25) and (5.40) based on the structural stress solutions with the fitting coefficients in Equation (5.17) can be as high as 10%. Although the computational K_{II} and K_2 solutions agree with the analytical K_{II} and K_2 solutions based on the structural stress solutions with the fitting coefficients in Equation (5.17) better than the analytical K_{II} and K_2 solutions based on the structural stress solutions in Equation (5.1), but spot welds in the square overlap parts of cross-tension specimens are under mode I dominant conditions. For general cases, the analytical stress intensity factor K_{I}, K_{II}, K_1 and K_2 solutions based on the structural stress solutions with only the equivalent coefficients in Equation (5.1) are more suitable to determine the in-plane K_{I}, K_{II}, K_1 and K_2 solutions for spot welds between square plates under opening and bending loading conditions than the analytical K_{I}, K_{II}, K_1 and K_2 solutions based on the structural stress solutions with both the equivalent and fitting coefficients in Equation (5.17). For similar material with equal thickness case, the structural stress solutions with both the equivalent and fitting coefficients are better in determining the stress intensity factor solutions.

5.5. Normalized stress intensity factor solutions for spot welds between square plates of different thicknesses and materials

As discussed earlier, the results of three-dimensional finite element analyses selectively confirmed the accuracy of the analytical stress intensity factor solutions for spot welds between square plates of different thicknesses and materials. However, the stress intensity factor solutions from the combinations of Equation (5.1) and Equations (5.41) and (5.42) are in general quite complex. The stress intensity factor solutions for spot welds between square plates of identical material ($\eta = 1$) and different thicknesses can be written in the normalized forms as

$$K_I = g_{kI}\left(\frac{b}{a}, \delta, \theta\right)\frac{F}{t_u\sqrt{t_u}} \tag{5.48}$$

$$K_{II} = g_{kII}\left(\frac{b}{a}, \delta, \theta\right)\frac{F}{t_u\sqrt{t_u}} \tag{5.49}$$

where g_{kI} and g_{kII} are the dimensionless geometric functions of b/a, δ and θ. For spot welds between square plates of different thicknesses and materials, the stress intensity factor solutions can be written in the normalized forms as

$$K_1 = g_{k1}\left(\frac{b}{a}, \delta, \eta, \theta\right)\frac{F}{t_u\sqrt{t_u}} \tag{5.50}$$

$$K_2 = g_{k2}\left(\frac{b}{a}, \delta, \eta, \theta\right)\frac{F}{t_u\sqrt{t_u}} \tag{5.51}$$

where g_{k1} and g_{k2} are the dimensionless geometric functions b/a, δ, η and θ. The in-plane equivalent stress intensity factor solutions for spot welds between square plates can be written in the normalized forms as

$$K_{eq} = g_{keq}\left(\frac{b}{a}, \delta, \eta, \theta\right)\frac{F}{t_u\sqrt{t_u}} \tag{5.52}$$

where g_{keq} is the dimensionless geometric functions b/a, δ, η and θ. Note that the stress intensity factor solutions at the critical locations are of interest here.

Figure 5.12 shows the geometric functions g_{kI}^{A}, g_{kII}^{A} and g_{keq}^{A} for spot welds between square plates of identical material ($\eta = 1$) with $\delta = 1$ and $\delta = 0.5$ as functions of b/a. The superscript *A* denotes the geometric functions at the critical location of point A. Note that the maximum values of the K_{I}, K_{II} and K_{eq} solutions for spot welds between square plates of identical material are located at the critical location of point A for $\delta \le 1$. The computational geometric functions g_{kI}^{A}, g_{kII}^{A} and g_{keq}^{A} are shown as symbols in Figure 5.12. As mention earlier, the computational geometric functions agree well with the geometric functions obtained from the analytical solutions in Equations (5.40), (5.41) and (5.42) based on the structural stress solutions in Equation (5.1). As the lower plate thickness increases (for the case of $\delta = 0.5$), the K_{II} solutions increase because the difference of the structural stresses between the upper and lower plates increases while the K_{I} solutions decrease. The K_{eq} solutions also decrease as the lower plate thickness decreases since the K_{I} solutions decrease and the spot weld are under mode I dominant conditions.

Figures 5.13, 5.14, 5.15, and 5.16 show the geometric functions g_{k1}^{A}, g_{k2}^{A}, g_{k1}^{B}, g_{k2}^{B}, g_{keq}^{A} and g_{keq}^{B} for spot welds between square plates of dissimilar materials between magnesium and steel, between aluminum and steel, between magnesium and aluminum, and between aluminum and copper with different thicknesses respectively. The

superscript *A* and *B* denote the geometric functions at the critical locations of points A and B, respectively. Figures 5.13(a), 5.14(a), 5.15(a) and 5.16(a) show geometric functions g_{k1}^{A}, g_{k2}^{A} and g_{keq}^{A} for Mg/Fe, Al/Fe, Mg/Al and Al/Cu welds in square plates for $\delta = 1$ and $\delta = 0.5$ as functions of b/a. The computational g_{k1}^{A}, g_{k2}^{A} and g_{keq}^{A} are shown as symbols in Figure 5.13(a), 5.14(a) and 5.15(a). Note that for spot welds joining sheets with $\eta \le 1$ and $\delta \le 1$ (when a softer and thinner plate is used as the upper plate and a stiffer and thicker plate is used as the lower plate), the maximum values of the K_1, K_2 and K_{eq} solutions for spot welds between square plates are located at the critical location of point A. As listed in Tables 5.3a and 5.3b, the values of the modulus ratio η for Mg/Fe, Al/Fe, Mg/Al and Al/Cu welds are 0.23, 0.34, 0.66, and 0.62, respectively. As mention earlier, the selected computational geometric functions g_{k1}^{A} and g_{keq}^{A} agree well with the geometric functions obtained from the analytical solutions in Equations (5.40), (5.41) and (5.42) based on the structural stress solutions in Equation (5.1). As shown in these figures, the trends of the K_1 and K_2 solutions for these four types of welds are quite similar. The results in Figures 5.13(a), 5.14(a), 5.15(a) and 5.16(a) also indicate that, as the thickness of the lower plates increase, the K_1 solutions decrease while the K_2 solutions increase. As shown in these figures, the K_1 solutions decrease with the increase of η. The K_2 solutions decrease significantly with the increase of η. The K_{eq} solutions also decrease with the increase of η and decrease of δ (as the lower plate becomes thicker). As η increases, the increases and decreases of K_1, K_2 and K_{eq} solutions increase as the lower plates become thicker.

Figures 5.13(b), 5.14(b), 5.15(b) and 5.16(b) show geometric functions g_{k1}^{A}, and g_{k2}^{A} for Fe/Mg, Fe/Al, Al/Mg and Cu/Al welds in square plates for $\delta = 1$ and $\delta = 0.5$ as functions of b/a. As listed in Tables 5.3a and 5.3b, the values of the modulus ratio η for Fe/Mg, Fe/Al, Al/Mg and Cu/Al welds are 4.43, 2.94, 1.51, and 1.61, respectively. As shown in these figures, the trends of the K_1 and K_2 solutions at the critical location of point A for these four types of welds are quite similar. The results in Figures 5.13(b), 5.14(b), 5.15(b) and 5.16(b) also indicate that, as the thickness of the lower plates increase, the K_1 solutions decrease while the K_2 solutions increase. As shown in these figures, the K_1 solutions decrease with the increase of η. The K_2 solutions decrease significantly with the increase of η. As η increases, the decreases and increases of K_1 and K_2 solutions increase as the lower plates become thicker.

Based on the analytical solutions, for spot welds joining sheets with $\eta > 1$ and $\delta \le 1$ (when a stiffer and thinner plate is used as the upper plate and a softer and thicker plate is used as the lower plate), the maximum values of the K_1, K_2 and K_{eq} solutions for spot welds between square plates are located at either the critical location of point A ($\theta = 0^{\circ}$) or point B ($\theta = 180^{\circ}$) depending upon the values of η and δ. Figures 5.13(c), 5.14(c), 5.15(c) and 5.16(c) show geometric functions g_{k1}^{B}, and g_{k2}^{B} for Fe/Mg, Fe/Al, Al/Mg and Cu/Al welds in square plates for $\delta = 1$ and $\delta = 0.5$ as functions of b/a. As shown in these figures, the trends of the K_1 and K_2 solutions at the critical location of point B for these four types of welds are quite similar. The results in Figures 5.13(c), 5.14(c), 5.15(c) and 5.16(c) also indicate that, as the thickness of the lower plates increase, the K_1

solutions decrease while the K_2 solutions increase. As shown in these figures, for $\delta = 1$, the K_1 solutions increase with the increase of η while the K_2 solutions decrease significantly with the increase of η. Note that, for $\delta = 1$, the K_I solutions for Fe/Mg, Fe/Al, Al/Mg and Cu/Al welds at the critical location of point B are equal to those for Mg/Fe, Al/Fe, Mg/Al and Al/Cu at the critical location of point A, respectively. Also the K_2 solutions for $\delta = 1$ have negative values. For $\delta \leq 1$, the K_1 and K_2 solutions decrease with the increase of η. As η increases, the decreases and increases of K_1 and K_2 solutions increase as the lower plates become thicker.

Figures 5.13(d), 5.14(d), 5.15(d) and 5.16(d) show geometric functions g_{keq}^{A} and g_{keq}^{B} for Fe/Mg, Fe/Al, Al/Mg and Cu/Al welds in square plates for $\delta = 1$ and $\delta = 0.5$ as functions of b/a. As shown in these figures, the trends of the K_{eq} solutions at the critical locations of points A and B for these four types of welds are quite similar. The results in Figures 5.13(d), 5.14(d), 5.15(d) and 5.16(d) also indicate that, as the thickness of the lower plates increase, the K_{eq} solutions at the critical locations of points A and B decrease. As shown in these figures, for $\delta = 1$, the K_{eq} solutions at the critical location of point B is larger than the K_{eq} solutions at the critical location of point A. As η increases, the K_{eq} solutions at the critical location of point A decrease while the K_{eq} solutions at the critical location of point B increase. As η increases, the difference between the K_{eq} solutions at the critical locations of points A and B increases. For $\delta = 0.5$, the K_{eq} solutions at the critical location of point A is larger than the K_{eq} solutions at the critical location of point B. The K_{eq} solutions at the critical locations of

points A and B decrease with the increase of η. As η increases, the difference between the K_{eq} solutions at the critical locations of points A and B decreases. For both critical locations of points A and B, as η increases, the decreases of K_{eq} solutions increase as the lower plates become thicker.

5.6. Conclusions

Closed-form stress intensity factor solutions for spot welds in square overlap parts of cross-tension specimens are investigated here. First, the closed-form analytical solutions for a rigid inclusion in a square plate under opening and bending loading conditions based on the closed-form analytical solutions of Lin and Pan are reviewed. Then, the J integral and stress intensity factor solutions for spot welds between square plates are presented in terms of the structural stresses for a strip model. The results of three-dimensional finite element analyses for spot welds between square plates of different thicknesses and materials are presented. The analytical stress stress intensity factor solutions at the critical locations for spot welds between square plates based on the structural stress solutions with the equivalent and fitting coefficients are compared with the computational results. The results indicate that, the computational equivalent stress intensity factor solutions agree well with those based on the structural stress solutions with only the equivalent coefficients. Based on the closed-form structural stress solutions, complete sets of the normalized stress intensity factor solutions for spot welds between square plates of different thicknesses and materials under opening and bending loading conditions are presented for combinations of steel, aluminum and magnesium

sheets and combinations of aluminum and copper sheets for convenient engineering applications.

Appendix: Derivation of the out-of-plane J integral solutions for spot welds in square overlap parts of cross-tension specimens.

Here, the strip model of Radaj and Zhang [4-6] is adopted to derive the out-of-plane J integral and stress intensity factor solutions for spot welds between square plates under opening and bending loading conditions. Figure 5.A1 shows the decomposition process of the out-of-plane shear stresses τ_{xz} of model A into those of models G and H. Note that Model A shows only the out-of-plane shear stress of Figure 5.5(b). Model G represents a strip model subjected to a linearly distributed out-of-plane shear strain γ which can be expressed as

$$\gamma = my + b \tag{5.A1}$$

where γ_{uo} is the out-of-plane shear strain at the outer surface of the upper strip ($y = t_u$) and γ_{lo} is the out-of-plane shear strain at the outer surface of the lower strip ($y = -t_l$). The linearly distributed shear strain γ is the linearly distributed out-of-plane shear strain on the right end of the strips of model A. The equilibrium condition in the z direction gives

$$m = \frac{-2\xi\delta\left(\tau_{ui}\delta^2 - \tau_{li}\right)\left(\xi\delta + 1\right)}{G_u t_u\left[\left(\xi\delta^2 + 1\right)^2 + 4\xi\left(\delta^3 + \delta^2 + \delta\right)\right]} \tag{5.A2}$$

$$b = \frac{-\xi\left(\tau_{ui}\delta^2 - \tau_{li}\right)\left(1 - \xi\delta^2\right)}{G_u\left[\left(\xi\delta^2 + 1\right)^2 + 4\xi\left(\delta^3 + \delta^2 + \delta\right)\right]} \tag{5.A3}$$

In Model H, the shear stresses τ'_{uo}, τ'_{ui}, τ'_{li} and τ'_{lo} on the left end of the inner (*i*) and outer (*o*) surfaces of the upper (*u*) and lower (*l*) strips, respectively, can be expressed as

$$\tau'_{uo} = -\tau_{ui} - G_u\left(mt_u + b\right) \tag{5.A4}$$

$$\tau'_{ui} = \tau_{ui} - G_u b \tag{5.A5}$$

$$\tau'_{li} = \tau_{li} - G_l b \tag{5.A6}$$

$$\tau'_{lo} = -\tau_{li} - G_l\left(-mt_l + b\right) \tag{5.A7}$$

Note that the J_3 solution for Model G based on Equations (5.23) – (5.24) is zero. Based on the linearly distributed out-of-plane shear stresses in Model H, the J_3 solution for Model H or Model A based on Equations (5.23) – (5.24) can be derived as

$$J_3 = \frac{t_u j_3}{6G_u} \tag{5.A8}$$

where

$$j_3 = \left(\tau_{ui} - \xi\delta C_{j1}C_{j2}\right)^2 + \frac{\xi}{\delta}\left(\tau_{li} - C_{j1}C_{j2}\right)^2 + 3C_{j1}^2\left\{\xi^2\left(\delta C_{j2} - C_{j3}\right)^2 + \frac{\xi}{\delta}\left(C_{j2} + C_{j3}\right)^2\right\} \tag{5.A9}$$

$$C_{j1} = \frac{\tau_{ui}\delta^2 - \tau_{li}}{\left(\xi\delta^2 + 1\right)^2 + 4\xi\left(\delta^3 + \delta^2 + \delta\right)} \tag{5.A10}$$

$$C_{j2} = \xi\delta + 1 \tag{5.A11}$$

$$C_{j3} = 1 - \xi\delta^2 \tag{5.A12}$$

Reference

[1] Pook LP. Fracture mechanics analysis of the fatigue behaviour of spot welds. Int J Fract 1975; 11: 173-176.

[2] Pook LP. Approximate stress intensity factors obtained from simple plate bending theory. Eng Frac Mech 1979; 12: 505-522.

[3] Radaj D. Stress singularity, notch stress and structural stress at spot–welded joints. Eng Fract Mech 1989; 34: 495-506.

[4] Radaj D, Zhang S. Stress intensity factors for spot welds between plates of unequal thickness. Eng Fract Mech 1991; 39: 391-413.

[5] Radaj D, Zhang S. Simplified formulae for stress intensity factors of spot welds. Eng Fract Mech 1991; 40: 233-236.

[6] Radaj D, Zhang S. Stress intensity factors for spot welds between plate of dissimilar materials. Eng Fract Mech 1992; 42: 233-236.

[7] Zhang S. Stress intensities at spot welds. Int J Fract 1997; 88: 167-185.

[8] Zhang S. Fracture mechanics solutions to spot welds. Int J Fract 2001; 112: 247-75.

[9] Pan N, Sheppard SD. Stress intensity factors in spot welds. Eng Frac Mech 2003; 70: 671-684.

[10] Wang DA, Lin SH, Pan J. Stress intensity factors for spot welds and associated kinked cracks in cup specimens. Int J Fatigue 2005; 27: 581-598.

[11] Wang DA, Lin PC, Pan J. Geometric functions of stress intensity factor solutions for spot welds in lap-shear specimens. Int J Solids Struct 2005; 42: 6299-6318.

[12] Lin PC, Wang DA, Pan J. Mode I stress intensity factor solutions for spot welds in lap-shear specimens. Int J Solids Struct 2007; 44: 1013-1037.

[13] Lin PC, Pan J. Closed-form structural stress and stress intensity factor solutions for spot welds under various types of loading conditions. Int J Solids Struct 2008; 45: 3996-4020.

[14] Lin PC, Pan J. Closed-form structural stress and stress intensity factor solutions for spot welds in commonly used specimens. Eng Fract Mech 2008; 75: 5187-5206.

[15] Muskhelishvili NI. Some Basic Problems of the Mathematical Theory of Elasiticiy. Noordhoff, Groningen; 1953

[16] Goland M. The influence of the shape and rigidity of an elastic inclusion of the transverse flexure of thin plates. J App Mech 1943; A-69-A-75.

[17] Timoshenko S, Woinowsky-Krieger S. Theory of Plate and Shells, 2nd ed. McGrow-Hill, NY; 1959.

[18] Lin PC, Lin ZL. Geometric functions of stress intensity factor solutions for spot welds in cross-tension specimens. To be submitted.

[19] Tran VX, Pan J. Analytical stress intensity factor solutions for resistance and friction stir spot welds in lap-shear specimens of different materials and thicknesses. Eng Frac Mech 2010; 77: 2611-2639.

[20] Sripichai K, Pan J. Closed-form structural stress and stress intensity factor solutions for spot welds in square plates under opening loading conditions. To be submitted

[21] Sripichai K, Pan J. Closed-form structural stress and stress intensity factor solutions for spot welds in square overlap parts of cross-tension specimens. To be submitted

[22] Rice JR. A path independent integral and the approximate analysis of strain concentration by notches and cracks. J App Mech 1968; 35: 379-386.

[23] Zhang S. Stress intensities derived from stresses around a spot welds. Int J Fract 1999; 99: 239-257.

[24] Suo Z, Hutchinson JW. Interface crack between two elastic layers. Int J Fract 1990; 43: 1-18.

[25] ABAQUS v6.7 User Manual. Providence, RI: SIMULIA; 2007

Table 5.1. The ratios of equivalent radius, b'/b, the equivalent coefficients, p_c, q_c and numerical coefficient, c_τ, for various ratios of the plate width to the rigid inclusion diameter, b/a.

b/a	3	5.91	7.94	10	15
b'/b	1.006	0.894	0.866	0.852	0.838
p_c	1.617	1.278	1.201	1.162	1.126
q_c	1.722	1.241	1.132	1.079	1.031
c_τ	-0.116	-0.112	-0.111	-0.111	-0.111

Table 5.2. The fitting coefficients k_{cII} and k_{cIII} for various ratios of the plate width to the connection diameter, b/a.

b/a	3	5.91	7.94	10	15
k_{cII}	0.520	0.556	0.561	0.563	0.565
k_{cIII}	2.875	2.794	2.783	2.774	2.768

Table 5.3a. The values of interface crack parameters between magnesium (Mg), aluminum (Al), and steel (Fe) sheets.

Spot weld	α	β	ε	η	ξ	δ	ω
Mg/Al	-0.203	-0.038	0.012	0.663	0.643	1.0	49.37
						0.5	50.05
Al/Fe	-0.493	-0.117	0.037	0.340	0.325	1.0	51.05
						0.5	51.81
Mg/Fe	-0.632	-0.136	0.044	0.225	0.209	1.0	51.30
						0.5	52.19
Al/Mg	0.203	0.038	-0.012	1.508	1.554	1.0	49.00
						0.5	49.88
Fe/Al	0.493	0.117	-0.037	2.942	3.074	1.0	48.00
						0.5	49.90
Fe/Mg	0.632	0.136	-0.044	4.436	4.777	1.0	48.52
						0.5	50.92

Table 5.3b. The values of interface crack parameters between aluminum (Al) and copper (Cu) sheets.

Spot weld	α	β	ε	η	ξ	δ	ω
Al/Cu	-0.233	-0.064	0.020	0.62	0.63	1.0	50.36
						0.5	50.98
Cu/Al	0.233	0.064	-0.020	1.61	1.58	1.0	48.05
						0.5	49.21

Table 5.4a. The normalized computational in-plane *J* integral and stress intensity factor solutions J_{xy}, K_{eq}, K_I and K_{II} for the ratio of the plate width to the spot weld diameter, b/a =7.94.

Nomalized K	Similar material, $\delta = 1.0$		Similar material, $\delta = 0.5$	
	Point A	Point B	Point A	Point B
$J_{xy}^{FEM} / J_{xy}^{SS}$	0.949	0.949	0.977	0.986
$K_{eq}^{FEM} / K_{eq}^{SS}$	0.974	0.974	0.988	0.993
K_I^{FEM} / K_I^{SS}	1.007	1.007	1.048	0.965
K_{II}^{FEM} / K_I^{SS}	0.180	-0.180	0.524	0.283
K_{II}^{SS} / K_I^{SS}	0.321	-0.321	0.637	0.161

Table 5.4b. The normalized computational in-plane *J* integral and stress intensity factor solutions J_{xy}, K_{eq}, K_1 and K_2 for the ratio of the plate width to the spot weld diameter b/a =7.94.

Nomalized K	Mg/Fe, $\delta = 1$		Mg/Fe, $\delta = 0.5$	
	Point A	Point B	Point A	Point B
$J_{xy}^{FEM} / J_{xy}^{SS}$	0.967	0.983	0.982	1.075
$K_{eq}^{FEM} / K_{eq}^{SS}$	0.983	0.991	0.991	1.037
K_1^{FEM} / K_1^{SS}	1.049	0.981	1.061	1.004
K_2^{FEM} / K_1^{SS}	0.389	0.145	0.582	0.544
K_2^{SS} / K_1^{SS}	0.542	0.008	0.700	0.460

Table 5.4c. The normalized computational in-plane J integral and stress intensity factor solutions J_{xy}, K_{eq}, K_1 and K_2 for the ratio of the plate width to the spot weld diameter b/a =7.94.

Nomalized K	Al/Fe, $\delta = 1$		Al/Fe, $\delta = 0.5$	
	Point A	Point B	Point A	Point B
$J_{xy}^{FEM} / J_{xy}^{SS}$	0.964	0.959	0.988	1.049
$K_{eq}^{FEM} / K_{eq}^{SS}$	0.982	0.979	0.994	1.024
K_1^{FEM} / K_1^{SS}	1.041	0.983	1.065	0.991
K_2^{FEM} / K_1^{SS}	0.327	0.034	0.562	0.469
K_2^{SS} / K_1^{SS}	0.485	-0.097	0.684	0.383

Table 5.4d. The normalized computational in-plane J integral and stress intensity factor solutions J_{xy}, K_{eq}, K_1 and K_2 for the ratio of the plate width to the spot weld diameter b/a =7.94.

Nomalized K	Mg/Al, $\delta = 1$		Mg/Al, $\delta = 0.5$	
	Point A	Point B	Point A	Point B
$J_{xy}^{FEM} / J_{xy}^{SS}$	0.950	0.952	0.973	1.039
$K_{eq}^{FEM} / K_{eq}^{SS}$	0.975	0.976	0.986	1.019
K_1^{FEM} / K_1^{SS}	1.022	1.000	1.053	0.980
K_2^{FEM} / K_1^{SS}	0.251	-0.091	0.556	0.379
K_2^{SS} / K_1^{SS}	0.407	-0.245	0.677	0.250

Table 5.5a. The normalized computational in-plane J integral and stress intensity factor solutions J_{xy}, K_{eq}, K_I and K_{II} for the ratio of the plate width to the spot weld diameter, b/a =7.94.

Nomalized K	Similar material, $\delta = 1.0$		Similar material, $\delta = 0.5$	
	Point A	Point B	Point A	Point B
$J_{xy}^{kc} / J_{xy}^{SS}$	0.936	0.936	0.802	1.316
$K_{eq}^{kc} / K_{eq}^{SS}$	0.967	0.967	0.896	1.147
K_I^{kc} / K_I^{SS}	1.000	1.000	0.926	1.112
K_{II}^{kc} / K_I^{SS}	0.180	0.180	0.521	0.337

Table 5.5b. The normalized analytical in-plane J integral and stress intensity factor solutions J_{xy}, K_{eq}, K_1 and K_2 for the ratio of the plate width to the spot weld diameter b/a =7.94.

Nomalized K	Mg/Fe, $\delta = 1$		Mg/Fe, $\delta = 0.5$	
	Point A	Point B	Point A	Point B
$J_{xy}^{kc} / J_{xy}^{SS}$	0.817	1.216	0.778	1.545
$K_{eq}^{kc} / K_{eq}^{SS}$	0.904	1.103	0.882	1.243
K_1^{kc} / K_1^{SS}	0.937	1.089	0.895	1.202
K_2^{kc} / K_1^{SS}	0.424	0.174	0.599	0.654

Table 5.5c. The normalized analytical in-plane J integral and stress intensity factor solutions J_{xy}, K_{eq}, K_1 and K_2 for the ratio of the plate width to the spot weld diameter b/a =7.94.

Nomalized K	Al/Fe, $\delta = 1$		Al/Fe, $\delta = 0.5$	
	Point A	Point B	Point A	Point B
$J_{xy}^{kc} / J_{xy}^{SS}$	0.838	1.123	0.783	1.494
$K_{eq}^{kc} / K_{eq}^{SS}$	0.916	1.060	0.885	1.222
K_1^{kc} / K_1^{SS}	0.951	1.063	0.902	1.178
K_2^{kc} / K_1^{SS}	0.362	0.061	0.581	0.571

Table 5.5d. The normalized analytical in-plane J integral and stress intensity factor solutions J_{xy}, K_{eq}, K_1 and K_2 for the ratio of the plate width to the spot weld diameter b/a =7.94.

Nomalized K	Mg/Al, $\delta = 1$		Mg/Al, $\delta = 0.5$	
	Point A	Point B	Point A	Point B
$J_{xy}^{kc} / J_{xy}^{SS}$	0.886	0.994	0.789	1.408
$K_{eq}^{kc} / K_{eq}^{SS}$	0.941	0.997	0.888	1.187
K_1^{kc} / K_1^{SS}	0.980	1.022	0.914	1.142
K_2^{kc} / K_1^{SS}	0.269	-0.093	0.562	0.440

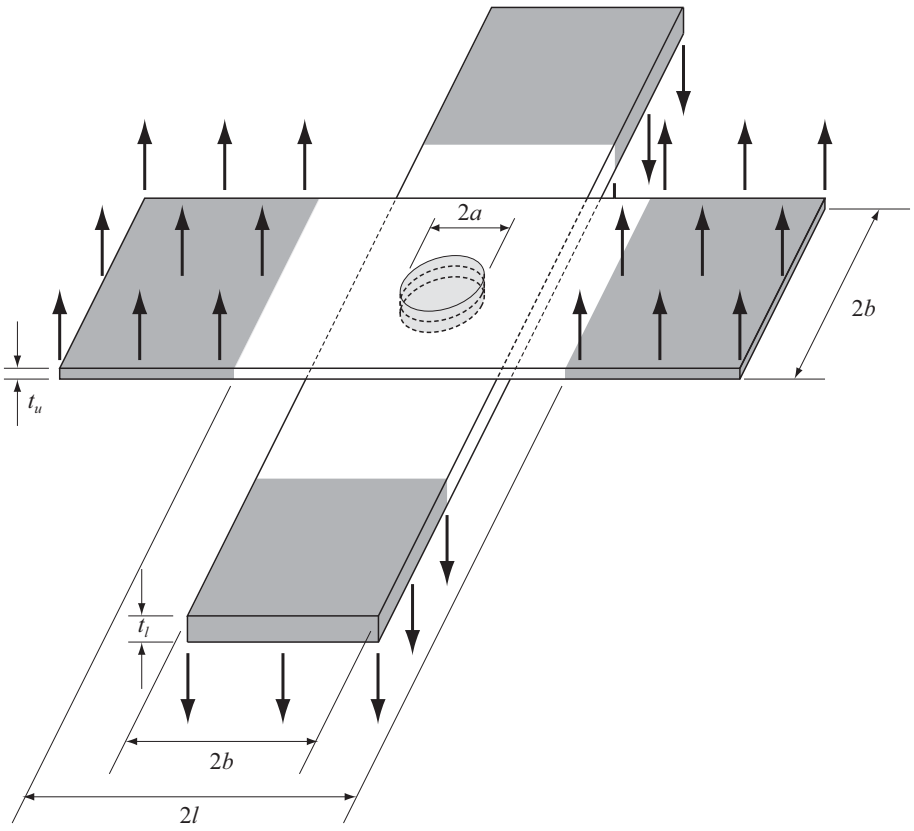

(a)

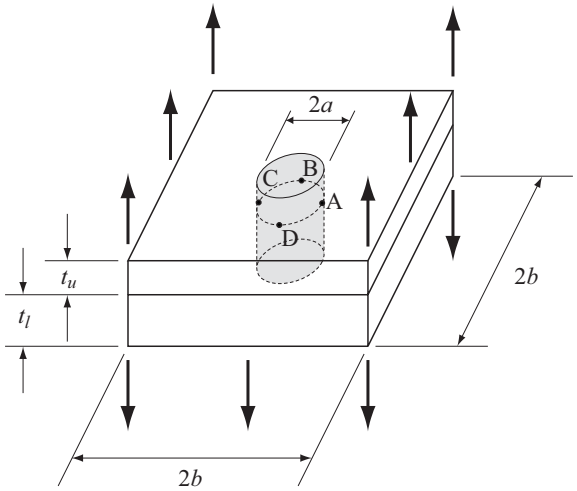

(b)

Figure 5.1. (a) A schematic of a cross-tension specimen and (b) a schematic of two square plates with connection or spot welds under opening and bending loading conditions.

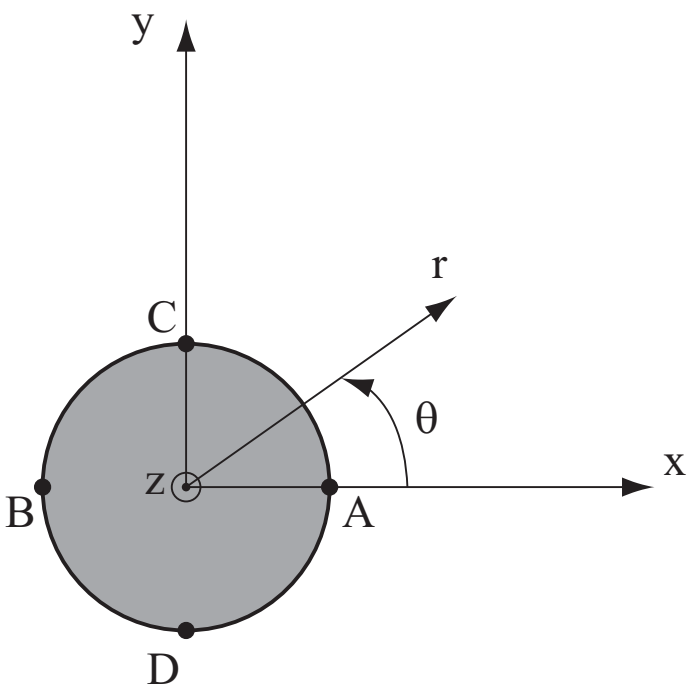

Figure 5.2. A schematic of a top view of the connection or spot weld (idealized as a rigid inclusion) in the upper plate of the specimen.

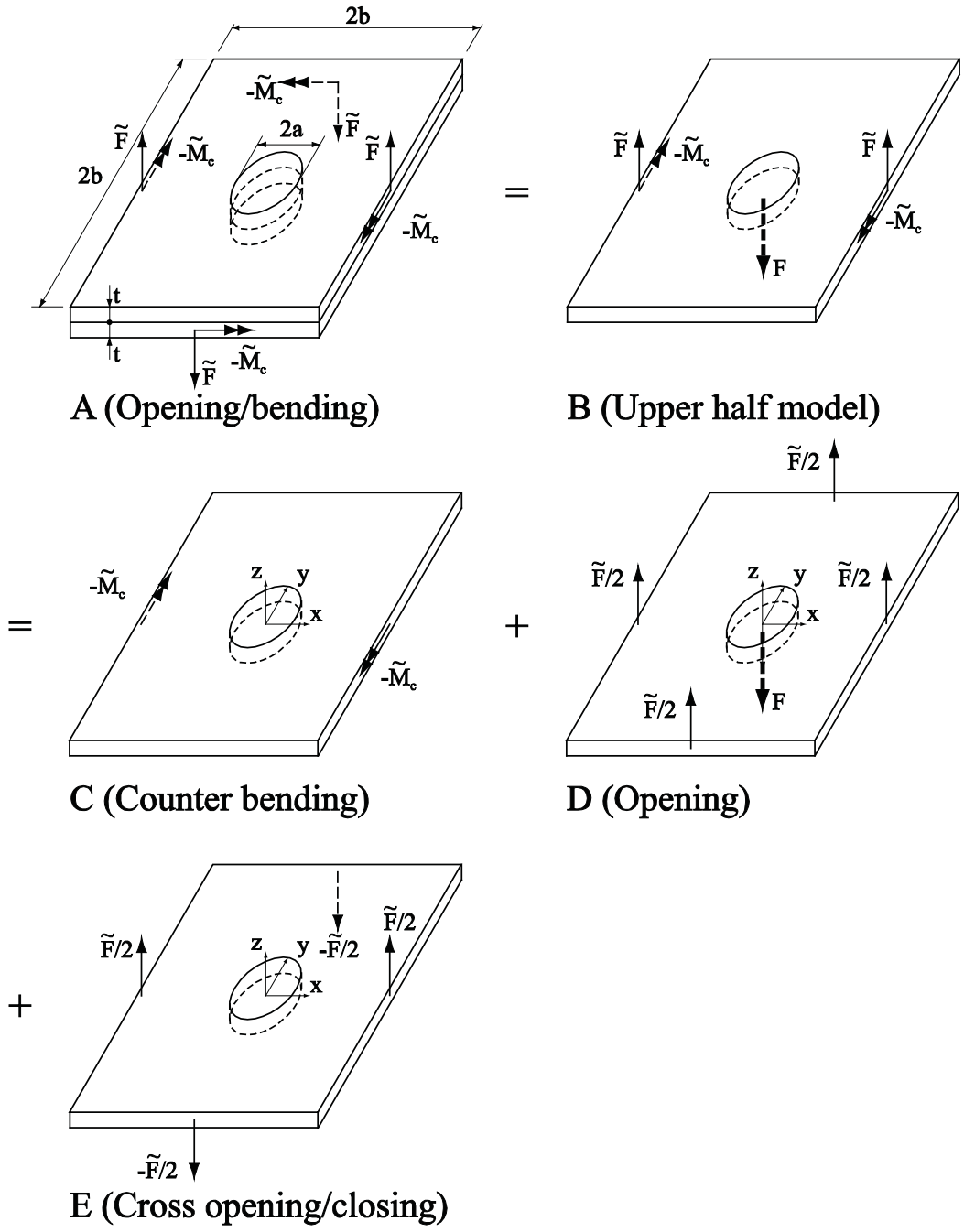

Figure 5.3. Decomposition of the load of a cross-tension specimen. Model A represent a spot weld in the central square part of a cross-tension specimen under opening loading conditions. Model B represents the upper half of model A. The forces of model B are approximately decomposed into three types of loads: counter bending (model C), opening (model D), and cross opening / closing (model E).

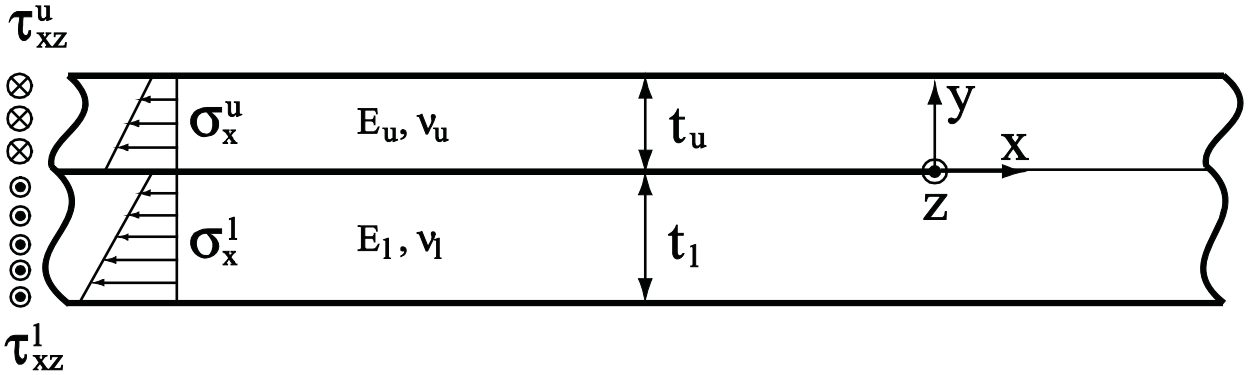

Figure 5.4. A two-dimensional model of two infinite strips made of different thicknesses and materials with connection under plane strain conditions.

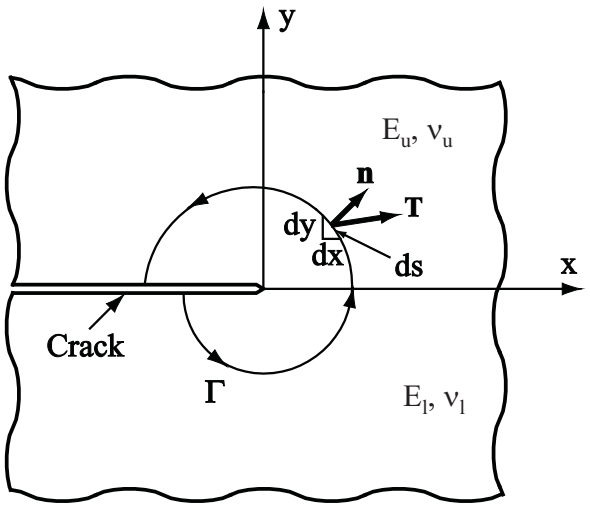

(a)

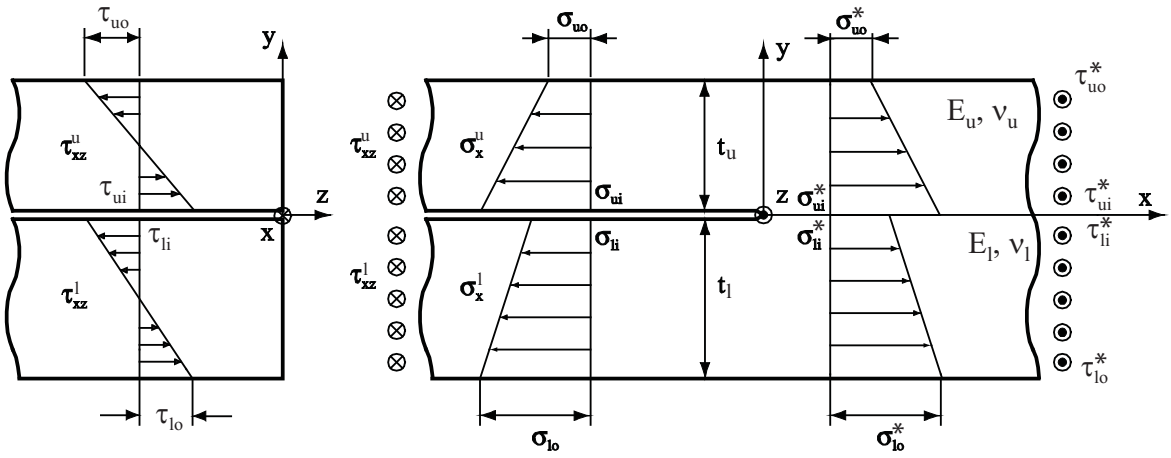

(b)

Figure 5.5. (a) A crack with contour Γ surrounding a crack tip and (b) the front and side views of the left part of the strip model near the crack tip.

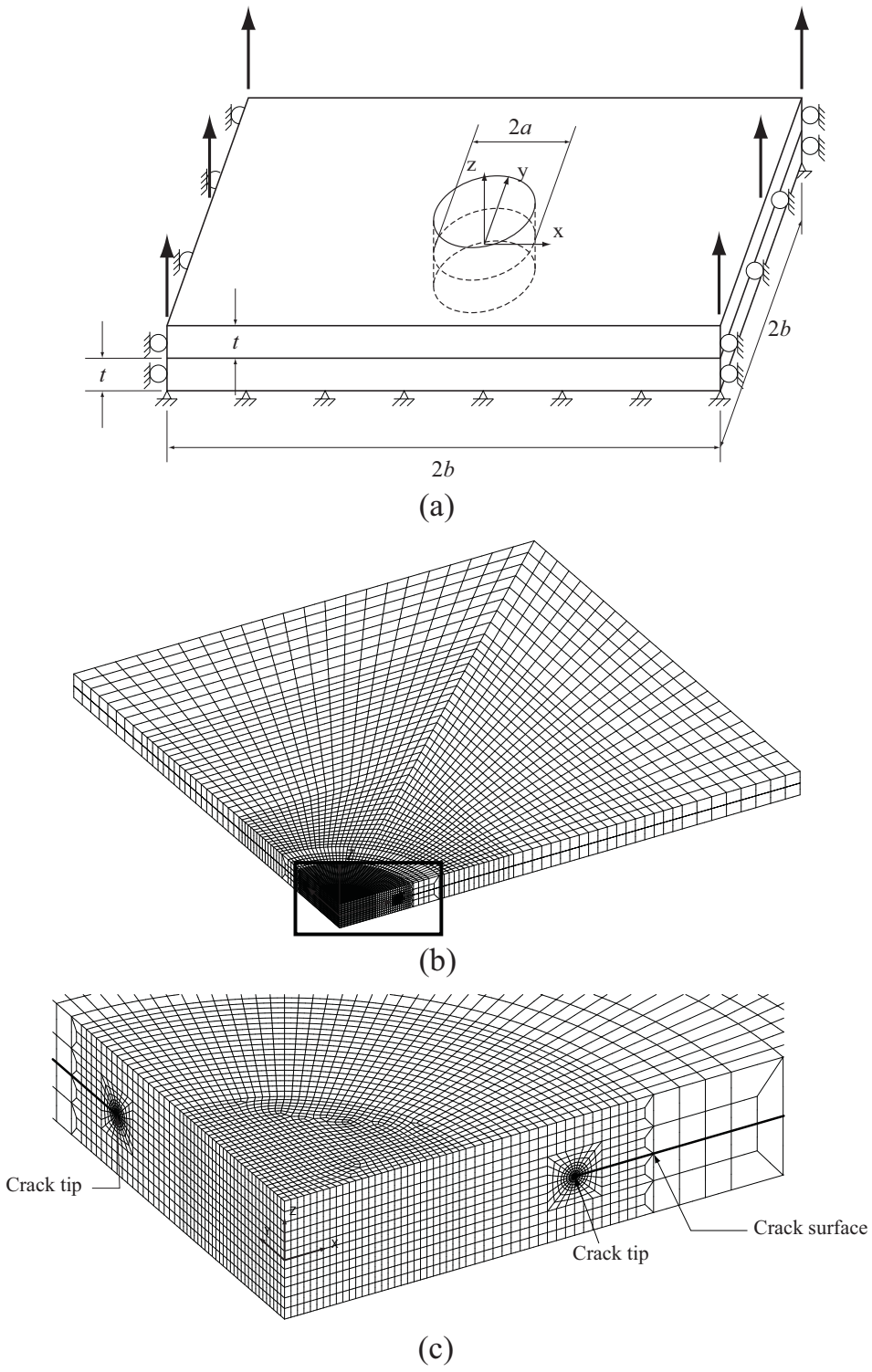

Figure 5.6. (a) A schematic of a three-dimensional finite element model of two square plates of equal thickness with connection under a uniform applied displacement and the roller boundary conditions. (b) A mesh of a three dimensional finite element model for $b/a = 7.94$ and (c) a close-up view of the mesh near the main crack front for model in (c).

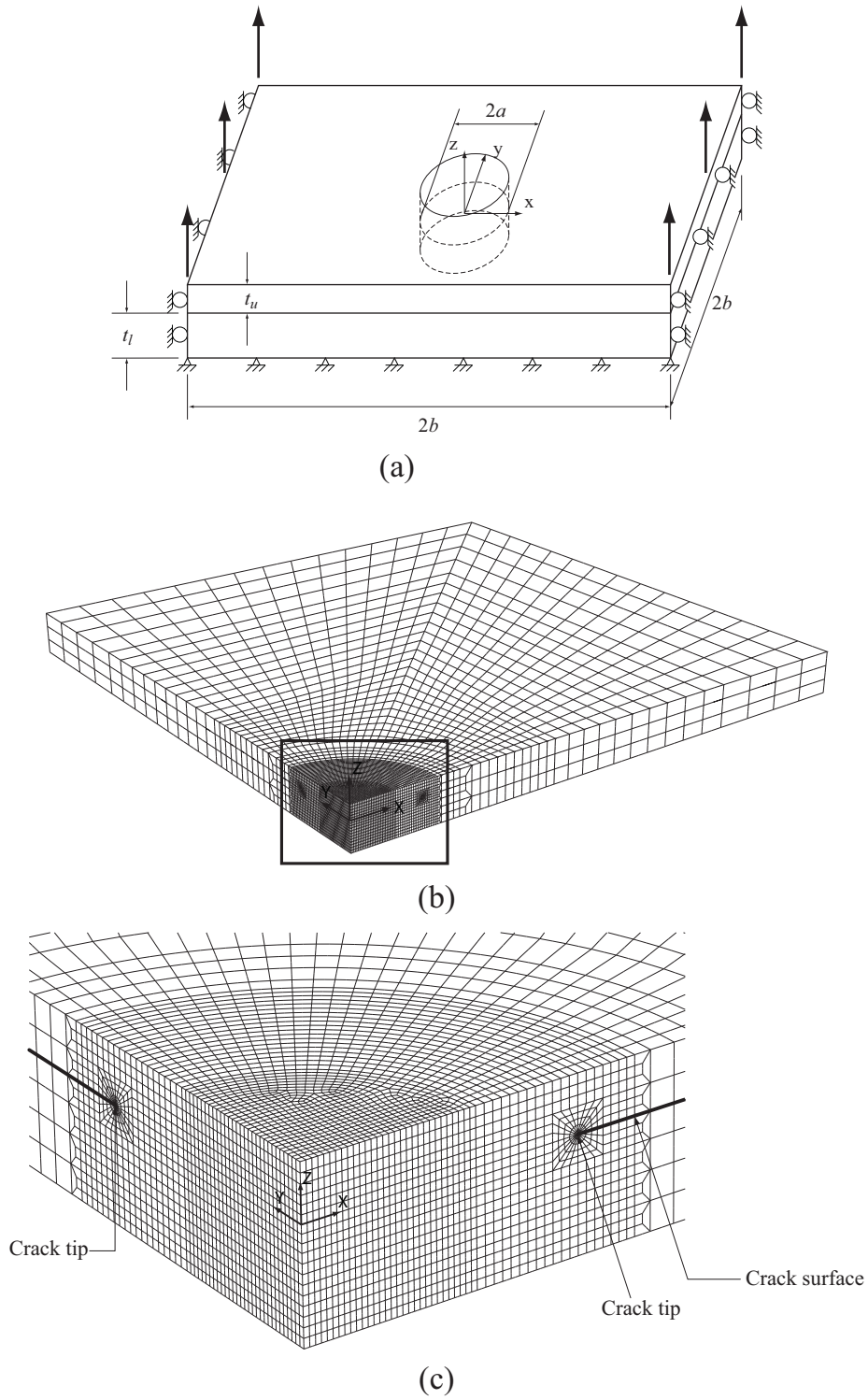

Figure 5.7. (a) A schematic of a three-dimensional finite element model of two square plates of unequal thicknesses with connection under a uniform applied displacement and the roller boundary conditions. (b) A mesh of a three dimensional finite element model for $b/a = 7.94$ and (c) a close-up view of the mesh near the main crack front for model in (c).

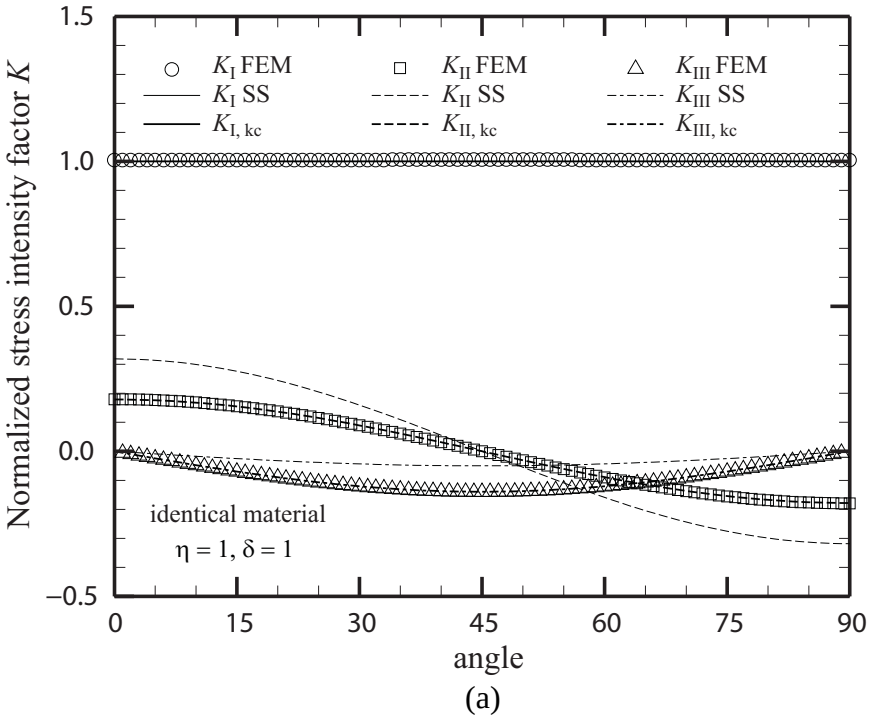

(a)

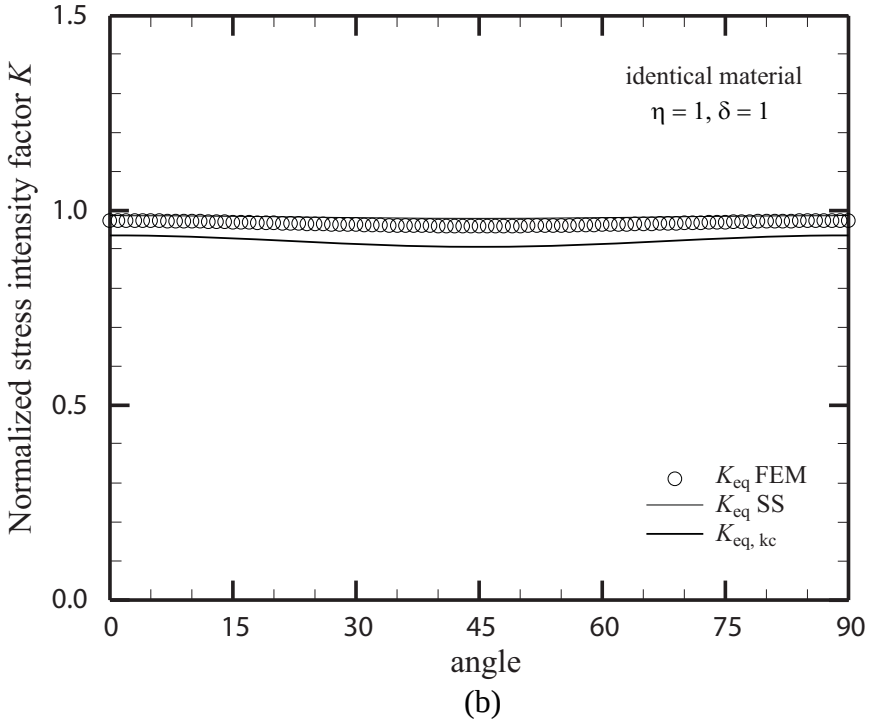

(b)

Figure 5.8. The distributions of (a) the normalized computational and analytical stress intensity factor K_{I}, K_{II} and K_{III} solutions and (b) the normalized computational, analytical equivalent stress intensity factor K_{eq} solutions for spot welds between square plates of identical material with equal thickness.

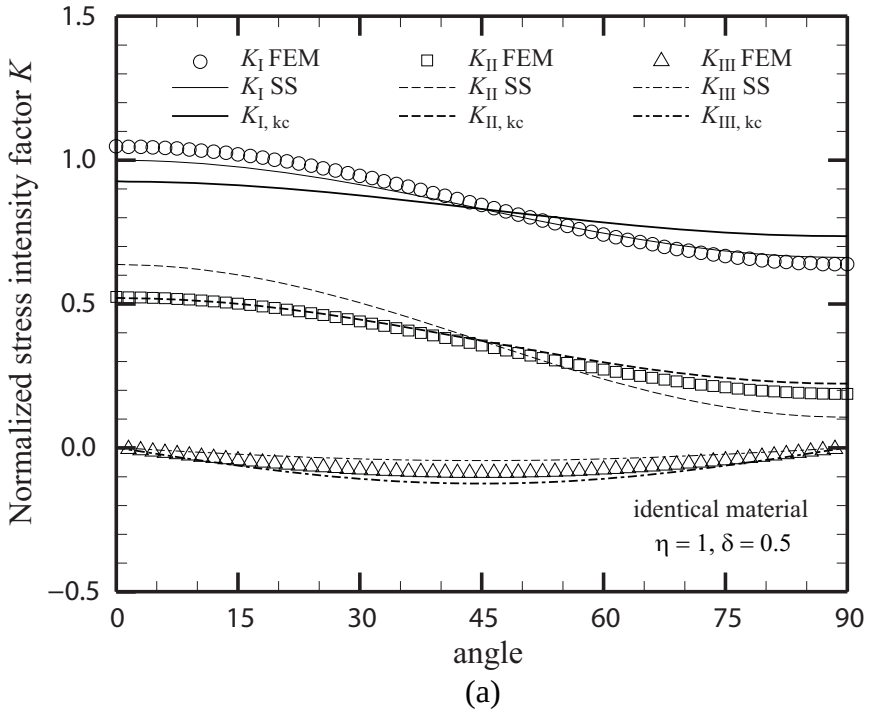

(a)

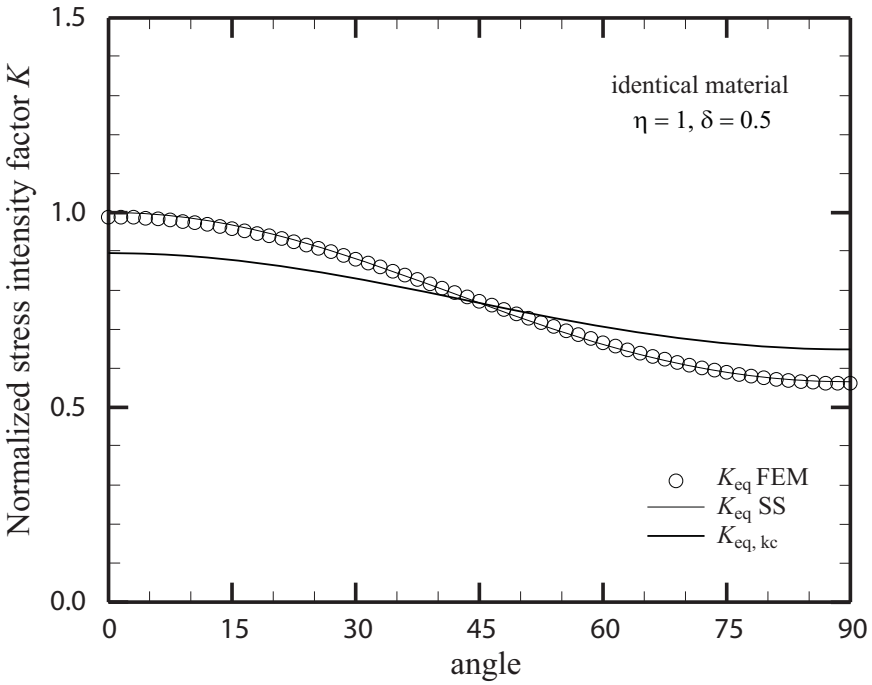

(b)

Figure 5.9. The distributions of (a) the normalized computational and analytical stress intensity factor K_{I}, K_{II} and K_{III} solutions and (b) the normalized computational, analytical equivalent stress intensity factor K_{eq} solutions for spot welds between square plates of identical material with unequal thicknesses.

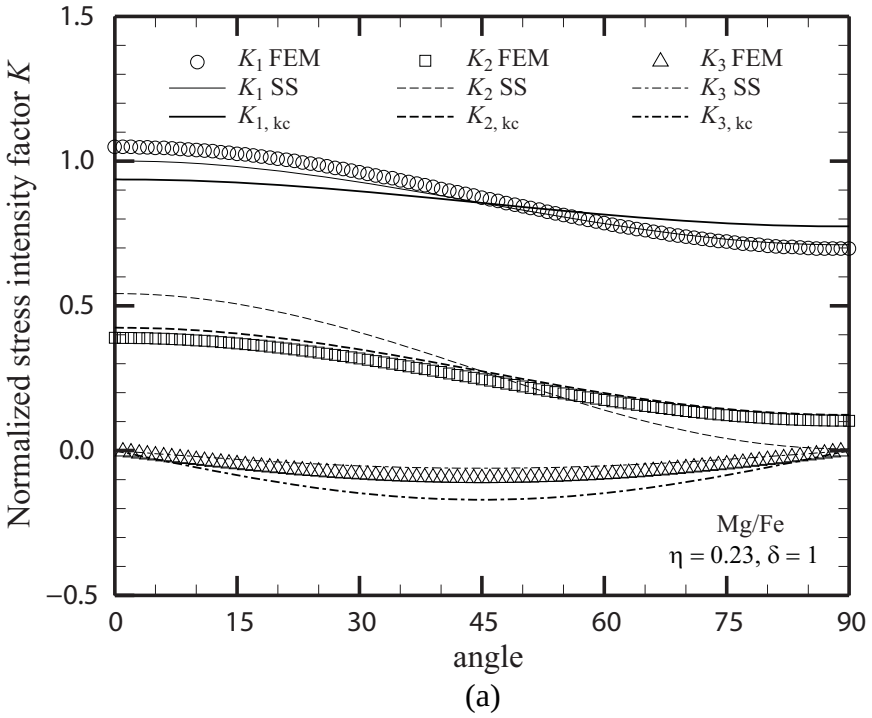

(a)

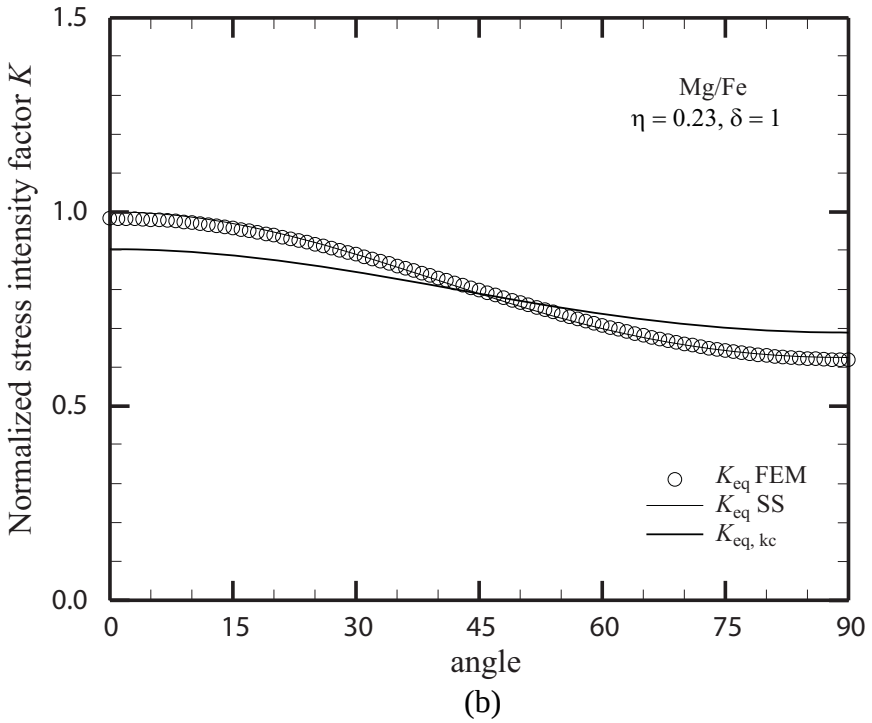

(b)

Figure 5.10. The distributions of (a) the normalized computational, analytical stress intensity factor K_1, K_2 and K_3 solutions and (b) the normalized computational, analytical equivalent stress intensity factor K_{eq} solutions for Mg/Fe spot welds between square plates of equal thickness.

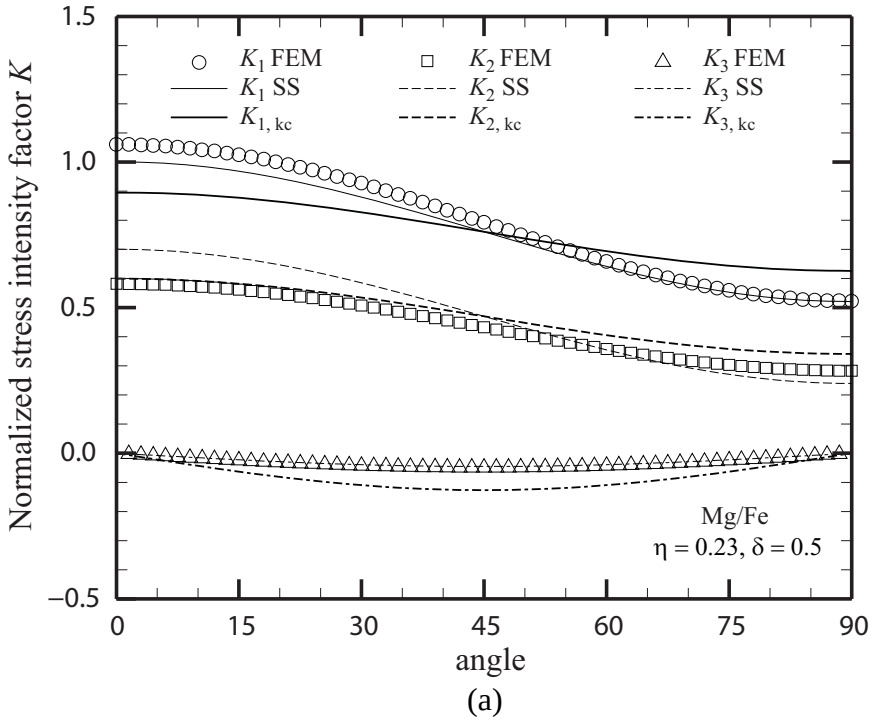

(a)

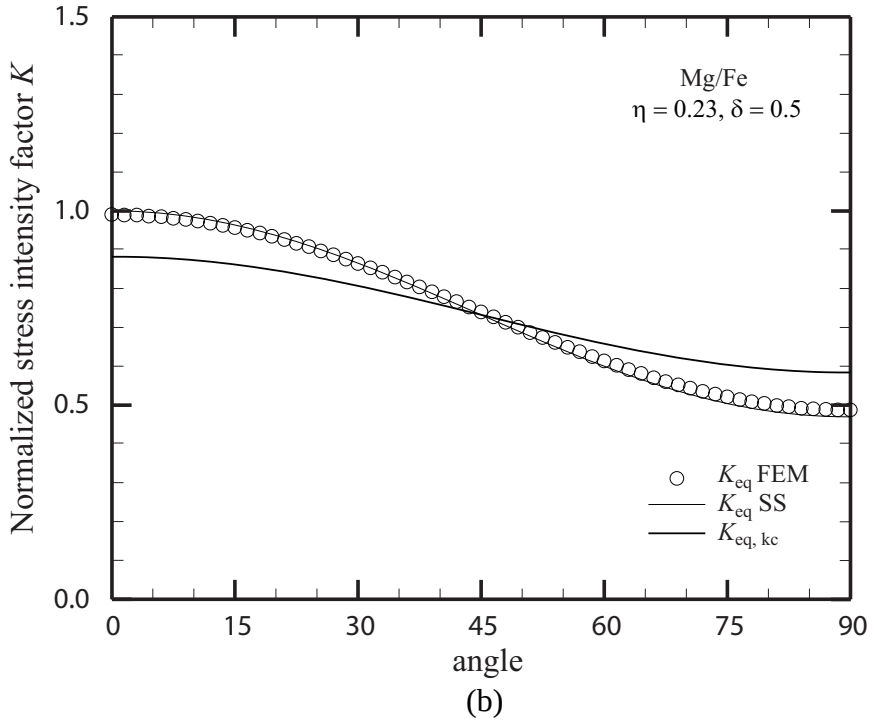

(b)

Figure 5.11. The distributions of (a) the normalized computational, analytical stress intensity factor K_1, K_2 and K_3 solutions and (b) the normalized computational, analytical equivalent stress intensity factor K_{eq} solutions for Mg/Fe spot welds between square plates of unequal thicknesses.

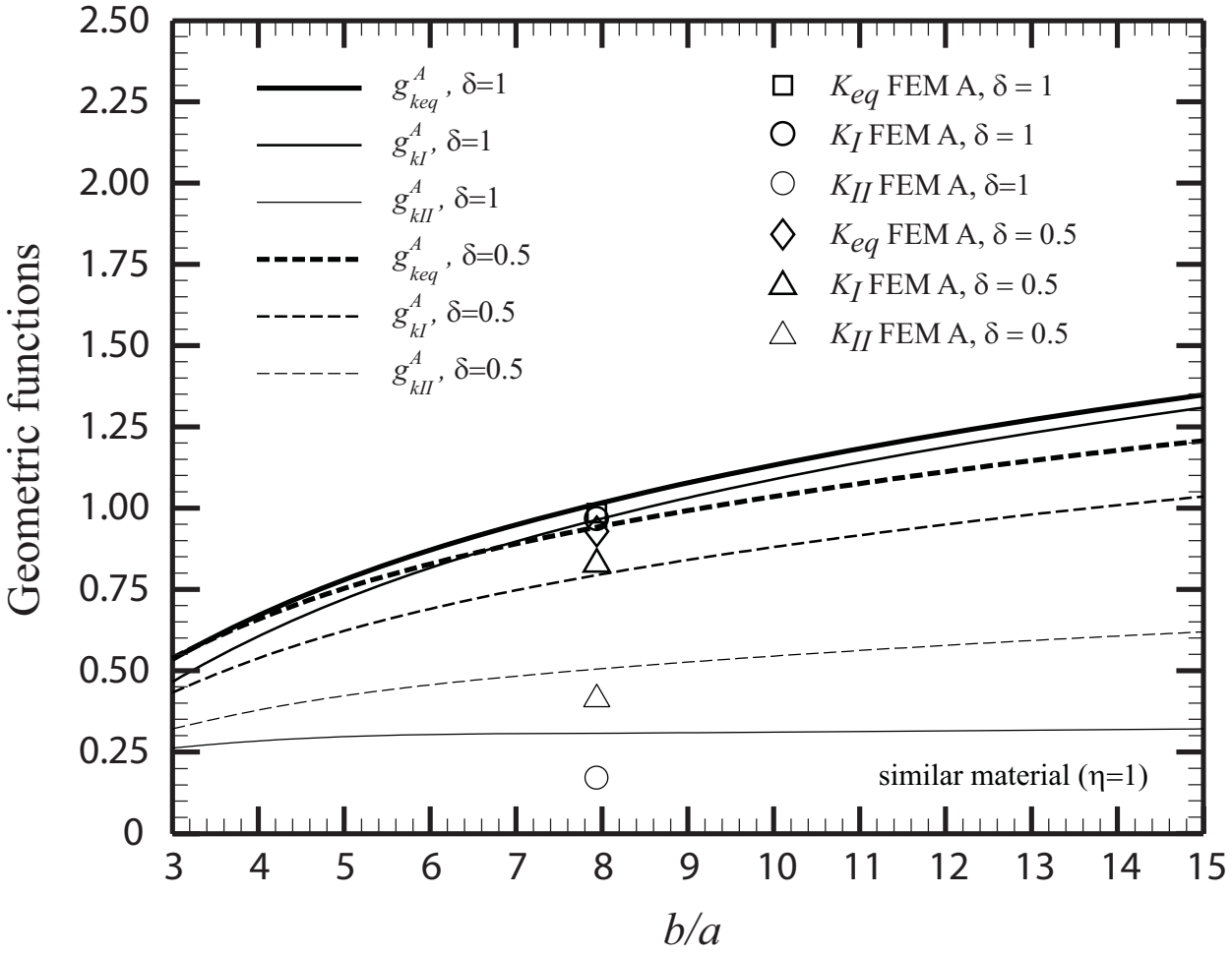

Figure 5.12. The geometric functions g^A_{kI}, g^A_{kII} and g^A_{keq} for spot welds in square plates of identical material for $\delta = 1$ and $\delta = 0.5$ as functions of b/a. The computational solutions are shown as symbols.

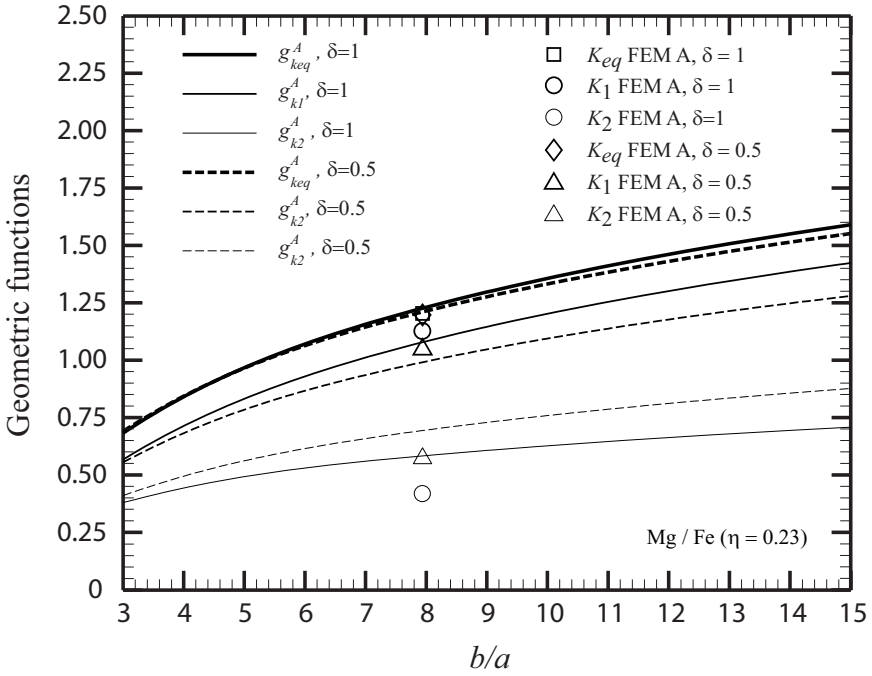
Geometric functions
b/a
Mg / Fe (η = 0.23)
g^A_{keq} , δ=1
g^A_{k1}, δ=1
g^A_{k2} , δ=1
g^A_{keq} , δ=0.5
g^A_{k2}, δ=0.5
g^A_{k2} , δ=0.5
K_{eq} FEM A, δ = 1
K_1 FEM A, δ = 1
K_2 FEM A, δ=1
K_{eq} FEM A, δ = 0.5
K_1 FEM A, δ = 0.5
K_2 FEM A, δ = 0.5

(a)

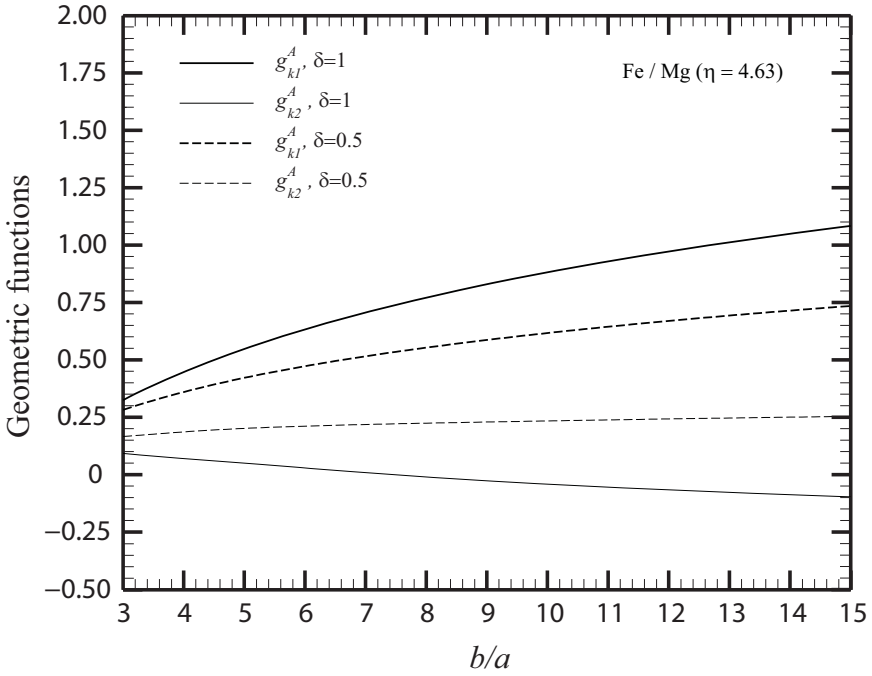
Geometric functions
b/a
Fe / Mg (η = 4.63)
g^A_{k1}, δ=1
g^A_{k2} , δ=1
g^A_{k1}, δ=0.5
g^A_{k2} , δ=0.5

(b)

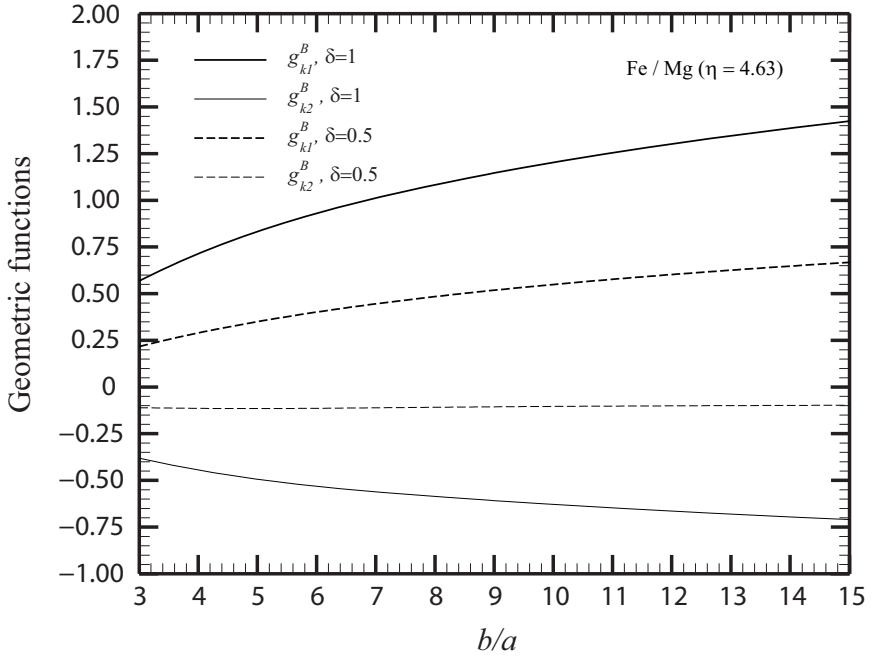

(c)

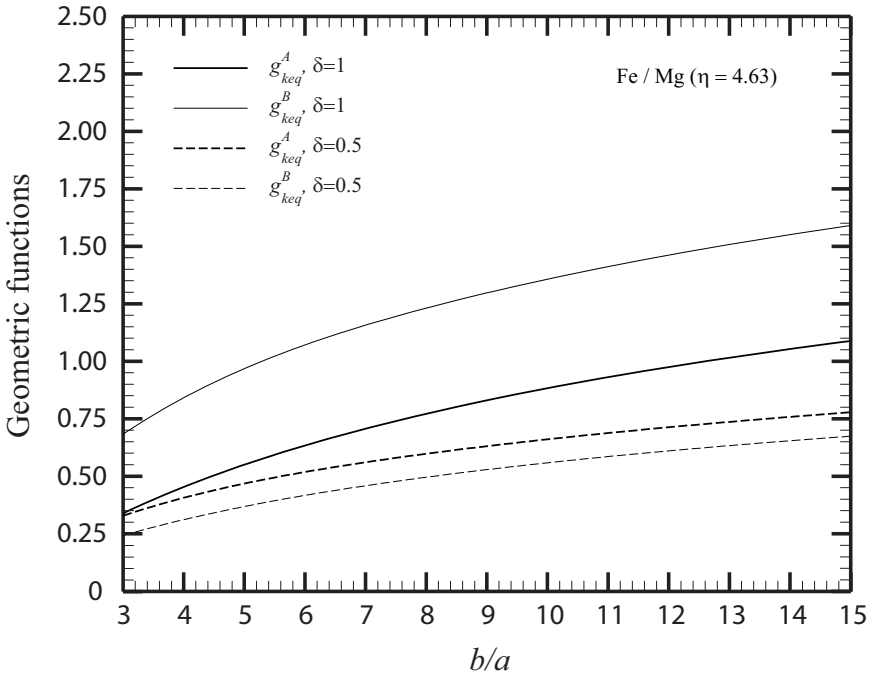

(d)

Figure 5.13. The geometric functions (a) g^A_{k1} and g^A_{k2} for Mg/Fe welds, (b) g^A_{k1} and g^A_{k2} for Fe/Mg welds, (c) g^B_{k1} and g^B_{k2} for Fe/Mg welds and (d) g^A_{keq} and g^B_{keq} for Fe/Mg welds with $\delta = 1$ and $\delta = 0.5$ as functions of b/a. The computational solutions were shown as symbols.

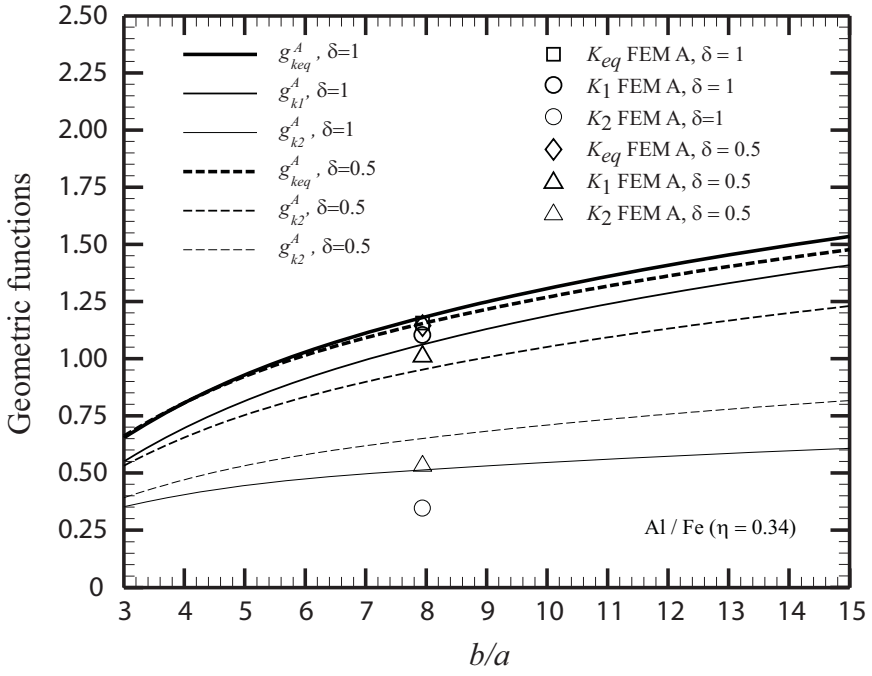
Geometric functions
b/a
g^A_{keq} , δ=1
g^A_{k1}, δ=1
g^A_{k2} , δ=1
g^A_{keq} , δ=0.5
g^A_{k2}, δ=0.5
g^A_{k2} , δ=0.5
K_{eq} FEM A, δ = 1
K_1 FEM A, δ = 1
K_2 FEM A, δ=1
K_{eq} FEM A, δ = 0.5
K_1 FEM A, δ = 0.5
K_2 FEM A, δ = 0.5
Al / Fe (η = 0.34)

(a)

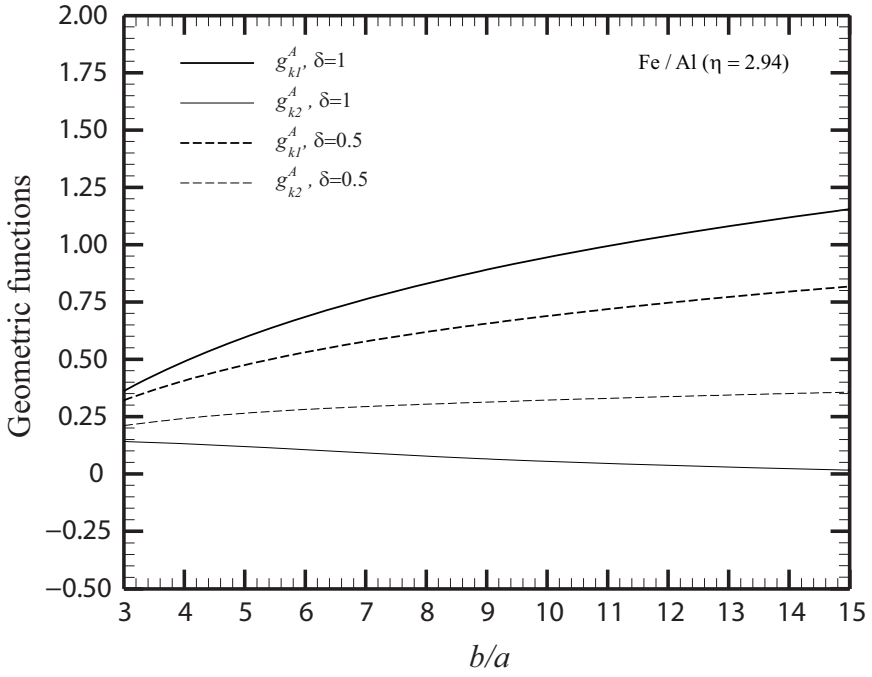
Geometric functions
b/a
g^A_{k1}, δ=1
g^A_{k2} , δ=1
g^A_{k1}, δ=0.5
g^A_{k2} , δ=0.5
Fe / Al (η = 2.94)

(b)

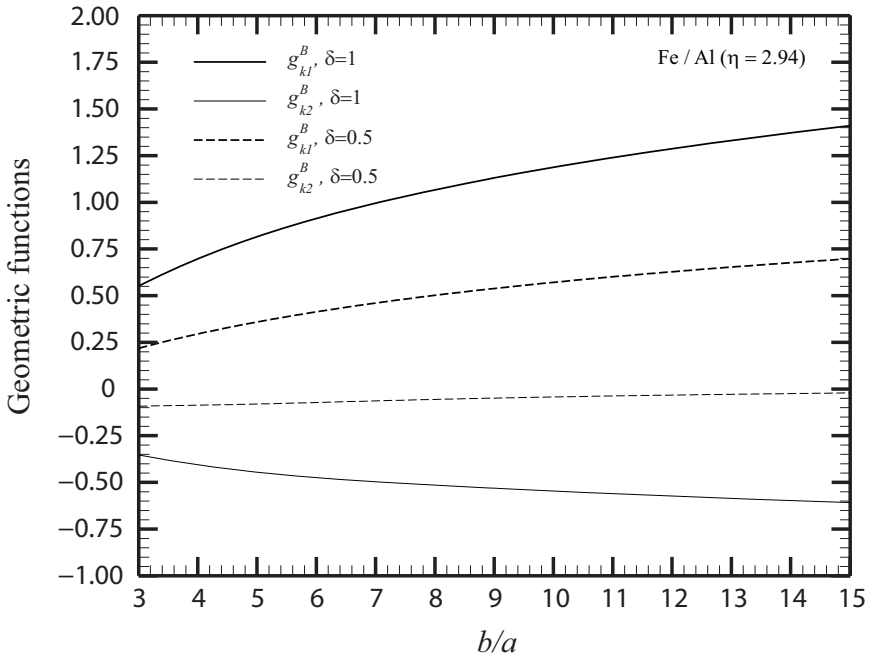

(c)

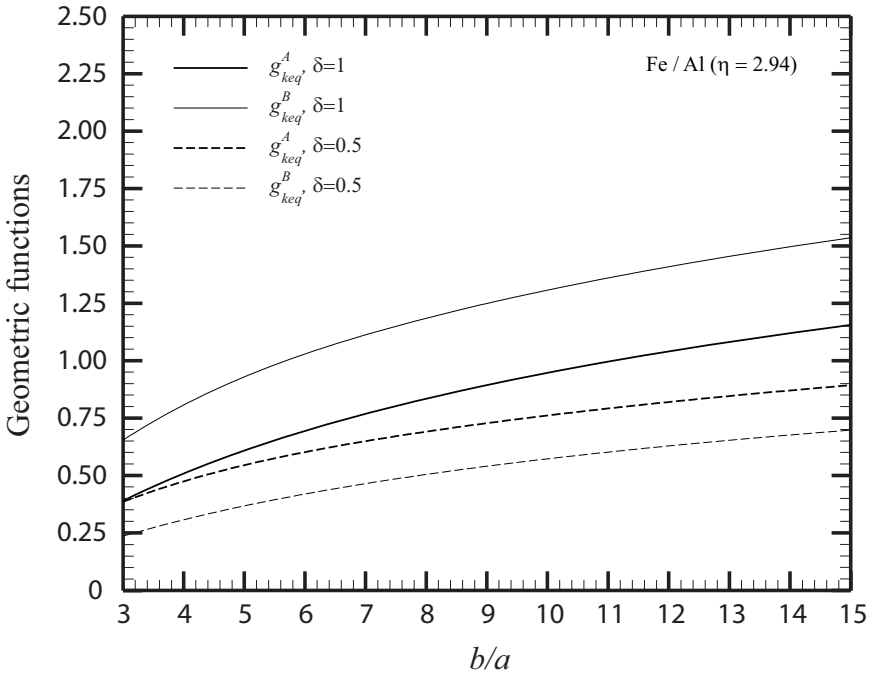

(d)

Figure 5.14. The geometric functions (a) g^A_{k1} and g^A_{k2} for Al/Fe welds, (b) g^A_{k1} and g^A_{k2} for Fe/Al welds, (c) g^B_{k1} and g^B_{k2} for Fe/Al welds and (d) g^A_{keq} and g^B_{keq} for Fe/Al welds with $\delta = 1$ and $\delta = 0.5$ as functions of b/a. The computational solutions were shown as symbols.

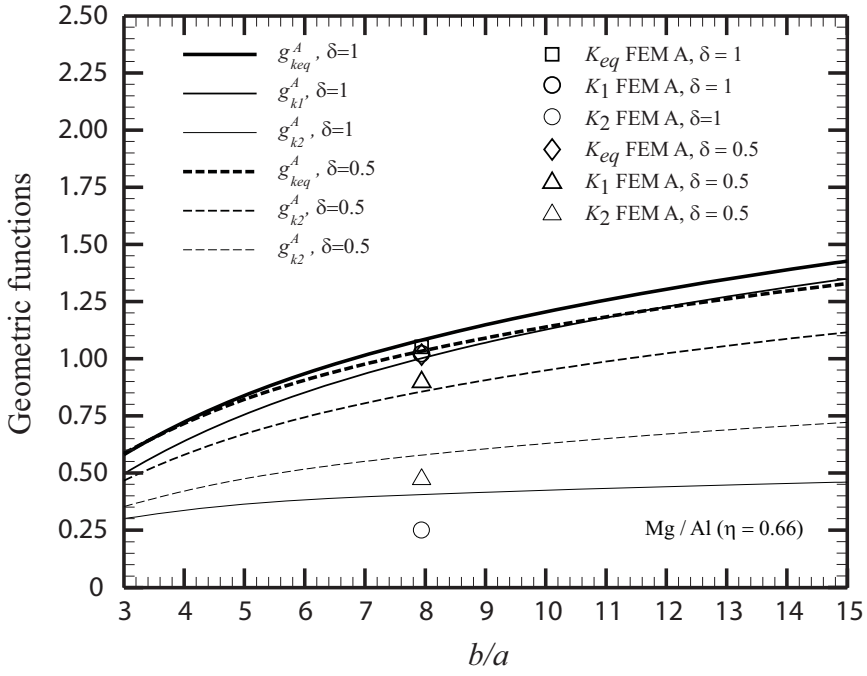
Geometric functions
b/a
g^A_{keq} , δ=1
g^A_{k1}, δ=1
g^A_{k2} , δ=1
g^A_{keq} , δ=0.5
g^A_{k2}, δ=0.5
g^A_{k2} , δ=0.5
K_{eq} FEM A, δ = 1
K_1 FEM A, δ = 1
K_2 FEM A, δ=1
K_{eq} FEM A, δ = 0.5
K_1 FEM A, δ = 0.5
K_2 FEM A, δ = 0.5
Mg / Al (η = 0.66)

(a)

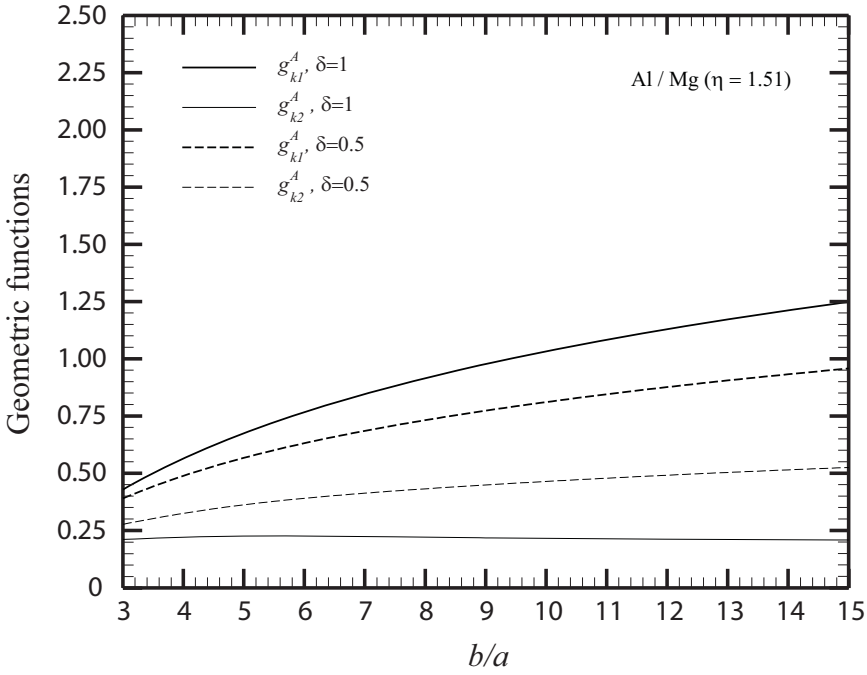
Geometric functions
b/a
g^A_{k1}, δ=1
g^A_{k2} , δ=1
g^A_{k1}, δ=0.5
g^A_{k2} , δ=0.5
Al / Mg (η = 1.51)

(b)

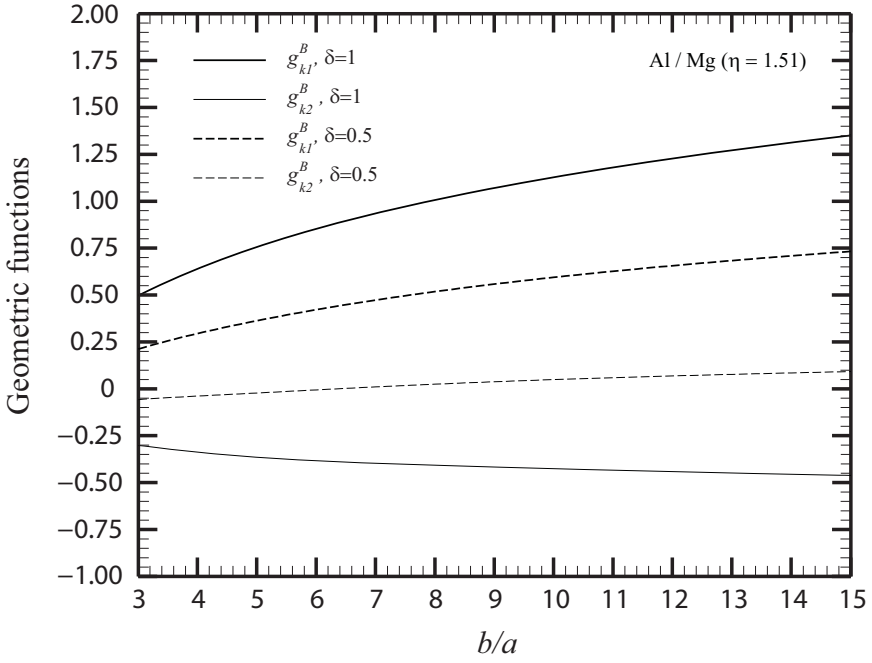

(c)

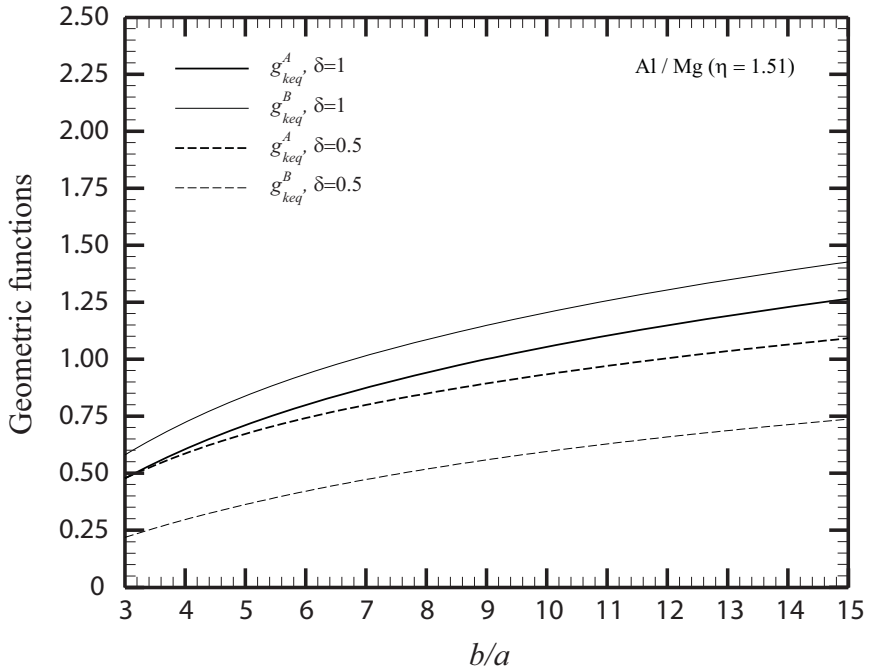

(d)

Figure 5.15. The geometric functions (a) g^A_{k1} and g^A_{k2} for Mg/Al welds, (b) g^A_{k1} and g^A_{k2} for Al/Mg welds, (c) g^B_{k1} and g^B_{k2} for Al/Mg welds and (d) g^A_{keq} and g^B_{keq} for Al/Mg welds with $\delta = 1$ and $\delta = 0.5$ as functions of b/a. The computational solutions were shown as symbols.

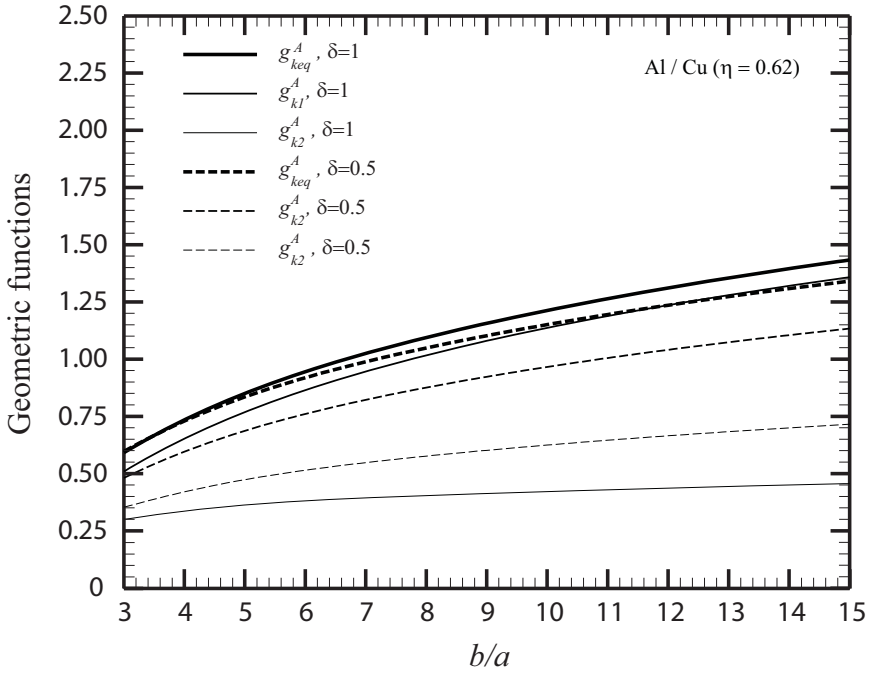
Geometric functions
b/a
Al / Cu (η = 0.62)
g^A_{keq} , δ=1
g^A_{k1}, δ=1
g^A_{k2} , δ=1
g^A_{keq} , δ=0.5
g^A_{k2}, δ=0.5
g^A_{k2} , δ=0.5

(a)

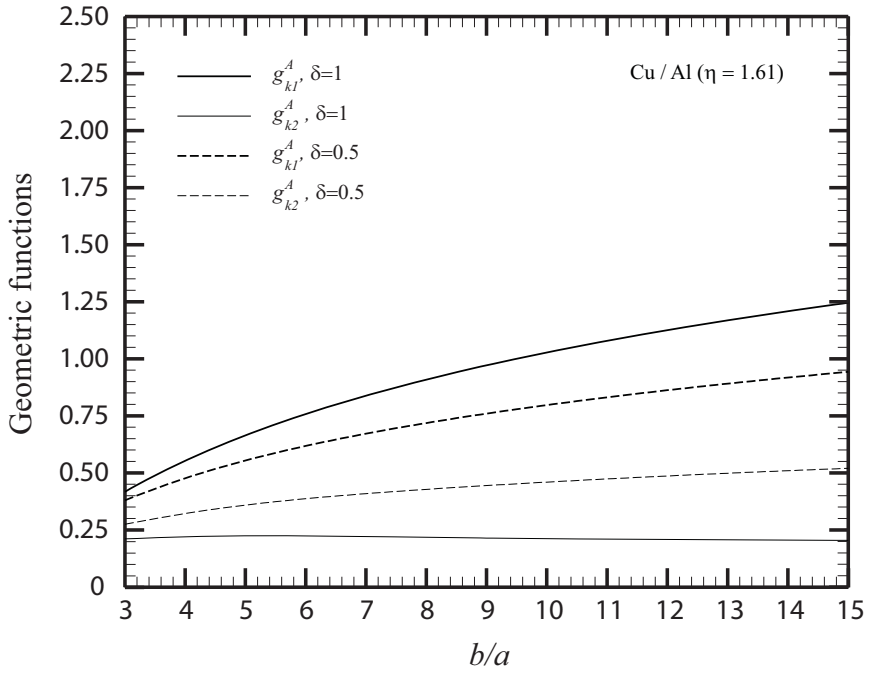
Geometric functions
b/a
Cu / Al (η = 1.61)
g^A_{k1}, δ=1
g^A_{k2} , δ=1
g^A_{k1}, δ=0.5
g^A_{k2} , δ=0.5

(b)

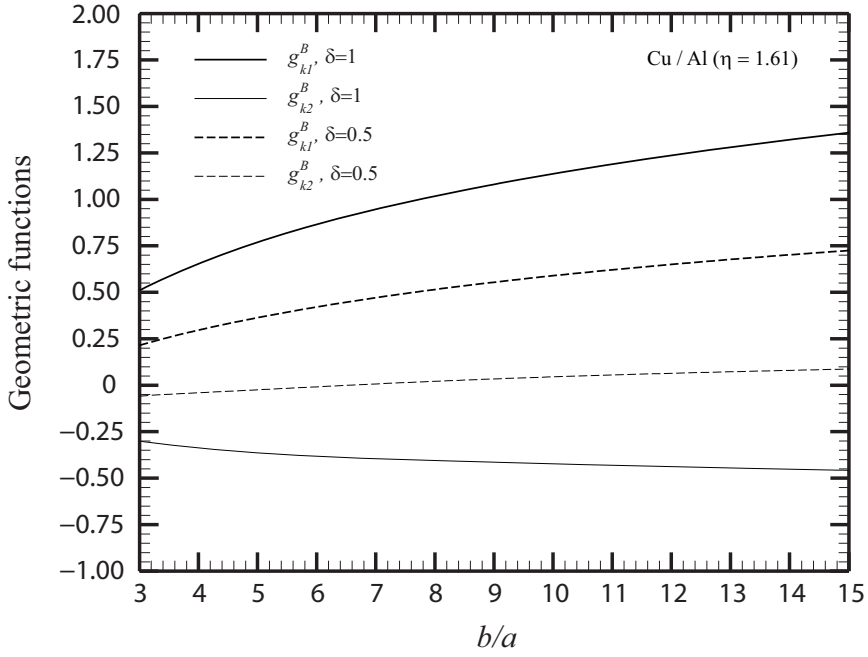

(c)

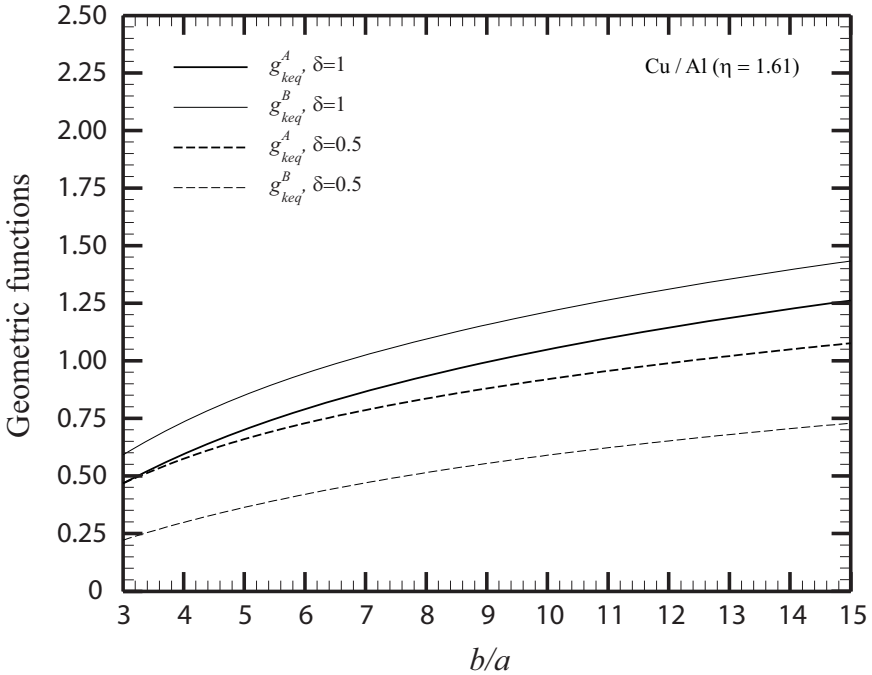

(d)

Figure 5.16. The geometric functions (a) g^A_{k1} and g^A_{k2} for Al/Cu welds, (b) g^A_{k1} and g^A_{k2} for Cu/Al welds, (c) g^B_{k1} and g^B_{k2} for Cu/Al welds and (d) g^A_{keq} and g^B_{keq} for Cu/Al welds with $\delta = 1$ and $\delta = 0.5$ as functions of b/a. The computational solutions were shown as symbols.

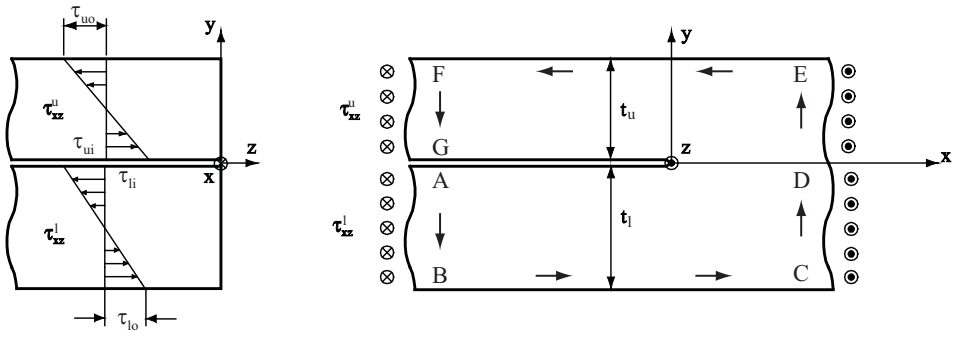

Model A

=

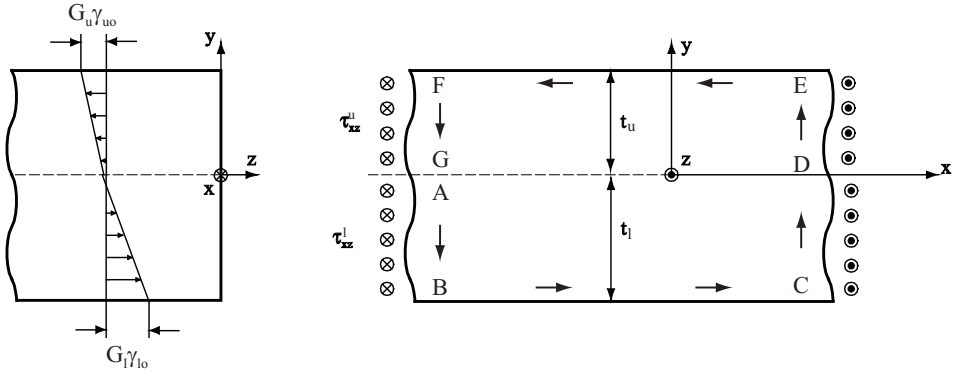

Model F

+

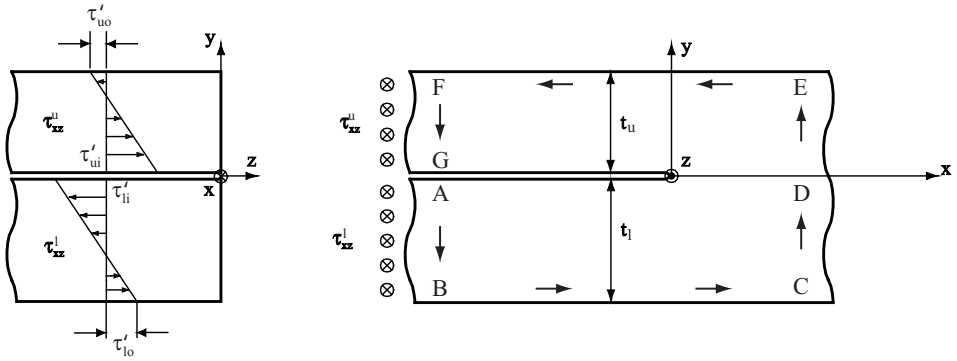

Model G

Figure 5.A1. The decomposition of the out-of-plane shear stress distribution of a strip model. Model A represents a spot weld under an out-of-plane shear loading condition. The out-of-plane shear loading condition of model A is decomposed into the loading conditions of models G and H.

.

CHAPTER VI

CONCLUSIONS

In Chapter II, Fatigue behavior of laser welds in lap-shear specimens of high strength low alloy (HSLA) steel is investigated based on experimental observations and two fatigue life estimation models. Fatigue experiments of laser welded lap-shear specimens are first reviewed. Analytical stress intensity factor solutions for laser welded lap-shear specimens based on the beam bending theory are derived and compared with the analytical solutions for two semi-infinite solids with connection. Finite element analyses of laser welded lap-shear specimens with different weld widths were also conducted to obtain the stress intensity factor solutions. Approximate closed-form stress intensity factor solutions based on the results of the finite element analyses in combination with the analytical solutions based on the beam bending theory and Westergaard stress function for a full range of the normalized weld widths are developed for future engineering applications. Next, finite element analyses for laser welded lap-shear specimens with two weld widths were conducted to obtain the local stress intensity factor solutions for kinked cracks as functions of the kink length. The computational results indicate that the kinked cracks are under dominant mode I loading conditions and the normalized local stress intensity factor solutions can be used in combination with the global stress intensity factor solutions to estimate fatigue lives of laser welds with the weld width as small as the sheet thickness. The global stress intensity factor solutions

and the local stress intensity factor solutions for vanishing and finite kinked cracks are then adopted in a fatigue crack growth model to estimate the fatigue lives of the laser welds. Also, a structural stress model based on the beam bending theory is adopted to estimate the fatigue lives of the welds. The fatigue life estimations based on the fatigue crack growth model with the local stress intensity factor solutions as functions of the kink length and the structural stress model are agree well with the experimental results.

In Chapter III, closed-form structural stress and stress intensity factor solutions for spot welds in square plates under opening loading conditions are investigated. First, the existing analytical axisymmetric solutions for a rigid inclusion in a circular plate with simply supported and clamped outer edges are reviewed. Then the results of axisymmetrical finite element analyses for a rigid inclusion in a circular plate are presented. The results indicate that the finite element model with one element across the plate thickness is an appropriate model to investigate the structural stress solutions for a rigid inclusion in a square plate to avoid the local effect of the reaction force due to the constraint applied to the rigid inclusion. Next, the results of three-dimensional finite element analyses for a rigid inclusion in a square plate with simply supported and clamped outer edges are presented. The results indicate that, as the ratio of the plate width to the rigid inclusion diameter becomes large about 6, the structural stress solutions along the circumference of the rigid inclusion become almost uniform. Approximate equivalent radius solutions are then determined in order to use the analytical structural stress solutions for a rigid inclusion in a circular plate to calculate the structural stress solutions along the circumference of the rigid inclusion in a square plate. Then, the results of three-dimensional finite element analyses for spot welds between square plates

of different thicknesses and materials are presented. The results indicate that the computational stress intensity factor solutions agree well with those based on the structural stress solutions with the equivalent radius. Based on the closed-form structural stress solutions, complete sets of the normalized stress intensity factor solutions for spot welds between square plates of different thicknesses and materials under opening loading conditions are presented for combinations of steel, aluminum and magnesium sheets and combinations of aluminum and copper sheets for convenient engineering applications.

In Chapter IV, closed-form structural stress and stress intensity factor solutions for spot welds in square overlap parts of cross-tension specimens are systematically examined and presented here. First, the closed-form analytical solutions for a rigid inclusion in a square plate of Lin and Pan are reviewed. Then the results of three-dimensional finite element analyses for a rigid inclusion in a square plate under opening and bending loading conditions are presented. The results indicate that, the structural stress solutions obtained from finite element analyses can be expressed as a constant plus a cosine function. The results of the opening force and constraint moment per unit length along the constrained outer edges indicates that the distributions of the opening force and constraint moment per unit length are non-uniform. The equivalent coefficients for the structural stress solutions for a rigid inclusion in a square plate are introduced in order to use the closed-form structural stress solutions of Lin and Pan to calculate the structural stress solutions along the circumference of the rigid inclusion in a square plate. The computational out-of-plane shear structural stress solution is also investigated. Due to the fact that the closed-form solutions based on the Kirchhoff plate theory are unable to capture the out-of-plane shear structural stress solution for a rigid inclusion in a square

plate under opening and bending loading conditions, the numerical out-of-plane shear structural stress solution is introduced based on the amplitude of the cosine function of the in-plane structural stress solutions. The numerical coefficient for the out-of-plane shear structural stress solution is also presented for selected values of b/a. Then, the results of three-dimensional finite element analyses for spot welds between square plates of similar material with equal thickness are presented. The results indicate that the computational stress intensity factor K_{I} solutions agree well with those based on the structural stress solutions with the equivalent coefficients. However, the computational stress intensity factor K_{II} solutions are lower than those based on the structural stress solutions with the equivalent coefficients. The computational stress intensity factor K_{III} solutions are higher than those based on the in-plane structural stress solutions with the equivalent and numerical coefficients. These may come from the flexibility of the spot welds between square plates under opening and bending loading conditions. The fitting coefficients for the stress intensity factor solutions are then introduced. The computational stress intensity factor K_{II} and K_{III} solutions agree well with those based on the closed-form structural stress solutions with the equivalent and numerical coefficients for the structural stress and the fitting coefficients for the stress intensity factor.

In Chapter V, closed-form stress intensity factor solutions for spot welds in square overlap parts of cross-tension specimens are investigated here. First, the closed-form analytical solutions for a rigid inclusion in a square plate under opening and bending loading conditions based on the closed-form analytical solutions of Lin and Pan are reviewed. Then, the J integral and stress intensity factor solutions for spot welds

between square plates are presented in terms of the structural stresses for a strip model. The results of three-dimensional finite element analyses for spot welds between square plates of different thicknesses and materials are presented. The analytical stress stress intensity factor solutions at the critical locations for spot welds between square plates based on the structural stress solutions with the equivalent and fitting coefficients are compared with the computational results. The results indicate that, the computational equivalent stress intensity factor solutions agree well with those based on the structural stress solutions with only the equivalent coefficients. Based on the closed-form structural stress solutions, complete sets of the normalized stress intensity factor solutions for spot welds between square plates of different thicknesses and materials under opening and bending loading conditions are presented for combinations of steel, aluminum and magnesium sheets and combinations of aluminum and copper sheets for convenient engineering applications.